A UNIFYING APPROACH TOWARDS THE GEOMETRICAL INSTABILITIES OF COMPRESSIBLE, MULTILAYER DOMAINS

A THESIS SUBMITTED TO
THE GRADUATE SCHOOL OF ENGINEERING AND SCIENCE
OF BILKENT UNIVERSITY
IN PARTIAL FULFILLMENT OF THE REQUIREMENTS FOR
THE DEGREE OF
MASTER OF SCIENCE
IN
MECHANICAL ENGINEERING

By
Ayşe Derya Bakiler
July 2022

A UNIFYING APPROACH TOWARDS THE GEOMETRICAL INSTABILITIES OF COMPRESSIBLE, MULTILAYER DOMAINS

By Ayşe Derya Bakiler

July 2022

We certify that we have read this thesis and that in our opinion it is fully adequate, in scope and in quality, as a thesis for the degree of Master of Science.

Ali Javili (Advisor)

Gökberk Kabacaoğlu

Serdar Göktepe

Approved for the Graduate School of Engineering and Science:

Orhan Arıkan
Director of the Graduate School

ABSTRACT

A UNIFYING APPROACH TOWARDS THE GEOMETRICAL INSTABILITIES OF COMPRESSIBLE, MULTILAYER DOMAINS

Ayşe Derya Bakiler
M.S. in Mechanical Engineering
Advisor: Ali Javili
July 2022

Instabilities that arise in layered systems have been a riveting course of study for the past few decades, having found utility in various fields, while also being frequently observed in biological systems. However, the *large deformation bifurcation analysis of compressible domains* remains vastly understudied compared to the *incompressible* case. In this work, we present a unifying approach for the instability analysis of multilayer *compressible* elastic domains under plane deformations, also extending the approach to include the general interface model and to capture growth-induced instabilities. First, a linear elastic, displacement-based approach to capture bilayer wrinkling is taken, outlining the basics of such an approach. Then, the large-deformation incremental analysis for a rectangular, compressible, hyperelastic domain under plane deformations is developed, which serves as a generic framework for other geometries. This framework is applied to beam, half-space, bilayer and trilayer structures. Next, the framework is extended to account for the general interface model, looking into coated half-spaces, coated beams, and bilayers with interfaces. Finally, the framework is derived to account for both compression and growth. Obtained analytical results for the onset of wrinkling are compared with computational simulations using the finite element method (FEM) enhanced with eigenvalue analysis, cultivating excellent agreements between analytical and numerical results all across the material and geometrical parameter spectrum, and portraying clearly the significant effect of compressibility on bifurcation behavior. The analytical framework presented here provides grounds for further works on other modes of instabilities and more complex geometries.

Keywords: Geometrical instabilities, buckling, compressibility, large deformations.

ÖZET

SIKIŞTIRILABİLİR ÇOK KATMANLI YAPILARIN GEOMETRİK İNSTABİLİTELERİNİ ANLAMAYA DOĞRU BÜTÜNLEYİCİ BİR YAKLAŞIM

Ayşe Derya Bakiler
Makine Mühendisliği, Yüksek Lisans
Tez Danışmanı: Ali Javili
Temmuz 2022

Çok katmanlı sistemlerde ortaya çıkan instabiliteler, biyolojik sistemlerde de sıklıkla gözlemlenmekle beraber, çeşitli alanlarda kullanım alanı bulmuştur ve son birkaç yıldır ilgi çekici bir araştırma konusu olmuştur. Bununla birlikte, *sıkıştırılabilir yapıların büyük deformasyonlar altında instabilite analizlerinin*, literatürde eksik kaldığı görülmektedir. Bu çalışmada, düzlem deformasyonları altında çok katmanlı *sıkıştırılabilir* elastik yapıların instabilite analizi için bütünleyici bir yaklaşım sunulmakta, ayrıca bu yaklaşım genel arayüz modelini içerecek ve büyümeye bağlı instabiliteleri yakalayacak şekilde genişletilmektedir. İlk olarak, iki katmanlı yapılardaki kırışmayı yakalamak için lineer elastik, deformasyona dayalı bir yaklaşım ele alınır. Daha sonra, tüm geometriler için genel bir analitik çerçeve görevi görecek, dikdörtgen, sıkıştırılabilir, hiperelastik bir yapı için büyük deformasyon instabilite analizi geliştirilir. Bu analitik çerçeve kiriş, yarı-sonsuz dikdörtgen, iki katmanlı ve üç katmanlı yapılara uygulanır. Geliştirilen çerçeve kaplanmış yarı-sonsuz dikdörtgenler, kaplanmış kirişler ve arayüzlü çift katmanlar üzerinden genel arayüz modelini hesaba katacak şekilde genişletilir. Son olarak, çerçeve hem sıkıştırma hem de büyümeyi hesaba katacak şekilde türetilir. Teorik sonuçların, özdeğer analizi ile geliştirilmiş sonlu elemanlar metodu kullanılarak elde edilen hesaplayımsal sonuçlar ile karşılaştırılması ile bütün parametreler için sonuçlar arasında mükemmel uyum elde edildiği ve sıkıştırılabilirliğin instabilite davranışını kayda değer şekilde etkilediği görülmüştür. Burada sunulan analitik çerçeve, diğer instabilite modları ve daha karmaşık geometriler hakkında daha fazla çalışma için zemin sağlamaktadır.

Anahtar sözcükler: Geometrik instabiliteler, burkulma, sıkıştırılabilme, büyük deformasyonlar.

Acknowledgement

I would like to express my sincere gratitude and admiration to my advisor, Professor Ali Javili, who has taught me almost everything I know and has helped me find what I truly want to do, always with the utmost kindness and patience. I am forever grateful to have you as my advisor and friend. I would also like to thank Professor Gökberk Kabacaoğlu and Professor Serdar Göktepe for taking part in my committee and for their invaluable feedback.

My sincere thanks go to my labmate Ekim, for always being there for me both in the lab and outside with unwavering support. I must also thank my dearest friend Dilan, for her love and support through the worst of times and the best of times, and for always inspiring me. My dearest, Deniz, thank you for being the wind in my back and light in my life.

Luna, thank you for blessing my life with your furry existence. Yunus, thank you for always motivating me and for your precious insights into my research. Dad, I could not have done this without you - thank you for the endless love and support.

I would like to dedicate this thesis to my Mom. Thank you for believing in me more than anyone and more than myself, and for making me who I am today.

Contents

1 Introduction **1**

1.1 Literature review 2

1.2 Organization of the manuscript 9

1.3 Key aspects and summary 10

2 Continuum mechanics at large deformations **11**

2.1 Notation and definitions 12

2.2 Kinematics 12

2.3 Governing equations 14

2.4 Constitutive behavior 14

2.5 Numerical approach 19

3 Small strain instabilities **25**

3.1 Effective stiffness of a half-space 25

3.2 Wrinkling of a growing layer 35

4 Finite strain instabilities due to compression 41

4.1 Theoretical framework 42

4.2 Half-space instability 49

4.3 Beam instability 53

4.4 Bilayer instability 61

4.5 Trilayer instability 70

5 Finite strain instabilities with interfacial mechanics 85

5.1 Interface models 86

5.2 Theoretical framework 87

5.3 Coated half-space instability 95

5.4 Coated beam instability 98

5.5 Bilayer with general interface model instability 101

6 Finite strain instabilities due to growth and compression 113

6.1 Theoretical framework 114

6.2 Uniaxial compression and growth in rectangular domains 116

6.3 Bilayer with growing film 120

7 Summary and outlook 126

A Further information on FEM using eigenvalue analysis 130

B Incompressible half-space **134**

C Non-linear Poisson's ratio **138**

List of Figures

2.1 Deformation of a continuum body. The continuum body occupies the material configuration $\mathcal{B}_0 \in \mathbb{R}^3$ at time $t = 0$ and is mapped to the spatial configuration $\mathcal{B}_t \in \mathbb{R}^3$ via the smooth nonlinear deformation map $\boldsymbol{\varphi}$. 13

2.2 Schematic illustration of the finite elements and approximation of an infinite half-space and associated boundary conditions suitable for the finite element method. The domain is truncated sufficiently far from the surface and must be long enough. 21

3.1 Illustration of a decaying surface wave through the infinite half-space representing the substrate here. The stationary wave $\boldsymbol{u}$ can be prescribed as the product of a decay part $\boldsymbol{w}(\eta)$ and a waviness term $\exp(ik\xi)$ in which $k > 0$ is the wavenumber. 28

3.2 Illustration of the stationary wave $\boldsymbol{u}$ for various wavenumbers k and at different depths η. According to the relation $\tau = k$ the decay coefficient τ must be identical to the wavenumber k in order to have an admissible wave function (3.7). Therefore, a surface wave with a larger wavelength decays slower compared to a wave with a smaller wavelength. 31

3.3 Numerical illustrations of u_ξ, u_η, $\sigma_{\xi\xi}$, $\sigma_{\eta\eta}$ and $\sigma_{\xi\eta}$ for a sample set of parameters $\mu_s = 10$, $\lambda_s = 100$ and $C = 0.15$. Analytical solution of the fields correspond to the displacement-based approach. . . . 33

3.4 Decomposition of the domain into the film and substrate. The film is perfectly bonded to the substrate at all times. The amplitude of the sinusoidal wave on the substrate and its decay versus depth η is schematically illustrated on the graph. 36

3.5 Comparison between analytical solution and computational simulations using the finite element method for growth induced instabilities of a thin film on a compliant substrate. For each case, both the critical growth g_{cr} and the critical wavelength ℓ_{cr} are shown in the graphs. 39

4.1 A qualitative representation of the generic rectangular domain under consideration, given together with the coordinate system and the applied deformations of $\boldsymbol{F}$ and $\boldsymbol{F} + \delta\boldsymbol{F}$. 42

4.2 Overview of the traction boundary conditions of the three problems covered in this work (from left to right): half-space, beam, bilayer and trilayer. 49

4.3 Illustration of Det$\boldsymbol{Q}$ and its roots. The non-trivial solutions of Det$\boldsymbol{Q} = 0$ for any α are highlighted and gathered separately as critical stretches λ_{cr}. Recall that for a given α Poisson's ratio is obtained as $\nu = \alpha/[1 + \alpha]$. 51

4.4 Analytical, numerical and curve-fit results for the critical λ at various values of α, where $\alpha = \nu/[1 - \nu]$ or alternatively, $\nu = \alpha/[1 + \alpha]$. 52

4.5 Plot of the integer λ_{cr} vs. n, for a beam of length $L = 60$, height $h = 1$ and compressibility $\nu = 0.95$, together with further possible modes of the instability that correspond to various wavenumbers k. The wavelength ℓ_{cr} corresponds to the referential length of the beam. The inset shows the pitchfork bifurcation pattern, i.e. compression vs. amplitude. 56

4.6 Surface plot of critical stretch λ_{cr}, with changing ratio h/L and compressibility ν (center), along with insets that show λ_{cr} vs. ν (left) and λ_{cr} vs. h/L (right), together with numerical findings, for a beam of length $L = 60$. 57

4.7 The buckled configuration obtained from numerical simulations, for a beam of length $L = 60$, for various h and Poisson's ratios ν. 58

4.8 The vertical and horizontal incremental displacement profiles along the height of a beam of length $L = 60$, for various h/L and Poisson's ratios ν. 59

4.9 Comparison of our results (Current) with the established Euler beam theory, for different compressibilities ν. Orange line indicates the percentage error that the Euler theory has compared to the current results. The error is computed by $|\varepsilon_{\text{cr}}^{\text{Euler}} - \varepsilon_{\text{cr}}^{\text{Curr.}}|/\varepsilon_{\text{cr}}^{\text{Curr.}} \times 100\%$. 60

4.10 The variation of λ_{cr} for values of k, for a range of stiffness ratio (E_f/E_s) and film and substrate compressibilities. 64

4.11 Graphs of λ_{cr} vs. different stiffness ratio measures (E_f/E_s) and (μ_f/μ_s) and ranges, for various ν_f and ν_s. 66

4.12 Plots of λ_{cr} vs. film and substrate compressibilities, displaying analytical results for various stiffness ratios E_f/E_s and for film thickness $h = 1$. 67

4.13 Plots of λ_{cr} vs. stiffness ratio displaying analytical and numerical results for various combinations of film and substrate compressibilities, for film thickness $h = 1$. Insets show the deformed configuration obtained from the numerical calculations for $E_f/E_s = 1000$ and $h = 1$. 68

4.14 Analytical and numerical results for critical wavelength ℓ_{cr} as a function of stiffness ratio E_f/E_s, for film thickness $h = 1$, $h = 0.5$ and $h = 0.25$, and various sets of Poisson's ratio for film and substrate. 69

4.15 The trilayer structure that is studied in this section (left), shown together with the degeneration of the structure into common cases that have been studied previously (right) at certain Young's moduli and Poisson's ratios for all domains. The previously established results for incompressible and compressible domains have been given together with their associated references (bottom). 73

4.16 Results of the developed analytical solution for a certain set of material parameters, together with numerical findings. The parameters and dimensions assumed here are based on that of a piezoelectric device in order to demonstrate the utility of the approach. 75

4.17 Results of the developed analytical solution for λ_{cr} vs. film-to-substrate stiffness ratio E_f/E_s and interphase-to-substrate stiffness ratio E_i/E_s, for three different Poisson's ratios for the whole structure, demonstrating that at the extremes the results recover those established in literature. The trilayer surface at $E_i/E_s = 1$ recovers the bilayer curve. 76

4.18 The effect of compressibility on the critical stretch λ_{cr} at the point of bifurcation, over a range of interphase-to-substrate stiffness ratios E_i/E_s, and for a set of film-to-substrate stiffness ratios E_f/E_s, for $h_f = 1$, $h_i = 0.1$ 77

4.19 The critical stretch λ_{cr} vs. E_i/E_s calculated for a set of Poisson's ratios and $E_f/E_s = 10$, 20 and 100, for $h_f = 1$, $h_i = 0.1$, presented together with numerical findings obtained through FEM enhanced with eigenvalue analysis. 78

4.20 The critical wavenumber k_{cr} vs. E_i/E_s calculated for various ν and $E_f/E_s = 10$, 20 and 100, for $h_f = 1$, $h_i = 0.1$, presented together with numerical findings obtained through FEM enhanced with eigenvalue analysis. 79

4.21 The effect of compressibility on the critical stretch λ_{cr} vs. E_i/E_S, calculated for a set of Poisson's ratios and interphase thickness $h_i = 0.1$, 1 and 100, for $E_f/E_s = 10$. 80

4.22 The effect of compressibility on the critical wavenumber k_{cr} vs. E_i/E_s, calculated for a set of Poisson's ratios and interphase thickness $h_i = 0.1$, 1 and 100, for $E_f/E_s = 10$. 81

4.23 The effect of interphase thickness h_i and interphase-to-substrate stiffness ratio E_i/E_s on critical stretch λ_{cr} (top) and critical wavenumber k_{cr} (bottom). 82

4.24 A close-up on the range of E_i/E_s over which mode switching occurs in the trilayer structure with $h_f = 1$, $h_i = 10$, $E_f/E_s = 10$, and $\nu_f = \nu_s = 0$, $\nu_i = 0.95$, demonstrating the bifurcation curves (left) and the resultant k_{cr} vs. E_i/E_s (right). 83

4.25 Incremental displacement profiles over a range of E_i/E_s, for $h_i = 0.1$ (top) and $h_i = 10$ (bottom), and $h_f = 1$, $E_f/E_s = 10$, and $\nu_f = \nu_i = \nu_s = 0.95$. 84

5.1 The four groups of interface models categorized by field jump conditions, namely as the perfect, elastic, cohesive and general interface models, where $\overline{\mu}$ is a surface elasticity parameter, and $\overline{c}$ is the cohesive stiffness parameter. 87

5.2 The deformation of a continuum body which occupies the material configuration $\mathcal{B}_0 \subset \mathbb{R}^3$ at time $t = 0$ that is mapped to the spatial configuration $\mathcal{B}_t \subset \mathbb{R}^3$ at any time $t > 0$ via the nonlinear deformation map $\boldsymbol{\varphi}$. The two sides of the body in the material configuration intersect at the interface $\mathcal{I}_0$. The interface is a zero-thickness layer that divides the bulk into the two parts $\mathcal{B}_0^-$ and $\mathcal{B}_0^+$ initially with $[\![\boldsymbol{X}]\!] = \boldsymbol{0}$, which through the mapping $\boldsymbol{\varphi}$ opens up, creating a displacement jump across the interface such that $[\![\boldsymbol{x}]\!] \neq \boldsymbol{0}$ is allowed for. 88

5.3 Table summarizing the key concepts and relations of the approach developed here. 93

5.4 Summarizing the boundary conditions applied for the domains considered here, namely for a coated beam, coated half-space, and bilayer with interface, together with the boundary conditions for limit cases of no interfacial effects and at incompressibility. This hierarchical structure elucidates the universality of the framework developed here accounting for (i) the compressibility of the domains and (ii) the general interface model. 94

5.5 Bifurcation curves for a coated half-space, i.e. the solutions for the system $\mathrm{Det}\,\boldsymbol{Q}\,(\,k\,,\,\lambda) \doteq 0$ for λ_{cr} over changing wavenumber k for fully compressible (left) and nearly incompressible (right) half-space, and plotted against dimensionless parameter $f = k\,\overline{\mu}/\mu$ (center) for both $\nu = 0$ and $\nu = 0.99$. Again, note that the plane-strain definition of Poisson's ratio is employed. That is, excluding the auxetic regime, $0 \leq \nu < 1$, where $\nu = 0$ indicates full compressibility and $\nu \to 1$ indicates incompressibility. This plane-strain definition relates to its 3D counterpart such that $\nu_{\mathrm{3D}} = \nu/(1+\nu)$. 97

5.6 Critical stretch λ_{cr} versus film-to-substrate stiffness ratio E_f/E_s, plotted over a range of cohesive stiffness $\overline{c}$, for a fully compressible bilayer structure with $h_f = 1$ and $\nu_f = \nu_s = 0$ (left), and an incompressible one with $\nu_f = \nu_s = 0.99$ (right). As $\overline{c} \to \infty$, the classical bilayer case is recovered. 105

5.7 Deformation profiles for a bilayer structure with different cohesive stiffnesses, $h_f = 1$ and $\nu_f = \nu_s = 0$, obtained from FEM enhanced with eigenvalue analysis. Deformation profiles are portrayed by looking at the eigenvector corresponding to the first negative eigenvalue. Color scale maps incremental displacement in the γ direction. 106

5.8 Surface graphs (center) of critical stretch λ_{cr} versus E_f/E_s and $\overline{c}$, for two different compressibilities, $\nu_f = \nu_s = 0$ and $\nu_f = \nu_s = 0.95$. 2D insets show projections of λ_{cr} versus E_f/E_s for several values of $\overline{c}$ (left), and λ_{cr} versus $\overline{c}$ for several values of E_f/E_s (right), for $h_f = 1$. 107

5.9 Surface graphs (center) of critical stretch λ_{cr} versus $\nu = \nu_f = \nu_s$ and $\overline{c}$, for stiffness ratio $E_f/E_s = 10$. 2D insets show projections of λ_{cr} versus ν for several values of $\overline{c}$ (left), and λ_{cr} versus $\overline{c}$ for several values of ν (right), for $h_f = 1$. 108

5.10 Critical stretch λ_{cr} versus cohesive stiffness $\overline{c}$, for different Poisson's ratio combinations for film and substrate, each row depicting a different stiffness ratio E_f/E_s, for $h_f = 1$. 109

5.11 Critical stretch λ_{cr} versus $\overline{c}$, displayed together with numerical findings, shown as points, over a range of stiffness ratio and combinations of film and substrate Poisson's ratio, for $h_f = 1$. 110

5.12 Critical wavelength k_{cr} versus $\overline{c}$, displayed together with numerical findings, shown as points, over a range of stiffness ratio and combinations of film and substrate Poisson's ratio, for $h_f = 1$. . . 111

5.13 Critical stretch λ_{cr} versus film thickness h_f, displayed together with numerical findings, shown as points, over a range of cohesive stiffness $\overline{c}$, for $E_f/E_s = 5$ and $\nu_f = \nu_s = 0.95$, as a continuous surface (left) and a 2D projection (center). The right inset displays an enlarged version of the upper range of the center inset. 112

6.1 Kinematics of growth with multiplicative decomposition of the deformation gradient $\boldsymbol{F}$ into it elastic part $\boldsymbol{F}_e$ and growth part $\boldsymbol{F}_g$. The material configuration $\mathcal{B}_0$ is mapped to the spatial configuration $\mathcal{B}_t$. The deformation gradient $\boldsymbol{F}$ maps the line elements $\mathrm{d}\boldsymbol{X}$ from $\mathcal{B}_0$ to $\mathrm{d}\boldsymbol{x}$ in $\mathcal{B}_t$ according to $\mathrm{d}\boldsymbol{x} = \boldsymbol{F} \cdot \mathrm{d}\boldsymbol{X}$. The intermediate state $\mathcal{B}_g$ is, in general, incompatible, and thus is not a "configuration". 114

6.2 The variation of g_{cr} for values of k, for a range of stiffness ratio (E_f/E_s) and film and substrate compressibilities. 123

6.3 The variation of g_{cr} over a range of stiffness ratio (E_f/E_s) and substrate compressibilities. To recover the Euler beam assumption, $\nu_f = \nu_s \to 0.99$. Light blue line denotes the small strain linear elastic approach in Chapter 3. Dark blue line is the solution found in Eq. 6.40. The percentage error between the two sets of results has been given on the y_2 axis. 124

6.4 The variation of g_{cr} and λ_{cr} over a range of stiffness ratio (E_f/E_s), for $\nu_s = \nu_f = 0.99$ (center). Critical growth g_{cr} plotted against stiffness ratio for zero compression (left), and critical stretch λ_{cr} against stiffness ratio for zero growth (right). 125

A.1 The six smallest eigenvalues of the tangent stiffness versus the stretch λ for various Poisson's ratios. The reference configuration corresponds to $\lambda = 1$ and compression is prescribed incrementally until λ_{cr} is reached. 131

A.2 Illustration of the smallest eigenvalues of the tangent stiffness of the domain for various Poisson's ratio together with their associated eigenvectors. The color pattern on the domain corresponds to the normalized displacement in the vertical direction. 132

A.3 Illustration of the domain, the finite element discretization and the deformation. The color bars show the normalized vertical displacement which is the eigenvector of the smallest eigenvalue imposed on the domain. The height of the fully compressible domain (left) remains constant in contrast to the nearly incompressible domain (right) whose height nearly doubles. 133

A.4 Illustration of the domain and the finite element discretization for various aspect ratios. 133

B.1 Illustration of Det $\boldsymbol{M}$ and its roots associated with Eq. (B.13). . . 137

C.1 Affine deformation of a unit domain under uni-axial tension test. Lateral deformations occur naturally to minimize the energy, while extension ε_{xx} is a prescribed value. 139

C.2 Comparison of the current kinetic nonlinear Poisson's ratio definition with previously established, kinematic definitions. 148

C.3 Illustration of the lateral stretch η versus Jacobian J and compressibility parameter α for 2D (left) and 3D (right). As we move towards full incompressibility, J converges to 1, as expected. . . . 150

List of Tables

C.1 Poisson's ratio in small-strain linear elasticity and its dual nature as a material parameter (left) or a geometrical definition (right). 140

C.2 Poisson's ratio at large deformations nonlinear elasticity. The geometrical description of Poisson's ratio has been extended to large deformations (top). We propose an extension of the material description of Poisson's ratio (bottom), via a variational approach. At the reference configuration, both nonlinear variants coincide with their linear counterparts in Table C.1. 141

C.3 Poisson's ratio at large deformations nonlinear elasticity. The geometrical description of Poisson's ratio has been extended to large deformations (top). Via a variational approach, we propose an extension of the material description of Poisson's ratio (bottom). 147

Chapter 1

Introduction

A constrained domain under compressive loads may buckle at a certain, critical load in order to release the built-up energy. While preventing the buckling of beams, columns or panels in standing structures has been historically the goal of many studies, stemming from the seminal works of Biot [1] and Allen [2], understanding and in turn harnessing these instabilities is now a riveting subject of study. Over the last few years, a large body of literature has been dedicated to harness instabilities of multilayer structures, finding applications in many fields, an example of which is biology, including understanding the wrinkling of skin [3–5], the buckling analysis of microtubules in cells [6], mechanics and development of folding in the brain [7–10] and airway [11,12], and modeling flowers [13]. Other applications include sensors [14–16], metamaterial design [17], measurement of material properties [18], dielectric plates [19, 20], tissue engineering [21], measurement of thin film properties [22, 23], and flexible electronics [24–28], to name a few.

This manuscript aims to provide a treatise on the geometrical instabilities of compressible, multilayer domains, undergoing large deformations, based on the contributions of the author in the past few years. Thus, substantial parts of this work have been compiled from the following publications [29–34]:

- A. Javili and A. D. Bakiler, "A displacement-based approach to geometric instabilities of a film on a substrate," *Mathematics and Mechanics of Solids*, vol. 24, pp. 2999–3023, 2019.
- A. D. Bakiler and A. Javili, "Bifurcation behavior of compressible elastic half-space under plane deformations," *International Journal of Non-Linear Mechanics*, vol. 126, p. 103553, 2020.
- A. D. Bakiler, B. Dortdivanlioglu, and A. Javili, "From beams to bilayers: A unifying approach towards instabilities of compressible domains under plane deformations," *International Journal of Non-Linear Mechanics*, vol. 135, p. 103752, 2021.
- A. D. Bakiler and A. Javili, "Wrinkling of a compressible trilayer domain under large plane deformations," *International Journal of Solids and Structures*, vol. 241, p. 111465, 2022.
- A. D. Bakiler and A. Javili, *A Different Catch for Poisson*, pp. 3–23. Cham: Springer International Publishing, 2022.
- A. D. Bakiler and A. Javili, "Understanding the role of interfacial mechanics on the wrinkling behavior of compressible bilayer structures under large plane deformations," *Mathematics and Mechanics of Solids*, DOI: 10.1177/10812865221094833, 2022.

1.1 Literature review

As it is clear from their myriad of applications, instabilities can occur in a large variety of geometries such as in thin membranes [35–38], beams, half-spaces, bilayer and multilayer structures and cylindrical or spherical geometries and shells [39–42], reviewed in [43]. This section reviews the works on several of these geometries and loading conditions.

Bilayer geometry

The bilayer structure is a structure of specific interest, where typically the bottom layer is much thicker and more compliant than the top layer. When this structure undergoes compressive stresses, regardless of its cause, at a critical level, wrinkles on the top layer emerge as the first type of instability. The wrinkling of deposited thin films on compliant substrates has been extensively studied and utilized in various applications [44–48] using both platinum and gold films on PDMS or other elastomers. The wrinkling of bilayer structures has been further investigated in [49–52] among others, while further modes of wrinkling, such as stripes, checkerboard, herringbone [53–56], other types of instabilities that form under compression, such as crease as an earlier mode of instability [57–60] or delamination [61, 62] have been studied. Conducting non-linear analyses on the bifurcation and post-bifurcation behavior of bilayers has likewise been subject to riveting studies, see [24, 54] among others. A key parameter that comes into play here to characterize post-buckling behavior is the non-linearity of the substrate [63, 64]. The post-bifurcation behavior is also of interest as it encompasses many curious phenomena such as folding [65, 66], ridge formation [67] as well as period doubling [63, 68]. Furthermore, modeling and simulation of buckling and post-buckling behavior [69, 70], phase diagrams of bifurcation behavior [71] and wave propagation in layered composites [72] have been conducted. Bilayer structures need not be flat; many have studied the effect of curvature [73, 74] on bilayer instability, while tubular [11, 40], conical [75] and spherical [39, 41] geometries have also been looked into. The film in a bilayer structure is usually assumed to be much stiffer than the substrate, but larger regimes of this "stiffness ratio" and its influence on bifurcation behavior have also been dealt with; see [68, 76] for discussion on the lower regime, and [77–79] for graded materials. Even though there are multitudes of works on the bifurcation of a bilayer system, to the best of our knowledge scarcely any of them, except for the very recent contribution [64], account for the *compressibility* of the material in a *large deformations framework*.

Beam geometry

Beam modeling has been typically used to model the top layer of the beam geometry, given its relative thickness compared to the substrate, see for instance the pioneering work of Biot [1] or more recently [29], as a plate, utilizing the von–Karman plate theory, see works [55, 80, 81] among others. Beam buckling in itself is an extensive area of research, covering many aspects such as snap-through behavior [82,83], viscoelasticity [84], post-buckling [85], nonlinearity [86], computational aspects [87], and non-local theories [88].

Half-space geometry

The substrate alone, the bottom layer of the bilayer geometry, may be modeled as an infinite half-space. The bifurcation behavior of an infinite half-space has been explored thoroughly, initially by Biot [89], then by [90–96], including discussions on creasing, e.g. [57], surface elasticity [97], and compressibility [30, 95, 97, 98]. However, the surface instabilities of a *compressible* elastic half-space remain elusive and have been studied merely in [95, 97–100], to the best of our knowledge, and thus subtle nuances of the problem and its solution may have been overlooked. Among these works, Usmani and Beatty [98, 99] studied quasi-static surface instabilities of an elastic half-space first. This was followed by Chadwick and Jarvis [100] who examined infinitesimal surface waves on a pre-stressed compressible elastic half-space. Later, Steigmann and Ogden [97] investigated compressible elastic solids, accounting for boundary coating, which was modeled using the surface elasticity [101–103]. In this work, Steigmann and Ogden [97] reported mainly on the influence of surface elasticity on bifurcation behavior. More recently, Murphy and Destrade [95] elaborated on the surface waves and surface stability for a pre-stretched semi-infinite elastic solid, in which the analysis assumes a power-law relation between the pre-stretches; thereby a "compressibility parameter" plays a crucial role. For an example of a compressible neo-Hookean material, Murphy and Destrade [95] carry out a detailed analysis and provide critical stretches for the whole range of the compressibility parameter.

Trilayer geometry

The trilayer structure is also of particular interest to this work, which also includes an interphase layer between the film and the substrate in a classical bilayer structure. The existence of the interphase layer has been found to substantially alter the instability behavior of the system [104]. Understanding the effects of the interphase layer on bifurcation behavior is key since in several applications, an adhesive layer is necessary between the so-called "film" and the (usually) more compliant material underneath referred to as "substrate". This adhesive joining method has been shown to have fundamental advantages over other joining methods [105], as the adhesive layer becomes a necessity in stretchable electronics applications [106], for instance in facilitating adhesion between normally incompatible materials, or allowing for "strain isolation" of the overlayed integrated circuits [28].

The trilayer structure has been studied by Stafford et al. [22], where the trilayer is inspired from the different properties a thin film has along its thickness, motivating the modeling of the thin film as a two-layer composite beam, under linear elasticity. Later on, Jia et al. [107] have followed a similar approach, wherein they have discovered two modes of wrinkling and have established separate solutions for both. Cheng et al. [108] have looked into the buckling behavior of a thin stiff film on a bilayer substrate, under plane strain conditions. Lejeune et al. [109] have explored the trilayer structure for relatively thin interphase layers and presented their findings in comparison to [22], and have established a solution that captures the entirety of the parameter regime, further showing how their findings can be applied to buckling-based metrology methods. Further extending this research, Lejeune et al. [110] have developed an algorithmic approach towards understanding the instabilities of multilayer materials, not restricted by layer thickness. Xia and Keten [111] have delved into the interfacial stiffening of the interface between the film and the substrate in bilayers and its influence on the mechanical behavior of the system under tension. More recently, the buckling of a thin stiff film on a bilayer structure has been explored through energy methods in the linear elastic framework, and in an incompressible, large deformation

framework by Wang et al. [112]. The post-buckling behavior and mode switching characteristics of a hyperelastic, incompressible trilayer has been very recently explored by Zhou et al. [113]. Also, Chen et al. [114] have looked into the post-wrinkling behavior of a bilayer on top of a substrate, using the composite beam approach and Timoshenko beam theory, constructing a phase diagram. The dynamic analysis of a corrugated thin film on a finite-thickness bilayer substrate has been recently conducted [115], wherein the effect of the interphase layer on the dynamic behavior of the system has been explored. Finally, Bi et al. [116] have looked into the trilayer structure with a finite thickness substrate, identifying global and local wrinkling modes in the structure. Other works include the topography-driven delamination of a buckling trilayer structure [117], numerical examples on the growth-induced instabilities of trilayer with growth-dependent material properties [118], and the wrinkling behavior of bilayer graphene sheets on top of a substrate [119]. Experimental works on trilayer instabilities include works on thermally induced instabilities [120] and the influence of the interphase layer on the formation of surface patterns [121].

To the best of our knowledge, the bifurcation behavior of a *compressible*, trilayer domain in a *large deformation* framework remains to be investigated. Since the assumption of incompressibility does not hold for most real applications, we believe, introducing compressibility into the picture can serve as a significant stepping stone towards understanding and harnessing the instabilities of trilayer and multilayer systems in several real applications. The current applications of multilayer structures utilize materials such as Polystrene [13, 22], graphene sheets [119], piezoelectrics, adhesives and epoxy [16], all of which can have Poisson's ratios that are far from being incompressible. Additionally, due to its wide applicability in biological modeling and the common use of compliant substrates in applications, the structures are known to undergo large deformations.

Extended bilayer geometry

A variation of the trilayer is a structure where layers are embedded inside an infinite or finite-thickness substrate. Such works have explored the different wave

modes encountered in the wrinkling of embedded films [122], the effect of an interphase layer between the embedded layers and the substrate by looking at a compressible interphase [123], uncovering various wrinkling modes such as nested wrinkling [124], and exploring the influence of layer distance and stiffness on bifurcation behavior [125].

Interface mechanics

An interface exists where two materials are bonded together. Unlike what is assumed in the great majority of the works on bilayer structures thus far, this bonding is subject to various imperfections, hence creating an interphase layer between the two [126], which plays a crucial role in determining the behavior of the structure. Until now, this interphase layer in bilayer structures has been commonly neglected by assuming perfect bonding between the layers, e.g. [52]. Alternatively, in very few contributions, the interphase effect has been treated as a layer of its own resulting in a trilayer structure [22], or it has been modeled via a cohesive interface model [127]. The cohesive interface model, however, is only one limit of the *general interface model* [128]. Stafford et al. [22] accounted for this interphase layer, motivated by the different properties a film on a substrate displays along its depth, and have paved the way for many contributions on trilayer systems [109, 110, 112, 113, 116, 129], also finding applications serving as an adhesive layer [16] or for strain-isolation [28]. Another way to capture the behavior of the interphase layer is to introduce a zero-thickness interface model in place of the interphase layer [130,131]. This zero-thickness interface model, for mechanical problems, is classified based on the continuity of the displacement and traction fields across this interface, and how these fields relate to interphase properties [132–134]. Incorporating an interface into the bilayer structure is crucial, as for instance allowing for displacement discontinuity across the interphase allows for phenomena such as delamination [61] to be captured. Even though there are some applications in which delamination is an undesired by-product of the manufacturing process [135,136], understanding and in turn harnessing delamination behavior [137] has become a crucial aspect of flexible electronics [72, 106] and

novel surface renewal mechanisms [138]. For further details on the analytical and computational aspects of the works done on each model, applications of interfaces in composites, and extensions to more sophisticated interface models, see [126]. More information about the different types of interface models has been given in the introduction to Chapter 5. To our knowledge, the general interface model has not yet been incorporated into bilayer instabilities. On the other hand, even with the cohesive interface layer, the available studies in the literature are limited to incompressible bilayers only.

Loading conditions

The loading which results in compressive sources leading to the structure to become unstable can be of different natures with different boundary conditions; their effects on the bifurcation behavior of a bilayer system have been explored in [76, 139, 140], among others. More specifically, compression can be induced by pre-stretch [52,64], pre-stress [141], thermal stress [53] or in biological systems, by differential growth [142–146]. Growth-induced buckling of biological structures is prevalent in different systems, such as airways [12, 40, 147], intestines [11], skin [3–5] and the brain [9, 129, 148, 149] Growth modeling and mechanics of growth explains the driving force behind the formation of various biological tissues as a result of constrained or differential growth, see the review by Kuhl [150].

Growth modeling

The modeling of growth has been pursued through the commonly accepted strategy in the context of continuum mechanics of multiplicatively decomposing the deformation into its growth and elastic parts, as proposed by Rodriguez et al. [151]. The mechanism of growth and its modeling has been a compelling area of study with focus on the kinematics, continuum mechanics treatment [151–157] and thermodynamics [158] or explaining growth using mixture theory [159–161]. Additionally, the growth of biological structures such as horns, tusks, rods or cells have been modeled and studied in [162–164] while growth models at sub-cellular

scales, plant growth and bone remodeling have been addressed in [165] among others. Hosseini et. al [166, 167] have elaborated on how mechanical forces shape the developing eye, through experiments and computational 3D models, focusing on differential growth in layers of the eye, see also [168, 169]. More specifically, growth induced instabilities in the bilayers have been used in explaining the formation of skin wrinkles [3], investigating the instabilities formed in artificial elastomeric skins [170], understanding the development and mechanics of brain folding [7–9, 149], and in exploring the development of patterns in growing tubular tissues [11, 147, 171, 172]. The buckling behavior of cylindrical geometries due to differential growth has been studied extensively by Moulton and Goriely [40] among others. Eskandari et al. [12] have studied mucosal folding in the post-buckling range, with the airway wall having temporally evolving material properties leading to elastosis. Skin growth [5] has also been investigated in several contributions, for example finding applications in tissue expansion [173] as a novel technique to allow for the growth of extra skin for reconstruction.

From a mathematical perspective, Yavari [155] have eliminated the use of an intermediary configuration in the approach of Rodriguez et al. [151] by constructing a geometry theory of growing solids, where the growing body remains stress-free in the material manifold, see also [145, 174, 175]. Taber [176] provides an extensive review of some of the works done on biomechanics of growth, along with remodeling and morphogenesis following the multiplicative decomposition approach. To the best of our knowledge, a large-deformation analytical solution to growth-induced instabilities of compressible domains has not yet been found.

1.2 Organization of the manuscript

This manuscript is organized as follows. A brief overview of continuum mechanics at finite deformations is given in Chapter 2, wherein the notation is introduced and the kinematics, governing equations, and constitutive behavior of the problem at hand are outlined, together with the numerical implementation of these using finite element method (FEM). Chapter 3 adopts a linear elastic material model

and outlines a displacement based approach to solve for the growth-induced instabilities of bilayer structures. In Chapter 4, the basis for the generic theoretical framework to capture the instabilities of compressible domains under compression is laid and then applied to several geometries. The generic interface model is then incorporated into the framework in Chapter 5, looking once again at its applications to various geometries. Chapter 6 extends the framework developed herein to include growth, and looks at the growth-induced instabilities of bilayers in a large deformation setting, comparing results to those in Chapter 3. Finally, Chapter 7 concludes this work and provides further outlook and research directions.

1.3 Key aspects and summary

In summary, this works aims to address the gaps in literature on the instabilities of compressible domains, with/without interfaces and allowing for growth, by constructing a generic, theoretical framework and comparing its results with FEM. Hence, the key objectives of this work are as follows:

- Develop a generic theoretical framework for the wrinkling of compressible multilayer domains under large deformations,
- Apply generic framework to half-space, beam, bilayer and trilayer geometries, and explore the effect of compressibility on bifurcation behavior, along with other material and geometrical parameters,
- Incorporate the general interface model to the generic framework such that interface and surface effects are also successfully captured,
- Extend the generic framework to account for *both compression-induced and growth-induced* instabilities, and compare growth-induced instabilities of bilayer structures to the linear elastic case,
- Compare all analytical solutions for the critical stretch at the onset of instability by computational results using the non-linear FEM enhanced with eigenvalue analysis.

Chapter 2

Continuum mechanics at large deformations

The objective of this chapter is to introduce the notation conventions and definitions adopted herein, and to give a brief overview of the non-linear, large deformation continuum mechanics framework that wil be used throughout this thesis. Note that this chapter is aimed to be a brief overview rather than a comprehensive summary; more detailed expositions on nonlinear continuum mechanics and its foundations can be found in [177–179], among others. To this extent, first, the notations and definitions are introduced, followed by the kinematics, governing equations, and constitutive behavior. Then, the material behavior of a compressible hyper-elastic neo-Hooekan domain is outlined, with the special/limit cases of incompressibility and linear elasticity written out next. Subsequently, instability analysis and related incremental quantities are elaborated on. Finally, the nonlinear finite element method (FEM) used herein to obtain the numerical results and its implementation will be elaborated on.

2.1 Notation and definitions

Direct notation is adopted throughout. Occasionally, the notation $\{\bullet\} := \{\circ\}$ is used to denote that $\{\bullet\}$ is defined as $\{\circ\}$, and $\{\bullet\} \doteq \{\circ\}$ is used to convey that $\{\bullet\}$ is set to $\{\circ\}$. The contraction of two second-order tensors $\boldsymbol{A}$ and $\boldsymbol{B}$ is denoted as $\boldsymbol{A} : \boldsymbol{B} = A_{ij}\, B_{ij}$, while $[\boldsymbol{A} \cdot \boldsymbol{B}]_{ij} = A_{is}\, B_{sj}$. Fourth-order constitutive tensors are written with a different font, such as $\mathbb{I}$ denoting the fourth-order identity tensor. The tensor product of two second-order tensors $\boldsymbol{A}$ and $\boldsymbol{B}$ is a fourth-order tensor $\mathbb{D} = \boldsymbol{A} \otimes \boldsymbol{B}$ with $D_{ijkl} = A_{ij}\, B_{kl}$. Two non-standard tensor products of two second-order tensors $\boldsymbol{A}$ and $\boldsymbol{B}$ are defined as $[\boldsymbol{A} \overline{\otimes} \boldsymbol{B}]_{ijkl} := A_{ik}\, B_{jl}$ and $[\boldsymbol{A} \underline{\otimes} \boldsymbol{B}]_{ijkl} := A_{il}\, B_{jk}$. The non-standard products of a fourth-order tensor $\mathbb{D}$ and a vector $\boldsymbol{b}$ are defined by $[\boldsymbol{b} \,\overline{\cdot}\, \mathbb{D}]_{ikl} = D_{ijkl}\, b_j$ and $[\mathbb{D} \,\overline{\cdot}\, \boldsymbol{b}]_{ikl} = D_{ijkl}\, b_k$. Interface quantities denoted as $\{\overline{\bullet}\}$ are distinguished from their bulk counterparts denoted as $\{\bullet\}$. The superscript $\{\bullet\}^+$ denotes a quantity on the plus side of the interface, while $\{\bullet\}^-$ denotes the minus side. The unit normal to the interface points from the minus side to the plus side of the interface. The jump of a quantity across the interface is defined by $[\![\{\bullet\}]\!] := \{\bullet\}^+ - \{\bullet\}^-$, whereas the average of a quantity is defined by $\{\!\{\{\bullet\}\}\!\} := \frac{1}{2}\,[\,\{\bullet\}^+ + \{\bullet\}^-\,]$. The notation ${}^{\mathcal{L}}\{\bullet\}$ is used as a shorthand to denotes the linearization of $\{\bullet\}$.

2.2 Kinematics

The purpose of this section is to summarize the kinematics in nonlinear continuum mechanics. Let $\mathcal{B}$ denote a continuum body that takes the material configuration $\mathcal{B}_0 \in \mathbb{R}^3$ initially at time $t = 0$ and is mapped to the spatial configuration $\mathcal{B}_t \in \mathbb{R}^3$ at a time t, as depicted in Fig. 2.1. Let $\mathbb{T} = [0, T] \subset \mathbb{R}_+$ denote the time domain. Note, we restrict the analysis only to quasi-static conditions and thus, time plays the role of a history parameter to order the sequence of events. We denote by the orientation preserving map $\boldsymbol{\varphi} : \mathcal{B}_0 \times \mathbb{T} \to \mathcal{B}_t$, a smooth deformation (motion) of the reference placement for any time $t \in \mathbb{T}$. The reference placement of particles in the material configuration $\mathcal{B}_0$ is denoted $\boldsymbol{X}$ with its counterpart $\boldsymbol{x}$ in the

spatial configuration $\mathcal{B}_t$. The nonlinear deformation map $\boldsymbol{\varphi}$ maps the placements of particles from the material to the spatial configuration according to

$$\boldsymbol{x} = \boldsymbol{\varphi}(\boldsymbol{X}, t) \;:\; \mathcal{B}_0 \times \mathbb{T} \to \mathcal{B}_t \qquad \Rightarrow \qquad \mathcal{B}_t = \boldsymbol{\varphi}(\mathcal{B}_0)\,. \tag{2.1}$$

The corresponding linear map from the material to the spatial configuration is the deformation gradient defined as $\boldsymbol{F} := \mathrm{Grad}\boldsymbol{\varphi}$. The deformation gradient maps a material line element $\mathrm{d}\boldsymbol{X} \in T\mathcal{B}_0$ to its spatial counterpart $\mathrm{d}\boldsymbol{x} \in T\mathcal{B}_t$ via $\mathrm{d}\boldsymbol{x} = \boldsymbol{F} \cdot \mathrm{d}\boldsymbol{X}$. Let $\mathrm{d}V$ and $\mathrm{d}v$ denote the volume elements of the bulk in the material and spatial configurations, respectively. The determinant of the deformation gradient is referred to as Jacobian defined by $J := \mathrm{Det}\boldsymbol{F}$ and measures the change of a volume element due to deformation via $\mathrm{d}v = J\,\mathrm{d}V$. Throughout the deformation, the surface of the domain is assumed smooth. The surface of the material configuration $\mathcal{B}_0$ is denoted as $\partial\mathcal{B}_0$. The unit outward normal to $\partial\mathcal{B}_0$ is denoted $\boldsymbol{N}$ in the material configuration with $\boldsymbol{n}$ being its counterpart in the spatial configuration.

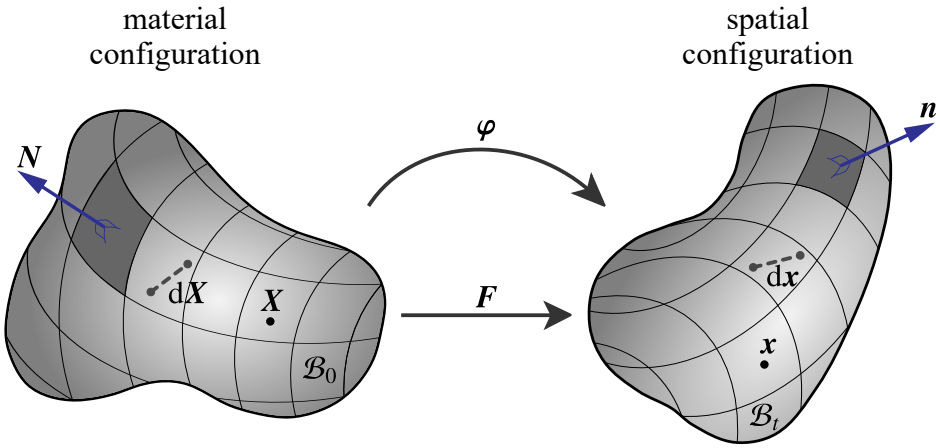


Figure 2.1: Deformation of a continuum body. The continuum body occupies the material configuration $\mathcal{B}_0 \in \mathbb{R}^3$ at time $t = 0$ and is mapped to the spatial configuration $\mathcal{B}_t \in \mathbb{R}^3$ via the smooth nonlinear deformation map $\boldsymbol{\varphi}$.

2.3 Governing equations

Equipped with the kinematics of the problem, we can elaborate on the governing equations next. The governing equations of finite strain continuum mechanics consist of the balances of linear momentum and angular momentum, or rather the balances of forces and moments, respectively. The linear momentum balance in the material configuration reads

$$\mathrm{Div}\boldsymbol{P} + \boldsymbol{b}_0 = \boldsymbol{0} \quad \text{on} \quad \mathcal{B}_0 \qquad \text{subject to} \qquad \boldsymbol{P}\cdot\boldsymbol{N} = \boldsymbol{t}_0 \quad \text{on} \quad \partial\mathcal{B}_0\,, \tag{2.2}$$

in which $\boldsymbol{P}$ denotes the Piola stress, $\boldsymbol{b}_0$ is the body force density per unit volume in the material configuration, and $\boldsymbol{t}_0$ is the traction on the boundary of the domain with the unit outward normal to domain boundary $\partial\mathcal{B}_0$ denoted as $\boldsymbol{N}$, whereas the angular momentum balance reads

$$\boldsymbol{P}\cdot\boldsymbol{F}^{\mathrm{t}} = \boldsymbol{F}\cdot\boldsymbol{P}^{\mathrm{t}}\,. \tag{2.3}$$

In general, $\boldsymbol{b}_0$ is externally applied and is prescribed in the problem definition. Henceforth, we focus on the problem in the absence of the externally prescribed body force density $\boldsymbol{b}_0$. The balance of angular momentum (2.3) holds a priori, via the material frame indifference associated with the choice of objective arguments for the constitutive model of the hyperelastic material behavior next.

2.4 Constitutive behavior

Constitutive models are phenomenologically proposed through the use of a free energy density [180], which is defined per unit reference volume. If this free energy is only a function of deformation gradient $\boldsymbol{F}$, it is referred to as the strain-energy function [178]. It follows that the strain-energy density function should be independent of rotation. To establish this, we can decompose the deformation

gradient into purely rotational and purely stretch components such that

$$\boldsymbol{F} = \boldsymbol{R} \cdot \boldsymbol{U} \,, \tag{2.4}$$

wherein $\boldsymbol{R}$ is the proper orthogonal rotation tensor, and $\boldsymbol{U}$ is defined as the right stretch tensor. The common approach to ensure that our energy is independent of changing $\boldsymbol{R}$ is to use the Cauchy Green deformation tensor $\boldsymbol{C} := \boldsymbol{F}^{\mathrm{t}} \cdot \boldsymbol{F}$, since $\boldsymbol{F}^{\mathrm{t}} \cdot \boldsymbol{F} = \boldsymbol{U}^{\mathrm{t}} \cdot \boldsymbol{R}^{\mathrm{t}} \cdot \boldsymbol{R} \cdot \boldsymbol{U}$ and due to the orthagonality of $\boldsymbol{R}$ which dictates that $\boldsymbol{R}^{\mathrm{t}} \cdot \boldsymbol{R} = \boldsymbol{I}$ and the symmetry of $\boldsymbol{U}$ which results in $\boldsymbol{U} = \boldsymbol{U}^{\mathrm{t}}$, the expression becomes $\boldsymbol{C} = \boldsymbol{U}^2$, thus independent of spatial rotations. The material behavior is assumed to be isotropic and homogeneous throughout this work. Isotropy means that the strain energy stored in the material does not change with material rotations. To ensure that our energy does not change by the material rotations of the body, the energy $\psi(\boldsymbol{C})$ must be a function of its three principal invariants $I_1(\boldsymbol{C})$, $I_2(\boldsymbol{C})$ and $I_3(\boldsymbol{C})$. These quantities I_i are called "invariants" because they remain invariant of the defined coordinate system or rotation of the tensor they are associated with. Finding the three invariants of $\boldsymbol{C}$ presents itself as an eigenvalue problem where

$$\mathrm{Det}[\,\boldsymbol{C} - \lambda_i \,\boldsymbol{I}\,] = 0 \,, \tag{2.5}$$

which renders the characteristic equation

$$\lambda_i^3 - I_1\,\lambda_i^2 + I_2\,\lambda_i - I_3 = 0 \,, \tag{2.6}$$

with λ_i being the spectral invariants, and their coefficients denoted as I_i being the principal invariants, which are in turn defined as

$$I_1 := \mathrm{Tr}\,\boldsymbol{C} \quad , \quad I_2 := \mathrm{Tr}\,\mathrm{Cof}\,\boldsymbol{C} \quad , \quad I_3 := \mathrm{Det}\,\boldsymbol{C} \,. \tag{2.7}$$

Hence, the generic form of an isotropic free energy density is $\psi = \psi(I_1, I_2, I_3)$ with I_1, I_2 and I_3 being the three principal invariants of the right Cauchy–Green tensor. Some examples of free energy functions of this form include

$$\begin{aligned} &\text{neo-Hookean:} && \psi = \tfrac{\mu}{2}\,[\,I_1 - 3\,] + f(J) \\ &\text{Mooney-Rivlin:} && \psi = \tfrac{\mu}{2}\,[\,I_1 - 3\,] - \tfrac{\mu}{2}\,[\,I_2 - 3\,] + f(J) \,, \end{aligned} \tag{2.8}$$

with μ being the shear modulus. The terms $f(J)$ serve to impose volumetric constraints related to compressibility. For homogenous isotropic materials the hyperelastic free energy per volume in the material configuration ψ is only a function of the deformation gradient $\boldsymbol{F}$. Accordingly, the corresponding Piola stress $\boldsymbol{P}$ is defined via $\boldsymbol{P} := \partial\psi/\partial\boldsymbol{F}$.

The method employed here to analyze the stability of a structure is a linear stability analysis. The domain deformed by $\boldsymbol{F}$ is further perturbed by an incremental displacement $\delta\boldsymbol{u}$, such that the deformation gradient for the incremental displacement $\delta\boldsymbol{F} = \mathrm{Grad}\,\delta\boldsymbol{u}$. The stability of the *perturbed* configuration is examined via looking at the linear momentum balance at the perturbed configuration

$$\mathrm{Div}(\boldsymbol{P} + \delta\boldsymbol{P}) \doteq \boldsymbol{0}\,, \tag{2.9}$$

where the incremental Piola stress $\delta\boldsymbol{P}$ reads

$$\delta\boldsymbol{P} = \boldsymbol{P}(\boldsymbol{F} + \delta\boldsymbol{F}) - \boldsymbol{P}(\boldsymbol{F}) = \frac{\mathrm{d}\boldsymbol{P}}{\mathrm{d}\boldsymbol{F}} : \delta\boldsymbol{F}\,. \tag{2.10}$$

Next, the expressions outlined here are particularized for certain material models and limits.

2.4.1 Compressible neo-Hookean material model

The energy density function adopted henceforth is a compressible neo-Hookean energy function, which is independent of I_2, with $\psi = \psi(I_1, I_3)$ being only a function of $I_1 = \boldsymbol{F} : \boldsymbol{F}$ and $I_3 = J^2$. The hyperelastic response of the domain herein is computed through the compressible neo-Hookean model [180] with the polyconvex free energy density

$$\psi(\boldsymbol{F}) = \frac{1}{2}\,\mu\,\left[\boldsymbol{F} : \boldsymbol{F} - 3 - 2\ln J\right] + \Lambda\left[\,\tfrac{1}{4}\left[J^2 - 1\right] - \tfrac{1}{2}\,\ln J\,\right] \quad , \quad J := \mathrm{Det}\boldsymbol{F}\,. \tag{2.11}$$

The coefficient Λ is the *first Lamé parameter*, where μ is the *second Lamé parameter*. However, the parameter Λ will henceforth be used in its alternate format

$$\Lambda = 2\mu\,\alpha \quad \text{where} \quad \alpha = \frac{\nu}{1-\nu}\,, \tag{2.12}$$

wherein the coefficient α shall be interpreted as a *compressibility parameter* which goes to infinity towards incompressibility, and to $\alpha = 0$ at full compressibility. Note that in this work, unless denoted otherwise, the plane-strain definition of Poisson's ratio is used, such that $\nu = 0$ indicates full compressibility and $\nu \to 1$ indicates incompressibility. Poisson's ratio ν relates to its well-known 3D counterpart through $\nu^{3\mathrm{D}} = \dfrac{\nu}{1+\nu}$ such that $\nu^{3\mathrm{D}} \to 0.5$ at the incompressibility limit. As we will see shortly, for the problem at hand, a nonlinear and more generic definition of Poisson's ratio is required. Moving forward, the Piola stress that derives from the free energy (2.11) reads

$$\boldsymbol{P} := \frac{\partial \psi}{\partial \boldsymbol{F}} = \mu\,\big[\,\boldsymbol{F} - \boldsymbol{F}^{-t}\,\big] + \mu\,\alpha\,\big[\,J^{\,2} - 1\,\big]\,\boldsymbol{F}^{-t}\,, \tag{2.13}$$

wherein the relation $\partial J/\partial \boldsymbol{F} = J\boldsymbol{F}^{\text{-t}}$ has been used. The derivative of the Piola stress (2.13) renders the fourth order tensor $\mathbb{A}$, which reads

$$\mathbb{A} := \frac{\partial \boldsymbol{P}}{\partial \boldsymbol{F}} = \mu\,[\,\mathbb{I} - \mathbb{D}\,] + \mu\,\alpha\,[\,J^2 - 1\,]\,\mathbb{D} + 2\,\mu\,\alpha\,J^2\,\boldsymbol{F}^{\text{-t}} \otimes \boldsymbol{F}^{\text{-t}}\,, \tag{2.14}$$

where

$$\mathbb{I} := \frac{\partial \boldsymbol{F}}{\partial \boldsymbol{F}} = \boldsymbol{i}\,\overline{\otimes}\,\boldsymbol{I} \quad \text{and} \quad \mathbb{D} := \frac{\partial \boldsymbol{F}^{\text{-t}}}{\partial \boldsymbol{F}} = -\boldsymbol{F}^{\text{-t}}\,\underline{\otimes}\,\boldsymbol{F}^{\text{-1}}\,. \tag{2.15}$$

In order to obtain the expression for incremental Piola stress $\delta\boldsymbol{P}$, we evaluate Eq. (2.10) using the established Piola stress (2.13). In other words,

$$\delta\boldsymbol{P} = \mathbb{A} : \delta\boldsymbol{F}\,, \tag{2.16}$$

which simplifies to

$$\delta\boldsymbol{P} = \mu\,\delta\boldsymbol{F} + \Big[\,1 - \mu\,\alpha\,[\,J^2 - 1\,]\,\Big]\,\boldsymbol{F}^{\text{-t}} \cdot \delta\boldsymbol{F}^{\text{t}} \cdot \boldsymbol{F}^{\text{-t}} + 2\,\mu\,\alpha\,J^2\,\boldsymbol{F}^{\text{-t}} : \delta\boldsymbol{F}\,\boldsymbol{F}^{\text{-t}}\,, \tag{2.17}$$

where

$$\mathbb{I} : \delta \boldsymbol{F} = \delta \boldsymbol{F} \quad \text{and} \quad \mathbb{D} : \delta \boldsymbol{F} = -\boldsymbol{F}^{-\mathrm{t}} \cdot \delta \boldsymbol{F}^{\mathrm{t}} \cdot \boldsymbol{F}^{-\mathrm{t}} \,. \tag{2.18}$$

2.4.2 Incompressible neo-Hookean material model

To simplify the approach and derivations, the material is sometimes assumed to be *fully incompressible*. The main feature of *incompressible materials* is that they do not allow for a change in their volumes, and therefore $\mathrm{d}v = \mathrm{d}V$ holds throughout the deformation. Although the incompressibility assumption is essentially an asymptotic limit which cannot be realistically achieved, this feature is apparent in many biological materials which carry Poisson's ratios very close to the incompressibility limit. The free energy of an incompressible material is then postulated to take the form

$$\psi = \psi(\boldsymbol{F}) - p\,[J-1] \qquad \Longrightarrow \qquad \psi = \frac{\mu}{2}\,[\boldsymbol{F} : \boldsymbol{F} - 3] - p\,[J-1] \;, \tag{2.19}$$

wherein $\psi(\boldsymbol{F})$ corresponds to the strain energy density at $J = 1$ and p serves as a Lagrange multiplier to ensure that the constraint $J = 1$ is exactly fulfilled. For an incompressible material with the free energy density (2.19), the Piola stress reads

$$\boldsymbol{P} = \mu\,\boldsymbol{F} - p\,\boldsymbol{F}^{-\mathrm{t}} \,, \tag{2.20}$$

in which we have used $\partial J / \partial \boldsymbol{F} = J \boldsymbol{F}^{-\mathrm{t}}$ and employed the constraint $J = 1$. Similarly, the incremental Piola stress can be found by

$$\delta \boldsymbol{P} = \mu\,\delta \boldsymbol{F} + p\,\boldsymbol{F}^{-\mathrm{t}} \cdot \delta \boldsymbol{F}^{\mathrm{t}} \cdot \boldsymbol{F}^{-\mathrm{t}} - \delta p\,\boldsymbol{F}^{-\mathrm{t}} \,. \tag{2.21}$$

2.4.3 Linear elastic material model

Until now, a non-linear finite deformation setting has been adopted. For small strains, materials can be assumed to behave in a linear manner. It is possible to

obtain the linear elastic model by linearizing the Piola stress such that

$$^{\mathcal{L}}\boldsymbol{P} = \boldsymbol{P}\Big|_{\boldsymbol{F}=\boldsymbol{I}} + \frac{\partial \boldsymbol{P}}{\partial \boldsymbol{F}}\Big|_{\boldsymbol{F}=\boldsymbol{I}} : [\,\boldsymbol{F}-\boldsymbol{I}\,] = \mathbb{A}\Big|_{\boldsymbol{F}=\boldsymbol{I}} : [\,\boldsymbol{F}-\boldsymbol{I}\,] \tag{2.22}$$

wherein the stiffness $\mathbb{A}$ given in (2.14) evaluated at $\boldsymbol{F}=\boldsymbol{I}$ renders

$$\mathbb{A} = \mu\,[\,\boldsymbol{I}\,\overline{\otimes}\,\boldsymbol{I} + \boldsymbol{I}\,\underline{\otimes}\,\boldsymbol{I}\,] + \Lambda\,\boldsymbol{I}\otimes\boldsymbol{I}\,, \tag{2.23}$$

where the identity tensors in the spatial configuration $\boldsymbol{i}$ and material configuration $\boldsymbol{I}$ are equal due to the small deformation assumption, hence both have been denoted as $\boldsymbol{I}$. Notice that the stiffness given in Eq. (2.23) is in fact the constitutive tensor commonly defined as $\mathbb{C}$. Similarly, the term $\boldsymbol{F}-\boldsymbol{I}$ acts only through its symmetric part and thus coincides with the infinitesimal strain $\boldsymbol{\varepsilon} := \mathrm{Grad}^{\mathrm{sym}}\boldsymbol{u}$. Hence, we can obtain the classical form for $\boldsymbol{\sigma}$

$$^{\mathcal{L}}\boldsymbol{P} \equiv \boldsymbol{\sigma} := \mathbb{C} : \boldsymbol{\varepsilon} \quad \text{with} \quad \mathbb{C} := 2\,\mu\,\mathbb{I}^{\mathrm{sym}} + 2\,\Lambda\,\mathbb{I}^{\mathrm{vol}}\,, \tag{2.24}$$

where

$$\mathbb{I}^{\mathrm{sym}} := \tfrac{1}{2}[\,\boldsymbol{I}\,\overline{\otimes}\,\boldsymbol{I} + \boldsymbol{I}\,\underline{\otimes}\,\boldsymbol{I}\,] \quad \text{and} \quad \mathbb{I}^{\mathrm{vol}} := \tfrac{1}{2}[\,\boldsymbol{I}\otimes\boldsymbol{I}\,]\,. \tag{2.25}$$

Note that the factor $\frac{1}{2}$ in the definition of $\mathbb{I}^{\mathrm{vol}}$ relates to our plane-strain assumption.

2.5 Numerical approach

This section details the computational implementation of the kinematics and governing equations established so far, via the finite element method (FEM), followed by deliberations on conducting instability analysis with FEM via eigenvalue analysis.

2.5.1 Computational implementation using FEM

The primary step towards the finite element implementation of the theory is to derive the weak form of the governing equations. To do so, the balance of linear momentum $(2.2)_1$ is multiplied from left with a test function $\delta\boldsymbol{\varphi} \in \mathcal{H}_0^1(\mathcal{B}_0)$, and then integrated over the domain $\mathcal{B}_0$, such that

$$\int_{\mathcal{B}_0} \delta\boldsymbol{\varphi} \cdot \mathrm{Div}\boldsymbol{P}\, \mathrm{d}V + \int_{\mathcal{B}_0} \delta\boldsymbol{\varphi} \cdot \boldsymbol{b}_0\, \mathrm{d}V = 0\,. \tag{2.26}$$

The weak form in (2.26) can be re-written using the identity

$$\delta\boldsymbol{\varphi} \cdot \mathrm{Div}\boldsymbol{P} = \mathrm{Div}(\delta\boldsymbol{\varphi} \cdot \boldsymbol{P}) - \boldsymbol{P} : \mathrm{Grad}\delta\boldsymbol{\varphi}\,, \tag{2.27}$$

such that

$$-\int_{\mathcal{B}_0} \boldsymbol{P} : \mathrm{Grad}\delta\boldsymbol{\varphi}\, \mathrm{d}V + \int_{\mathcal{B}_0} \mathrm{Div}(\delta\boldsymbol{\varphi} \cdot \boldsymbol{P})\, \mathrm{d}V + \int_{\mathcal{B}_0} \delta\boldsymbol{\varphi} \cdot \boldsymbol{b}_0\, \mathrm{d}V = 0\,. \tag{2.28}$$

Finally, employing the divergence theorem and rearranging yields

$$\int_{\mathcal{B}_0} \boldsymbol{P} : \mathrm{Grad}\delta\boldsymbol{\varphi}\, \mathrm{d}V - \int_{\mathcal{B}_0} \delta\boldsymbol{\varphi} \cdot \boldsymbol{b}_0\, \mathrm{d}V - \int_{\partial\mathcal{B}_0} \delta\boldsymbol{\varphi} \cdot \boldsymbol{t}_0\, \mathrm{d}A = 0\,. \tag{2.29}$$

Next, as shown in Fig. 2.2, the weak form (2.29) is discretized using finite elements. For the finite element analysis, it is virtually impossible to capture an *infinite* half-space. Instead, the domain is truncated sufficiently far from the surface and roller supports are added at the bottom, illustrated also in Fig. 2.2. The roller supports prevent the displacements in the vertical direction but do not pose any restriction on the displacements in the horizontal direction.

Shape functions are employed for the discretization process, such that a single point $\boldsymbol{x}$ in the deformed configuration can be approximated as $\boldsymbol{x} \simeq \sum_{\alpha=1}^{npe} N^\alpha \boldsymbol{x}^\alpha$, where N^α is the shape function at that point. A similar approximation applies to the reference coordinates $\boldsymbol{X} \simeq \sum_{\alpha=1}^{npe} N^\alpha \boldsymbol{X}^\alpha$, and $\delta\boldsymbol{\varphi} \simeq \sum_{\alpha=1}^{npe} N^\alpha \delta\boldsymbol{\varphi}^\alpha$. Within the non-linear finite element setting, the left-hand side of (2.29) *approximately*

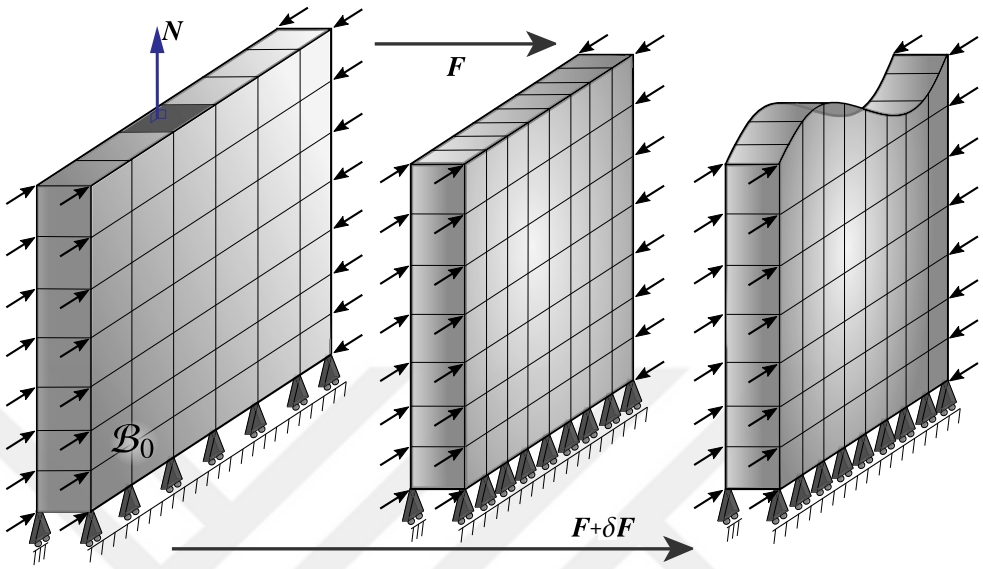


Figure 2.2: Schematic illustration of the finite elements and approximation of an infinite half-space and associated boundary conditions suitable for the finite element method. The domain is truncated sufficiently far from the surface and must be long enough.

transforms to a residual vector $\boldsymbol{R}(\boldsymbol{\varphi})$ that must vanish $\boldsymbol{R}(\boldsymbol{\varphi}) \doteq \boldsymbol{0}$. Setting the residual vector to zero leads to solving a non-linear system of equations using the Newton–Raphson scheme. The consistent linearization of the resulting system of equations yields

$$\boldsymbol{R}(\boldsymbol{\varphi}_{k+1}) \doteq \boldsymbol{0} \quad \text{with} \quad \boldsymbol{R}(\boldsymbol{\varphi}_{k+1}) = \boldsymbol{R}(\boldsymbol{\varphi}_k) + \frac{\partial \boldsymbol{R}}{\partial \boldsymbol{\varphi}}\Big|_k \cdot \Delta\boldsymbol{\varphi} \doteq \boldsymbol{0}\,, \tag{2.30}$$

and

$$\boldsymbol{\varphi}_{k+1} \quad = \boldsymbol{\varphi}_k + \Delta\boldsymbol{\varphi}\,, \tag{2.31}$$

wherein $\boldsymbol{K} := \partial \boldsymbol{R}/\partial \boldsymbol{\varphi}$ is often referred to as the stiffness matrix. Via the discretization of Eq. (2.29) and since for our case $\boldsymbol{b}_0 = \boldsymbol{0}$ and $\boldsymbol{t}_0 = \boldsymbol{0}$, the discretized residual vector reads

$$\boldsymbol{R}^I(\boldsymbol{\varphi}) := \int_{\mathcal{B}_0} \boldsymbol{P} : \mathrm{Grad} N^I \,\mathrm{d}V = \boldsymbol{0}\,, \tag{2.32}$$

wherein the index $\{\bullet\}^I$ serves as a global counter and is equivalent to the counter

α after assembly. The stiffness matrix then, after discretization, reads

$$\boldsymbol{K}^{IJ} = \frac{\partial \boldsymbol{R}^I}{\partial \boldsymbol{\varphi}^J} = \int_{\mathcal{B}_0} \frac{\partial}{\partial \boldsymbol{\varphi}^J} \Big(\boldsymbol{P} \cdot \mathrm{Grad} N^I \Big) \mathrm{d}V = \int_{\mathcal{B}_0} \frac{\partial \boldsymbol{P}}{\partial \boldsymbol{\varphi}^J} \,\bar{:}\, \mathrm{Grad} N^I \mathrm{d}V \,. \tag{2.33}$$

In order to calculate the partial derivative

$$\frac{\partial \boldsymbol{P}}{\partial \boldsymbol{\varphi}^J} = \frac{\partial \boldsymbol{P}}{\partial \boldsymbol{F}} : \frac{\partial \boldsymbol{F}}{\partial \boldsymbol{\varphi}^J} \,, \tag{2.34}$$

we define the deformation gradient $\boldsymbol{F}$ in terms of the shape functions such that

$$\boldsymbol{F} = \mathrm{Grad} \boldsymbol{\varphi} \approx \mathrm{Grad}(\, N^\alpha \, \boldsymbol{\varphi}^\alpha \,) = \boldsymbol{\varphi}^\alpha \otimes \mathrm{Grad} N^\alpha \,, \tag{2.35}$$

which renders the derivative $\partial \boldsymbol{F} / \partial \boldsymbol{\varphi}^J$ to be

$$\frac{\partial \boldsymbol{F}}{\partial \boldsymbol{\varphi}^J} = \frac{\partial \boldsymbol{\varphi}^\alpha}{\partial \boldsymbol{\varphi}^J} \,\overline{\otimes}\, \mathrm{Grad} N^\alpha = \boldsymbol{I} \,\overline{\otimes}\, \mathrm{Grad} N^J \,, \tag{2.36}$$

which when used in the stiffness equation (2.33) yields

$$\boldsymbol{K}^{IJ} = \int_{\mathcal{B}_0} \Big[\frac{\partial \boldsymbol{P}}{\partial \boldsymbol{F}} : \big[\, \boldsymbol{I} \,\overline{\otimes}\, \mathrm{Grad} N^J \, \big] \Big] \,\bar{:}\, \mathrm{Grad} N^I \mathrm{d}V \,. \tag{2.37}$$

Finally, recalling that we defined the fourth order tensor $\mathbb{A} := \partial \boldsymbol{P} / \partial \boldsymbol{F}$ and simplifying renders the final stiffness

$$\boldsymbol{K}^{IJ} = \int_{\mathcal{B}_0} \Big[\, \mathbb{A} : \big[\, \boldsymbol{I} \,\overline{\otimes}\, \mathrm{Grad} N^J \, \big] \Big] \,\bar{:}\, \mathrm{Grad} N^I \mathrm{d}V \,, \tag{2.38}$$

or

$$\boldsymbol{K}^{IJ} = \int_{\mathcal{B}_0} \mathrm{Grad} N^I \,\bar{:}\, \mathbb{A} \cdot \mathrm{Grad} N^J \, \mathrm{d}V \,, \tag{2.39}$$

For the numerical results presented in this work, the energy model given in Sec. 2.4.1 and the corresponding tangent stiffness (2.14) has been used. The method elaborated on in this section briefly outlined the structure and governing equations of a non-linear FEM code. Next, we look at how to capture instabilities using this framework.

2.5.2 Instability analysis using FEM

The underlying feature of the computational study here is that (i) the perturbations are suppressed and (ii) the finite element method is enhanced with eigenvalue analysis. When the structure becomes unstable and bifurcates, at the onset of this bifurcation, there exist two residual vectors which have the same value, in other words

$$\delta \boldsymbol{R} = \boldsymbol{0} \qquad \Rightarrow \qquad \boldsymbol{R}(\boldsymbol{\varphi}_I) = \boldsymbol{R}(\boldsymbol{\varphi}_J)\,. \tag{2.40}$$

Recalling the applied Newton–Raphson scheme to minimize the residual (2.30) which would dictate that

$$\boldsymbol{R}(\boldsymbol{\varphi}_J) = \boldsymbol{R}(\boldsymbol{\varphi}_I) + \boldsymbol{K}(\boldsymbol{\varphi}_I) \cdot \Delta\widetilde{\boldsymbol{\varphi}}\,, \tag{2.41}$$

we obtain the condition that at the onset of instability

$$\boldsymbol{K}(\boldsymbol{\varphi}_I) \cdot \Delta\widetilde{\boldsymbol{\varphi}} = \boldsymbol{0}\,, \tag{2.42}$$

which now presents itself as a simple eigenvalue problem for the stiffness $\boldsymbol{K}$. The eigenspace representation of the stiffness matrix of a system with n degrees of freedom reads

$$\boldsymbol{K}_{n\times n} = \sum_{i=1}^{n} K_i\, \boldsymbol{\lambda}_i \otimes \boldsymbol{\lambda}_i\,, \tag{2.43}$$

in which K_i and $\boldsymbol{\lambda}_i$, denote eigenvalues and their associated *unit* eigenvectors, respectively. From a computational perspective, instabilities occur when the smallest positive eigenvalue of the stiffness matrix approaches zero, and hence the critical stretch is achieved exactly where the smallest eigenvalue reaches zero.

In summary, to investigate the onset of wrinkling under plane deformations, we start from the reference configuration and we *incrementally* prescribe compression in the horizontal direction. After prescribing displacements of each increment, we let the domain relax via iterations of a Newton–Raphson scheme. The equilibrium state is reached when the L_2-norm of the residual reaches zero. Throughout the iterations, the quadratic rate of convergence associated with the Newton–Raphson scheme is consistently obtained. At each increment, we carry out an eigenvalue

analysis at the equilibrium configuration. If all the eigenvalues are positive, we proceed with the next increment. If any of the eigenvalues is sufficiently close to zero, then (i) we record the prescribed stretch as the critical stretch λ_{cr}, (ii) we compute the eigenvector of the smallest eigenvalue and impose it as a deformation and (iii) we terminate the computations. Further information on FEM with eigenvalue analysis and how the numerical studies in this work were conducted can be found in Appendix A.

This concludes this chapter on large deformation continuum mechanics from theoretical and numerical aspects. Next, we look at the application of the theory established here to different geometries and boundary conditions.

Chapter 3

Small strain instabilities

The main goal of this chapter is to elaborate on a linear elastic approach to the instabilities of a wrinkling bilayer domain. Even though it is known that soft matter exhibit non-linear behavior as they go through large deformations, it is possible to approximate their behavior under small deformations by using a linear elastic approach. The derivations here are concerned with a growing, thin, stiff film placed on a more compliant substrate. Within these constraints, the compressive stresses within the film result from growth only and no compression on the whole domain, which in turn corresponds to a stress-free substrate at the onset of wrinkling behaving according to small-strain linear elasticity. Section 3.1 establishes the framework to calculate the effective stiffness of a wrinkled substrate. Then, the wrinkling of a growing film embedded on top of this substrate is analyzed theoretically and numerically in Sec. 3.2.

3.1 Effective stiffness of a half-space

The objective of this section is to compute the resistance (equivalent stiffness) of an infinite half-space (substrate) against prescribing a sinusoidal deformation on its surface. A commonly accepted strategy to compute the substrate equivalent

stiffness dates back to the seminal work of Allen [2] and employs the Airy stress functions. While the Allen solution is correct, due to its reliance on Airy functions, it is limited to two-dimensional linear isotropic problems and its success depends entirely on choosing an appropriate Airy function. A key feature here is to propose a displacement-based approach to compute the equivalent stiffness of the substrate without recourse to Airy stress functions and hence, suitable for three-dimensional as well as anisotropic problems. Unlike Allen's solution, the current approach can even be formally applied to finite deformations, as we will see in Chapter 4.

Let $\boldsymbol{u}$ denote the displacement field in the substrate and $\boldsymbol{\varepsilon}$ be the associated strain field. The Cauchy stress $\boldsymbol{\sigma}$ is related to the strain $\boldsymbol{\varepsilon}$ via a linear mapping $\mathbb{C}$ where $\mathbb{C}$ is referred to as the constitutive tensor. General field equations of elasticity are

$$\boldsymbol{\varepsilon} = \nabla^{\text{sym}}\boldsymbol{u} \quad , \quad \nabla \times \boldsymbol{\varepsilon} \times \nabla = \boldsymbol{0} \quad , \quad \text{div}\boldsymbol{\sigma} = \boldsymbol{0} \quad , \quad \boldsymbol{\sigma} = \mathbb{C} : \boldsymbol{\varepsilon}\,, \tag{3.1}$$

in which Eq. $(3.1)_2$ ensures the compatibility of the strain field and Eq. $(3.1)_3$ is the linear momentum balance in the absence of body forces. The angular momentum balance requires the symmetry of the stress field $\boldsymbol{\sigma}$ which is satisfied a priori via the symmetry properties of the constitutive tensor $\mathbb{C}$ and thus, is omitted from the equations. Note, the strain $\boldsymbol{\varepsilon}$ can be computed from the stress $\boldsymbol{\sigma}$ via the inverse of the constitutive tensor as

$$\boldsymbol{\varepsilon} = \mathbb{C}^{\text{-1}} : \boldsymbol{\sigma} \qquad \text{with} \qquad \mathbb{C}^{\text{-1}} = \frac{1}{2\mu_s}\,\mathbb{I}^{\text{sym}} - \frac{\lambda_s}{2\mu_s[\mu_s + \lambda_s]}\,\mathbb{I}^{\text{vol}}\,. \tag{3.2}$$

The general field equations of elasticity (3.1) can be reformulated depending on the nature of the problem of interest. Such reformulations fall into two categories of *Stress-based approach* and *Displacement-based approach* briefly addressed below. A *Stress-based approach* will be briefly summarized first and then will be followed by the *Displacement-based approach* developed herein.

3.1.1 Stress-based approach

Stress formulation also referred to as *Beltrami–Michell equation* is obtained through imposing the strain compatibility $(3.1)_2$ in terms of stresses using the constitutive relation $(3.1)_4$ and then imposing the linear momentum balance $(3.1)_3$ as

$$\begin{aligned} &\nabla \times \boldsymbol{\varepsilon} \times \nabla = \mathbf{0} \quad \text{with} \quad \boldsymbol{\varepsilon} = \mathbb{C}^{-1} : \boldsymbol{\sigma} \quad \Rightarrow \quad \nabla \times \mathbb{C}^{-1} : \boldsymbol{\sigma} \times \nabla = \mathbf{0}\,, \\ &\nabla \times \mathbb{C}^{-1} : \boldsymbol{\sigma} \times \nabla = \mathbf{0} \quad \text{with} \quad \mathrm{div}\boldsymbol{\sigma} = \mathbf{0} \quad \Rightarrow \quad \text{Beltrami–Michell equation}\,, \end{aligned} \tag{3.3}$$

which for the two-dimensional plane-strain problem of interest here reads

$$\Delta(\boldsymbol{\sigma} : \boldsymbol{i}) = 0 \qquad \text{with} \qquad \Delta\{\bullet\} = \mathrm{div}(\nabla\{\bullet\}) = \frac{\partial^2\{\bullet\}}{\partial\xi^2} + \frac{\partial^2\{\bullet\}}{\partial\eta^2}\,, \tag{3.4}$$

where $\Delta\{\bullet\}$ denotes the Laplacian operator. Note, the stress formulation is more appropriate to use with traction-type boundary condition problems. The governing equation for the stress formulation even in two-dimensional problems is still rather complex and analytical solutions are commonly determined through an Airy stress function ϕ satisfying the biharmonic equation

$$\Delta\Delta\phi = 0 \quad \text{with} \quad \Delta\Delta\{\bullet\} = \Delta(\Delta\{\bullet\}) = \frac{\partial^4\{\bullet\}}{\partial\xi^4} + 2\,\frac{\partial^4\{\bullet\}}{\partial\xi^2\partial\eta^2} + \frac{\partial^4\{\bullet\}}{\partial\eta^4}\,, \tag{3.5}$$

whereby $\Delta\Delta\{\bullet\}$ denotes the biharmonic operator. For the Airy stress function ϕ, the stresses

$$\sigma_{\xi\xi} = \frac{\partial^2\phi}{\partial\eta^2} \quad , \quad \sigma_{\xi\eta} = -2\,\frac{\partial^2\phi}{\partial x\partial y} \quad , \quad \sigma_{\eta\eta} = \frac{\partial^2\phi}{\partial\xi^2}\,, \tag{3.6}$$

satisfy the Beltrami–Michell equation (3.4) a priori. Once the stresses are calculated, the strains can be obtained via the constitutive relation $(3.1)_4$ and eventually, integrating the strains renders the displacement field in the domain. Clearly, the stress based approach relies completely on the choice of the Airy stress functions. In order to construct a more generic and robust theoretical framework, we develop the displacement-based approach elaborated on next.

3.1.2 Displacement-based approach

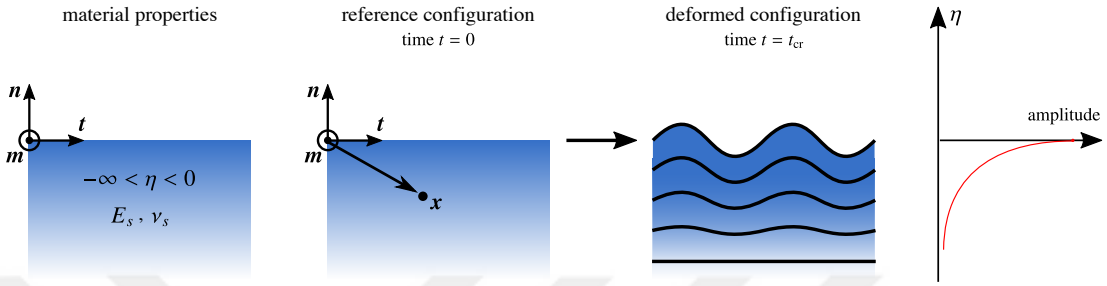


Figure 3.1: Illustration of a decaying surface wave through the infinite half-space representing the substrate here. The stationary wave $\boldsymbol{u}$ can be prescribed as the product of a decay part $\boldsymbol{w}(\eta)$ and a waviness term $\exp(ik\xi)$ in which $k > 0$ is the wavenumber.

Let $\boldsymbol{u}$ denote a hypothetical stationary wave on the surface of the substrate (infinite half-space) as illustrated in Fig. 3.1. The stationary wave lies on the plane spanned by the orthogonal basis $\{\boldsymbol{t}, \boldsymbol{n}, \boldsymbol{m}\}$ where $\boldsymbol{m} = \boldsymbol{t} \times \boldsymbol{n}$ is the outward direction along which the wave function remains constant corresponding to the associated plane-strain condition. The wave function $\boldsymbol{u}$ is constructed such that it decays through the substrate meaning that its amplitude vanishes asymptotically when the depth approaches infinity. Let $\xi = \boldsymbol{x} \cdot \boldsymbol{t}$ and $\eta = \boldsymbol{x} \cdot \boldsymbol{n}$ denote the components of an arbitrary position vector $\boldsymbol{x}$. The stationary wave $\boldsymbol{u}$ can be prescribed as the product of a part $\boldsymbol{w}(\eta)$ and a waviness term $\exp(ik\xi)$ in which $k > 0$ is the wavenumber and is related to the wavelength ℓ via $k = 2\pi/\ell$. Therefore, the wave function $\boldsymbol{u}$ reads

$$\boldsymbol{u} = \boldsymbol{w}(\eta) \exp(ik\xi) \,. \tag{3.7}$$

To proceed, the wave function $\boldsymbol{u}$ is imposed as the deformation of the substrate and its admissible format satisfying the linear momentum balance is derived. The balance of linear momentum in the substrate reads $\mathrm{div}\boldsymbol{\sigma} = \boldsymbol{0}$ with the stress strain relation $\boldsymbol{\sigma} = \mathbb{C} : \boldsymbol{\varepsilon}$. Inserting the strain $\boldsymbol{\varepsilon}$ in terms of the wave function $\boldsymbol{u}$ and

using the symmetry properties of the constitutive tensor $\mathbb{C}$ yields

$$\operatorname{div}\boldsymbol{\sigma} = \operatorname{div}(\mathbb{C} : \boldsymbol{\varepsilon}) = \operatorname{div}(\mathbb{C} : \nabla\boldsymbol{u}) = [\nabla(\mathbb{C} : \nabla\boldsymbol{u})] : \boldsymbol{i} = [\mathbb{C} : \nabla\nabla\boldsymbol{u}] : \boldsymbol{i} = \boldsymbol{0}\,. \tag{3.8}$$

Using the chain rule

$$\nabla\{\bullet\} = \frac{\partial\{\bullet\}}{\partial\xi} \otimes \boldsymbol{t} + \frac{\partial\{\bullet\}}{\partial\eta} \otimes \boldsymbol{n}\,, \tag{3.9}$$

the second gradient of the wave function $\boldsymbol{u}$ is obtained as

$$\begin{aligned}
&\boldsymbol{u} = \boldsymbol{w}(\eta)\, \exp(ik\xi)\,,\\
&\nabla\boldsymbol{u} = [\, \boldsymbol{w}' \otimes \boldsymbol{n} + ik\, \boldsymbol{w} \otimes \boldsymbol{t}\,] \exp(ik\xi)\,,\\
&\nabla\nabla\boldsymbol{u} = \Big[\, \boldsymbol{w}'' \otimes \boldsymbol{n} \otimes \boldsymbol{n} + ik[\boldsymbol{w}' \otimes \boldsymbol{t} \otimes \boldsymbol{n} + \boldsymbol{w}' \otimes \boldsymbol{n} \otimes \boldsymbol{t}] - k^2\, \boldsymbol{w} \otimes \boldsymbol{t} \otimes \boldsymbol{t} \Big] \exp(ik\xi)\,.
\end{aligned} \tag{3.10}$$

Inserting $\mathbb{C}$ from Eq. (2.24) and $\nabla\nabla\boldsymbol{u}$ from Eq. $(3.10)_3$ into the linear momentum balance (3.8) yields the ordinary differential equation

$$\begin{aligned}
\big[\, \mu_s\, \boldsymbol{i} + [\lambda_s + \mu_s]\, \boldsymbol{n} \otimes \boldsymbol{n}\, \big] \cdot \boldsymbol{w}'' + ik\, \big[\, [\mu_s + \lambda_s]\, [\boldsymbol{n} \otimes \boldsymbol{t} + \boldsymbol{t} \otimes \boldsymbol{n}]\, \big] \cdot \boldsymbol{w}'\\
- k^2\, \big[\, \mu_s\, \boldsymbol{i} + [\lambda_s + \mu_s]\, \boldsymbol{t} \otimes \boldsymbol{t}\, \big] \cdot \boldsymbol{w} = \boldsymbol{0}\,,
\end{aligned} \tag{3.11}$$

which can be written as

$$\boldsymbol{A} \cdot \boldsymbol{w}'' + ik\, \boldsymbol{B} \cdot \boldsymbol{w}' - k^2\, \boldsymbol{C} \cdot \boldsymbol{w} = \boldsymbol{0}\,, \tag{3.12}$$

where

$$\begin{aligned}
\boldsymbol{A} &:= \mu_s\, \boldsymbol{i} + [\lambda_s + \mu_s]\, \boldsymbol{n} \otimes \boldsymbol{n}\,,\\
\boldsymbol{B} &:= [\mu_s + \lambda_s]\, [\boldsymbol{n} \otimes \boldsymbol{t} + \boldsymbol{t} \otimes \boldsymbol{n}]\,,\\
\boldsymbol{C} &:= \mu_s\, \boldsymbol{i} + [\lambda_s + \mu_s]\, \boldsymbol{t} \otimes \boldsymbol{t}\,.
\end{aligned} \tag{3.13}$$

Next, the differential equation (3.12) is solved in order to obtain the admissible forms of the wave function $\boldsymbol{u}$. In doing so, it proves convenient to rewrite the differential equation (3.12) as

$$\boldsymbol{w}'' + ik\, \boldsymbol{A}^{-1} \cdot \boldsymbol{B} \cdot \boldsymbol{w}' - k^2\, \boldsymbol{A}^{-1} \cdot \boldsymbol{C} \cdot \boldsymbol{w} = \boldsymbol{0}\,, \tag{3.14}$$

in which $\boldsymbol{A}^{-1}$ is obtained via applying the Sherman–Morrison formula as

$$\boldsymbol{A}^{-1} = \frac{1}{\mu_s}\boldsymbol{i} - \frac{\lambda_s + \mu_s}{\mu_s[\lambda_s + 2\mu_s]}\boldsymbol{n} \otimes \boldsymbol{n}\,. \tag{3.15}$$

To proceed, the second-order differential equation (3.14) is decomposed into a system of two first-order differential equations as $\boldsymbol{W}' = \boldsymbol{M} \cdot \boldsymbol{W}$ with

$$\boldsymbol{W} = \begin{bmatrix} \boldsymbol{w} \\ \boldsymbol{w}' \end{bmatrix} \;\Rightarrow\; \boldsymbol{W}' = \begin{bmatrix} \boldsymbol{w}' \\ \boldsymbol{w}'' \end{bmatrix} = \boldsymbol{M} \cdot \boldsymbol{W}\,, \tag{3.16}$$

with

$$\boldsymbol{M} := \begin{bmatrix} \boldsymbol{0} & \boldsymbol{i} \\ k^2\,\boldsymbol{A}^{-1} \cdot \boldsymbol{C} & -ik\,\boldsymbol{A}^{-1} \cdot \boldsymbol{B} \end{bmatrix}, \tag{3.17}$$

since

$$\begin{bmatrix} \boldsymbol{w}' \\ \boldsymbol{w}'' \end{bmatrix} = \begin{bmatrix} \boldsymbol{w}' \\ k^2\boldsymbol{A}^{-1} \cdot \boldsymbol{C} \cdot \boldsymbol{w} - ik\boldsymbol{A}^{-1} \cdot \boldsymbol{B} \cdot \boldsymbol{w}' \end{bmatrix} = \begin{bmatrix} \boldsymbol{0} & \boldsymbol{i} \\ k^2\boldsymbol{A}^{-1} \cdot \boldsymbol{C} & -ik\boldsymbol{A}^{-1} \cdot \boldsymbol{B} \end{bmatrix} \begin{bmatrix} \boldsymbol{w} \\ \boldsymbol{w}' \end{bmatrix}. \tag{3.18}$$

The system $\boldsymbol{W}' = \boldsymbol{M} \cdot \boldsymbol{W}$ is essentially a differential equation of the first order, which has the generic solution $\boldsymbol{W} = \boldsymbol{a}\exp(\tau\eta)$ where τ is the decay coefficient. Plugging in the proposed solution into the system (3.16) yields the eigenvalue problem $[\boldsymbol{M} - \tau\boldsymbol{I}] \cdot \boldsymbol{a} = \boldsymbol{0}$ whose non-trivial solutions correspond to the condition $\det(\boldsymbol{M} - \tau\,\boldsymbol{I}) = 0$ which can be represented in the matrix format as

$$[\boldsymbol{M} - \tau\,\boldsymbol{I}] = \begin{bmatrix} -\tau & 0 & 1 & 0 \\ 0 & -\tau & 0 & 1 \\ k^2[1+\alpha_s] & 0 & -\tau & -ik\alpha_s \\ 0 & k^2[1-\beta_s] & -ik\alpha_s[1-\beta_s] & -\tau \end{bmatrix}, \tag{3.19}$$

where

$$\alpha_s := \frac{\lambda_s + \mu_s}{\mu_s} \qquad \text{and} \qquad \beta_s := \frac{\lambda_s + \mu_s}{\lambda_s + 2\mu_s}\,, \tag{3.20}$$

which eventually yields

$$\det(\boldsymbol{M} - \tau\,\boldsymbol{I}) = 0 \quad \Rightarrow \quad [k^2 - \tau^2]^2 = 0 \quad \Rightarrow \quad \tau = \pm k\,. \tag{3.21}$$

From the solution $\tau = \pm k$, only $\tau = k$ satisfies the decay condition at $\eta \to -\infty$, hence is the only acceptable solution. The generic bounded solution of the differential equation (3.14) obtained by solving for the eigenvectors corresponding to $\tau > 0$, see [29] for more details, reads

$$\boldsymbol{w}(\eta) = \frac{1}{k}\left[\left[Ci - D\frac{2\mu_s i}{k[\mu_s + \lambda_s]} - Di\eta\right]\boldsymbol{t} + \left[C + D\frac{1}{k} - D\eta\right]\boldsymbol{n}\right]\exp(k\eta)\,, \quad (3.22)$$

in which the constants C and D can be specified via imposing the boundary conditions. Inserting the decay function $\boldsymbol{w}$ into the wave function $\boldsymbol{u} = \boldsymbol{w}(\eta)\,\exp(ik\xi)$ reads

$$\boldsymbol{u} = \frac{1}{k}\left[\left[Ci - D\frac{2\mu_s i}{k[\mu_s + \lambda_s]} - Di\eta\right]\boldsymbol{t} + \left[C + D\frac{1}{k} - D\eta\right]\boldsymbol{n}\right]\exp(k\,[i\xi + \eta])\,. \quad (3.23)$$

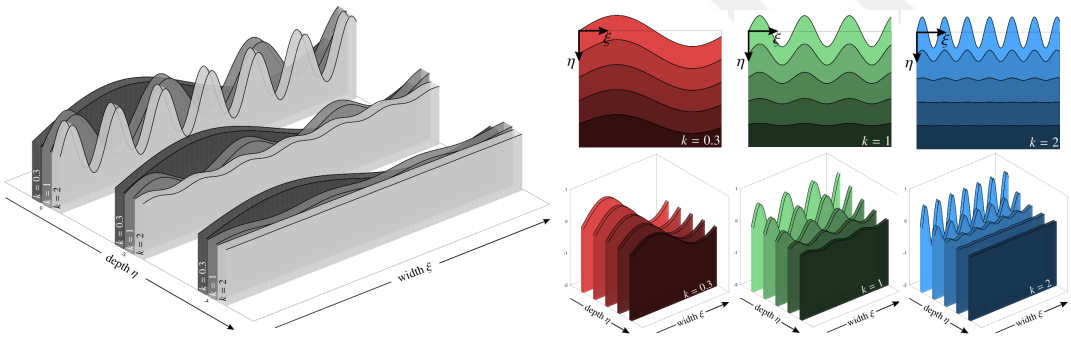


Figure 3.2: Illustration of the stationary wave $\boldsymbol{u}$ for various wavenumbers k and at different depths η. According to the relation $\tau = k$ the decay coefficient τ must be identical to the wavenumber k in order to have an admissible wave function (3.7). Therefore, a surface wave with a larger wavelength decays slower compared to a wave with a smaller wavelength.

The relation $\tau = k$ is significant since it indicates that the decay coefficient τ must be identical to the wavenumber k in order to have an admissible wave function (3.7). Therefore, the surface waves with larger wavenumbers decay faster along the depth of the substrate. In other words, the waves with larger wavelength decay slower and thus their effect vanishes at large depth η, as shown in Fig. 3.2. This observation is particularly remarkable from a computational perspective. In finite element simulations, the infinite half-space must be approximated as a

domain with a prescribed depth. The finding (3.21) indicates that the finite depth of the substrate in numerical simulations can have a considerable influence on the results depending on the wavelength itself. Based on the relation $\tau = k$, from a computational perspective, one can adjust the depth of the substrate according to the wavelength so as to obtain comparable solutions.

At the surface of the substrate corresponding to $\eta = 0$, the displacement is identical to that of the wrinkling film. Note, the wrinkling of the film is associated with its internal growth and the compressive residual stress thereof but no actual geometrical compression is applied. At this point, we need to apply boundary conditions to the generic displacement form obtained in (3.23). At the top surface of the half-space, we assume that the resultant displacements are only in the vertical direction, i.e. that the horizontal displacement at the surface $\eta = 0$ at the onset of bifurcation is zero. We impose this boundary condition as $\boldsymbol{v}_{\xi}\big|_{\eta=0} = 0$. The displacement in the ξ-direction, $\boldsymbol{v}_{\xi}$, and η-direction, $\boldsymbol{v}_{\eta}$ correspond to the $\boldsymbol{t}$-component and $\boldsymbol{n}$-component of $\boldsymbol{u}$, respectively. The hypothetical wave $\boldsymbol{u}$ on the surface reads

$$\boldsymbol{u}\big|_{\eta=0} = \frac{1}{k}\left[\left[Ci - D\frac{2\mu_s i}{k[\mu_s+\lambda_s]}\right]\boldsymbol{t} + \left[C + D\frac{1}{k}\right]\boldsymbol{n}\right]\exp(ik\xi)\,. \tag{3.24}$$

Imposing the boundary condition $\boldsymbol{v}_{\xi}\big|_{\eta=0} = 0$, yields the key relation

$$\frac{D}{C} = k\,\frac{\mu_s+\lambda_s}{2\mu_s}\,, \tag{3.25}$$

between the constants C and D rendering the wave function on the surface as

$$\boldsymbol{u}\big|_{\eta=0} = C\,\frac{1}{k}\left[\frac{3\mu_s+\lambda_s}{2\mu_s}\right]\boldsymbol{n}\,\exp(ik\xi)\,. \tag{3.26}$$

Hence, the wave function $\boldsymbol{u}$ reads

$$\boldsymbol{u} = C\left[\left[-\frac{\mu_s+\lambda_s}{2\mu_s}i\eta\right]\boldsymbol{t} + \left[\frac{3\mu_s+\lambda_s}{2\mu_s k} - \frac{\mu_s+\lambda_s}{2\mu_s}\eta\right]\boldsymbol{n}\right]\exp(k\,[i\xi+\eta])\,. \tag{3.27}$$

Remark. *The assumption behind the boundary condition* $\boldsymbol{v}_{\xi}\big|_{\eta=0} = 0$ *stems*

from the understanding that at the onset of buckling at the surface, the displacements only exist in the vertical direction, since the Euler beam to be placed at this surface only bears information about vertical displacement $\boldsymbol{v}$*. This Euler beam approximation of the top layer results in increasing error as the beam gets thicker or more compressible, as we will see in the next chapter. Even though this is an assumption we make here, we later confirm its validity through the numerical results for the cases of a thin film on top of a substrate and at small deformations. Note that within a large deformations framework, this assumption is no longer valid and needs to be framed differently to be able to reflect the boundary conditions of the problem, which will be carried out in Chapter 4.* □

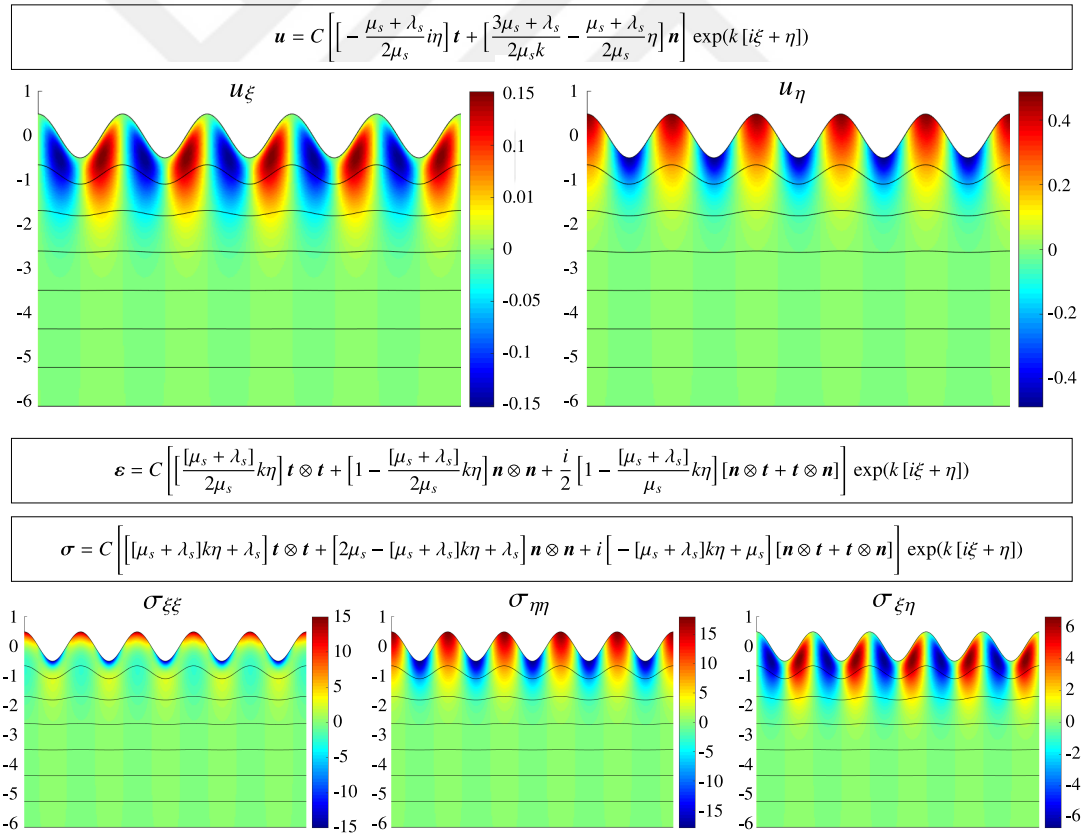


Figure 3.3: Numerical illustrations of u_ξ, u_η, $\sigma_{\xi\xi}$, $\sigma_{\eta\eta}$ and $\sigma_{\xi\eta}$ for a sample set of parameters $\mu_s = 10$, $\lambda_s = 100$ and $C = 0.15$. Analytical solution of the fields correspond to the displacement-based approach.

Equipped with the admissible wave function (3.27), the next step is to compute the traction on the surface of the substrate. The traction $\boldsymbol{f}$ on the surface $\eta = 0$

is obtained via the Cauchy relation $\boldsymbol{f} = \boldsymbol{\sigma} \cdot \boldsymbol{n}$ whereby $\boldsymbol{\sigma}$ is the Cauchy stress on the surface as

$$\boldsymbol{f} = \boldsymbol{\sigma} \cdot \boldsymbol{n} = \boldsymbol{\sigma}\big|_{\eta=0} \cdot \boldsymbol{n} = \Big[\mathbb{C} : \boldsymbol{\varepsilon}\big|_{\eta=0}\Big] \cdot \boldsymbol{n} = \Big[\mathbb{C} : [\nabla \boldsymbol{u}]\big|_{\eta=0}\Big] \cdot \boldsymbol{n}\,. \tag{3.28}$$

Therefore to proceed, we compute the displacement gradient on the surface. The gradient of the admissible wave function (3.27) reads

$$\begin{aligned}\nabla \boldsymbol{u} &= \frac{\partial \boldsymbol{u}}{\partial \xi} \otimes \boldsymbol{t} + \frac{\partial \boldsymbol{u}}{\partial \eta} \otimes \boldsymbol{n} \\ &= ik\, \boldsymbol{u} \otimes \boldsymbol{t} + k\, \boldsymbol{u} \otimes \boldsymbol{n} + C \left[-\frac{\mu_s + \lambda_s}{2\mu_s} i\, \boldsymbol{t} \otimes \boldsymbol{n} - \frac{\mu_s + \lambda_s}{2\mu_s}\, \boldsymbol{n} \otimes \boldsymbol{n} \right] \exp(k\,[i\xi + \eta])\,,\end{aligned} \tag{3.29}$$

and reduces on the surface to

$$[\nabla \boldsymbol{u}]\,\big|_{\eta=0} = C \left[\frac{3\mu_s + \lambda_s}{2\mu_s} i\, \boldsymbol{n} \otimes \boldsymbol{t} - \frac{\mu_s + \lambda_s}{2\mu_s} i\, \boldsymbol{t} \otimes \boldsymbol{n} + \boldsymbol{n} \otimes \boldsymbol{n} \right] \exp(ik\xi)\,. \tag{3.30}$$

The surface stress is then calculated as

$$\boldsymbol{\sigma}\big|_{\eta=0} = C \left[\mu_s\, i\, [\boldsymbol{n} \otimes \boldsymbol{t} + \boldsymbol{t} \otimes \boldsymbol{n}] + [2\mu_s + \lambda_s]\, \boldsymbol{n} \otimes \boldsymbol{n} + \lambda_s\, \boldsymbol{t} \otimes \boldsymbol{t} \right] \exp(ik\xi)\,, \tag{3.31}$$

which is notably symmetric, as expected. Finally, the surface traction $\boldsymbol{f}$ reads

$$\boldsymbol{f} = \boldsymbol{\sigma}\big|_{\eta=0} \cdot \boldsymbol{n} = C \left[\mu_s\, i\, \boldsymbol{t} + [2\mu_s + \lambda_s]\, \boldsymbol{n} \right] \exp(ik\xi)\,, \tag{3.32}$$

or more specifically

$$f_\xi := [\boldsymbol{f}]_\xi \equiv -C\, \mu_s \sin(k\xi) \quad \text{and} \quad f_\eta := [\boldsymbol{f}]_\eta \equiv C\, [2\mu_s + \lambda_s] \cos(k\xi)\,. \tag{3.33}$$

The effective stiffness of the substrate can be understood as the ratio $f_\eta / \boldsymbol{v}_\eta$ indicating the resistance of the substrate against prescribing the wave function $\boldsymbol{v}_\eta$ on its surface. Inserting the vertical surface wave $\boldsymbol{v}_\eta$ from Eq. (3.27) and the

vertical surface traction f_η from Eq. $(3.33)_2$ yields

$$K_s^{\text{eff}} = \frac{f_\eta}{\boldsymbol{v}_\eta} = \frac{C\,[2\mu_s + \lambda_s]\cos(k\xi)}{C\,\dfrac{3\mu_s + \lambda_s}{2\mu_s k}\cos(k\xi)} \quad \Rightarrow \quad K_s^{\text{eff}} = \frac{2\mu_s\,[2\mu_s + \lambda_s]}{3\mu_s + \lambda_s}\,k\,. \tag{3.34}$$

The problem formulation so far has been in terms of the Lamé parameters μ_s and λ_s. Nonetheless, it is possible to carry out the derivations in terms of other pairs of parameters such as the elastic modulus E_s and Poisson's ratio ν_s. A remarkable outcome is that while K_s^{eff} in terms of the Lamé parameters differs for plane-strain and plane-stress, translating K_s^{eff} in terms of E_s and ν_s renders identical forms for both cases as

$$K_s^{\text{eff}}(E_s, \nu_s) = \frac{2E_s}{[3 - \nu_s][1 + \nu_s]}\,k\,. \tag{3.35}$$

This finding is significant since it provides a unified formulation for both the plane-strain and plane-stress conditions.

3.2 Wrinkling of a growing layer

This section details on growth induced instabilities of a thin growing film. To begin with, the thin film is assumed to be on top of a deep (infinite half-space) compliant substrate, as illustrated in Fig. 3.4. The analytical solution of this problem is derived based on the equivalent stiffness of the substrate (3.35). The analytical solution is illustrated next using numerical examples and its key features are discussed. One underlying assumption of this section is that at the onset of wrinkling the substrate is stress-free which shall be revisited if other scenarios are to be considered. Various extensions of the proposed approach to more complicated cases and to introduce pre-stretch as well as nonlinearities into the picture are possible and will be done in the upcoming chapters.

In order to derive the analytical solution for wrinkling of a growing thin film on an infinite half-space, we decompose the domain into two subdomains, namely,

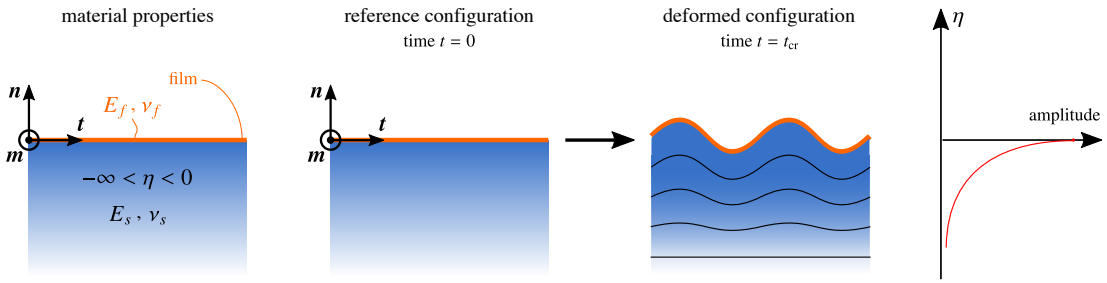


Figure 3.4: Decomposition of the domain into the film and substrate. The film is perfectly bonded to the substrate at all times. The amplitude of the sinusoidal wave on the substrate and its decay versus depth η is schematically illustrated on the graph.

the film and the substrate, as shown in Fig. 3.4. Then each subdomain is treated separately and their corresponding deformations are superimposed according to the geometrical constraint of *perfect bonding* between the film and the substrate. That is, the film is constantly adhered to the substrate and cannot detach from it and thus, the deformation of the film must be identical to that of the substrate. The elastic modulus and Poisson's ratio of the film are denoted E_f and ν_f, respectively. The growing elastic film fixed at both ends resembles a thin beam under compression wherein the compression results from the accumulation of the residual stresses due to growth. Furthermore, the interaction of the film with the substrate manifests itself as a distributed force on the film. If $\boldsymbol{v}$ denotes the deflection of a thin beam, the classical governing equation of the beam reads

$$E_f\, I\, \boldsymbol{v}'''' + \sigma\, b\, h\, \boldsymbol{v}'' = f\,, \tag{3.36}$$

in which E_f and I are the elastic modulus and the moment of inertia of the beam, respectively. The Euler beam solution used herein inherently carries an incompressibility assumption; thus, ν_f does not appear in our derivations but the film is assumed to be incompressible. The *compressive stress* along the film due to growth is denoted σ and f on the right-hand side denotes the distributed force on the beam in the orthogonal direction. Note, positive values for σ correspond to compression based on our definition. The fundamental solution of the film equation (3.36) for the deflection $\boldsymbol{v}$ is of sinusoidal form. On the other hand, for a sinusoidal deflection function on the surface of the substrate, the force

distribution reads

$$f = -b\, K_s^{\text{eff}}\, \boldsymbol{v} \qquad \text{with} \qquad K_s^{\text{eff}} = \frac{2E_s}{[3-\nu_s][1+\nu_s]}\, k\,, \tag{3.37}$$

where $k = 2\pi/\ell$ is the wavenumber of the deflection $\boldsymbol{v}$. The minus sign in front of f is due to the fact that the force f in Eq. (3.37) is the (reaction) force exerted from the substrate on the film hence, negative of the force on the surface of the substrate.

Next, we insert the distributed force $(3.37)_1$ into the governing equation of the film (3.36). Also, the moment of inertia for a film with a rectangular cross-section of the width b and height h is $I = bh^3/12$. Finally, considering the sinusoidal nature of the deflection, the relation $\boldsymbol{v}'' = -k^2\, \boldsymbol{v}$ holds and yields

$$\frac{1}{12} E_f\, h^3\, k^4\, \boldsymbol{v} - \sigma\, h\, k^2\, \boldsymbol{v} = -\frac{2E_s}{[3-\nu_s][1+\nu_s]}\, k\, \boldsymbol{v}\,, \tag{3.38}$$

resulting in

$$\sigma = \frac{1}{12} E_f\, h^2\, k^2 + \frac{2E_s}{[3-\nu_s][1+\nu_s]}\, \frac{1}{hk}\,, \tag{3.39}$$

for the compressive stress σ in the film due to growth. In order to calculate the critical wavenumber k_{cr} at the onset of the *growth induced instability*, we set the derivative of the stress σ with respect to k to zero and after some manipulation k_{cr} reads

$$\frac{\partial \sigma}{\partial k} = 0 \qquad \Rightarrow \qquad k_{\text{cr}} = \frac{1}{h} \left[\frac{12E_s}{E_f\, [3-\nu_s][1+\nu_s]} \right]^{\frac{1}{3}}\,, \tag{3.40}$$

from which the critical induced stress in the film σ_{cr} and the associated critical strain $\varepsilon_{\text{cr}} = \sigma_{\text{cr}}/E_f$ can be obtained by inserting k_{cr} into Eq. (3.39) as

$$\sigma_{\text{cr}} = E_f \left[\frac{3E_s}{2E_f\, [3-\nu_s][1+\nu_s]} \right]^{\frac{2}{3}} \qquad , \qquad \varepsilon_{\text{cr}} = \left[\frac{3E_s}{2E_f\, [3-\nu_s][1+\nu_s]} \right]^{\frac{2}{3}}\,. \tag{3.41}$$

Notice that at the incompressible limit where $\nu_s \to 1$, the expression for critical

strain ε_{cr} in Eq. $(3.41)_2$ recovers the well established solution [52]

$$\varepsilon_{\text{cr}} = \frac{1}{4}\left[\frac{3E_s}{E_f}\right]^{\frac{2}{3}} . \tag{3.42}$$

Eventually, the critical wavelength ℓ_{cr} and the critical growth g_{cr} can be computed as $\ell_{\text{cr}} = 2\pi/k_{\text{cr}}$ and $g_{\text{cr}} = \varepsilon_{\text{cr}}/[1-\varepsilon_{\text{cr}}]$ thereby a positive strain is assumed to be compressive. Note, the final results here are formally identical to those given by Allen [2].

We emphasize that the relation between the compressive strain in the film and the film growth reads $g = \varepsilon/[1-\varepsilon]$, or alternatively $\varepsilon = g/[1+g]$, in which g is the (anisotropic) film growth coefficient along the film itself with $g > 0$ indicating growth and $g < 0$ corresponding to shrinkage. Also, throughout the previous derivations it is assumed that a positive strain is compressive which complies with our sign convention for growth g. In other words, shrinkage of the film results in negative (tensile) strain and growth of the film leads to positive (compressive) strain in the film. In view of a finite deformation setting, the growth tensor can be constructed via $\boldsymbol{F}_g = [1+g]\,\overline{\boldsymbol{I}}$ in which $\overline{\boldsymbol{I}} = \boldsymbol{I} - \boldsymbol{N}\otimes\boldsymbol{N}$ is the identity tensor along the film with $\boldsymbol{N}$ being the unit normal vector to the film.

Next, we compare briefly the analytical solution with the numerical results obtained from computational simulations using the finite element method via an eigenvalue analysis. In the analytical approach, the geometrical instabilities are implicitly accounted for via buckling analysis of the film. However, the computational simulations are based on the nonlinear finite strain theory of continuum mechanics where the geometrical nonlinearity is absolutely crucial to capture geometric instabilities.

Figure 3.2 gathers an exhaustive comparison between the numerical results using the finite element method and the analytical solution for a broad range of film to substrate stiffness ratios denoted E_f/E_s. The comparative studies are carried out for different film thicknesses and also for three different Poisson's ratios. For each Poisson's ratio and film thickness, both the critical growth g_{cr}

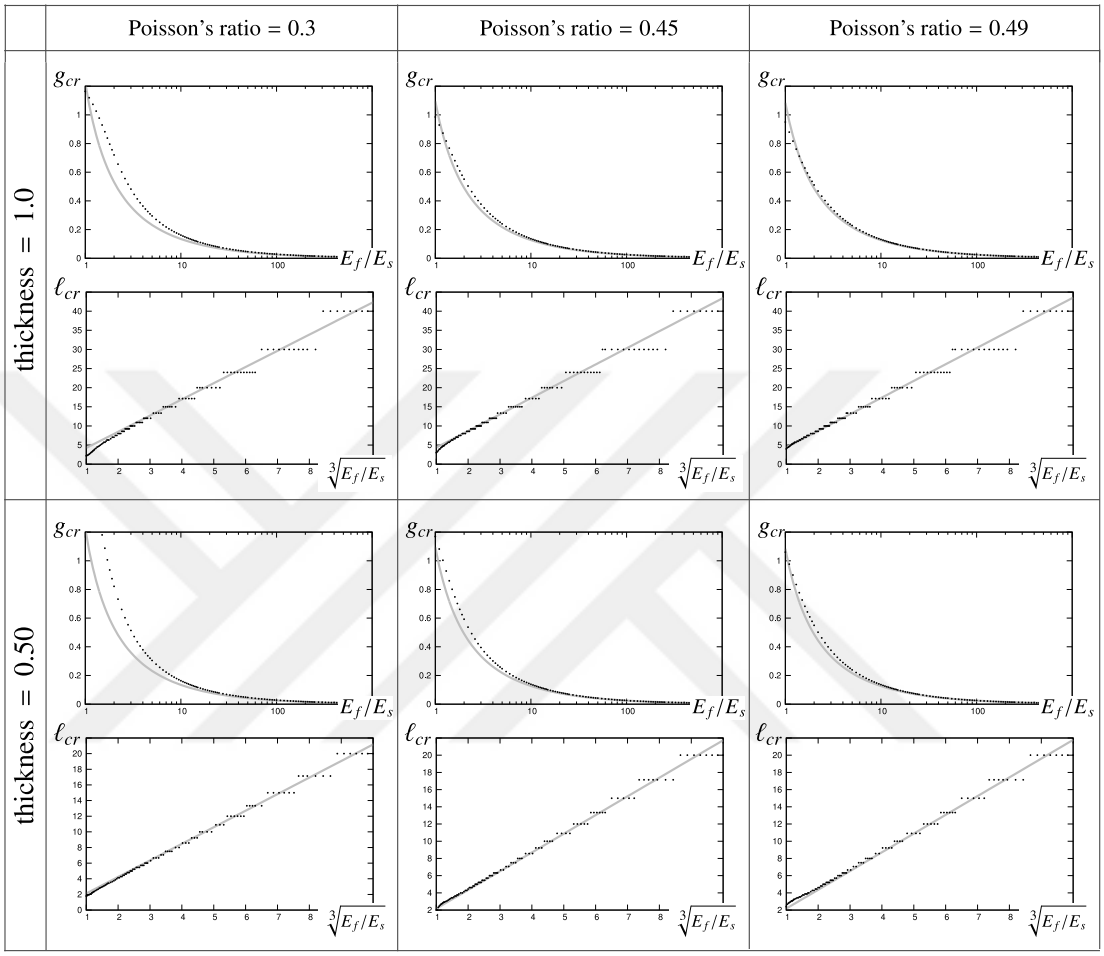


Figure 3.5: Comparison between analytical solution and computational simulations using the finite element method for growth induced instabilities of a thin film on a compliant substrate. For each case, both the critical growth g_{cr} and the critical wavelength ℓ_{cr} are shown in the graphs.

and the critical wavelength ℓ_{cr} are plotted. Motivated from the analytical solution, the horizontal axis for the critical wavelength ℓ_{cr} is chosen as the third root of the stiffness ratio so as to recover the linear dependence. The solid lines indicate the analytical solution while the points are the results of the computational simulations using the finite element method in accordance with [181], see also [182]. Unlike for the critical growth g_{cr}, the numerical results for the critical wavelength ℓ_{cr} exhibit a step-wise behavior due to the fact that the underlying finite element discretization can only comply with multiples of half-wavelength but cannot be infinitely refined to continuously conform with the larger wavelengths

corresponding to larger stiffness ratios.

Overall, the analytical solution and computational results are in excellent agreement and notably so for larger Poisson's ratio. However, we also observe that towards smaller stiffness ratios, the disparity between the analytical and numerical results increase. This is expected since in the smaller stiffness ratio regime the deformations can no longer be assumed to be small. Hence, the need for a non-linear, large deformation framework which can also capture the instability of the film and substrate, account for a non-linear beam also, arises. Chapter 4 deals with establishing and analyzing this framework, inspired by the displacement-based approach developed here and the shortcomings of the linear elastic and thin-film approach.

Chapter 4

Finite strain instabilities due to compression

The main objective of this chapter is to develop a generic framework to capture the wrinkling instability of compressible, hyper-elastic domains going under plane deformations. Among the plethora of works in the field on multilayer instabilities, very few focus on the compressible regime of materials. Most commonly, the incompressibility assumption is employed with the justification that the instabilities seen in biological structures, and the concerned applications using hydrogels etc. are all very close to the incompressibility regime. While this may be true for some biological matter, recent works are showing that, for instance, brain tissue [183] and hydrogels [184] may indeed possess compressible characteristics. With the goal of understanding the instability behavior of compressible domains in mind, this chapter is structured as follows. Section 4.1 outlines a generic, theoretical framework that is suitable for a variety of problems with different geometries and loading conditions. The rest of the chapter focuses on the application of this framework to half-space, beam, bilayer, and finally, trilayer structures.

4.1 Theoretical framework

The starting point of this section is the compressible free energy density (2.11) and related Piola stress (2.13) established previously in Chapter 2. The goal here is to keep the theoretical framework as generic as possible so that it remains applicable to various problems and geometries.

The problem at hand is to analyze the wrinkling of a rectangular domain under compression, as given in Fig. 4.1. The directions ξ, γ and ζ correspond to the width, height and thickness of the domain, respectively. The equations and terms defined in this section are not particularized to a specific set of material parameters, but correspond to a generic domain of shear modulus μ and compressibility ν. The problem considered here is for a pure homogeneous deformation with the deformation gradient $\boldsymbol{F}$ defined as

$$\boldsymbol{F} = \lambda\, \boldsymbol{e}_\xi \otimes \boldsymbol{e}_\xi + \eta\, \boldsymbol{e}_\gamma \otimes \boldsymbol{e}_\gamma + 1\, \boldsymbol{e}_\zeta \otimes \boldsymbol{e}_\zeta\,, \tag{4.1}$$

where λ is the stretch in the ξ direction, and η is the stretch in the γ direction, and is related to J through $J = \mathrm{Det}\,\boldsymbol{F}$. Since we are dealing with plane-deformations, the stretch in the ζ direction remains 1 throughout the derivations.

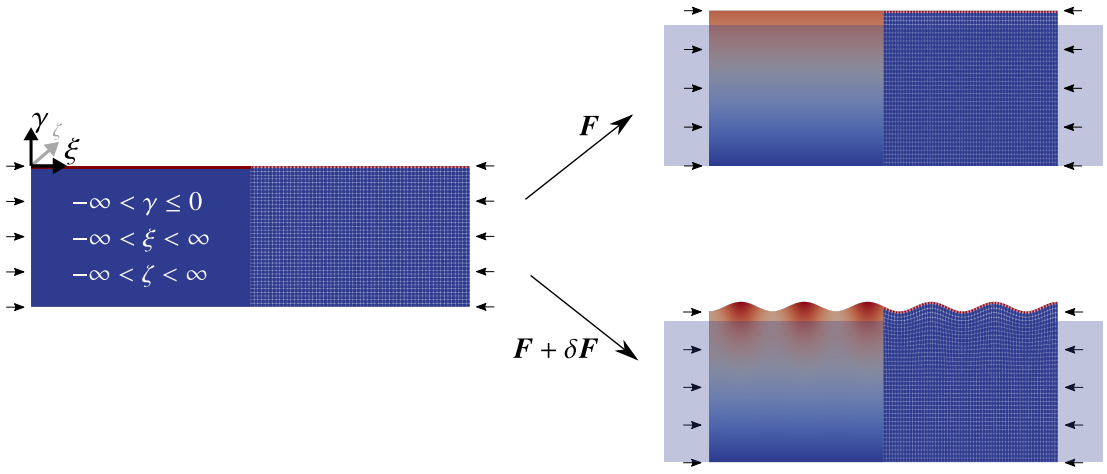


Figure 4.1: A qualitative representation of the generic rectangular domain under consideration, given together with the coordinate system and the applied deformations of $\boldsymbol{F}$ and $\boldsymbol{F} + \delta\boldsymbol{F}$.

Recall that the free energy density in the bulk of a compressible, hyperelastic domain is given by

$$\psi(\boldsymbol{F}) := \frac{1}{2}\,\mu\,[\boldsymbol{F}:\boldsymbol{F}-3-2\ln J]+\Lambda\,[\,\tfrac{1}{4}\,[J^2-1]-\tfrac{1}{2}\,\ln J\,] \quad , \quad J:=\mathrm{Det}\boldsymbol{F}\,. \tag{4.2}$$

By carrying out a variational study, we can set the variation of the free energy density (4.2) under the prescribed deformation gradient (4.1) to zero, in other words, minimize the energy of the structure under the prescribed deformation. Doing so renders the key non-linear Poisson's ratio relation

$$\nu = \frac{1-\eta^{\,-2}}{1-\lambda^2}\,. \tag{4.3}$$

The nonlinear Poisson's ratio (4.3) is an elemental part of this formulation for the instabilities of a compressible domain, as it can also be rearranged into

$$\eta = \sqrt{1+\alpha}/\sqrt{1+\alpha\,\lambda^2}\,, \tag{4.4}$$

which allows us to determine the corresponding vertical stretch, η, for a certain applied horizontal stretch, λ, depending on the compressibility of the material, represented by the parameter α. Intermediary steps to obtain this relation (4.3) and further deliberation on non-linear Poisson's ratio can be found in Appendix C and in more detail in [33].

Remark on nonlinear Poisson's ratio. *The concept of nonlinear Poisson's ratio has been introduced by Beatty and Stalnaker [185] as* $\nu = -[$*lateral contractive strain*$]/[$*extensional strain measure*$]$*, which is indeed a measure for the compressibility of a material. For large deformations, the definitions of strain measures can differ, resulting in different nonlinear Poisson function definitions. For instance, one commonly used definition is "strain* $=$ *stretch* $-\,1$*" attributed to Biot, which renders a nonlinear Poisson's ratio of* $\nu = [1-\eta]/[\lambda-1]$*. Several other strain measures and corresponding nonlinear Poisson's ratios have been reviewed in [186]. The nonlinear Poisson's ratio (4.3), however, is fundamentally different from those available in the literature as it is not based on strain measures, but derives from the kinetics of the problem at hand, namely the*

uniaxial tension condition. □

Moving forward, incremental analysis is employed to inspect the stability of the equilibrium configuration via analyzing the equilibrium of the finitely deformed configuration and a perturbation thereof, as shown in Fig. 4.1. Here, the incremental deformation gradient $\delta \boldsymbol{F}$ derives from the incremental, horizontal and vertical deformation functions δu and δv, respectively, such that

$$\delta \boldsymbol{u} := \begin{bmatrix} \delta u \\ \delta v \end{bmatrix} \quad , \quad [\,\delta \boldsymbol{F}\,] = \begin{bmatrix} \delta u_{,\xi} & \delta u_{,\gamma} \\ \delta v_{,\xi} & \delta v_{,\gamma} \end{bmatrix} . \tag{4.5}$$

At the perturbed configuration, the linear momentum balance reads $\mathrm{Div}\,(\boldsymbol{P} + \delta \boldsymbol{P}) = \boldsymbol{0}$. Since the divergence operator is a linear operator, we can write this balance as $\mathrm{Div}\,\boldsymbol{P} + \mathrm{Div}\,\delta \boldsymbol{P} = \boldsymbol{0}$. The first term $\mathrm{Div}\,\boldsymbol{P} = \boldsymbol{0}$ due to the uniform deformation gradient and the cartesian coordinate system employed in this problem, is trivially satisfied. Thus, the balance equation we need to satisfy becomes

$$\mathrm{Div}\,\delta \boldsymbol{P} = \boldsymbol{0}\,. \tag{4.6}$$

Using the form of the incremental Piola stress $\delta \boldsymbol{P}$ that has been previously given in Eq. (2.17) together with the established deformation gradients, the expression for incremental Piola stress reads

$$\frac{\delta \boldsymbol{P}}{\mu} = \begin{bmatrix} \delta u_{,\xi} & \delta u_{,\gamma} \\ \delta v_{,\xi} & \delta v_{,\gamma} \end{bmatrix} + D \begin{bmatrix} \eta^2\, \delta u_{,\xi} & \lambda\, \eta\, \delta v_{,\xi} \\ \lambda\, \eta\, \delta u_{,\gamma} & \lambda^2\, \delta v_{,\gamma} \end{bmatrix} + 2\,\alpha \big[\, \eta\, \delta u_{,\xi} + \lambda\, \delta v_{,\gamma}\,\big] \begin{bmatrix} \eta & 0 \\ 0 & \lambda \end{bmatrix}, \tag{4.7}$$

where the parameter D has been defined for the sake of brevity as

$$D := \frac{1 - \alpha\,[\,J^2 - 1\,]}{J^2} \qquad \text{and} \qquad J \to 1 \quad \Rightarrow \quad D \to \eta^2\,, \tag{4.8}$$

in which from Eq. (4.3) we deduce that D at the incompressibility limit tends to η^2. Evaluating the incremental linear momentum balance (4.6) with the incremental Piola stress (4.7) renders the system of equations

$$\begin{cases} [\delta u_{,\xi,\xi} + \delta u_{,\gamma,\gamma}] + \omega\, \left[\eta^{\,2}\, \delta u_{,\xi,\xi} + \lambda\eta\, \delta v_{,\xi,\gamma}\right] = 0\,, \\ [\delta v_{,\xi,\xi} + \delta v_{,\gamma,\gamma}] + \omega\, \left[\lambda\eta\, \delta u_{,\gamma,\xi} + \lambda^2\, \delta v_{,\gamma,\gamma}\right] = 0\,, \end{cases} \tag{4.9}$$

with $\omega := D+2\alpha = 1/J^{\,2} + \alpha + \alpha/J^{\,2}$, yielding a differential equation in terms of the incremental displacement functions. The proposed incremental displacements which constitute a general solution to the differential equation (4.9) read

$$\begin{cases} \delta u = A\, \exp{(r\,\gamma)}\, \sin{(k\,\xi)}\,, \\ \delta v = B\, \exp{(r\,\gamma)}\, \cos{(k\,\xi)}\,, \end{cases} \qquad \Rightarrow \qquad \delta \boldsymbol{u} = \boldsymbol{T}\, \boldsymbol{E}(\gamma)\, \boldsymbol{\Xi}\,, \tag{4.10}$$

with

$$\boldsymbol{T} := \begin{bmatrix} \sin(k\xi) & 0 \\ 0 & \cos(k\xi) \end{bmatrix}\,,\ \boldsymbol{E}(\gamma) := \begin{bmatrix} \exp(r\gamma) & 0 \\ 0 & \exp(r\gamma) \end{bmatrix}\,,\ \boldsymbol{\Xi} := \begin{bmatrix} A \\ B \end{bmatrix}\,, \tag{4.11}$$

where k is the wavenumber, and r is the *decay coefficient* for the term $\exp(r\,\gamma)$ often referred to as the *decay function*. The associated derivatives of the incremental displacements (4.10) are then plugged into differential equation (4.9) and simplified to obtain the set of equations

$$\begin{cases} \Big[\, [\, r^2 - k^2\,] - \omega\, \eta^2\, k^2 \,\Big]\, A - \omega\, \lambda\, \eta\, k\, r\, B = 0\,, \\ \Big[\, [\, r^2 - k^2\,] + \omega\, \lambda^2\, r^2 \,\Big]\, B + \omega\, \lambda\, \eta\, k\, r\, A = 0\,, \end{cases} \tag{4.12}$$

with its matrix representation

$$\boldsymbol{Z}(r) \cdot \boldsymbol{\Xi} = \boldsymbol{0} \ \text{ with } \ \boldsymbol{Z}(r) := \begin{bmatrix} \big[\, r^2 - k^2\,\big] - \omega\, \eta^2\, k^2 & -\omega\, \lambda\, \eta\, k\, r \\ \omega\, \lambda\, \eta\, k\, r & \big[\, r^2 - k^2\,\big] + \omega\, \lambda^2\, r^2 \end{bmatrix}. \tag{4.13}$$

To solve the homogeneous system (4.13) for its non-trivial solutions, the determinant of the coefficient matrix is set to zero, which furnishes the condition

$$\text{Det}\, \boldsymbol{Z}(r) = 0 \quad \Rightarrow \quad \big[\, r^2 - k^2\,\big]\, \big[\, [\, r^2 - k^2\,] + \omega\, [\, \lambda^2\, r^2 - \eta^2\, k^2\,]\,\big] = 0\,, \tag{4.14}$$

that has four solutions

$$r_1 = \, k \qquad , \qquad r_2 = k\sqrt{\rho} \qquad , \qquad r_3 = -\, k \qquad , \qquad r_4 = -\, k\sqrt{\rho}\,. \tag{4.15}$$

where

$$\rho := \frac{1+\omega\,\eta^2}{1+\omega\,\lambda^2}\,. \tag{4.16}$$

Notice that one of the relations uncovered here, that $r \propto k$, is identical to that uncovered in Eq. (3.21), which further demonstrates the parallelism among the two approaches. Similarly, the set of solutions $r_{2,4}$ obtained here can be regarded as a product of the non-linearity now taken into account, since this set was missing in the linear elastic case. This can also be seen from how at incompressibility i.e. $\omega \to \infty$, and at small strains hence as $\lambda \to 1$, the second set of equations actually render the same solution as the first.

Remark. *This uncovered relation $r \propto \pm k$ is of significance because it demonstrates that the decay coefficient must be proportional to the wavenumber in order to have an admissible solution. This implies that the surface waves with higher wavenumber decay faster along the height of the half-space, with the speed of decay being scaled in in certain cases, such as in $r_{2,4}$, by the coefficient $\sqrt{\rho}$ which fundamentally relates to the compressibility of the domain, via the applied stretch. Note that at incompressibility, $\sqrt{\rho} \to 1/\lambda^2$, which at the reference configuration becomes $\sqrt{\rho} \to 1$, recovering exactly the single solution in Eq. (3.21). For more deliberations on the incompressible solution to the half-space problem, see Appendix B. With wavenumber being inversely proportional to wavelength, waves which have a larger wavelength decay slower and thus, their effect travels further down in the half-space. This observation is especially important in the computational setting using the finite element method because, as mentioned earlier, the half-space must be truncated at a certain height* sufficiently *far away from the surface. The decay coefficients (4.15) indicate that the finite height of the half-space, which relies on the wavelength itself, may influence the numerical results, if not carefully chosen. Based on $r \propto k$, in the computational setting, one shall adjust the height of the half-space such that the approximation of an infinite half-space via truncation at a specific height does not influence the numerical findings.* □

The proposed, generic form of the incremental displacement functions (4.10) now need to be updated in order to accommodate for the four possible values of r, namely the possible solutions of the system, such that $\delta u = A_i \exp(r_i\,\gamma)\,\sin(k\,\xi)$

and $\delta v = B_i \exp(r_i\,\gamma)\cos(k\,\xi)$, summed over the repeated index i. The set of vectors $\boldsymbol{\Xi}$ corresponding to the solutions (4.15) then allows for us to obtain expressions relating the constants A_1, A_2, A_3, and A_4 of the horizontal incremental displacement δu, to B_1, B_2, B_3, and B_4 of the vertical incremental displacement δv as

$$\begin{aligned} \boldsymbol{Z}(r_1)\cdot\boldsymbol{\Xi}_1 = \mathbf{0} \;\Rightarrow\; A_1 = -\,B_1\,\frac{\lambda}{\eta} \quad &, \quad \boldsymbol{Z}(r_3)\cdot\boldsymbol{\Xi}_3 = \mathbf{0} \;\Rightarrow\; A_3 = \;B_3\,\frac{\lambda}{\eta}\,, \\ \boldsymbol{Z}(r_2)\cdot\boldsymbol{\Xi}_2 = \mathbf{0} \;\Rightarrow\; A_2 = -\,B_2\,\frac{\theta}{\lambda\eta} \quad &, \quad \boldsymbol{Z}(r_4)\cdot\boldsymbol{\Xi}_4 = \mathbf{0} \;\Rightarrow\; A_4 = \;B_4\,\frac{\theta}{\lambda\eta}\,, \end{aligned} \tag{4.17}$$

with $\theta := [\,\rho\,[\,1+\omega\,\lambda^2\,]-1]/[\omega\sqrt{\rho}]$. From this point on, with the remaining unknown coefficients, B_1, B_2, B_3, and B_4, it proves necessary to write the displacement functions in matrix form. That is

$$\begin{aligned} \delta\boldsymbol{u} = &\begin{bmatrix} \sin(k\xi) & 0 \\ 0 & \cos(k\xi) \end{bmatrix} \begin{bmatrix} -\dfrac{\lambda}{\eta} & -\dfrac{\theta}{\lambda\eta} \\ 1 & 1 \end{bmatrix} \begin{bmatrix} \exp(r_1\gamma) & 0 \\ 0 & \exp(r_2\gamma) \end{bmatrix} \begin{bmatrix} B_1 \\ B_2 \end{bmatrix} \\ &+ \begin{bmatrix} \sin(k\xi) & 0 \\ 0 & \cos(k\xi) \end{bmatrix} \begin{bmatrix} \dfrac{\lambda}{\eta} & \dfrac{\theta}{\lambda\eta} \\ 1 & 1 \end{bmatrix} \begin{bmatrix} \exp(r_3\gamma) & 0 \\ 0 & \exp(r_4\gamma) \end{bmatrix} \begin{bmatrix} B_3 \\ B_4 \end{bmatrix}, \end{aligned} \tag{4.18}$$

which will henceforth be written in its shorter form, which reads

$$\delta\boldsymbol{u} = \boldsymbol{T}\,{}^{1}_{2}\boldsymbol{G}\,{}^{1}_{2}\boldsymbol{E}(\gamma)\,{}^{1}_{2}\boldsymbol{B} + \boldsymbol{T}\,{}^{3}_{4}\boldsymbol{G}\,{}^{3}_{4}\boldsymbol{E}(\gamma)\,{}^{3}_{4}\boldsymbol{B} \;\text{ with }\; \boldsymbol{T} := \begin{bmatrix} \sin(k\xi) & 0 \\ 0 & \cos(k\xi) \end{bmatrix}, \tag{4.19}$$

and in which

$$\begin{aligned} {}^{1}_{2}\boldsymbol{G} &:= \begin{bmatrix} -\dfrac{\lambda}{\eta} & -\dfrac{\theta}{\lambda\eta} \\ 1 & 1 \end{bmatrix}, \; {}^{1}_{2}\boldsymbol{E}(\gamma) := \begin{bmatrix} \exp(r_1\gamma) & 0 \\ 0 & \exp(r_2\gamma) \end{bmatrix}, \; {}^{1}_{2}\boldsymbol{B} := \begin{bmatrix} B_1 \\ B_2 \end{bmatrix}, \\ {}^{3}_{4}\boldsymbol{G} &:= \begin{bmatrix} \dfrac{\lambda}{\eta} & \dfrac{\theta}{\lambda\eta} \\ 1 & 1 \end{bmatrix}, \; {}^{3}_{4}\boldsymbol{E}(\gamma) := \begin{bmatrix} \exp(r_3\gamma) & 0 \\ 0 & \exp(r_4\gamma) \end{bmatrix}, \; {}^{3}_{4}\boldsymbol{B} := \begin{bmatrix} B_3 \\ B_4 \end{bmatrix}. \end{aligned} \tag{4.20}$$

The superscript notation has been introduced here for the sake of brevity. The subscripts of the terms have been reserved for differentiating between different domains, i.e. film and substrate, as it will be necessary in Section 4.4.

Equipped with the updated displacement functions, the last step is to solve for the remaining coefficients B_1, B_2, B_3, and B_4, which will be achieved through imposing the boundary conditions of a particular problem. This step is key because it is where the geometry of the problem and the incremental loading conditions come into play. The steps taken until this point are independent of the dimensions and boundary conditions of the rectangular domain, and thus remain generic and suitable to impose the boundary conditions that will follow next. In order to apply traction boundary conditions specific to the problems at hand, a relation for the traction at a surface of the domain is needed, dictated by $\delta\boldsymbol{t} = \delta\boldsymbol{P}\cdot\boldsymbol{N}$. For the upper (lateral) surface of the domain for instance, this unit normal reads $\boldsymbol{N} = \boldsymbol{e}_\gamma$, which after some mathematical steps, results in which can be written more concisely as

$$\delta\boldsymbol{t} = \begin{bmatrix} \delta P_{12} \\ \delta P_{22} \end{bmatrix} = -\mu\, k\, \boldsymbol{T}^{\frac{1}{2}}\boldsymbol{W}^{\frac{1}{2}}\boldsymbol{E}(\gamma)^{\frac{1}{2}}\boldsymbol{B} + \mu\, k\, \boldsymbol{T}^{\frac{3}{4}}\boldsymbol{W}^{\frac{3}{4}}\boldsymbol{E}(\gamma)^{\frac{3}{4}}\boldsymbol{B}\ , \tag{4.21}$$

in which

$$\begin{aligned} {}^{-\frac{1}{2}}\boldsymbol{W} &:= \begin{bmatrix} -\dfrac{\lambda}{\eta} - D\,\lambda\,\eta & -\sqrt{\rho}\,\dfrac{\theta}{\lambda\eta} - D\,\lambda\,\eta \\ [1 + D\lambda^2] & \sqrt{\rho}\,[1 + \omega\,\lambda^2] - 2\,\alpha\,\theta \end{bmatrix}, \\ {}^{\frac{3}{4}}\boldsymbol{W} &:= \begin{bmatrix} -\dfrac{\lambda}{\eta} - D\,\lambda\,\eta & -\sqrt{\rho}\,\dfrac{\theta}{\lambda\eta} - D\,\lambda\,\eta \\ -[1 + D\,\lambda^2] & -\sqrt{\rho}\,[1 + \omega\,\lambda^2] + 2\,\alpha\,\theta \end{bmatrix}. \end{aligned} \tag{4.22}$$

The traction $\delta\boldsymbol{t}$ for the lower (lateral) surface of the domain is exactly minus the expression (4.21) as $\boldsymbol{N} = -\boldsymbol{e}_\gamma$. The traction in the domain on lateral surfaces is our point of departure, and one of the key distinguishing factors for the derivations in the following sections. In the next sections, the relations obtained in this section are particularized to obtain the solution for a beam, half-space, and finally a bilayer geometry. The traction boundary conditions at different surfaces of these geometries are given in Fig. 4.2.

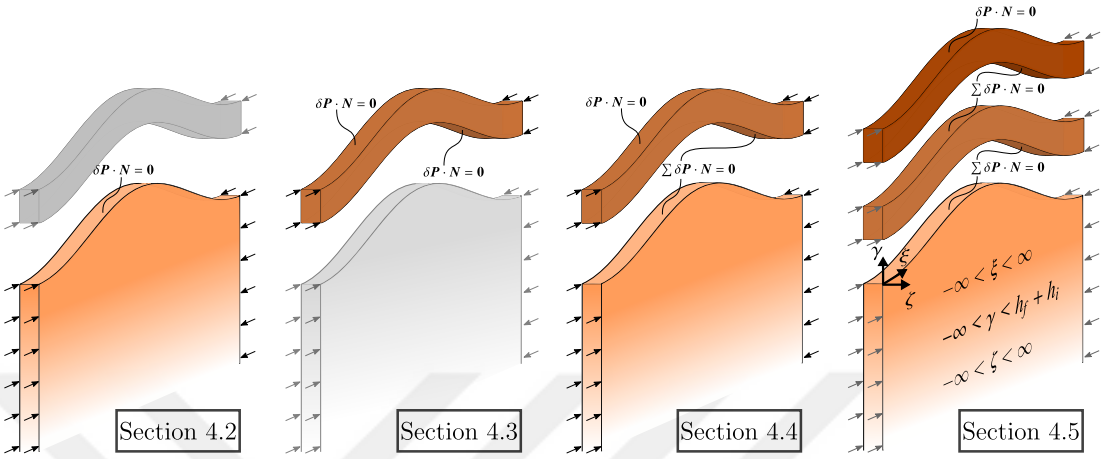


Figure 4.2: Overview of the traction boundary conditions of the three problems covered in this work (from left to right): half-space, beam, bilayer and trilayer.

4.2 Half-space instability

In this section the bifurcation of a compressible half-space will be briefly worked through using the unifying approach established in Section 4.1. The generic incremental displacement functions (4.19) for a half-space of shear modulus μ and Poisson's ratio ν, prior to imposing boundary conditions, read

$$\delta \boldsymbol{u} = \boldsymbol{T}\, {}^{\frac{1}{2}}\boldsymbol{G}\, {}^{\frac{1}{2}}\boldsymbol{E}(\gamma)\, {}^{\frac{1}{2}}\boldsymbol{B} + \boldsymbol{T}\, {}^{\frac{3}{4}}\boldsymbol{G}\, {}^{\frac{3}{4}}\boldsymbol{E}(\gamma)\, {}^{\frac{3}{4}}\boldsymbol{B}\,. \tag{4.23}$$

We now apply the boundary conditions of the system in order to determine the relations between the constants proposed and eventually solve for the bifurcation behavior of the system, hence particularize the solution to a half-space. In the case of a half-space, (i) the incremental displacements decay and eventually disappear as we move towards $\gamma \to -\infty$, owing to the geometry being an infinite half-space and (ii) the top surface is traction free.

Firstly, the displacements in both the ξ and γ directions should vanish as $\gamma \to -\infty$. Imposing this condition on the incremental displacement functions (4.23) and looking at the decay coefficients in ${}^{\frac{1}{2}}\boldsymbol{E}$ and ${}^{\frac{3}{4}}\boldsymbol{E}$, see Eq. (4.20), the second term of (4.23) increases without bounds as $\gamma \to -\infty$, owing to the sign of its decay coefficients in ${}^{\frac{3}{4}}\boldsymbol{E}$. Hence, the constants B_3 and B_4 must be zero so that the

condition of displacements vanishing in the half-space is satisfied. This renders the *admissible* incremental displacement functions in the half-space to be

$$\delta \boldsymbol{u} = \boldsymbol{T}\, {}^{\frac{1}{2}}\boldsymbol{G}\, {}^{\frac{1}{2}}\boldsymbol{E}(\gamma)\, {}^{\frac{1}{2}}\boldsymbol{B}\,. \tag{4.24}$$

Secondly, we turn to the traction boundary condition, which would be applied through the traction expression for the half-space, i.e. the reduced form of Eq. (4.21) for the half-space $\delta \boldsymbol{t} = -\mu\, k\, \boldsymbol{T}\, {}^{\frac{1}{2}}\boldsymbol{W}\, {}^{\frac{1}{2}}\boldsymbol{E}(\gamma)\, {}^{\frac{1}{2}}\boldsymbol{B}$. Note that the second term of the generalized traction equation (4.21) vanishes for the half-space case, since the displacement boundary condition dictates that the constants B_3 and B_4 are zero. The traction boundary condition for the half-space is that the top surface is traction-free. That is,

$$-\mu\, k\, \boldsymbol{T}\, {}^{\frac{1}{2}}\boldsymbol{W}\, {}^{\frac{1}{2}}\boldsymbol{E}(0)\, {}^{\frac{1}{2}}\boldsymbol{B} = \boldsymbol{0}\,, \tag{4.25}$$

where ${}^{\frac{1}{2}}\boldsymbol{E}(0) = \boldsymbol{I}$, yielding the homogeneous system

$$\mu\, k\, \boldsymbol{T}\, [-\, {}^{\frac{1}{2}}\boldsymbol{W}]\, {}^{\frac{1}{2}}\boldsymbol{B} = \boldsymbol{0}\,, \tag{4.26}$$

or alternatively

$$\boldsymbol{Q}\, {}^{\frac{1}{2}}\boldsymbol{B} = \boldsymbol{0} \qquad \text{with} \qquad \boldsymbol{Q} := -\, {}^{\frac{1}{2}}\boldsymbol{W}. \tag{4.27}$$

Solving $\mathrm{Det}\, \boldsymbol{Q} = 0$ for λ, while making use of the non-linear Poisson's relation (4.4), gives us the critical stretch λ_{cr} at which the structure bifurcates. The non-linear Poisson's relation (4.4) allows for us the write the vertical stretch η in terms of compressibility and applied stretch λ and renders the system (4.27) to be only a function of λ.

Before analyzing the solutions of $\mathrm{Det}\boldsymbol{Q} = 0$, we evaluate it at the incompressibility limit. At the limit of $\nu \to 1$ we established previously that $D \to \eta^2$, $\omega \to \infty$, $\alpha \to \infty$ and $\rho \to \eta^2/\lambda^2$ with $\eta = 1/\lambda$. Inserting all these into Eq. (4.27) results in a polynomial that, in essence, is identical to the solution by Biot [89]. That is

$$\mathrm{Det}\boldsymbol{Q}\Big|_{\nu\to 1} = 0 \qquad \Rightarrow \qquad [\,\lambda^4 + 2\lambda + 1\,][\,\lambda^4 - 2\lambda + 1\,] = 0\,, \tag{4.28}$$

and since the first term is strictly positive, it yields

$$[\,\lambda - 1\,][\,\lambda^3 + \lambda^2 + \lambda - 1\,] = 0 \qquad \Rightarrow \qquad \lambda_{cr} = 1.0 \quad \text{and} \quad \lambda_{cr} = 0.5437\,, \tag{4.29}$$

recovering exactly the critical stretches at the incompressibility limit.

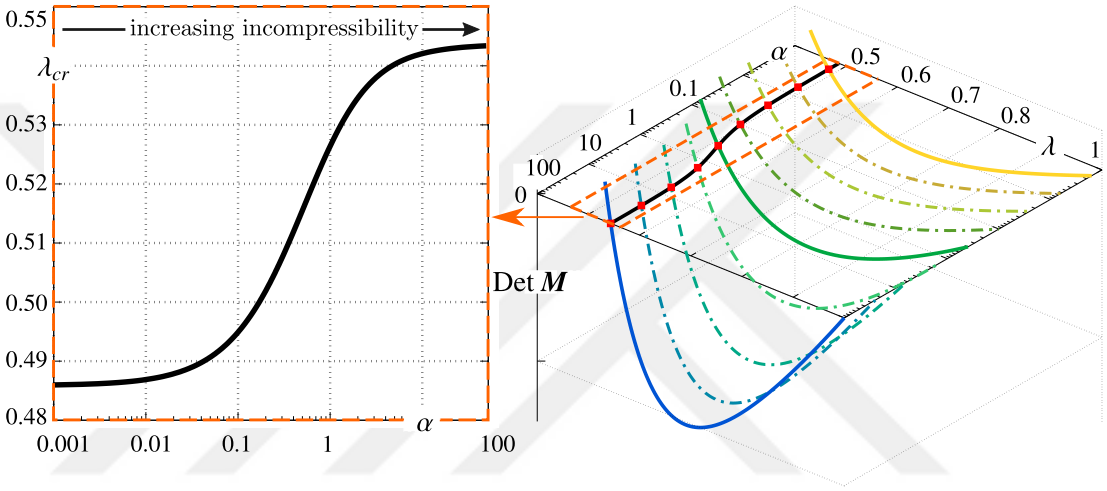


Figure 4.3: Illustration of Det$\boldsymbol{Q}$ and its roots. The non-trivial solutions of Det$\boldsymbol{Q} = 0$ for any α are highlighted and gathered separately as critical stretches λ_{cr}. Recall that for a given α Poisson's ratio is obtained as $\nu = \alpha/[1+\alpha]$.

The determinant of the matrix $\boldsymbol{Q}$ is essentially a function of the stretch λ and α. However, a closed-form explicit solution for its roots does not exist. Figure 4.3 illustrates the behavior of Det$\boldsymbol{Q}$ with respect to λ and α. It should be noted that the bifurcation point of a half-space is independent of both the shear modulus of the half-space and the wavenumber k. For any α there exists exactly two solutions; one trivial solution at the reference configuration and a critical stretch $\lambda_{cr} < 0.5437$. The non-trivial solutions of Det$\boldsymbol{Q} = 0$ for any α are highlighted and gathered separately as critical stretches λ_{cr}. The upper bound for the critical stretch $\lambda_{cr} = 0.5437$ corresponds to incompressible elastic materials with $\alpha \to \infty$. The lower bound for the critical stretch $\lambda_{cr} = 0.4859$ corresponds to fully compressible elastic materials with $\nu = 0$, or alternatively $\alpha = 0$. For compressible materials with $0 \leq \alpha < \infty$, or alternatively $0 \leq \nu < 1$, the critical stretch lies between the two bounds. Recall that for a given α Poisson's ratio is obtained as $\nu = \alpha/[1+\alpha]$.

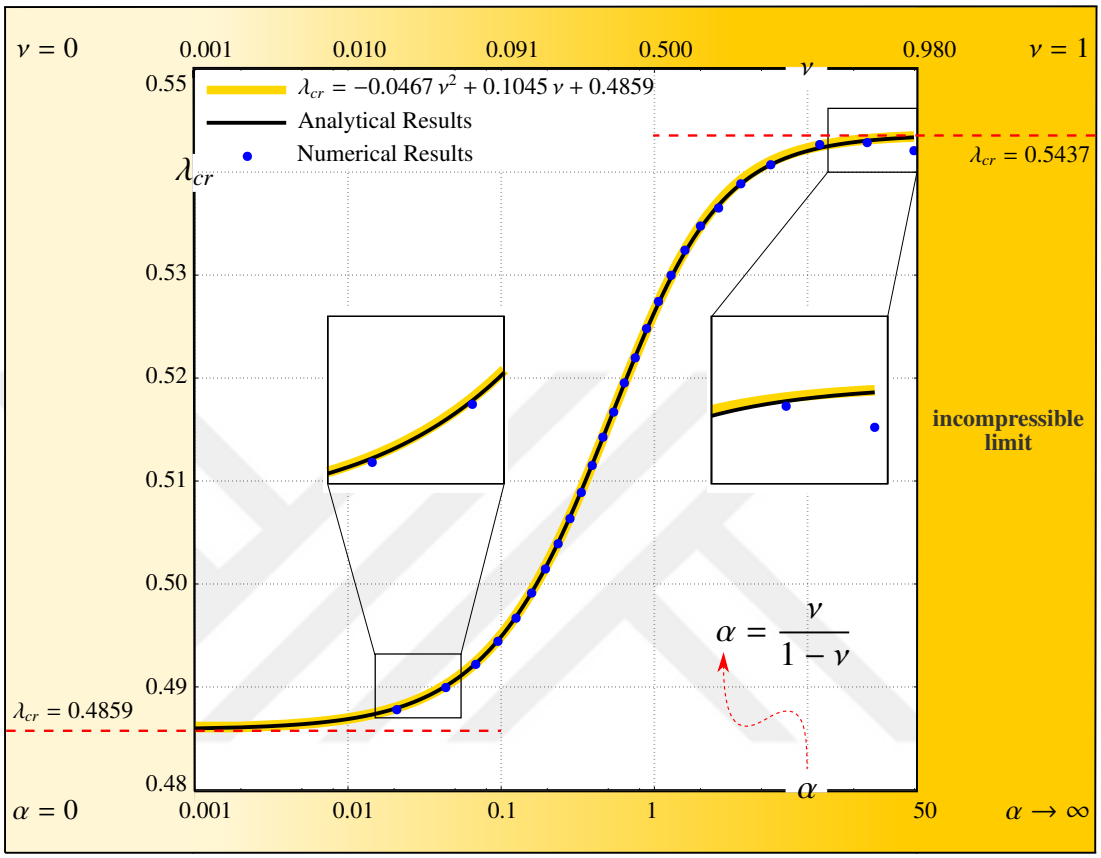


Figure 4.4: Analytical, numerical and curve-fit results for the critical λ at various values of α, where $\alpha = \nu/[1-\nu]$ or alternatively, $\nu = \alpha/[1+\alpha]$.

Figure 4.4 elaborates further on the critical stretches as a function of Poisson's ratio ν, or alternatively α. Moreover, it provides the numerical solution using computational simulations for the whole range of ν. The analytical solution of $\mathrm{Det}\boldsymbol{Q} = 0$ shows an excellent agreement with the numerical results obtained using the finite element method. The details of the computational simulations are omitted here for the sake of brevity but it follows exactly the procedure explained in Section 2.5. Only close to the incompressibility limit the numerical solution shows a minor deviation from the analytical one. Nonetheless, this minor disagreement is merely due to the numerical issues intrinsic to the finite element method at the vicinity of incompressibility. More precisely, we have carried out the computational simulations using standard quadratic Lagrange elements that are known to exhibit volumetric locking at nearly incompressibility limit. The analytical solution of $\mathrm{Det}\boldsymbol{Q} = 0$ is implicit. It is, however, possible to provide

an explicit estimate for λ_{cr} by fitting a curve to the solutions of $\mathrm{Det}\boldsymbol{Q} = 0$ for a large set of ν. In particular, we have observed that the quadratic polynomial

$$\lambda_{cr} = -\,0.0467\,\nu^2 + 0.1045\,\nu + 0.4859\,, \tag{4.30}$$

fits extremely well to the analytical solution. The significance of the estimate (4.30) lies in its simplicity and its accuracy. In summary, at the fully compressible limit, the critical stretch is found to be $\sqrt{-2+\sqrt{5}}$, which is in agreement with [95]; at the incompressible limit, the critical stretch is 0.5437 that is in agreement with the literature.

4.3 Beam instability

This section particularizes the generic first steps in Section 4.1 to account for the bifurcation behavior of a beam of height h and length L. The incremental deformation functions for a beam of shear modulus μ and compressibility ν now read

$$\delta\boldsymbol{u} = \boldsymbol{T}\,{}^{\frac{1}{2}}\boldsymbol{G}\,{}^{\frac{1}{2}}\boldsymbol{E}(\gamma)\,{}^{\frac{1}{2}}\boldsymbol{B} + \boldsymbol{T}\,{}^{\frac{3}{4}}\boldsymbol{G}\,{}^{\frac{3}{4}}\boldsymbol{E}(\gamma)\,{}^{\frac{3}{4}}\boldsymbol{B}\,. \tag{4.31}$$

To proceed, we impose the first traction boundary condition for a beam geometry, starting from the top surface, which is traction free. Hence, we evaluate the expression (4.21) at the top surface of the beam, i.e. at $\gamma = h$, and set it to zero,

$$\delta\boldsymbol{t}\,|_{\gamma=h} = \boldsymbol{0} \quad \Rightarrow \quad -\mu\,k\,\boldsymbol{T}\,{}^{\frac{1}{2}}\boldsymbol{W}\,{}^{\frac{1}{2}}\boldsymbol{E}(h)\,{}^{\frac{1}{2}}\boldsymbol{B} + \mu\,k\,\boldsymbol{T}\,{}^{\frac{3}{4}}\boldsymbol{W}\,{}^{\frac{3}{4}}\boldsymbol{E}(h)\,{}^{\frac{3}{4}}\boldsymbol{B} = \boldsymbol{0}\,. \tag{4.32}$$

Rearranged, the traction-free top surface boundary condition (4.32) yields the relation

$${}^{\frac{3}{4}}\boldsymbol{B} = \boldsymbol{b}\,{}^{\frac{1}{2}}\boldsymbol{B} \quad \text{with} \quad \boldsymbol{b} := \left[{}^{\frac{3}{4}}\boldsymbol{W}\,{}^{\frac{3}{4}}\boldsymbol{E}(h)\right]^{-1}{}^{\frac{1}{2}}\boldsymbol{W}\,{}^{\frac{1}{2}}\boldsymbol{E}(h)\,. \tag{4.33}$$

Moving to the bottom side of the beam, the traction on this surface of the beam

reads

$$\delta \boldsymbol{t}\,|_{\gamma=0} = \boldsymbol{0} \qquad \Rightarrow \qquad \mu\, k\, \boldsymbol{T}\, {}^{\frac{1}{2}}\boldsymbol{W}\, {}^{\frac{1}{2}}\boldsymbol{E}(0)\, {}^{\frac{1}{2}}\boldsymbol{B} - \mu\, k\, \boldsymbol{T}\, {}^{\frac{3}{4}}\boldsymbol{W}\, {}^{\frac{3}{4}}\boldsymbol{E}(0)\, {}^{\frac{3}{4}}\boldsymbol{B} = \boldsymbol{0}\,, \tag{4.34}$$

where ${}^{\frac{1}{2}}\boldsymbol{E}(0)$ and ${}^{\frac{3}{4}}\boldsymbol{E}(0)$ are the matrices ${}^{\frac{1}{2}}\boldsymbol{E}(\gamma)$ and ${}^{\frac{3}{4}}\boldsymbol{E}(\gamma)$ evaluated at $\gamma = 0$, hence equal the identity tensor $\boldsymbol{I}$. Finally, using the newly uncovered relation (4.33) for the constants B_3 and B_4, which bears information about the traction-free surface at $\gamma = h$, in Eq. (4.34) and simplifying, we obtain the final form

$$\mu\, k\, \boldsymbol{T} \left[{}^{\frac{1}{2}}\boldsymbol{W} - {}^{\frac{3}{4}}\boldsymbol{W}\, \boldsymbol{b} \right] {}^{\frac{1}{2}}\boldsymbol{B} = \boldsymbol{0}\,, \tag{4.35}$$

or alternatively

$$\boldsymbol{Q}\, {}^{\frac{1}{2}}\boldsymbol{B} = \boldsymbol{0} \qquad \text{with} \qquad \boldsymbol{Q} := {}^{\frac{1}{2}}\boldsymbol{W} - {}^{\frac{3}{4}}\boldsymbol{W}\, \boldsymbol{b}\,. \tag{4.36}$$

Solving for the non-trivial solutions of the system (4.36) for λ through setting $\operatorname{Det} \boldsymbol{Q} = 0$ would give us the critical stretch, λ_{cr}, at the onset of instability. At this point, it proves necessary to look more carefully at the expression $\operatorname{Det} \boldsymbol{Q} = 0$. Upon careful inspection of its components, we see that $\boldsymbol{Q}$ is a function of λ, and η, together with the unknown wavenumber k and the parameters beam thickness h, and beam Poisson's ratio ν. Once again, a crucial move here is to use the non-linear Poisson's ratio relation (4.3) to relate λ and η, so that $\operatorname{Det} \boldsymbol{Q} = 0$ becomes only a function of λ, that can be solved for a λ_{cr} at a specific ν.

One remaining essential point in solving for the critical stretch λ_{cr} is finding a suitable wavenumber k which still remains unspecified. Since we are dealing with a beam which is bounded on two sides on supports, we have to indicate the displacement boundary conditions at the two ends of the beam, as these support conditions affect the bifurcation behavior. These boundary conditions need not be imposed when dealing with an infinite half-space. The beam under consideration is assumed to be clamped on both sides. This suggests that (i) the incremental displacement in the horizontal direction, δu, is zero at both ends of the beam, and (ii) the vertical component of incremental displacement, δv, is the

same at both ends. These constraints, see Eq. (4.31), can be summarized as

$$\begin{cases} \delta u\,|_{\xi=0} = \delta u\,|_{\xi=L} = 0 \quad \Rightarrow \quad \sin(k\,L) = 0 \quad \Rightarrow \quad k = \dfrac{n\,\pi}{L}\,, \\ \delta v\,|_{\xi=0} = \delta v\,|_{\xi=L} \quad \Rightarrow \quad \cos(k\,0) = \cos(k\,L) \quad \Rightarrow \quad k = \dfrac{2\,n\,\pi}{L}\,, \end{cases} \tag{4.37}$$

where n is an integer. Looking at the results obtained from (4.37), we can conclude that the (referential) wavenumber k in the incremental displacements should take the form $2\,n\,\pi/L$ where L is the undeformed length of the beam. Note that the condition $(4.37)_2$ may also be interpreted as a symmetry constraint. Assuming that the stretch $\lambda_{\rm cr}$ relates to compression via $1 - \lambda_{\rm cr}$, it follows that the n which renders the smallest amount of compression would correspond to the first bifurcation. That is, the largest $\lambda_{\rm cr}$ should be determined together with its associated wavenumber k to be representative of the first mode of instability that is reached as the beam is subjected to axial loading from "no compression" at $\lambda = 1$ to a certain critical amount of compression at $\lambda_{\rm cr}$. Hence, the acceptable value of n and the corresponding $\lambda_{\rm cr}$ can be found by $\lambda_{\rm cr} = \max\{\,\lambda\,|\,\mathrm{Det}\,\boldsymbol{Q}\,(\,2n\pi/L\,,\,\lambda\,) = 0\,,\,\forall\, n \in \mathbb{R}^+\,\}$, as shown in Fig. 4.5. In Fig. 4.5, we see that as n increases, the critical stretch decreases. The solution for $\lambda_{\rm cr}$ at $n = 0$ is not acceptable because it suggests an infinitely long wave, i.e. the flat beam at $\lambda_{\rm cr} = 1$, hence being the trivial solution. The largest non-trivial $\lambda_{\rm cr}$ occurs at $n = 1$. This is the case for all dimensions and compressibilities, proving the definition $k = 2\pi/L$ for a beam clamped on both sides under compression.

Remark on clamped boundary conditions for a beam. *The obtained solution here is valid for the double-clamped support boundary condition (4.37). It should be noted that in the case of a vertical roller support on the right side of the beam, i.e. where the condition* $(4.37)_2$ *is no longer enforced, the only imposition on* k *remains to be* $k = n\,\pi/L$*. In this case, again the first acceptable solution of* λ_{cr} *turns out to be at* $n = 1$*, however this mode now corresponds to* $k = \pi/L$*, which renders a half-wave deformation that is asymmetric.* □

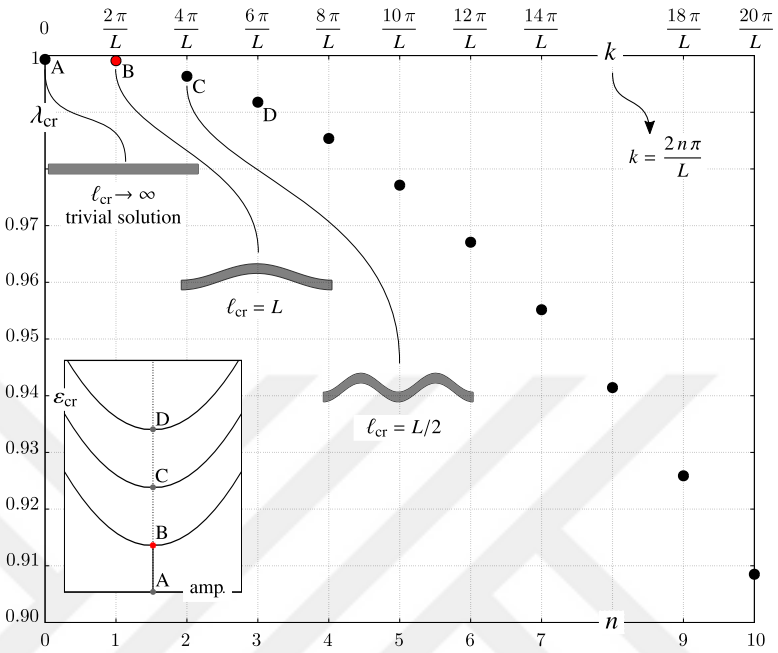


Figure 4.5: Plot of the integer λ_{cr} vs. n, for a beam of length $L = 60$, height $h = 1$ and compressibility $\nu = 0.95$, together with further possible modes of the instability that correspond to various wavenumbers k. The wavelength ℓ_{cr} corresponds to the referential length of the beam. The inset shows the pitchfork bifurcation pattern, i.e. compression vs. amplitude.

Solving for λ_{cr} in $\text{Det}\,\boldsymbol{Q} = 0$ renders the non-trivial solution of the homogeneous system (4.36), and is enough to determine the stretch at the onset of the instability; whereas the corresponding vector equips us with a relation among the two remaining coefficients B_1 and B_2, and is key in calculating and drawing the displacement profile of the incremental deformation (4.31). The results shown in Fig. 4.6 present the first part of the findings, namely how λ_{cr} changes for a range of beam dimensions and compressibilities.

It is important to note here that λ_{cr} is independent of the shear modulus μ as it is visible from (4.35), hence the results in Fig. 4.6 look at various Poisson's ratios and beam thicknesses. We see that Poisson's ratio of the beam and its thickness affect the bifurcation behavior together. For smaller h/L ratios, a very little amount of compression is required for the instability to occur. At these ratios, the compressibility of the beam does not have a significant effect on its bifurcation behavior; as the beam is much longer than it is thick, there is not

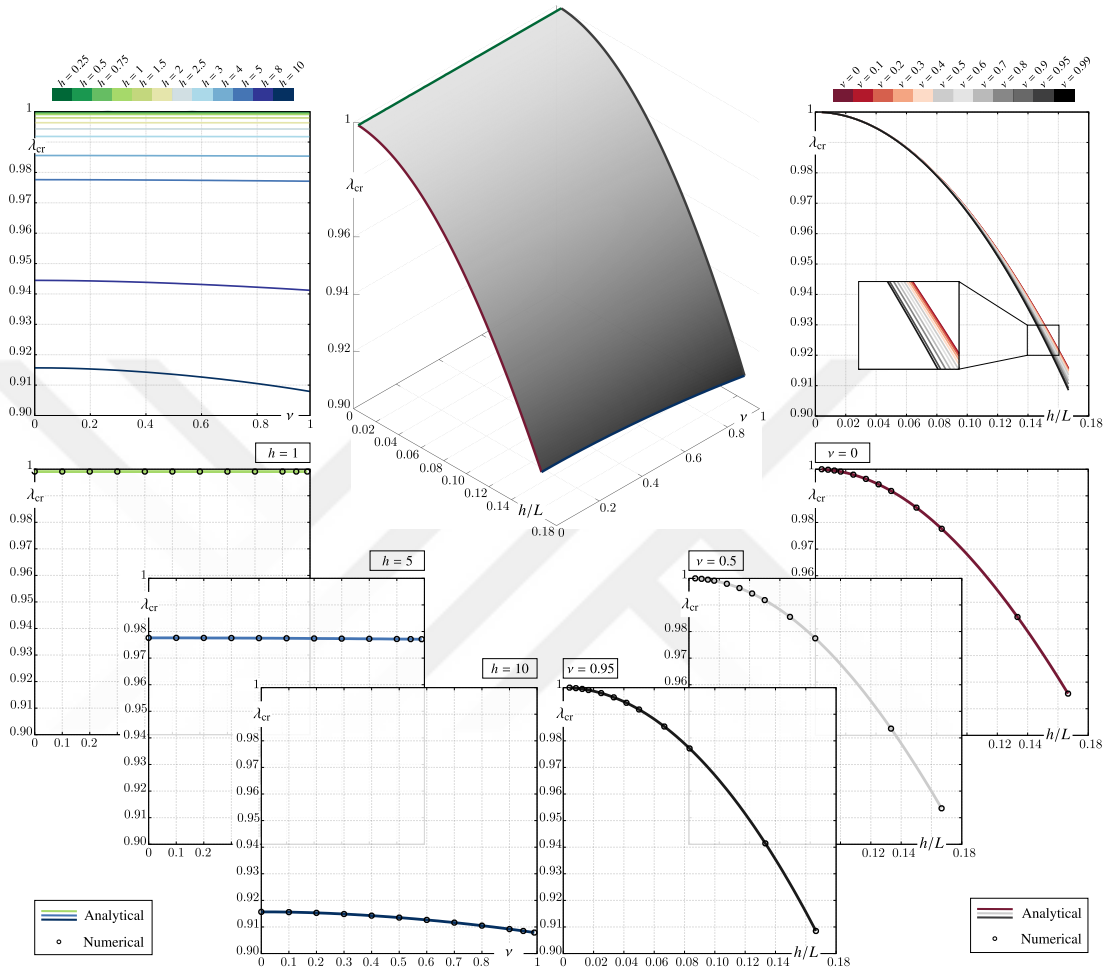


Figure 4.6: Surface plot of critical stretch λ_{cr}, with changing ratio h/L and compressibility ν (center), along with insets that show λ_{cr} vs. ν (left) and λ_{cr} vs. h/L (right), together with numerical findings, for a beam of length $L = 60$.

"enough thickness" for the Poisson effect to develop through and influence the results. As the thickness of the beam increases relative to its length and shear forces start coming into play more significantly, the effect of the Poisson ratio is much more pronounced. The effect of Poisson's ratio can be seen clearly in the top right inset, which shows that at larger h/L, the results of beams of different compressibilities start deviating from one another. The bottom insets in Fig. 4.6 show results for select h/L (left) and ν (right) together with numerical results. *The numerical results obtained with FEM, all throughout the range for compressibility and slenderness, match the analytical findings perfectly.* Numerical results for the deformation of the beam structure can be found in Fig. 4.7,

where the buckled configuration of the beam is presented for three different beam thicknesses and compressibilities. The figure clearly highlights the influence of compressibility on the shape of the final buckled configuration.

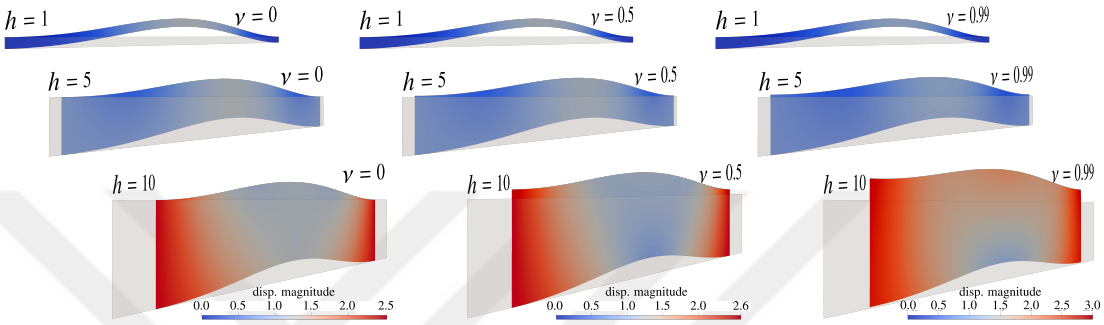


Figure 4.7: The buckled configuration obtained from numerical simulations, for a beam of length $L = 60$, for various h and Poisson's ratios ν.

Figure 4.8 illustrates the second part of our findings, which are the incremental displacement profiles of the beam at the point of bifurcation, for a range of h and ν values. The lines in Fig. 4.8 are analytical calculations of the displacement functions, δu and δv, and are calculated by finding the corresponding vector composed of B_1 and B_2, for the critical stretch λ_{cr} in the system (4.36), and using this relation together with (4.33) in Eq. (4.31). The points represent numerical findings. Numerical data for the displacement profile is given by the eigenvector corresponding to the first negative eigenvalue of the stiffness matrix. The displacements are shown for a range of γ values, ranging from 0 to h, where the displacements along different γ through the thickness of the beam have been obtained, with each shown along the length of the beam ξ ranging from 0 to $L = 60$. Both the analytically calculated and numerically obtained sets of displacement data here have been normalized. First of all, an excellent agreement between the analytical calculations and numerical data is obtained, as the two sets of data coincide exactly all throughout the length and thickness of the beam, for all Poisson's ratios and thicknesses. An interesting finding is shown in the insets of the incremental vertical displacement δv graphs. For a beam that is much longer than in it is wide, e.g. for $h/L = 1/60$, the vertical displacements along the height of the beam are identical, as it can be seen in the first column of Fig. 4.8. However, with increasing thickness and increasing incompressibility,

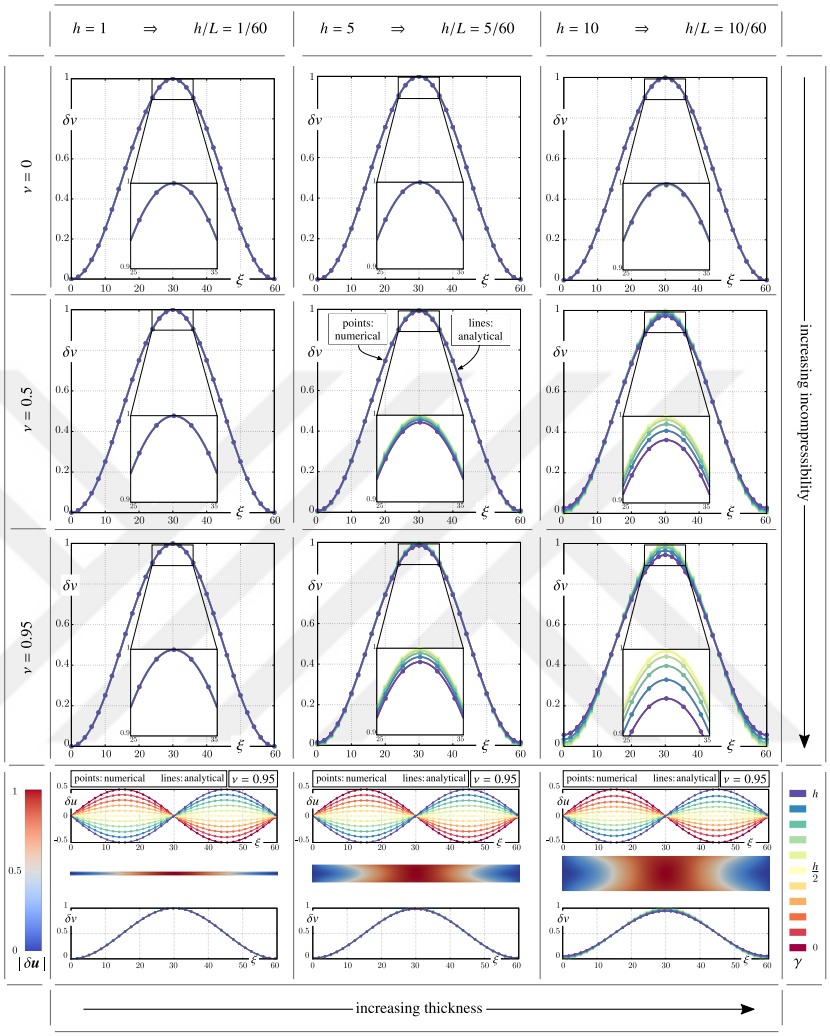


Figure 4.8: The vertical and horizontal incremental displacement profiles along the height of a beam of length $L = 60$, for various h/L and Poisson's ratios ν.

decay along the vertical axis of the beam becomes more pronounced, with the largest variation seen for a beam with $h/L = 1/6$ and $\nu = 0.95$. This finding enforces our understanding from Fig. 4.6, where the Poisson effect became more influential at higher ν and higher thicknesses h. This conclusion is especially important since most beam theories, such as the Euler beam theory, readily assume an incompressible and highly slender beam, and the proposed deflection functions for these beams are composed of sinusoidal functions, all of which are solely functions of the horizontal direction, ξ. Hence, any variation along the vertical axis of the beam, and naturally the effect of compressibility on it, is neglected,

given the "slender beam" assumption. It should be pointed out that *the inclusion of the decay function, which is a function of γ only, in the proposed general solution for the incremental displacement functions is exactly what allows for us to perfectly capture the displacement profile of an increasingly incompressible and thicker beam.*

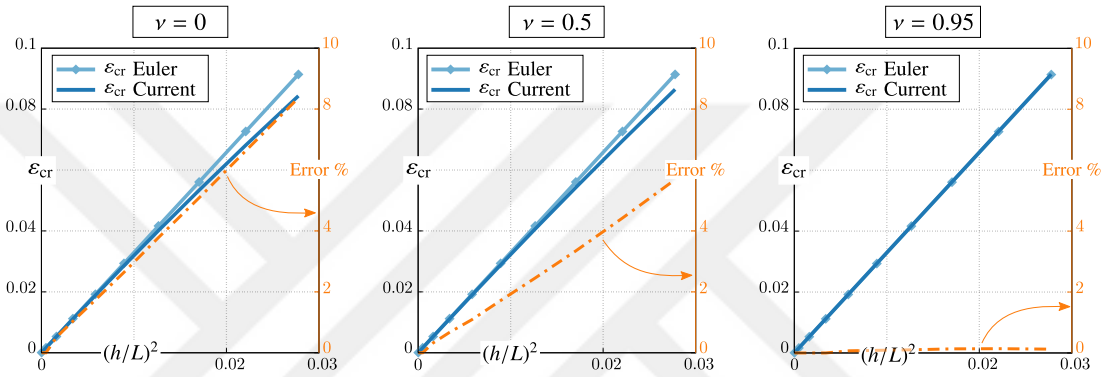


Figure 4.9: Comparison of our results (Current) with the established Euler beam theory, for different compressibilities ν. Orange line indicates the percentage error that the Euler theory has compared to the current results. The error is computed by $|\varepsilon_{\text{cr}}^{\text{Euler}} - \varepsilon_{\text{cr}}^{\text{Curr.}}|/\varepsilon_{\text{cr}}^{\text{Curr.}} \times 100\%$.

Finally, a comparison of our results with the classical Euler beam theory for the onset of bifurcation of a beam with a set of material and geometrical parameters is given in Fig. 4.9. The well established [187] Euler buckling stress, σ_{cr}, for a clamped-clamped beam reads $\sigma_{\text{cr}} = \frac{E\,I\,4n^2\pi^2}{A\,L^2}$, where E is the Young's modulus, I is the moment of inertia which for a rectangular beam reads $I = b\,h^3/12$, where h is the beam thickness and b is the width, A is the cross-sectional area given by bh, and L is the length of the beam. The critical strain ε_{cr} relates to critical stress such that $\varepsilon_{\text{cr}} = \sigma_{\text{cr}}/E$, which renders the Euler critical strain $\varepsilon_{\text{cr}} = \left[\frac{h}{L}\right]^2 \frac{n^2\pi^2}{3}$. For the sake of comparison, the current results have been given in terms of critical strain, ε_{cr}, rather than the previously formulated critical stretch, λ_{cr}. The two are related through the relation $\varepsilon_{\text{cr}} = \lambda_{\text{cr}} - 1$ wherein negative strain indicates compression, and the negative sign is omitted here for convenience. Clearly, the difference between the two results vanish for lower h/L ratios, i.e. for increasingly slender beams. As the ratio h/L increases, the error between the two results also increases. However, since the Euler theory is not a function of compressibility but carries in itself the assumption of an incompressible beam, the error between the

two results decrease as we move towards incompressibility, eventually reaching almost zero at $\nu = 0.95$.

Remark on computational aspects. *The numerical results presented here are obtained through the in-house non-linear FEM computational framework with embedded eigenvalue analysis, with the details given in [30]. For computational efficiency, the minimization scheme - which given a certain prescribed extensional displacement λ calculates the corresponding lateral displacement η - can also be replaced by the key non-linear Poisson's ratio relation (4.3). This allows one to calculate the extensional and lateral displacements, i.e. the deformation gradient, by only knowing the Poisson's ratio of the beam, in a single increment and without the need for an incremental minimization scheme. Using this non-iterative method also provides a work-around for the adverse affects such as longer computation times or element-locking faced near incompressibility.* □

4.4 Bilayer instability

Moving from the buckling of a compressible half-space and of a compressible beam, we can now derive the relations for the bifurcation behavior of a film on top of a substrate in a non-linear, large deformations framework. This section elaborates on the bifurcation behavior of a bilayer undergoing large, plane deformations, which essentially consists of the "beam" from Section 4.3 being put on top of the compliant, elastic half-space from Section 4.2, and deforming them together. However, to be able to compare our results with those presented in Chapter 3, we later need to also account for growth in our formulation, so that we can have a stress-free initial configuration with a growing film. In Chapter 6 the generic framework is further generalized to include growth.

For the remainder of this section, the growth of the film and substrate are simply assumed to be zero and only compression is applied to the structure. The beam in Section 4.3 now becomes a film, with shear modulus μ_f and Poisson's ratio ν_f, and the half-space in Section 4.2 now becomes the substrate with shear

modulus μ_s and Poisson's ratio ν_s, constituting a bilayer structure. Every defined quantity until this point which is a function of material parameters will henceforth be denoted with the corresponding subscript, in order to differentiate between the beam (film) and half-space (substrate) contributions. Parameters which are universal among the film and substrate in a bilayer structure, e.g. wavenumber k or coordinates ξ and γ, are denoted without subscripts, for both film and substrate quantities. Now we have a new "surface", namely the interface between the film and the substrate, where we need to superimpose the bilayer counterparts of the two complementary equations (4.34) and (4.25), which dictate the traction on the bottom of the film and top of the substrate, respectively. For the case of a bilayer geometry, however, the sum of tractions at the bottom of the film and top of the substrate equates to zero, posing essentially a *traction-continuity* condition. Additionally, to ensure *displacement-continuity* we impose that the incremental displacement at the bottom of the film is identical to that on the top of the substrate. That is, $[\![\delta \boldsymbol{u}]\!] = \boldsymbol{0}$ holds at $\gamma = 0$, where $[\![\delta \boldsymbol{u}]\!]$ denotes the incremental displacement jump at the interface.

The boundary condition we impose on the bilayer structure first is the traction-free surface at $\gamma = h$. Recall that we had already applied this condition when looking at the bifurcation of a beam in Section 4.3, where we imposed a traction-free surface condition on the top of the beam through Eq. (4.32). Imposing the traction-free boundary condition at $\gamma = h$ yields the relation

$$ {}^{\frac{3}{4}}\boldsymbol{B}_f = \boldsymbol{b}\, {}^{\frac{1}{2}}\boldsymbol{B}_f \quad \text{with} \quad \boldsymbol{b} := \left[{}^{\frac{3}{4}}\boldsymbol{W}_f \, {}^{\frac{3}{4}}\boldsymbol{E}_f(h) \right]^{-1} {}^{\frac{1}{2}}\boldsymbol{W}_f \, {}^{\frac{1}{2}}\boldsymbol{E}_f(h)\,, \tag{4.38} $$

that is identical to the relation (4.33). Secondly, we look at the traction on the bottom surface of the beam and the top surface of the substrate. Recalling and summing Eqs. (4.34) and (4.25) such that $\delta \boldsymbol{t}_f \,|_{\gamma=0} + \delta \boldsymbol{t}_s \,|_{\gamma=0} = \boldsymbol{0}$, renders

$$ \mu_f \, k \, \boldsymbol{T} \, {}^{\frac{1}{2}}\boldsymbol{W}_f \, {}^{\frac{1}{2}}\boldsymbol{B}_f - \mu_f \, k \, \boldsymbol{T} \, {}^{\frac{3}{4}}\boldsymbol{W}_f \, {}^{\frac{3}{4}}\boldsymbol{B}_f - \mu_s \; k \; \boldsymbol{T} \, {}^{\frac{1}{2}}\boldsymbol{W}_s \, {}^{\frac{1}{2}}\boldsymbol{B}_s \; = \boldsymbol{0}\,. \tag{4.39} $$

Subsequently, inserting the relation (4.38) into Eq. (4.39) furnishes

$$ \mu_f \, \boldsymbol{T} \left[{}^{\frac{1}{2}}\boldsymbol{W}_f \; - {}^{\frac{3}{4}}\boldsymbol{W}_f \; \boldsymbol{b} \right] {}^{\frac{1}{2}}\boldsymbol{B}_f - \mu_s \, \boldsymbol{T} \, {}^{\frac{1}{2}}\boldsymbol{W}_s \, {}^{\frac{1}{2}}\boldsymbol{B}_s \; = \boldsymbol{0}\,, \tag{4.40} $$

and since ${}^{\frac{1}{2}}\boldsymbol{E}_f(0) = \boldsymbol{I}$ and ${}^{\frac{3}{4}}\boldsymbol{E}_f(0) = \boldsymbol{I}$, the traction continuity can be expressed as

$$\mu_f \boldsymbol{T}\ \boldsymbol{Q}_f\ {}^{\frac{1}{2}}\boldsymbol{B}_f + \mu_s \boldsymbol{T}\ \boldsymbol{Q}_s\ {}^{\frac{1}{2}}\boldsymbol{B}_s\ = \boldsymbol{0}\,, \tag{4.41}$$

with

$$\begin{aligned} \boldsymbol{Q}_f &:= {}^{\frac{1}{2}}\boldsymbol{W}_f - {}^{\frac{3}{4}}\boldsymbol{W}_f\ \boldsymbol{b}\,, \\ \boldsymbol{Q}_s &:= -{}^{\frac{1}{2}}\boldsymbol{W}_s\,. \end{aligned} \tag{4.42}$$

Now turning to the displacement-continuity condition, equipped with both the incremental displacement functions for the film (4.31) and the substrate (4.24), we can evaluate these at $\gamma = 0$ and set them equal to each other, resulting in

$$\delta\boldsymbol{u}_f\,|_{\gamma=0} = \delta\boldsymbol{u}_s\,|_{\gamma=0} \qquad \Rightarrow \qquad \boldsymbol{T}\ {}^{\frac{1}{2}}\boldsymbol{G}_f\ {}^{\frac{1}{2}}\boldsymbol{B}_f + \boldsymbol{T}\ {}^{\frac{3}{4}}\boldsymbol{G}_f\ {}^{\frac{3}{4}}\boldsymbol{B}_f = \boldsymbol{T}\ {}^{\frac{1}{2}}\boldsymbol{G}_s\ {}^{\frac{1}{2}}\boldsymbol{B}_s\,. \tag{4.43}$$

Again, using the relation (4.38), and rearranging, yields

$${}^{\frac{1}{2}}\boldsymbol{B}_s = \boldsymbol{A}\ {}^{\frac{1}{2}}\boldsymbol{B}_f\,, \tag{4.44}$$

with

$$\boldsymbol{A} := {}^{\frac{1}{2}}\boldsymbol{G}_s^{\text{-}1}\ \left[{}^{\frac{1}{2}}\boldsymbol{G}_f + {}^{\frac{3}{4}}\boldsymbol{G}_f\ \boldsymbol{b}\right]. \tag{4.45}$$

Finally, we evaluate the traction continuity condition at the interface (4.41) by plugging in the relation we obtained from the displacement-continuity condition (4.44). This results in

$$\left[\mu_f\,\boldsymbol{Q}_f + \mu_s\,\boldsymbol{Q}_s\ \boldsymbol{A}\right]{}^{\frac{1}{2}}\boldsymbol{B}_f = \boldsymbol{0}\,, \tag{4.46}$$

that can be alternatively expressed in the canonical form

$$\boldsymbol{Q}\ {}^{\frac{1}{2}}\boldsymbol{B}_f = \boldsymbol{0} \qquad \text{with} \qquad \boldsymbol{Q} := \frac{\mu_f}{\mu_s}\,\boldsymbol{Q}_f + \boldsymbol{Q}_s\,\boldsymbol{A}\,. \tag{4.47}$$

Furthermore, it also proves useful to employ Young's modulus E to account for the stiffness of the structure instead of the shear modulus. That is

$$\boldsymbol{Q}\ {}^{\frac{1}{2}}\boldsymbol{B}_f = \boldsymbol{0} \qquad \text{with} \qquad \boldsymbol{Q} := \frac{E_f}{E_s}\,\frac{[1+\nu_s]}{[1+\nu_f]}\,\boldsymbol{Q}_f + \boldsymbol{Q}_s\,\boldsymbol{A}\,, \tag{4.48}$$

and the parameter E_f/E_s is denoted as the stiffness ratio of the structure. Solving for the non-trivial solutions of the system (4.48), i.e. solving for λ in $\mathrm{Det}\,\boldsymbol{Q} = 0$, would give us a critical stretch λ_{cr} at which the structure bifurcates. Upon careful inspection of the system (4.48) and its components, we see that the parameter k, the wavenumber, still remains to be defined, or rather obtained. To this end, we employ a minimization scheme similar to that in Section 4.3, however in this case the wavenumber k is no longer discrete, but is continuous. The aim is the same: the value of k which maximizes the obtained λ_{cr}, hence the wavenumber that occurs in the minimum amount of compression, is sought.

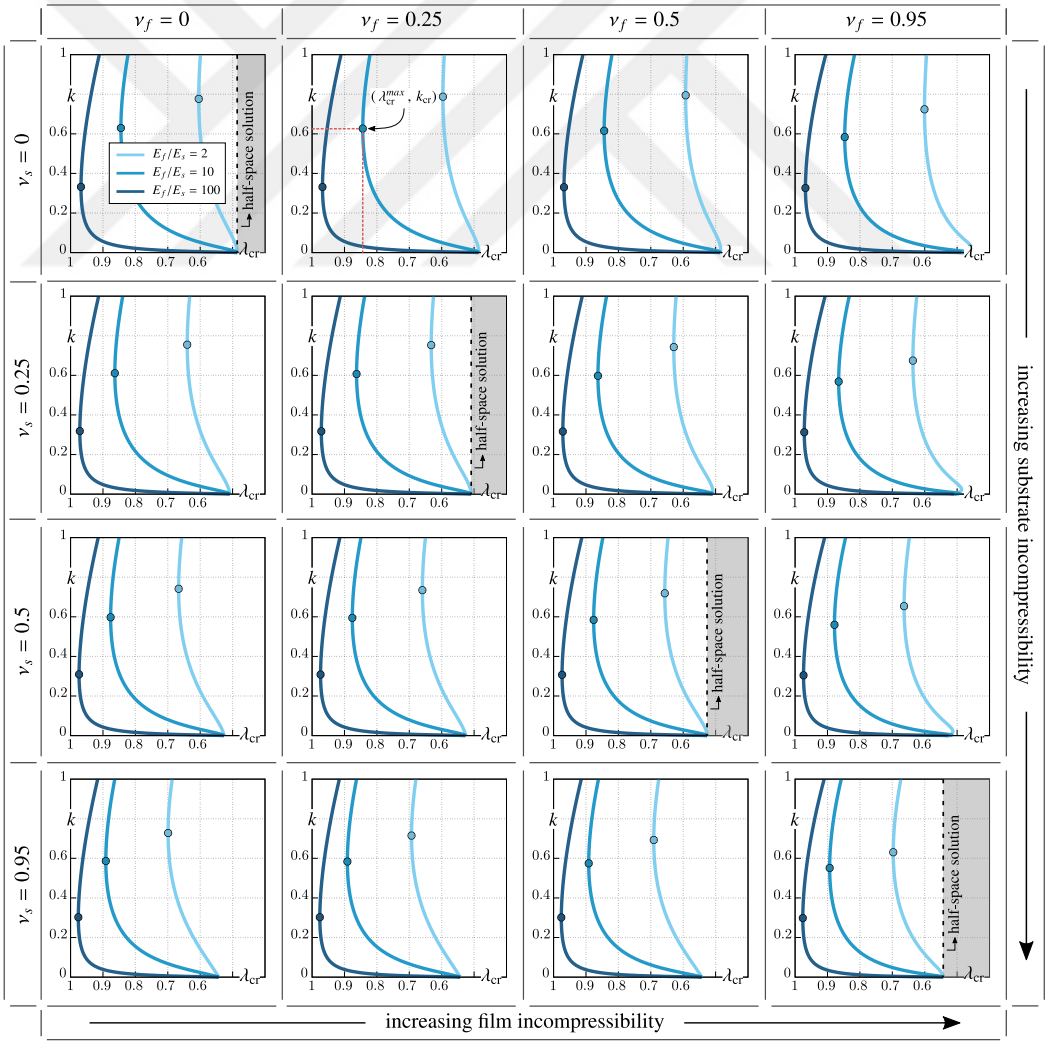


Figure 4.10: The variation of λ_{cr} for values of k, for a range of stiffness ratio (E_f/E_s) and film and substrate compressibilities.

The results are shown in Fig. 4.10, where the variance of critical stretch λ_{cr} with changing wavenumber k is shown, for bilayer structures of different material properties. As we move from a stretch $\lambda_{\text{cr}} = 1$, meaning no compression, the k corresponding to the maximum λ_{cr} gives us the point of bifurcation, shown by the points on each line. For the bilayer systems with the same film and substrate compressibility, i.e. the graphs on the diagonal in Fig. 4.10, as stiffness ratio E_f/E_s gets closer to 1, the line approaches the asymptotic vertical solution highlighted, corresponding to a half-space solution, which suggests that there are infinitely many solutions for the wavenumber at a single λ_{cr}. This is also apparent from the solution to the half-space given in (4.26), where clearly the solution λ_{cr} is independent of wavenumber k. For each stiffness ratio and Poisson's ratio pair, the critical stretch λ_{cr}, and the corresponding wavenumber k for the bilayer system can be determined as such.

Fig. 4.11 shows how the critical stretch λ_{cr} obtained through this method changes with stiffness ratio and compressibility. The top row of graphs in Fig. 4.11 portray the bifurcation behavior of a compressible bilayer system for different film and substrate compressibilities, with the stiffness ratio ranging from $E_f/E_s = 1$ to $E_f/E_s = 1000$. It can be seen that the compressibility of the substrate, given a certain compressibility for the film, renders increasingly different results towards stiffness ratio 1. As stiffness ratio is increased, the effect of compressibility on the bifurcation behavior decreases, and the solutions merge. The value stiffness ratio 1 is of particular importance, since with equal film and substrate Poisson's ratio, it designates the half-space solution. The bottom two rows of Fig. 4.11 look at a wider range of stiffness ratio, where stiffness ratio is defined both in terms of Young's modulus, as E_f/E_s (middle row), and in terms of shear modulus, as μ_f/μ_s (bottom row). As stiffness ratio decreases beyond 1, it is expected that the influence of the film should also decrease dramatically, and hence that the bifurcation behavior should not be influenced by a further decrease in the stiffness ratio, with the behavior of the structure being henceforth dominated by the substrate. An interesting feature is discernible here in the vicinity of stiffness ratio 1: while for a stiffness ratio measure in terms of Young's modulus, graphs corresponding to substrates of different Poisson's ratio all sharply transition at

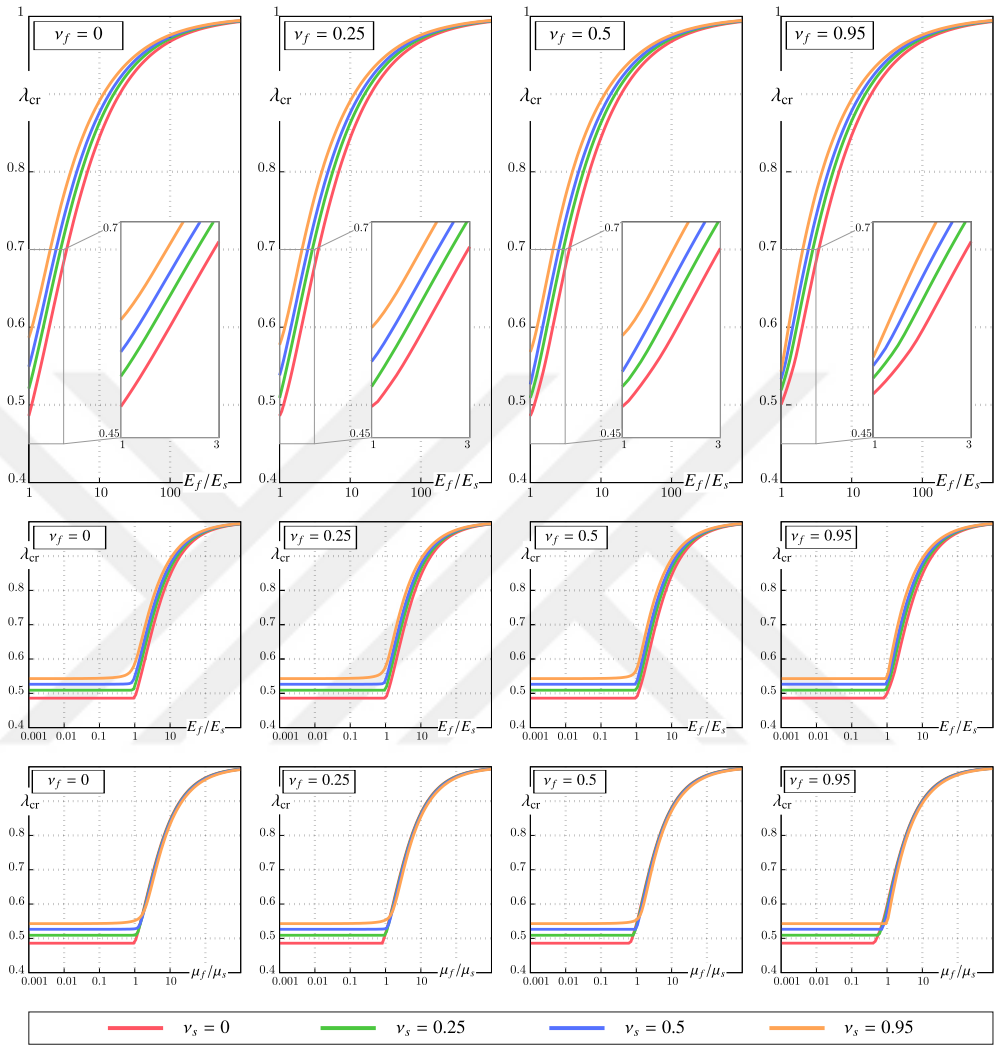


Figure 4.11: Graphs of λ_{cr} vs. different stiffness ratio measures (E_f/E_s) and (μ_f/μ_s) and ranges, for various ν_f and ν_s.

stiffness ratio 1, conversely, for a stiffness ratio measure in terms of shear modulus μ this transition point seems to be influenced by the compressibility of the substrate. Additionally, for a stiffness ratio measure with shear modulus, all the lines for different substrate compressibilities, i.e. the four lines in each inset, converge to almost a single solution as stiffness ratio increases beyond 1, while changing film compressibility still affects the shape of this "single" solution curve.

A 3-D representation of the results displayed in Fig. 4.11 can be found in

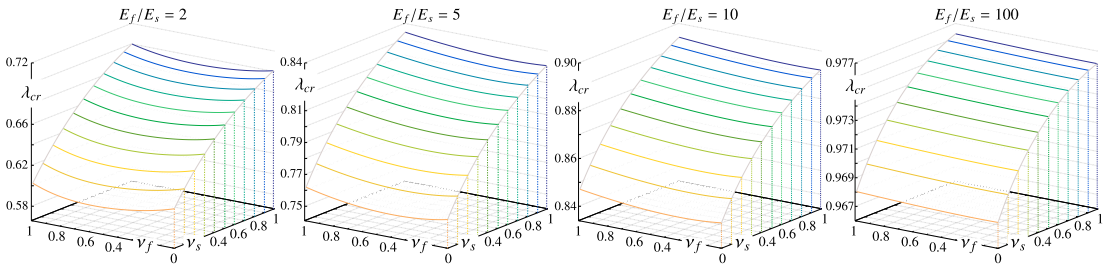


Figure 4.12: Plots of λ_{cr} vs. film and substrate compressibilities, displaying analytical results for various stiffness ratios E_f/E_s and for film thickness $h = 1$.

Fig. 4.12, wherein the variation of λ_{cr} for a bilayer system of various compressibilities ν_f and ν_s have been shown for different stiffness ratios. Similarly, the variation of λ_{cr} with respect to substrate Poisson's ratio ν_s is shown to decrease significantly as stiffness ratio increases, with the same trend holding for the influence of film Poisson's ratio. Here, the results displayed are for the stiffness ratio measure of E_f/E_s.

In Fig. 4.13, numerical results are presented together with analytical results. The numerical results presented here are for a domain of length $L = 60$ and film thickness $h = 1$, and have been obtained by using a non-linear FEM framework with embedded eigenvalue analysis. The insets show the deformed configuration obtained from the numerical studies at the point of bifurcation, for $E_f/E_s = 1000$ and film thickness $h = 1$. The effect of compressibility on the deformation profile can be seen clearly from these insets. An excellent agreement is observed between our analytical results and the numerical results for λ_{cr}, even for a nearly incompressible structure. While the results for different pairs of film and substrate Poisson's ratio portray similar behaviors, they exhibit differences as we move towards lower stiffness ratio. For instance, while the bilayer with $\nu_f = 0.95$ and $\nu_s = 0.95$ (bottom right inset) exhibits the well-known $\lambda_{\text{cr}} = 0.544$ solution near a stiffness ratio of 1, when the film is made fully compressible, such that $\nu_f = 0$ and $\nu_s = 0.95$ (bottom left inset), this solution changes dramatically.

Another characteristic property of a wrinkled bilayer system is the wavelength of its formed wrinkles. Hence, finally, one can obtain the critical wavelength ℓ_{cr} data from our analytical solution, simply by using the previously mentioned k_{cr}

value, which is related to critical wavelength by the relation $\ell_{\text{cr}} = 2\,\pi/k_{\text{cr}}$. Critical wavelength, as opposed to critical stretch, is influenced by film thickness. The critical wavelength as it changes with stiffness ratio, for different film thicknesses and film and substrate compressibilities, is given in Fig. 4.14, along with numerical findings.

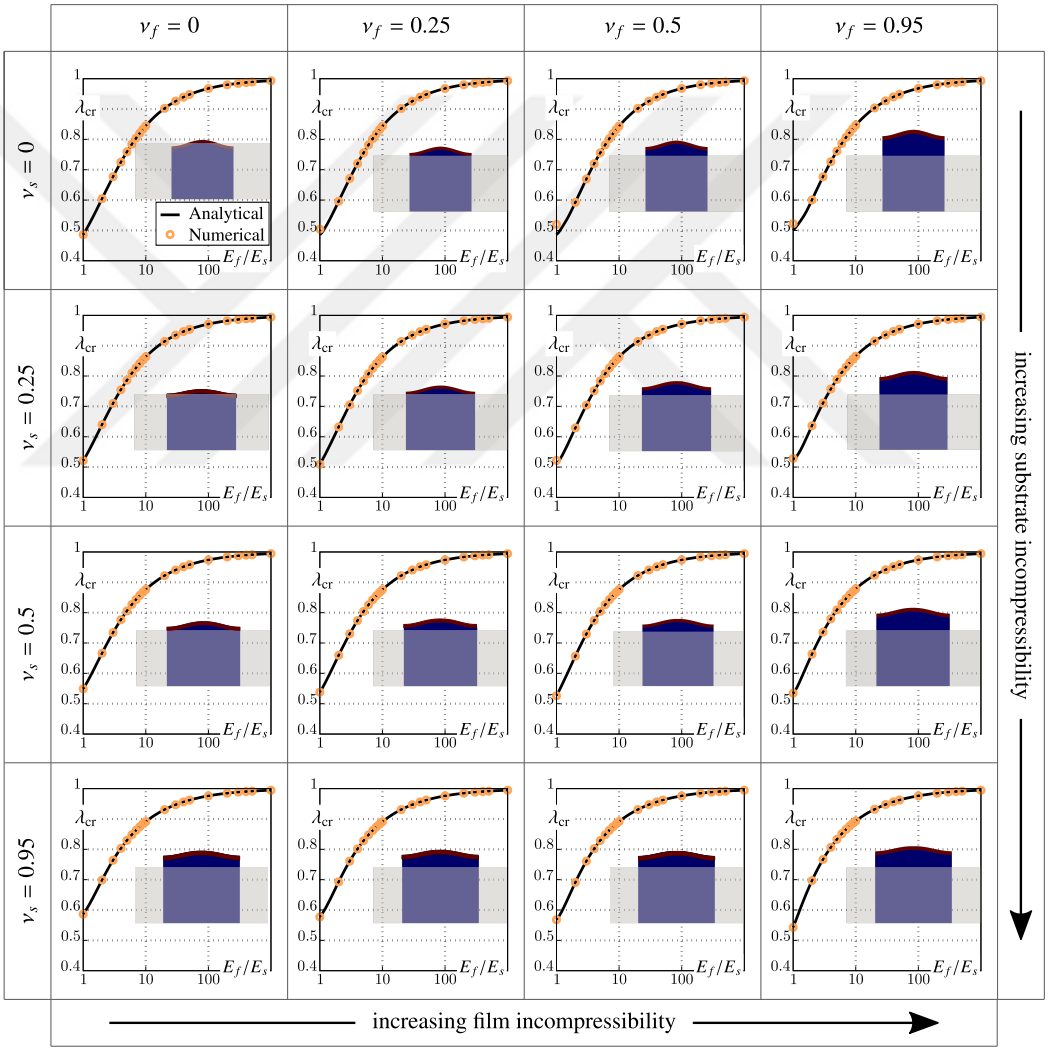


Figure 4.13: Plots of λ_{cr} vs. stiffness ratio displaying analytical and numerical results for various combinations of film and substrate compressibilities, for film thickness $h = 1$. Insets show the deformed configuration obtained from the numerical calculations for $E_f/E_s = 1000$ and $h = 1$.

Once more, the analytical results match the numerical results almost perfectly. The numerical data exhibit step-wise behavior which results essentially from the

discretization of the domain into elements, and because the critical wavenumber in the computational setting is obtained by counting the number of waves in the buckled configuration, in which only full waves or half-waves can be accounted for. It can be seen that the substrate Poisson's ratio is more influential on the critical wavelength compared to the film Poisson's ratio: while rows of graphs exhibit seemingly identical behavior and results, the difference between the graphs is most pronounced among the ones in a column, i.e. for a single film Poisson's ratio and varying substrate Poisson's ratio.

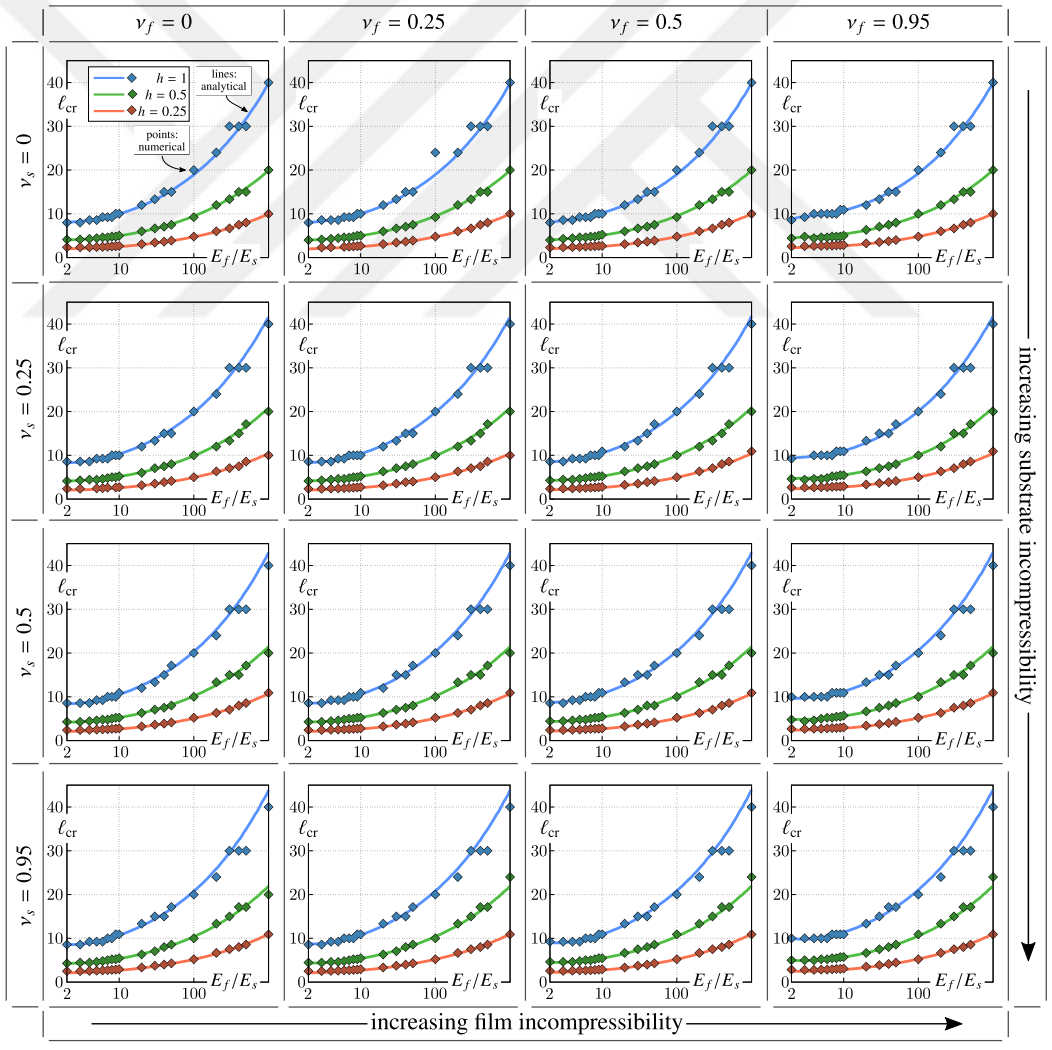


Figure 4.14: Analytical and numerical results for critical wavelength ℓ_{cr} as a function of stiffness ratio E_f/E_s, for film thickness $h = 1$, $h = 0.5$ and $h = 0.25$, and various sets of Poisson's ratio for film and substrate.

4.5 Trilayer instability

Next, we want to particularize this generic approach for the case of a "trilayer structure" via imposing appropriate boundary conditions, as given in Fig. 4.2. The trilayer structure has been referred to by many names in the literature such as "half-space coated by double-layer" [113] or "bilayer on a substrate" [107]. Here, the trilayer consists of a film on top, an interphase layer, and a substrate at the bottom, distinguished by subscripts $\{\bullet\}_f$, $\{\bullet\}_i$, and $\{\bullet\}_s$, respectively. Using the introduced generic approach, it is possible to solve for the bifurcation behavior of the trilayer system by prescribing the necessary boundary conditions to the corresponding domains. The first boundary condition is the traction-free top surface of the structure, i.e. the upper surface of the film at $\gamma = h_f + h_i$, which yields

$$\delta \boldsymbol{t}\Big|_{\gamma=h_f+h_i} \doteq \boldsymbol{0} \;\; \Rightarrow \;\; {}^{\frac{3}{4}}\boldsymbol{B}_f = \boldsymbol{b}\, {}^{\frac{1}{2}}\boldsymbol{B}_f \,, \tag{4.49}$$

with

$$\boldsymbol{b} := \left[{}^{\frac{3}{4}}\boldsymbol{W}_f \, {}^{\frac{3}{4}}\boldsymbol{E}_f(h_f + h_i) \right]^{-1} {}^{\frac{1}{2}}\boldsymbol{W}_f \, {}^{\frac{1}{2}}\boldsymbol{E}_f(h_f + h_i) \,, \tag{4.50}$$

relating the two sets of constants, ${}^{\frac{3}{4}}\boldsymbol{B}_f$ and ${}^{\frac{1}{2}}\boldsymbol{B}_f$. The second boundary condition is at the interface between the film and the interphase, namely at $\gamma = h_i$. In this work, all the interfaces are considered to be a "perfect interface", where (i) displacement jump is zero and (ii) traction continuity is assumed across the interface [188]. To this extent, the boundary conditions to be applied at the interface between the film and the interphase are two fold, such that (i) $[\![\delta \boldsymbol{u}]\!] = \boldsymbol{0}$, and (ii) $\sum \delta \boldsymbol{P} \cdot \boldsymbol{N} = \boldsymbol{0}$. Here, the jump operator denotes the operation $[\![\{\bullet\}]\!] = \{\bullet\}^+ - \{\bullet\}^-$, along the unit normal. For the interface at $\gamma = h_i$, the displacement jump condition reads $[\![\delta \boldsymbol{u}]\!]\Big|_{\gamma=h_i} = \delta \boldsymbol{u}_f\Big|_{\gamma=h_i} - \delta \boldsymbol{u}_i\Big|_{\gamma=h_i} \doteq \boldsymbol{0}$, and using the relation (4.49) together with the displacement jump condition renders the relation

$${}^{\frac{1}{2}}\boldsymbol{B}_f = \boldsymbol{A}_f \, \boldsymbol{T}_f^{-1} \, \boldsymbol{T}_i^{-1} \left[{}^{\frac{1}{2}}\boldsymbol{G}_i \, {}^{\frac{1}{2}}\boldsymbol{E}_i(h_i) \, {}^{\frac{1}{2}}\boldsymbol{B}_i + {}^{\frac{3}{4}}\boldsymbol{G}_i \, {}^{\frac{3}{4}}\boldsymbol{E}_i(h_i) \, {}^{\frac{3}{4}}\boldsymbol{B}_i \right] , \tag{4.51}$$

with

$$\boldsymbol{A}_f := \left[{}^{\frac{1}{2}}\boldsymbol{G}_f \, {}^{\frac{1}{2}}\boldsymbol{E}_f(h_i) + {}^{\frac{3}{4}}\boldsymbol{G}_f \, {}^{\frac{3}{4}}\boldsymbol{E}_f(h_i) \, \boldsymbol{b} \right]^{-1} . \tag{4.52}$$

On the other hand, the traction continuity condition at $\gamma = h_i$, namely $\sum \delta \boldsymbol{P} \cdot \boldsymbol{N}\Big|_{\gamma=h_i} = \delta \boldsymbol{P}_f \Big|_{\gamma=h_i} \cdot [-\boldsymbol{N}] + \delta \boldsymbol{P}_i \Big|_{\gamma=h_i} \cdot \boldsymbol{N} \doteq \boldsymbol{0}$, used together with the previously obtained relations (4.49) and (4.51) renders the following expression relating ${}^{\frac{3}{4}}\boldsymbol{B}_i$ and ${}^{\frac{1}{2}}\boldsymbol{B}_i$,

$$ {}^{\frac{3}{4}}\boldsymbol{B}_i = \boldsymbol{L}\, {}^{\frac{1}{2}}\boldsymbol{B}_i \quad \text{where} \quad \boldsymbol{L} := {}^{\frac{3}{4}}\boldsymbol{L}^{-1}\, {}^{\frac{1}{2}}\boldsymbol{L}\,, \tag{4.53} $$

with

$$ \begin{aligned} {}^{\frac{1}{2}}\boldsymbol{L} := \Bigg[& -\left[{}^{\frac{1}{2}}\boldsymbol{W}_f\, {}^{\frac{1}{2}}\boldsymbol{E}_f(h_i) - {}^{\frac{3}{4}}\boldsymbol{W}_f\, {}^{\frac{3}{4}}\boldsymbol{E}_f(h_i)\, \boldsymbol{b} \right] \quad \boldsymbol{A}_f\, \boldsymbol{T}_f^{-1}\, \boldsymbol{T}_i\, {}^{\frac{1}{2}}\boldsymbol{G}_i\, {}^{\frac{1}{2}}\boldsymbol{E}_i(h_i) \\ & + \frac{\mu_i}{\mu_f}\, \frac{k_i}{k_f}\, \boldsymbol{T}_f^{-1}\, \boldsymbol{T}_i\, {}^{\frac{1}{2}}\boldsymbol{W}_i\, {}^{\frac{1}{2}}\boldsymbol{E}_i(h_i) \Bigg], \\ {}^{\frac{3}{4}}\boldsymbol{L} := \Bigg[& \left[{}^{\frac{1}{2}}\boldsymbol{W}_f\, {}^{\frac{1}{2}}\boldsymbol{E}_f(h_i) - {}^{\frac{3}{4}}\boldsymbol{W}_f\, {}^{\frac{3}{4}}\boldsymbol{E}_f(h_i)\, \boldsymbol{b} \right] \quad \boldsymbol{A}_f\, \boldsymbol{T}_f^{-1}\, \boldsymbol{T}_i\, {}^{\frac{3}{4}}\boldsymbol{G}_i\, {}^{\frac{3}{4}}\boldsymbol{E}_i(h_i) \\ & + \frac{\mu_i}{\mu_f}\, \frac{k_i}{k_f}\, \boldsymbol{T}_f^{-1}\, \boldsymbol{T}_i\, {}^{\frac{3}{4}}\boldsymbol{W}_i\, {}^{\frac{3}{4}}\boldsymbol{E}_i(h_i) \Bigg]. \end{aligned} \tag{4.54} $$

Before moving to the interface between the interphase and the substrate, we impose the half-space condition on the substrate, such that the displacements should decay to zero as $\gamma \to -\infty$, rendering the set of constants ${}^{\frac{3}{4}}\boldsymbol{B}_s$ to be set to zero. At the interphase-substrate interface at $\gamma = 0$, we impose once more the displacement and traction continuity. Setting the displacement jump at the interphase-substrate interface to zero via $[\![\delta \boldsymbol{u}]\!]\Big|_{\gamma=0} = \delta \boldsymbol{u}_i \Big|_{\gamma=0} - \delta \boldsymbol{u}_s \Big|_{\gamma=0}$, and again by using the previously obtained relations between the constants, we obtain

$$ {}^{\frac{1}{2}}\boldsymbol{B}_s = {}^{\frac{1}{2}}\boldsymbol{G}_s^{-1}\, \boldsymbol{T}_s^{-1}\, \boldsymbol{T}_i \left[{}^{\frac{1}{2}}\boldsymbol{G}_i + {}^{\frac{3}{4}}\boldsymbol{G}_i\, \boldsymbol{L} \right] {}^{\frac{1}{2}}\boldsymbol{B}_i\,. \tag{4.55} $$

In order to ensure traction continuity at the interface between the interphase and the substrate, we set $\sum \delta \boldsymbol{P} \cdot \boldsymbol{N}\Big|_{\gamma=0} = \delta \boldsymbol{P}_i \Big|_{\gamma=0} \cdot [-\boldsymbol{N}] + \delta \boldsymbol{P}_s \Big|_{\gamma=0} \cdot \boldsymbol{N} \doteq \boldsymbol{0}$, which used together with the relations found previously relating the various constants (4.49), (4.51), (4.53) and (4.55), and after some simplification yields,

$$ \boldsymbol{Q}\, {}^{\frac{1}{2}}\boldsymbol{B}_i = \boldsymbol{0} \text{ with } \boldsymbol{Q} := \left[\frac{\mu_i}{\mu_s}\, {}^{\frac{1}{2}}\boldsymbol{W}_i - {}^{\frac{3}{4}}\boldsymbol{W}_i\, \boldsymbol{L} - {}^{\frac{1}{2}}\boldsymbol{W}_s\, {}^{\frac{1}{2}}\boldsymbol{G}_s^{-1} \left[{}^{\frac{1}{2}}\boldsymbol{G}_i + {}^{\frac{3}{4}}\boldsymbol{G}_i\, \boldsymbol{L} \right] \right], \tag{4.56} $$

where $\boldsymbol{L} = {}^{\frac{3}{4}}\boldsymbol{L}^{-1}\,{}^{\frac{1}{2}}\boldsymbol{L}$ according to (4.53) with ${}^{\frac{1}{2}}\boldsymbol{L}$ and ${}^{\frac{3}{4}}\boldsymbol{L}$ simplified from (4.54) to

$$
\begin{aligned}
{}^{\frac{1}{2}}\boldsymbol{L} &:= \left[-\left[{}^{\frac{1}{2}}\boldsymbol{W}_f\, {}^{\frac{1}{2}}\boldsymbol{E}_f(h_i) - {}^{\frac{3}{4}}\boldsymbol{W}_f\, {}^{\frac{3}{4}}\boldsymbol{E}_f(h_i)\, \boldsymbol{b} \right] \boldsymbol{A}_f\, {}^{\frac{1}{2}}\boldsymbol{G}_i\, {}^{\frac{1}{2}}\boldsymbol{E}_i(h_i) + \frac{\mu_i}{\mu_f}\, {}^{\frac{1}{2}}\boldsymbol{W}_i\, {}^{\frac{1}{2}}\boldsymbol{E}_i(h_i) \right], \\
{}^{\frac{3}{4}}\boldsymbol{L} &:= \left[\left[{}^{\frac{1}{2}}\boldsymbol{W}_f\, {}^{\frac{1}{2}}\boldsymbol{E}_f(h_i) - {}^{\frac{3}{4}}\boldsymbol{W}_f\, {}^{\frac{3}{4}}\boldsymbol{E}_f(h_i)\, \boldsymbol{b} \right] \boldsymbol{A}_f\, {}^{\frac{3}{4}}\boldsymbol{G}_i\, {}^{\frac{3}{4}}\boldsymbol{E}_i(h_i) + \frac{\mu_i}{\mu_f}\, {}^{\frac{3}{4}}\boldsymbol{W}_i\, {}^{\frac{3}{4}}\boldsymbol{E}_i(h_i) \right].
\end{aligned}
\tag{4.57}
$$

Solving the expression (4.56) for λ by setting $\mathrm{Det}\boldsymbol{Q} = 0$ would render the critical stretch λ_{cr} at which bifurcation occurs. Looking at the derived form, stiffnesses of the domains are present in the two stiffness ratios which appear, namely that of film-to-substrate μ_f/μ_s, and interphase-to-substrate μ_i/μ_s, which can be expressed in terms of Young's modulus and Poisson's ratio as

$$
\frac{\mu_f}{\mu_s} = \frac{E_f}{E_s}\,\frac{[1+\nu_s]}{[1+\nu_f]} \qquad \text{and} \qquad \frac{\mu_i}{\mu_s} = \frac{E_i}{E_s}\,\frac{[1+\nu_s]}{[1+\nu_i]}\,. \tag{4.58}
$$

Remark on wavenumber. *One simplification that has been done to obtain Eq. (4.56) stems from the observation that the system remains a function of ξ as long as the matrices $\boldsymbol{T}_s$, $\boldsymbol{T}_i$ and $\boldsymbol{T}_f$ are present in the equation. There are two instances that these appear in our relations, namely in the forms ${\boldsymbol{T}_f}^{-1}\boldsymbol{T}_i$ and ${\boldsymbol{T}_s}^{-1}\boldsymbol{T}_i$. However, note that due to having perfect bonding between the layers, the film, interphase, and substrate all exhibit the same wrinkling wavenumber at bifurcation and therefore $k_f = k_i = k_s$. Imposing this condition makes these two instances of ${\boldsymbol{T}_f}^{-1}\boldsymbol{T}_i$ and ${\boldsymbol{T}_s}^{-1}\boldsymbol{T}_i$ basically disappear. That is, $k = k_f = k_i = k_s$ such that ${\boldsymbol{T}_f}^{-1}\boldsymbol{T}_i = \boldsymbol{I}$ and ${\boldsymbol{T}_s}^{-1}\boldsymbol{T}_i = \boldsymbol{I}$. It should be noted here that for the case of a perfect interface, with the layers bonded to each other and delamination not allowed, this assumption holds and is physically sound. We see that this assumption is also naturally observed through the numerical simulations, although not explicitly imposed.* □

Remark on the generality of the solution. *The compressibility parameter α is present throughout the analysis here. Via setting $\alpha \to \infty$, the analytical solution reduces to its incompressible counterpart. Furthermore, by following through with the approach developed here and imposing suitable material parameters, one*

can recover the bifurcation solutions of a bilayer system or Biot half-space instability, previously studied in literature. For instance, when $E_f = E_i$ and $\nu_f = \nu_i$, the film and interphase act together as the top layer of a bilayer structure, with the substrate being the bottom layer, as shown in Fig. 4.15, and solving the system (4.56) renders the bilayer solution. □

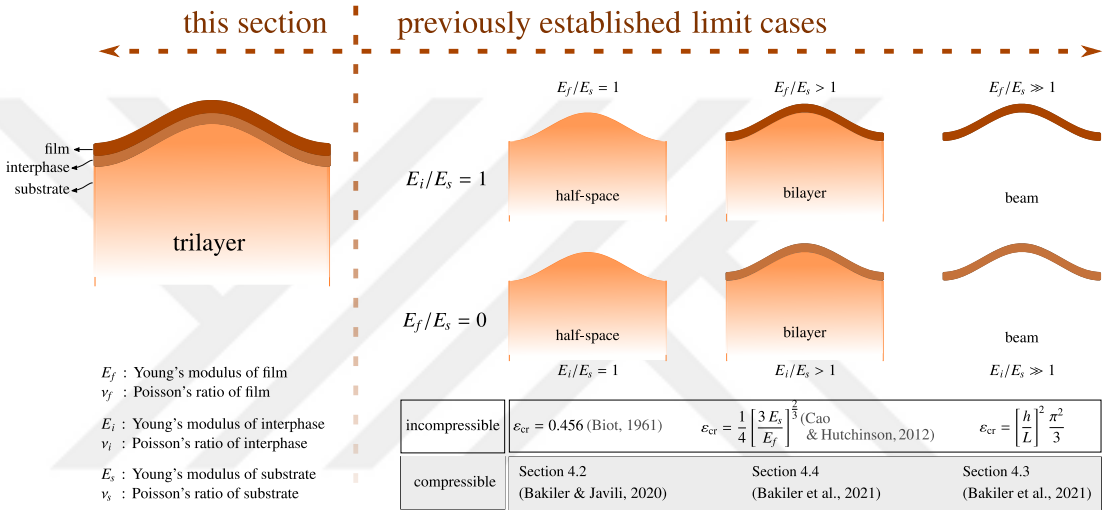


Figure 4.15: The trilayer structure that is studied in this section (left), shown together with the degeneration of the structure into common cases that have been studied previously (right) at certain Young's moduli and Poisson's ratios for all domains. The previously established results for incompressible and compressible domains have been given together with their associated references (bottom).

Next, we present the findings of the theoretical analysis together with numerical findings. The problem is solved for various dimensions of h_i and h_f, over a wide range of stiffness ratios E_i/E_s and E_f/E_s, and most importantly, throughout the whole compressibility regime, namely between $0 \leq \nu < 1$. Furthermore, the analytical findings are compared with numerical findings, obtained using our in-house finite element (FE) package enhanced with eigenvalue analysis.

Solving Eq. (4.56) for λ for each k yields a bifurcation curve of λ_{cr} vs. k. The maximum of this curve λ_{cr}, and the corresponding k_{cr} is the point of bifurcation, as it will be the first mode to encounter when compressing the domain starting from the reference configuration at $\lambda = 1$. In other words,

$$\lambda_{\text{cr}} = \max\{\, \lambda \,|\, \text{Det}\, \boldsymbol{Q}\,(\,k\,,\,\lambda\,,\,\eta_f\,,\,\eta_i\,,\,\eta_s) = 0\,,\, \forall\, k \in \mathbb{R}^+ \,\}\,. \tag{4.59}$$

Clearly, the relation to be solved still remains a function of the vertical stretches, η_f, η_i, η_s. At this point, the non-linear Poisson's ratio relation (4.4) is to be employed such that

$$\eta_f = \frac{\sqrt{1+\alpha_f}}{\sqrt{1+\alpha_f\,\lambda^2}} \quad , \quad \eta_i = \frac{\sqrt{1+\alpha_i}}{\sqrt{1+\alpha_i\,\lambda^2}} \quad , \quad \eta_s = \frac{\sqrt{1+\alpha_s}}{\sqrt{1+\alpha_s\,\lambda^2}}\,. \tag{4.60}$$

Using these relations (4.60) in order to solve Eq. (4.56) yields $\lambda_{\rm cr} = \max\{\,\lambda\,|\,\mathrm{Det}\,\boldsymbol{Q}\,(\,k\,,\,\lambda) \,=\, 0\,,\,\forall\, k \,\in\, \mathbb{R}^+\,\}$. Hence, the k value which maximizes the resultant $\lambda_{\rm cr}$ is sought for every set of material and geometrical parameters.

The first results demonstrated here are intended to emphasize the utility of the compressible and large-deformations framework developed herein. Hence, the material parameters and dimensions assumed for this example are based on those of a smart composite beam, as studied in [16], in order to accentuate that several conventional materials used in smart structures and flexible electronics are indeed far from the incompressible limit that is usually studied in the literature on the subject. Figure 4.5 displays the critical stretch for the onset of bifurcation $\lambda_{\rm cr}$ and the corresponding critical wavenumber $k_{\rm cr}$, over a range of interphase-to-substrate stiffness ratios E_i/E_s, together with numerical findings. The exact Poisson's ratios given in [16] is used for the three layers, as well as the device dimensions, such that $h_f = 1$ and $h_i = 0.1$, and the film-to-substrate stiffness ratio $E_f/E_s = 10$ is assumed. Note that the substrate in this case is considered to be an infinite half-space, hence our solution is not a function of substrate depth. Similarly, the solution obtained here corresponds to an infinite length of the domain and therefore, the length of the domain does not introduce an additional length-scale in the bifurcation behavior of the trilayer structure.

The analytical and numerical results shown in Fig. 4.5 outline the general bifurcation behavior of a trilayer structure under uniaxial compression. For very high and low stiffness ratios E_i/E_s, the critical stretch required to induce wrinkling approaches unity, which suggests that the structure becomes highly sensitive to any small amount of compression induced away from the reference configuration.

A very low stiffness ratio E_i/E_s suggests a relatively stiff substrate, and a relatively very compliant interphase, and given that here $E_f/E_s \gg 1$, this suggests that the film itself behaves as a delaminated, slender beam, which is known to buckle with a very small amount of compression. Similarly, a very high stiffness ratio E_i/E_s suggests basically a bilayer structure with very high interphase-to-substrate stiffness ratio; thus the film would become virtually ineffective as the stiffness ratio E_i/E_s approaches 10^6, and in this structure the interphase itself would now behave as a slender beam, as also outlined in Fig. 4.15. The critical wavenumber demonstrates a compelling two-peak behavior, which will be further explored in other examples. Furthermore, the interesting behavior of critical wavenumber as the stiffness of the interphase with respect to the substrate is varied shows the versatility of the approach and how the interphase layer can be used to tune the wrinkling behavior of the system through the modification of its material parameters.

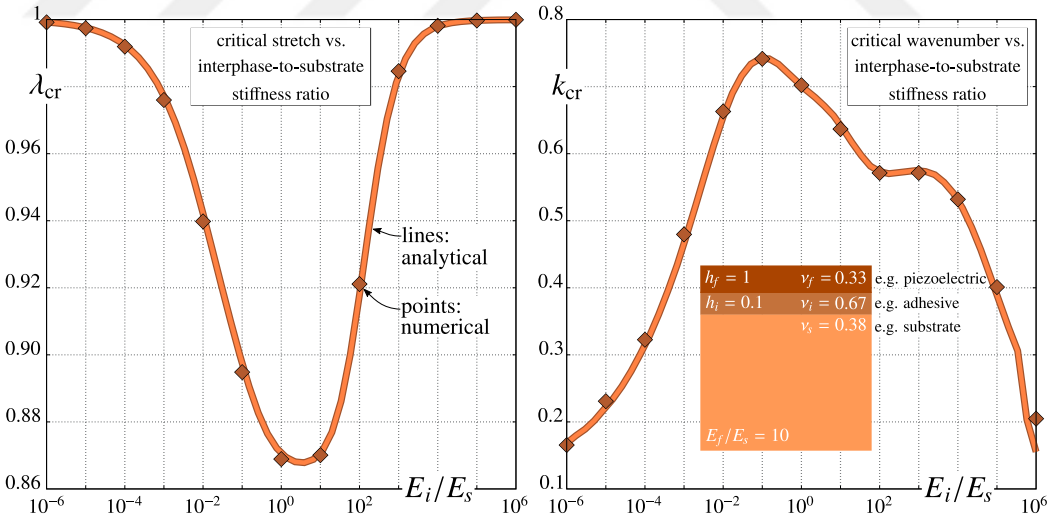


Figure 4.16: Results of the developed analytical solution for a certain set of material parameters, together with numerical findings. The parameters and dimensions assumed here are based on that of a piezoelectric device in order to demonstrate the utility of the approach.

Before moving deeper into the analysis of the trilayer structure, we demonstrate in Fig. 4.17 how the solution derived herein recovers some of the previously established results in literature as summarized in Fig. 4.15. We explore how the critical stretch λ_{cr} changes with respect to E_f/E_s and E_i/E_s, where all layers have the

same Poisson's ratio. Note that at the plane where $E_i/E_s = 1$, the trilayer structure becomes a bilayer, and hence the solution renders the critical stretch curve for a compressible bilayer structure. As both stiffness ratios E_f/E_s and E_i/E_s approach unity, the structure increasingly resembles a half-space. Accordingly, the obtained λ_{cr} at these limits can be seen to approach the well-known Biot solution [89] at the incompressible end (right), and the results obtained in [30,95] for a compressible half-space at the other compressible insets (center and left).

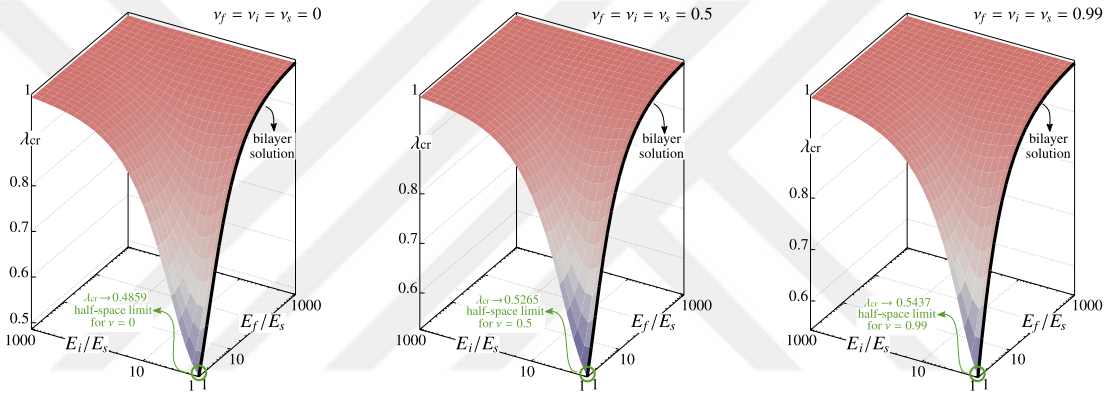


Figure 4.17: Results of the developed analytical solution for λ_{cr} vs. film-to-substrate stiffness ratio E_f/E_s and interphase-to-substrate stiffness ratio E_i/E_s, for three different Poisson's ratios for the whole structure, demonstrating that at the extremes the results recover those established in literature. The trilayer surface at $E_i/E_s = 1$ recovers the bilayer curve.

Figure 4.18 expounds the effect of compressibility on the bifurcation behavior of a trilayer structure, focusing on critical stretch λ_{cr} obtained through the developed analytical solution. In order to explore the influence of the compressibility of the film, substrate and interphase and to narrow down the parameter space, for the examples hereon out, the film and substrate will be assumed to have the same Poisson's ratio, solely for the purpose of simplification and brevity of the discussion. It should be emphasized, however, that the analytical framework developed here is suitable for all layers to have different Poisson's ratio, as demonstrated in Fig. 4.5. Each column in Fig. 4.18 looks at a certain Poisson's ratio for the film and the substrate; together with three different film-to-substrate stiffness ratios $E_f/E_s = 10$, 20, and 100, and three different interphase Poisson's ratios $\nu_i = 0$, 0.5, and 0.95. There are several significant observations; the critical stretch range over E_i/E_s changes drastically over the three different film-to-substrate stiffness

ratios; for instance, for the trilayers with $E_f/E_s = 100$, shown in shades of green, the critical stretch is relatively large, and varies between $0.96 < \lambda_{cr} < 1$. As film-to-substrate stiffness ratio decreases, the critical stretch required for bifurcation decreases, which demonstrates the necessity of using a large-deformation approach. In the range of parameters where the interphase is less compliant than the substrate, i.e. $E_i/E_s < 1$, changing the compressibility of the interphase significantly affects the critical stretch for all E_f/E_s stiffness ratios. Furthermore, it can be seen that changing the compressibility of the film and substrate influences the shape of the critical stretch curve. The behavior seen in the last window of sub-figures in the bottom of Fig. 4.18 has been observed frequently in literature, however, the remaining part of the figure displays the rest of the big picture that has been missed so far due to the incompressibility assumption.

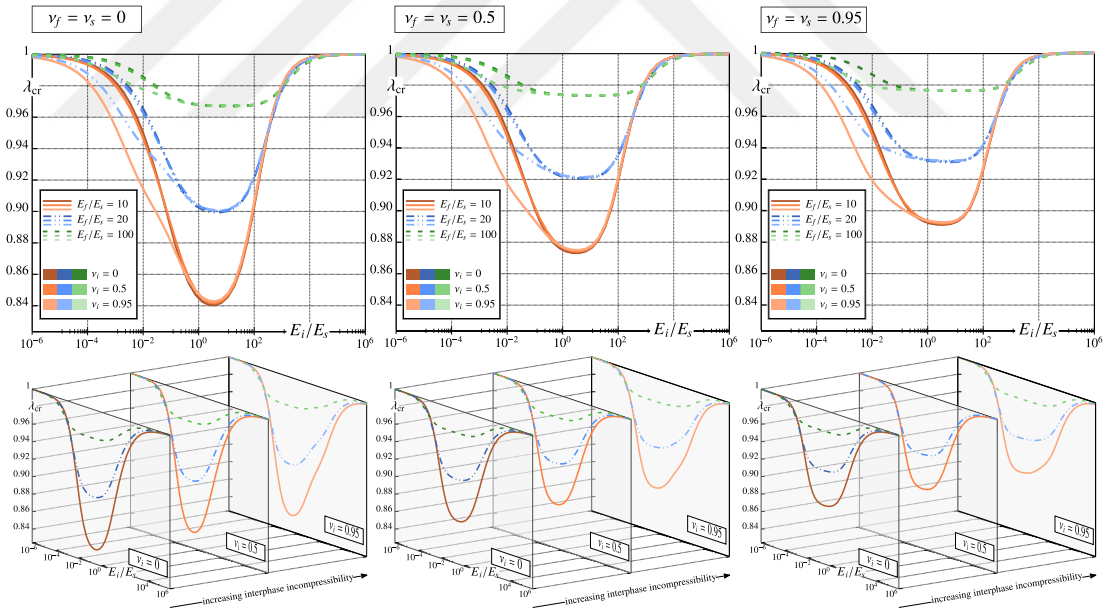


Figure 4.18: The effect of compressibility on the critical stretch λ_{cr} at the point of bifurcation, over a range of interphase-to-substrate stiffness ratios E_i/E_s, and for a set of film-to-substrate stiffness ratios E_f/E_s, for $h_f = 1$, $h_i = 0.1$

Figure 4.19 shows the analytical results obtained here together with numerical findings. The numerical findings have been obtained by using our in-house, large deformation FE code, which uses eigenvalue analysis in order to capture instabilities [181]. For the numerical computations, a domain of width 240 with 240 biquadratic Lagrange elements along the width has been used. The film

and interphase thickness have been set as $h_f = 1$, and $h_i = 0.1$, unless stated otherwise. Since an infinite half-space cannot be realized computationally, the substrate has been truncated sufficiently deep, and horizontal rollers have been placed on the bottom edge of the domain, whereas the bottom corners are fixed completely and the left and right edges are on vertical rollers, subjected to a prescribed deformation along the horizontal direction. More information about the eigenvalue analysis and boundary conditions used herein can be found in [30]. The analytical and numerical results are in excellent agreement all throughout the compressibility regime, even close to incompressibility. The evolution of the critical stretch curve throughout the compressibility spectrum can be seen more clearly here in the different insets of Fig. 4.19.

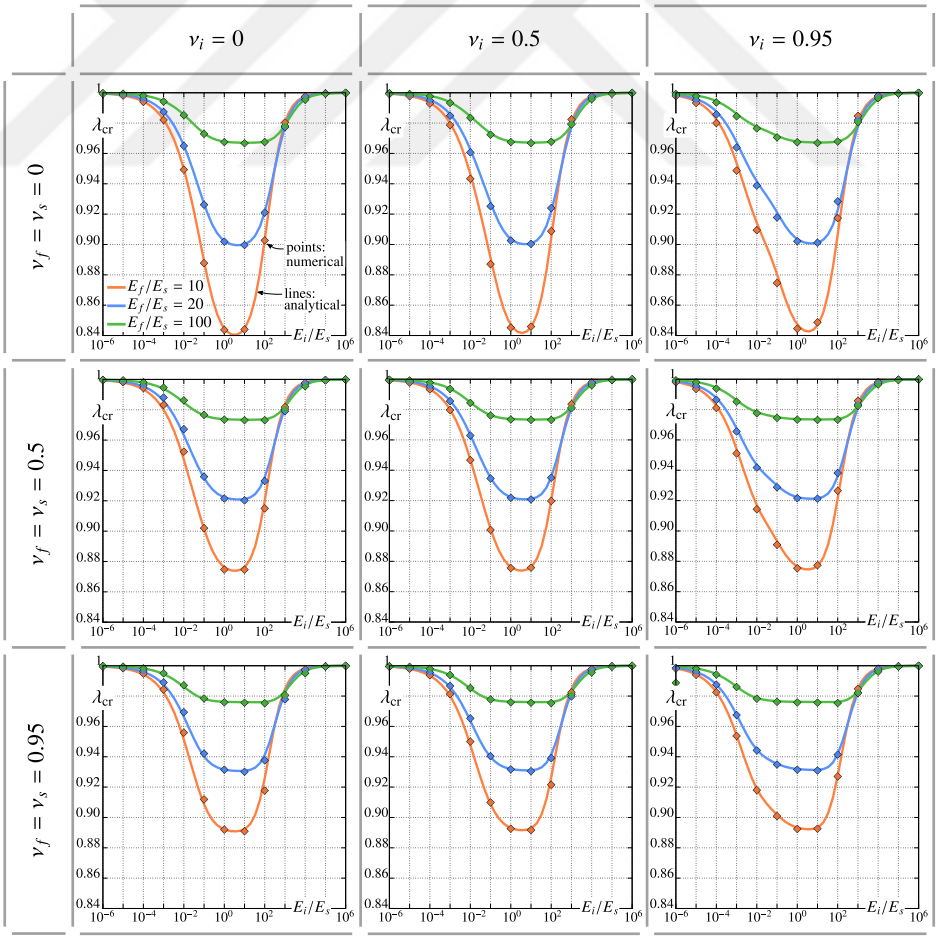


Figure 4.19: The critical stretch λ_{cr} vs. E_i/E_s calculated for a set of Poisson's ratios and $E_f/E_s = 10$, 20 and 100, for $h_f = 1$, $h_i = 0.1$, presented together with numerical findings obtained through FEM enhanced with eigenvalue analysis.

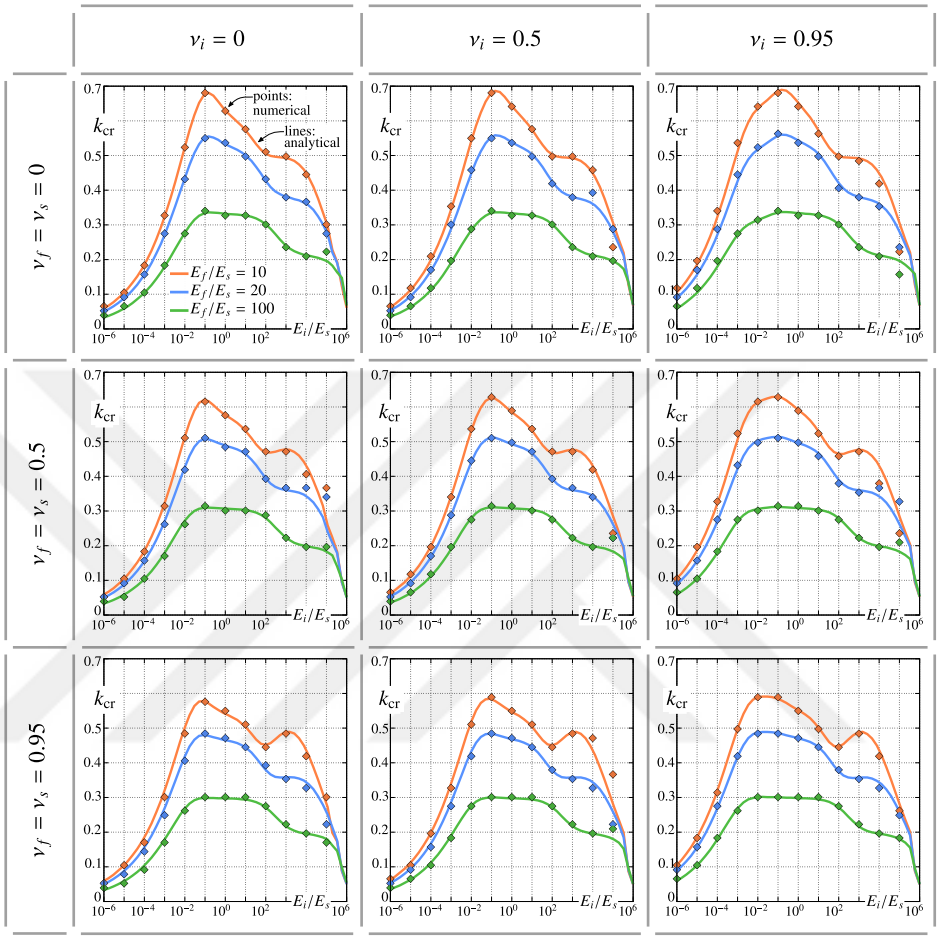


Figure 4.20: The critical wavenumber k_{cr} vs. E_i/E_s calculated for various ν and $E_f/E_s = 10$, 20 and 100, for $h_f = 1$, $h_i = 0.1$, presented together with numerical findings obtained through FEM enhanced with eigenvalue analysis.

Figure 4.20 is the counterpart of Fig. 4.19, displaying the behavior of critical wavenumber throughout the compressibility regime together with numerical results. For stiffness ratio $E_f/E_s = 10$, the critical wavenumber displays an interesting behavior in that it takes on a double-peak structure as the trilayer becomes "more incompressible"; this structure is most pronounced in the inset at the bottom right corner. The second peak seems to become less pronounced as the film-to-substrate stiffness ratio is increased. As it will be seen later, this double peak behavior is a part of a larger picture which also relates to the two modes of wrinkling observed in trilayer structures, see for instance [107]. Once more, the analytical findings obtained here are in great agreement with the numerical

findings. The divergence of the two sets of results at very high E_i/E_s stiffness ratios may be triggered by the high sensitivity of the problem at that range of parameters, where bifurcation happens at a very small compression away from the reference configuration.

Next, the influence of interphase height on bifurcation behavior will be elucidated via several examples. Figure 4.21 elaborates on how the critical stretch for bifurcation λ_{cr} changes with respect to stiffness ratio E_i/E_s, for three different interphase heights $h_i = 0.1$, 1, and 10, as the film thickness remains at $h_f = 1$, and $E_f/E_s = 10$. As the interphase becomes thicker than the film, the critical stretch curve forms into a sharp peak with its minimum around stiffness ratio $E_i/E_s = 1$, with bifurcation occurring at almost 30% stretch.

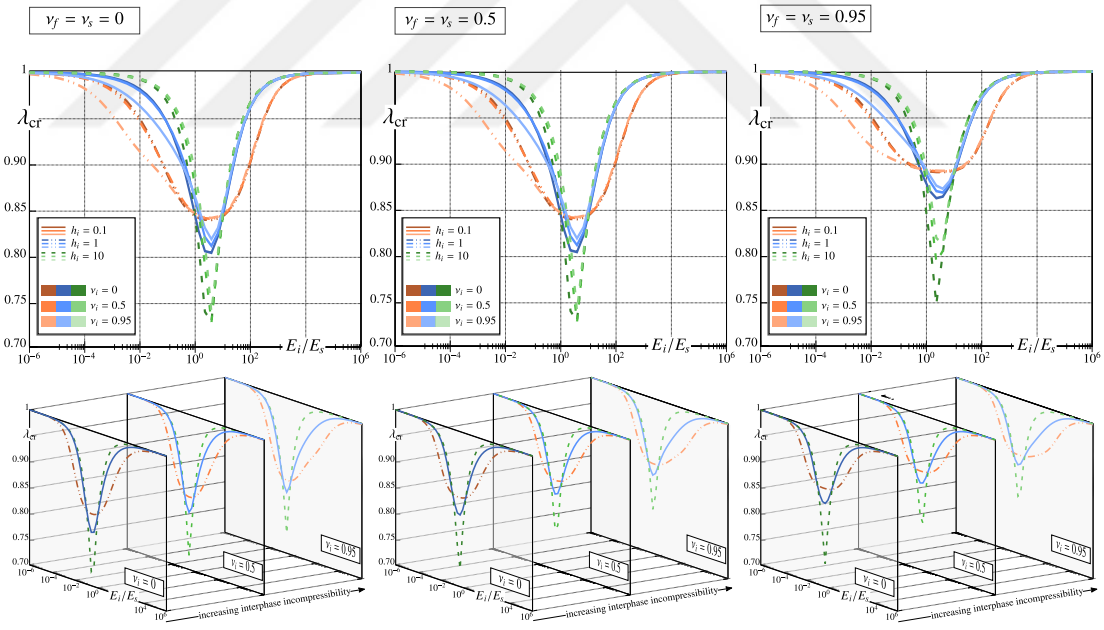


Figure 4.21: The effect of compressibility on the critical stretch λ_{cr} vs. E_i/E_S, calculated for a set of Poisson's ratios and interphase thickness $h_i = 0.1$, 1 and 100, for $E_f/E_s = 10$.

Looking also at the behavior of critical wavenumber with respect to E_i/E_s again for the same interphase thicknesses, and the effect of compressibility on the problem behavior, Fig. 4.22 displays the analytical findings. Similar to the critical stretch, the compressibility of the interphase ν_i seems to influence the critical wavenumber significantly for stiffness ratio $E_i/E_s < 1$, however, this influence

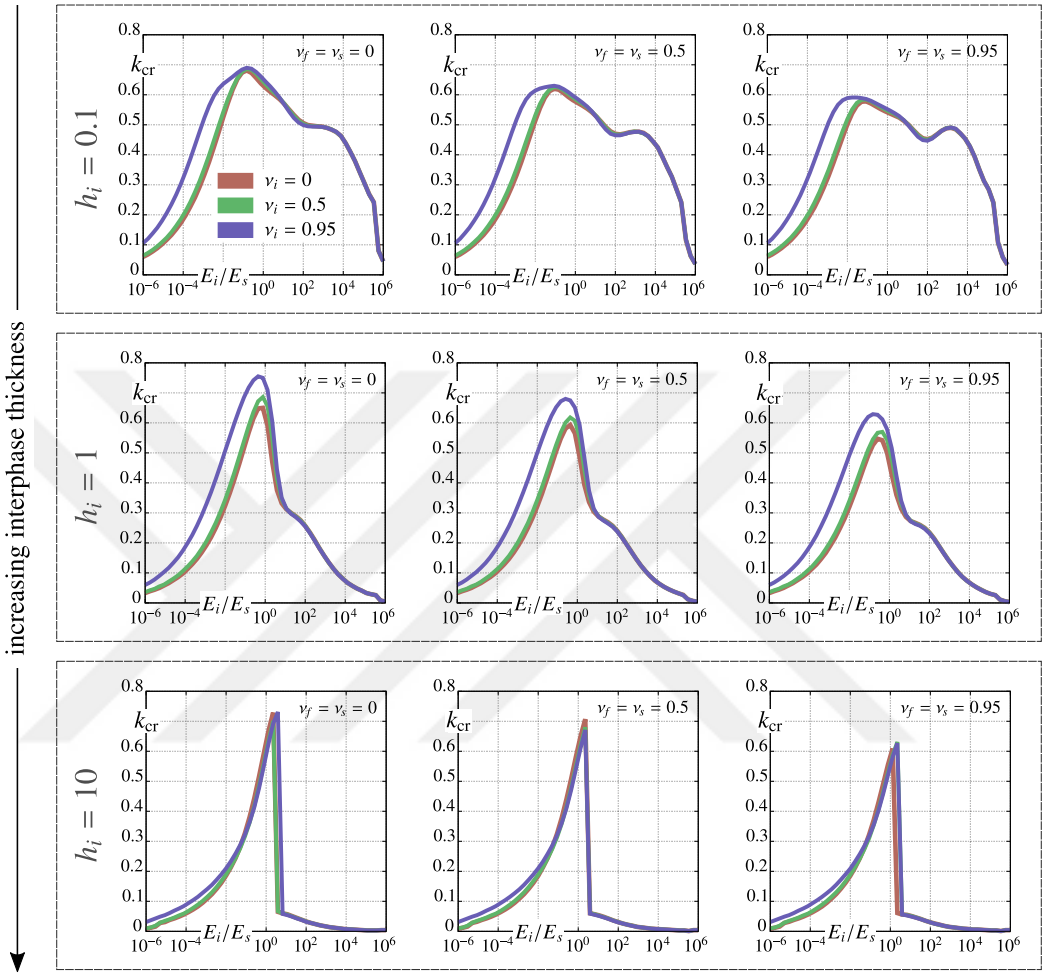


Figure 4.22: The effect of compressibility on the critical wavenumber k_{cr} vs. E_i/E_s, calculated for a set of Poisson's ratios and interphase thickness $h_i = 0.1$, 1 and 100, for $E_f/E_s = 10$.

seems to become less significant as interphase height is increased. Furthermore, the previously observed sharp transition from a "short-wave" mode into a "long-wave" mode is observed here when $h_i = 10$ (bottom row). The stiffness ratio E_i/E_s at which this mode-transition occurs seems to be affected very little by changing compressibility.

A crucial and key element of the theoretical formulation developed herein is that both modes can be captured analytically by a single-part solution, as opposed to the two-part solution developed in [107]; which allows for us to understand that the two-mode behavior is actually a part of a larger, continuous solution. The

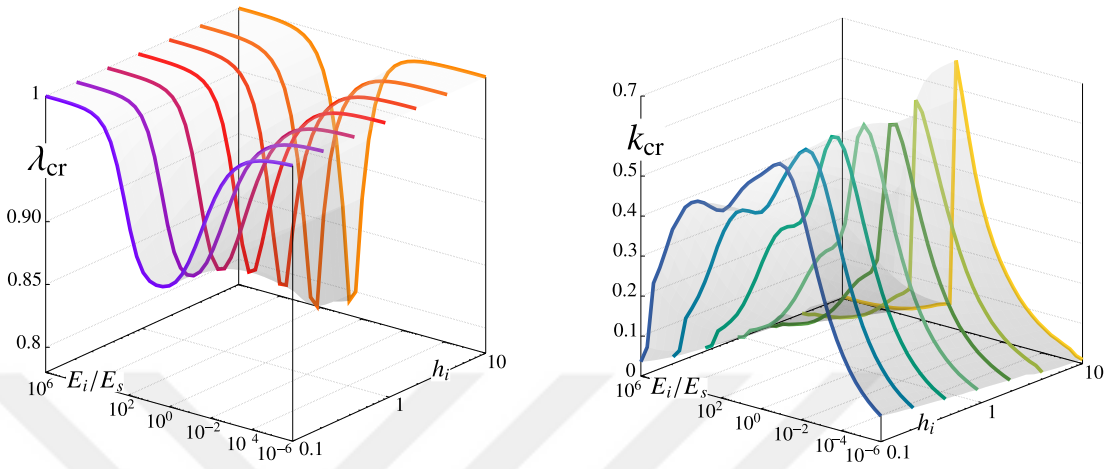


Figure 4.23: The effect of interphase thickness h_i and interphase-to-substrate stiffness ratio E_i/E_s on critical stretch λ_{cr} (top) and critical wavenumber k_{cr} (bottom).

continuity and versatility of the solution developed herein is further emphasized in Fig. 4.23, where critical stretch λ_{cr} and critical wavenumber k_{cr} are displayed with respect to stiffness ratio E_i/E_s and interphase thickness h_i. The whole range of thicknesses between $h_i = 0.1$ and $h_i = 10$ are studied, where $h_f = 1$, $E_f/E_s = 10$, and $\nu_f = \nu_i = \nu_s = 0.5$. It can be seen that the two-peak shape of the critical wavenumber k_{cr} curve transitions into the well-known two-mode solution, as the critical stretch λ_{cr} transitions into its sharp peak shape. Looking at the theoretical results, there seems to be no single "parameter" or set of parameters at which the two-mode transition occurs; rather than that, the problem gradually transforms itself into the two-mode solution as interphase thickness increases.

Furthermore, the two modes themselves can be captured by the single theoretical solution developed here, as elucidated further in Fig. 4.24. The left inset of Fig. 4.24 shows the bifurcation curves where the wavenumber k which renders the largest critical stretch, i.e. occurs at the smallest amount of compression, is used to determine the point of bifurcation of the system. Each curve here is the bifurcation curve for a different E_i/E_s in the range $1 \leq E_i/E_s \leq 10$. The transition here for these set of parameters is between $E_i/E_s = 3$ and $E_i/E_s = 4$; as the bifurcation curve slowly transforms as E_i/E_s is increased, between $E_i/E_s = 3$ and $E_i/E_s = 4$, the maximum, i.e. the bifurcation point, shifts. The right inset of

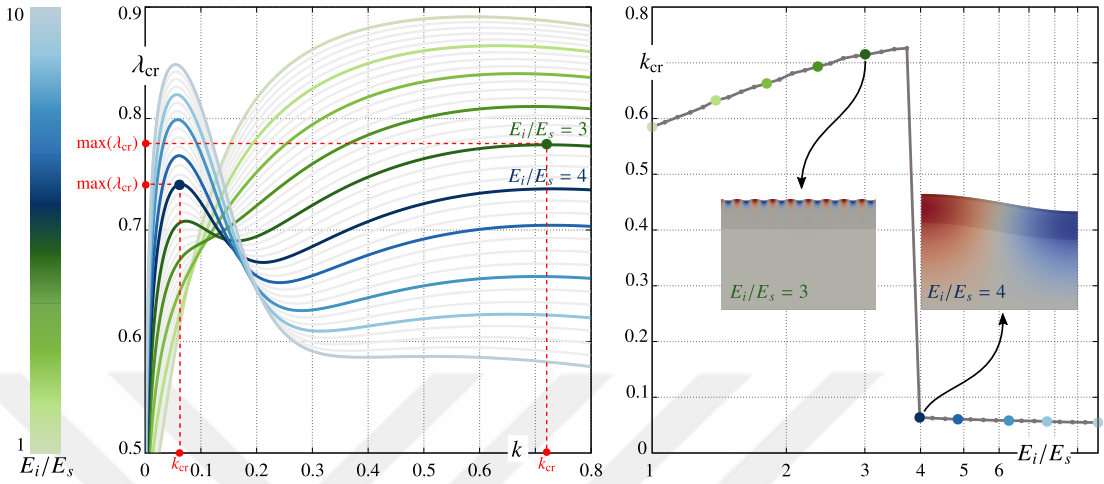


Figure 4.24: A close-up on the range of E_i/E_s over which mode switching occurs in the trilayer structure with $h_f = 1$, $h_i = 10$, $E_f/E_s = 10$, and $\nu_f = \nu_s = 0$, $\nu_i = 0.95$, demonstrating the bifurcation curves (left) and the resultant k_{cr} vs. E_i/E_s (right).

Fig. 4.24 shows the k_{cr} findings for the chosen range of E_i/E_s. For $E_i/E_s < 4$ the short-wave mode is preferred; this mode is pictured through numerical findings. The short-wave mode is fundamentally the wrinkling of the film, on top of the interphase and substrate. Note that the short-wave mode does not mean that only the film is wrinkling, but it rather means that the wrinkling decays quickly through the depth of the structure. Similarly, the long-wave mode which we see here for $E_i/E_s > 4$ can be seen in the drawing obtained from numerical findings, is similar to the "whole structure" buckling.

Finally, the displacement profiles of the wrinkled configuration of the trilayer domain are elucidated in Fig. 4.25. Here, the deformation patterns seen in the wrinkled trilayer structure with interphase thickness $h_i = 0.1$ (top) and $h_i = 10$ (bottom) have been obtained from the analytical formulation derived herein, and using the proposed incremental displacements functions for each domain, for compressibility $\nu_f = \nu_i = \nu_s = 0.95$, $E_f/E_s = 10$ and $h_f = 1$. The inset A (top) illustrates clearly the effect of an interphase layer between the film and the substrate. In this case, $E_i/E_s = 10^{-4}$, hence the interphase layer is much more compliant than the substrate, which results in a strain-isolation behavior that is crucial in the design of flexible electronics [28] and cannot be achieved with a

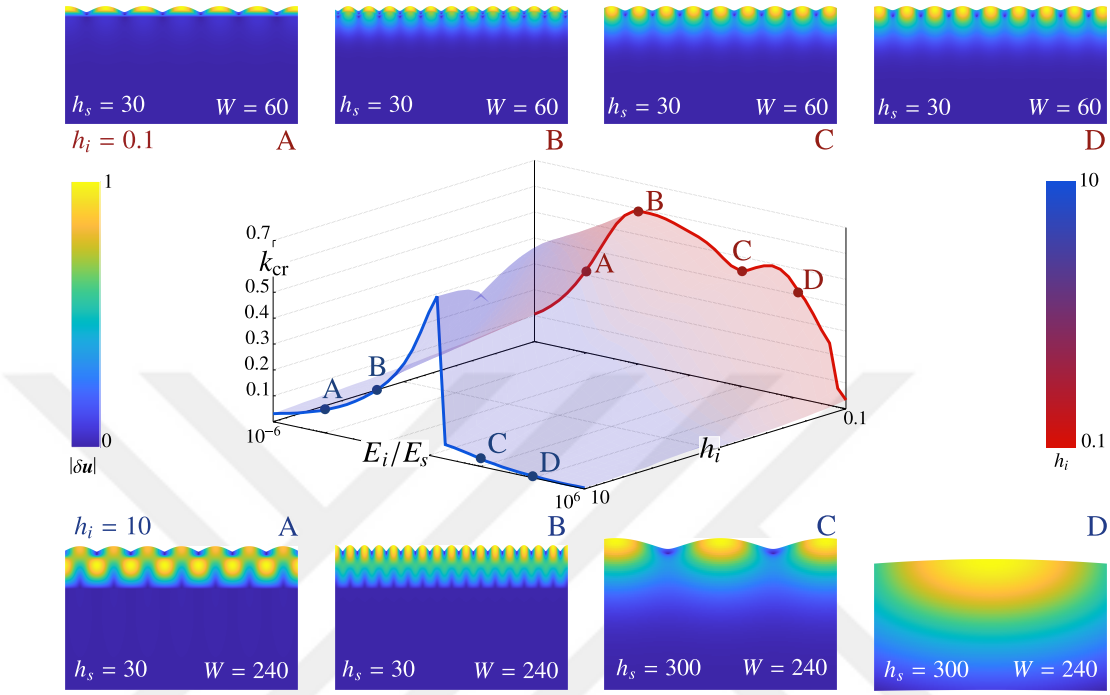


Figure 4.25: Incremental displacement profiles over a range of E_i/E_s, for $h_i = 0.1$ (top) and $h_i = 10$ (bottom), and $h_f = 1$, $E_f/E_s = 10$, and $\nu_f = \nu_i = \nu_s = 0.95$.

classical bilayer structure. In other words, the displacements in the film due to wrinkling decay through the interphase, before reaching the substrate; hence, in common applications where the film is metal and the substrate is a polymer, this intermediate layer facilitates better adhesion and compatibility between the two. As the interphase layer becomes less compliant, the incremental displacements can be seen to travel further down the substrate. The bottom row visualizes the two-mode wrinkling behavior captured here, with interphase thickness $h_i = 10$. For the short-wave mode, shown in insets A and B (bottom), the displacements also decay along the interphase until they reach the substrate. For the long-wave mode, however, the substrate thickness which was ideally imposed as infinitely long in our analytical solution because of the half-space boundary condition, needs to be increased such that the displacement profile has "enough thickness" to decay through. Accordingly, for the parameters given in C and D (bottom), if substrate thickness was to be reduced such that displacements are not allowed to fully decay, a global buckling behavior in the structure would be observed.

Chapter 5

Finite strain instabilities with interfacial mechanics

It is well established where more than one material is concerned, there always exists an interphase region between different constituents whose mechanical modeling has presented itself as a long lasting challenge. To address these gaps in the literature, this chapter incorporates the general interface model into the generic framework developed so far. The general interface model combines the cohesive and elastic interface models allowing for both jumps in the displacement and traction fields. The formulation of generalized interfaces in a variationally consistent manner for finite deformations [128] will serve as the basis of the interface analysis in this work. To this extent, first off the different interface models are shortly summarized in Section 5.1. In Section 5.2, the governing equations in Chapter 2 and theoretical framework formulated in Section 4.1 for the bulk are first briefly summarized and then their surface counterparts are formulated. Subsequently, the developed framework will be applied to explore coated half-space, coated beam and bilayer with interface structures.

5.1 Interface models

Figure 5.1 outlines schematically the four categories under which interface models can be grouped depending on the continuity of the displacement and traction fields, briefly reviewed below. For further details on the analytical and computational aspects of the works done on each model, applications of interfaces in composites, and extensions to more sophisticated interface models, see [126].

- *The perfect interface model* refers to the trivial interfaces in which both the displacement and traction are continuous across the interface, and is also referred to as free singular surfaces [189]. Since this assumption of continuity in both fields is the most elementary one, it is referred to as the "perfect model", and all other subsequent models with discontinuities are thus referred to as "imperfect models".

- *The cohesive (spring-type) interface model* is a type of imperfect interface model in which displacement jumps are allowed for but the traction across the interface is assumed to be continuous. The seminal works on the topic include those of Barenblatt [190, 191] and Dugdale [192], while the model has found applications in peeling [193], delamination [194–196], debonding [197], fracture [198, 199] and crack growth [200–203], along with computational implementations [204, 205].

- *The elastic (stress-type) interface model* allows for a traction jump across the interface, while assuming that the displacement field remains continuous. Also identified as thermodynamic singular surfaces [189], the traction jump across this interface model is a result of the tension along the interface together with the curvature and relates to the generalized Young–Laplace equation [103, 206], and has roots in the surface elasticity theory of Gurtin and Murdoch [101]. Interface elasticity theory [207, 208] has been further extended in [102, 209] among others.

- *The general interface model* combines the cohesive and elastic interface models, allowing for both jumps in the displacement and traction fields.

Contrary to the previous models, this model is more recent and has been studied in a few works, for instance in [133, 210–213], and further extended in [126]. While the cohesive interface model is formulated as the asymptotic limit of a thin "soft" interphase, and the elastic interface model as the limit of a thin "stiff" interphase, the general interface model encompasses the whole range. The formulation of generalized interfaces in a variationally consistent manner for finite deformations [128] will serve as the basis of the interface analysis in this work.

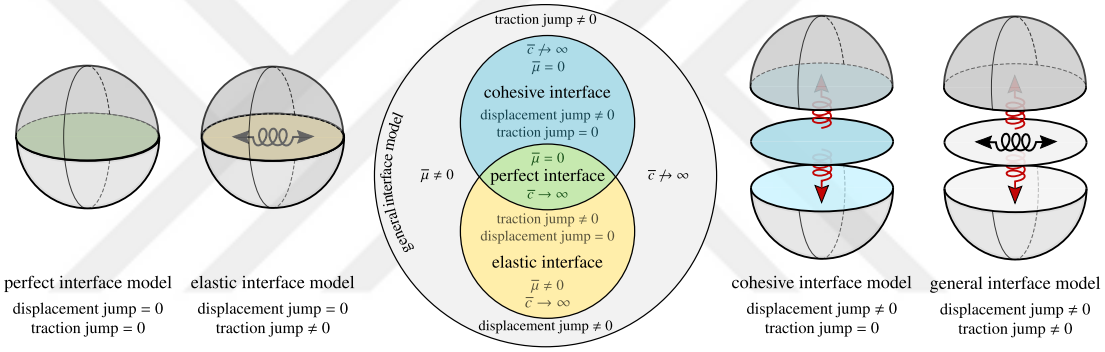


Figure 5.1: The four groups of interface models categorized by field jump conditions, namely as the perfect, elastic, cohesive and general interface models, where $\overline{\mu}$ is a surface elasticity parameter, and $\overline{c}$ is the cohesive stiffness parameter.

5.2 Theoretical framework

The material and spatial configurations of a continuum body with an interface is depicted in Fig. 5.2 showing a continuum body that initially takes the material configuration $\mathcal{B}_0 \in \mathbb{R}^3$ at time $t = 0$ with $\boldsymbol{X}$ denoting the reference placement of particles of the bulk in this configuration. The bulk of the material configuration is mapped to its spatial configuration $\mathcal{B}_t \in \mathbb{R}^3$ at a time t via the nonlinear deformation map $\boldsymbol{\varphi}$ according to $\boldsymbol{x} = \boldsymbol{\varphi}(\boldsymbol{X}, t)$ with $\boldsymbol{x}$ denoting the current placement of particles in the spatial configuration. The particles on the interface are mapped from their material configuration $\mathcal{I}_0$ to their spatial configuration $\mathcal{I}_t$ through the mapping

$$\overline{\boldsymbol{x}} = \overline{\boldsymbol{\varphi}}(\overline{\boldsymbol{X}}, t) \qquad \text{where} \qquad \overline{\boldsymbol{\varphi}} = \{\!\{\boldsymbol{\varphi}\}\!\}\,. \tag{5.1}$$

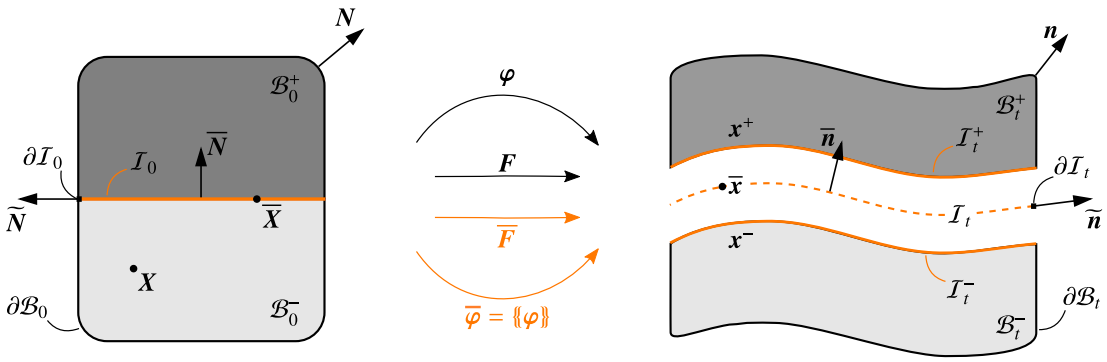


Figure 5.2: The deformation of a continuum body which occupies the material configuration $\mathcal{B}_0 \subset \mathbb{R}^3$ at time $t = 0$ that is mapped to the spatial configuration $\mathcal{B}_t \subset \mathbb{R}^3$ at any time $t > 0$ via the nonlinear deformation map $\boldsymbol{\varphi}$. The two sides of the body in the material configuration intersect at the interface $\mathcal{I}_0$. The interface is a zero-thickness layer that divides the bulk into the two parts $\mathcal{B}_0^-$ and $\mathcal{B}_0^+$ initially with $[\![\boldsymbol{X}]\!] = \boldsymbol{0}$, which through the mapping $\boldsymbol{\varphi}$ opens up, creating a displacement jump across the interface such that $[\![\boldsymbol{x}]\!] \neq \boldsymbol{0}$ is allowed for.

The projection of the identity tensor $\boldsymbol{I}$ onto the interface renders the interface identity tensor $\overline{\boldsymbol{I}} = \boldsymbol{I} - \overline{\boldsymbol{N}} \otimes \overline{\boldsymbol{N}}$, where $\overline{\boldsymbol{N}}$ is the unit normal to the interface in the material configuration, pointing from the minus side to the plus side of the interface, whereas $\overline{\boldsymbol{n}}$ denotes its spatial counterpart. The deformation gradient for material points in the bulk is defined once again as $\boldsymbol{F} := \mathrm{Grad}\boldsymbol{\varphi}$. The interfacial counterpart of deformation gradient, $\overline{\boldsymbol{F}}$, can be obtained by projecting $\mathrm{Grad}\overline{\boldsymbol{\varphi}}$ onto the interface, i.e. $\overline{\boldsymbol{F}} = \mathrm{Grad}\overline{\boldsymbol{\varphi}} \cdot \overline{\boldsymbol{I}}$, which can also be expressed via relation (5.1) as $\overline{\boldsymbol{F}} = \mathrm{Grad}(\{\!\{\boldsymbol{\varphi}\}\!\}) \cdot \overline{\boldsymbol{I}} = \{\!\{\mathrm{Grad}(\boldsymbol{\varphi})\}\!\} \cdot \overline{\boldsymbol{I}} = \{\!\{\boldsymbol{F}\}\!\} \cdot \overline{\boldsymbol{I}}$. For the problem at hand for a uni-axial tension/compression under plane-strain constraints, the deformation gradient reads $\boldsymbol{F} = \mathrm{Diag}(\lambda\,, \eta, 1)$, with λ and η being the horizontal and vertical stretches, and its interfacial counterpart can be constructed via $\overline{\boldsymbol{F}} = \boldsymbol{F} \cdot \overline{\boldsymbol{I}}$, since both parts of the domain undergo the same applied stretch $\lambda = \lambda_f = \lambda_s$. Recall that in the absence of body forces, quasi-static large-deformation continuum mechanics is governed by the fundamental equilibrium equation $\mathrm{Div}\boldsymbol{P} = \boldsymbol{0}$ in $\mathcal{B}_0$. On the other hand, in the absence of interface force densities, the interface balance equations [128] read

$$\overline{\mathrm{Div}}\,\overline{\boldsymbol{P}} + [\![\boldsymbol{P}]\!] \cdot \overline{\boldsymbol{N}} = \boldsymbol{0} \text{ on } \mathcal{I}_0 \text{ (along) and } \overline{\boldsymbol{t}} - \{\!\{\boldsymbol{P}\}\!\} \cdot \overline{\boldsymbol{N}} = \boldsymbol{0} \text{ on } \mathcal{I}_0 \text{ (across)}\,. \quad (5.2)$$

It should be noted that in the case where the stress along the interface $\overline{\boldsymbol{P}} = \boldsymbol{0}$, the balance equation $(5.2)_1$ reduces to $[\![\boldsymbol{P}]\!] \cdot \overline{\boldsymbol{N}} = \boldsymbol{0}$, which can also be written as the sum of tractions across the interface set to zero, ensuring traction continuity, i.e. $\sum \boldsymbol{P} \cdot \boldsymbol{N} = \boldsymbol{0}$.

Once again, the behavior of the hyperelastic domain here will be modeled via a compressible neo-Hookean model [180] with the polyconvex free energy density

$$\psi(\boldsymbol{F}) = \tfrac{1}{2}\,\mu\,[\boldsymbol{F} : \boldsymbol{F} - 3 - 2\ln J] + 2\,\mu\,\alpha\,[\,\tfrac{1}{4}\,[J^2 - 1] - \tfrac{1}{2}\,\ln J\,]\,. \tag{5.3}$$

The interface counterpart of the free energy density $\overline{\psi}$ as a function of interface deformation gradient $\overline{\boldsymbol{F}}$ and interface displacement jump $\overline{\boldsymbol{f}} := [\![\boldsymbol{x}]\!]$ is

$$\overline{\psi}(\overline{\boldsymbol{F}}, \overline{\boldsymbol{f}}) = \tfrac{1}{2}\,\overline{\mu}\,\left[\overline{\boldsymbol{F}} : \overline{\boldsymbol{F}} - 2 - 2\ln \overline{J}\right] + \tfrac{1}{2}\,\overline{\Lambda}[\,\tfrac{1}{2}\,[\overline{J}^2 - 1] - \ln \overline{J}\,] + \tfrac{1}{2}\,\overline{c}\,\overline{\boldsymbol{f}} \cdot \overline{\boldsymbol{f}}\,, \tag{5.4}$$

with $\overline{J} := \overline{\mathrm{Det}\boldsymbol{F}}$, and where $\overline{\mu}$ and $\overline{\Lambda}$ are interface material parameters which correspond to the in-plane interface response. Both $\overline{\mu}$ and $\overline{\Lambda}$ can be referred to as interface Lamé parameters, with units of N/m. The parameter $\overline{c}$ is indicative of the resistance of the interface to opening, hence relating to the orthogonal stiffness of the interface, having the unit of $\mathrm{N/m^3}$. For the following formulations, we set $\overline{\Lambda} = 0$ without loss of generality and work only with $\overline{\mu}$, since in the 2D setting here both of these parameters serve the same purpose of relating to the resistance of the interface to a change in length along the interface. Clearly, the perfect interface model is recovered when $\overline{\mu} \to 0$ and $\overline{c} \to \infty$. Recall that the Piola stress that derives from the free energy (2.11) reads

$$\boldsymbol{P} := \frac{\partial \psi}{\partial \boldsymbol{F}} = \mu\,[\,\boldsymbol{F} - \boldsymbol{F}^{-t}\,] + \mu\,\alpha\,[\,J^{\,2} - 1\,]\,\boldsymbol{F}^{-t}\,, \tag{5.5}$$

whereas its interfacial counterparts are

$$\overline{\boldsymbol{P}} := \frac{\partial \overline{\psi}}{\partial \overline{\boldsymbol{F}}} = \overline{\mu}\,[\,\overline{\boldsymbol{F}} - \overline{\boldsymbol{F}}^{\text{-t}}\,] \qquad \text{and} \qquad \overline{\boldsymbol{t}} = \frac{\partial \overline{\psi}}{\partial \overline{\boldsymbol{f}}} = \overline{c}\,\overline{\boldsymbol{f}}\,. \tag{5.6}$$

We now proceed with the incremental approach to study the instabilities of the bulk of the domain and the surface. The incremental balance equations of the

bulk follow exactly those formulated in Section 4.1 and will not be repeated here for the sake of brevity. We first need to formulate the incremental counterparts of the interface balance equations (5.2), which read

$$\begin{aligned} &\overline{\mathrm{Div}}\,\delta\overline{\boldsymbol{P}} + [\![\delta\boldsymbol{P}]\!]\cdot\overline{\boldsymbol{N}} = \boldsymbol{0} \qquad &&\text{on} \qquad \mathcal{I}_0\ (\text{along})\,, \\ &\delta\overline{\boldsymbol{t}} - \{\!\{\delta\boldsymbol{P}\}\!\}\cdot\overline{\boldsymbol{N}} = \boldsymbol{0} \qquad &&\text{on} \qquad \mathcal{I}_0\ (\text{across})\,. \end{aligned} \tag{5.7}$$

In order to evaluate (5.7), we need to derive the interface counterpart of the incremental Piola stress (4.7), which can be obtained through

$$\delta\overline{\boldsymbol{P}} = \frac{\partial\overline{\boldsymbol{P}}}{\partial\overline{\boldsymbol{F}}} : \delta\overline{\boldsymbol{F}} = \overline{\mu}\,[\,\overline{\mathbb{I}} - \overline{\mathbb{D}}\,] : \delta\overline{\boldsymbol{F}}\,, \tag{5.8}$$

where

$$\begin{aligned} \overline{\mathbb{I}} &:= \frac{\partial\overline{\boldsymbol{F}}}{\partial\overline{\boldsymbol{F}}} = \boldsymbol{i}\,\overline{\otimes}\,\overline{\boldsymbol{I}}\,, \\ \overline{\mathbb{D}} &:= \frac{\partial\overline{\boldsymbol{F}}^{-\mathrm{t}}}{\partial\overline{\boldsymbol{F}}} = -\overline{\boldsymbol{F}}^{-\mathrm{t}}\,\underline{\otimes}\,\overline{\boldsymbol{F}}^{-1} + [\,\overline{\boldsymbol{n}}\otimes\overline{\boldsymbol{n}}\,]\,\overline{\otimes}\,[\,\overline{\boldsymbol{F}}^{-1}\cdot\overline{\boldsymbol{F}}^{-\mathrm{t}}\,]\,, \end{aligned} \tag{5.9}$$

and $\overline{\boldsymbol{P}}$ is the Piola stress along the interface defined in (5.6). Accordingly, since $\overline{\mathbb{I}} : \delta\overline{\boldsymbol{F}} = \delta\overline{\boldsymbol{F}}$ the interfacial counterpart of the incremental Piola stress in Eq. (4.7) can be written as

$$\delta\overline{\boldsymbol{P}} = \overline{\mu}\,\delta\overline{\boldsymbol{F}} + \overline{\mu}\,\overline{\boldsymbol{F}}^{-\mathrm{t}}\cdot\delta\overline{\boldsymbol{F}}^{\mathrm{t}}\cdot\overline{\boldsymbol{F}}^{-\mathrm{t}} - \overline{\mu}\,\frac{1}{\lambda^2}\,\delta\overline{\boldsymbol{F}} : [\,\overline{\boldsymbol{n}}\otimes\boldsymbol{e}_\xi\,]\,\overline{\boldsymbol{n}}\otimes\boldsymbol{e}_\xi\,. \tag{5.10}$$

Note that unit tangents to the interface *prior to the onset of instability* in both the material and spatial configurations coincide with $\boldsymbol{e}_\xi$, since before wrinkling the interface remains flat. Similarly, unit normals to the *interface* prior to the onset of instability, $\overline{\boldsymbol{N}}$ and $\overline{\boldsymbol{n}}$ in the material and spatial configurations, respectively, coincide with $\boldsymbol{e}_\gamma$ pointing upwards. A similar approach can be taken to formulate the incremental interface deformation gradient $\delta\overline{\boldsymbol{F}} = \{\!\{\delta\boldsymbol{F}\}\!\}\cdot\overline{\boldsymbol{I}}$, which in matrix representation reads

$$[\,\delta\overline{\boldsymbol{F}}\,] = \frac{1}{2}\begin{bmatrix} \delta u_{f,\xi} + \delta u_{s,\xi} & \delta u_{f,\gamma} + \delta u_{s,\gamma} \\ \delta v_{f,\xi} + \delta v_{s,\xi} & \delta v_{f,\gamma} + \delta v_{s,\gamma} \end{bmatrix}\cdot\begin{bmatrix} 1 & 0 \\ 0 & 0 \end{bmatrix} = \frac{1}{2}\begin{bmatrix} \delta u_{f,\xi} + \delta u_{s,\xi} & 0 \\ \delta v_{f,\xi} + \delta v_{s,\xi} & 0 \end{bmatrix}. \tag{5.11}$$

It should be noted that the tensor $\delta\overline{\boldsymbol{F}}$ in Eq. (5.11) has been denoted in matrix notation wherein the basis vectors correspond to the material configuration. Though a matrix notation is commonly accepted to express rank-sufficient tensors, it proves particularly problematic for rank-deficient tensors, such as $\delta\overline{\boldsymbol{F}}$ here, and therefore it results in a column of zeros associated with the derivatives with respect to the direction orthogonal to the interface. The incremental interface Piola stress (5.10) hence, after some mathematical simplifications, becomes

$$[\,\delta\overline{\boldsymbol{P}}\,] = \frac{\overline{\mu}}{2\lambda^2}\begin{bmatrix} [\,\lambda^2+1\,]\,\delta u_{f,\xi} + [\,\lambda^2+1\,]\,\delta u_{s,\xi} & 0 \\ [\,\lambda^2-1\,]\;\delta v_{f,\xi} + [\,\lambda^2-1\,]\,\delta v_{s,\xi} & 0 \end{bmatrix}. \tag{5.12}$$

Equipped with the interfacial incremental Piola stress relation, we can now return to the incremental interface balance equations (5.7) and we evaluate $\overline{\mathrm{Div}}\,\delta\overline{\boldsymbol{P}}$. The interface divergence operator indicates the divergence along the interface, which furnishes

$$\overline{\mathrm{Div}}\,\delta\overline{\boldsymbol{P}} = \frac{\overline{\mu}}{2\lambda^2}\begin{bmatrix} [\,\lambda^2+1\,]\,[\,\delta u_{f,\xi,\xi} + \delta u_{s,\xi,\xi}\,] \\ [\,\lambda^2-1\,]\,[\,\delta v_{f,\xi,\xi} + \delta v_{s,\xi,\xi}\,] \end{bmatrix}. \tag{5.13}$$

Using the updated forms of the incremental displacement functions and their partial derivatives, Eq. (5.13) can then be expressed concisely as

$$\begin{aligned}\overline{\mathrm{Div}}\,\delta\overline{\boldsymbol{P}} = \frac{\overline{\mu}}{2}\Big[\, & k_f^2\,\boldsymbol{T}_f\,{}^{\frac{1}{2}}\boldsymbol{M}_f\,{}^{\frac{1}{2}}\boldsymbol{E}_f(\gamma)\,{}^{\frac{1}{2}}\boldsymbol{B}_f + k_f^2\,\boldsymbol{T}_f\,{}^{\frac{3}{4}}\boldsymbol{M}_f\,{}^{\frac{3}{4}}\boldsymbol{E}_f(\gamma)\,{}^{\frac{3}{4}}\boldsymbol{B}_f \\ & + k_s^2\,\boldsymbol{T}_s\,{}^{\frac{1}{2}}\boldsymbol{M}_s\,{}^{\frac{1}{2}}\boldsymbol{E}_s(\gamma)\,{}^{\frac{1}{2}}\boldsymbol{B}_s + k_s^2\,\boldsymbol{T}_s\,{}^{\frac{3}{4}}\boldsymbol{M}_s\,{}^{\frac{3}{4}}\boldsymbol{E}_s(\gamma)\,{}^{\frac{3}{4}}\boldsymbol{B}_s\Big],\end{aligned} \tag{5.14}$$

where

$$\boldsymbol{T}_f = \begin{bmatrix} \sin(k_f\,\xi) & 0 \\ 0 & \cos(k_f\,\xi) \end{bmatrix}, \quad \boldsymbol{T}_s = \begin{bmatrix} \sin(k_s\,\xi) & 0 \\ 0 & \cos(k_s\,\xi) \end{bmatrix}, \tag{5.15}$$

with

$$\begin{aligned} {}^{\frac{1}{2}}\boldsymbol{E}_f(\gamma) &:= \begin{bmatrix} \exp(k_f\gamma) & 0 \\ 0 & \exp(k_f\sqrt{\rho_f}\,\gamma) \end{bmatrix}, \\ {}^{\frac{3}{4}}\boldsymbol{E}_f(\gamma) &:= \begin{bmatrix} \exp(-k_f\gamma) & 0 \\ 0 & \exp(-k_f\sqrt{\rho_f}\,\gamma) \end{bmatrix}, \end{aligned} \tag{5.16}$$

and

$$
\begin{aligned}
{}^{1}_{2}\boldsymbol{E}_s(\gamma) &:= \begin{bmatrix} \exp(k_s\gamma) & 0 \\ 0 & \exp(k_s\sqrt{\rho_s}\,\gamma) \end{bmatrix}, \\
{}^{3}_{4}\boldsymbol{E}_s(\gamma) &:= \begin{bmatrix} \exp(-k_s\gamma) & 0 \\ 0 & \exp(-k_s\sqrt{\rho_s}\gamma) \end{bmatrix},
\end{aligned}
\tag{5.17}
$$

and with

$$
\begin{aligned}
{}^{1}_{2}\boldsymbol{M}_f &= \begin{bmatrix} [\,\lambda^2+1\,]\,\dfrac{1}{\lambda\eta_f} & [\,\lambda^2+1\,]\,\dfrac{\theta_f}{\lambda^3\,\eta_f} \\ -\dfrac{[\,\lambda^2-1\,]}{\lambda^2} & -\dfrac{[\,\lambda^2-1\,]}{\lambda^2} \end{bmatrix}, \quad {}^{1}_{2}\boldsymbol{B}_f = \begin{bmatrix} {}^{1}B_f \\ {}^{2}B_f \end{bmatrix}, \\
{}^{3}_{4}\boldsymbol{M}_f &= \begin{bmatrix} -[\,\lambda^2+1\,]\,\dfrac{1}{\lambda\eta_f} & -[\,\lambda^2+1\,]\,\dfrac{\theta_f}{\lambda^3\,\eta_f} \\ -\dfrac{[\,\lambda^2-1\,]}{\lambda^2} & -\dfrac{[\,\lambda^2-1\,]}{\lambda^2} \end{bmatrix}, \quad {}^{3}_{4}\boldsymbol{B}_f = \begin{bmatrix} {}^{3}B_f \\ {}^{4}B_f \end{bmatrix}, \\
{}^{1}_{2}\boldsymbol{M}_s &= \begin{bmatrix} [\,\lambda^2+1\,]\,\dfrac{1}{\lambda\eta_s} & [\,\lambda^2+1\,]\,\dfrac{\theta_s}{\lambda^3\,\eta_s} \\ -\dfrac{[\,\lambda^2-1\,]}{\lambda^2} & -\dfrac{[\,\lambda^2-1\,]}{\lambda^2} \end{bmatrix}, \quad {}^{1}_{2}\boldsymbol{B}_s = \begin{bmatrix} {}^{1}B_s \\ {}^{2}B_s \end{bmatrix}, \\
{}^{3}_{4}\boldsymbol{M}_s &= \begin{bmatrix} -[\,\lambda^2+1\,]\,\dfrac{1}{\lambda\eta_s} & -[\,\lambda^2+1\,]\,\dfrac{\theta_s}{\lambda^3\,\eta_s} \\ -\dfrac{[\,\lambda^2-1\,]}{\lambda^2} & -\dfrac{[\,\lambda^2-1\,]}{\lambda^2} \end{bmatrix}, \quad {}^{3}_{4}\boldsymbol{B}_s = \begin{bmatrix} {}^{3}B_s \\ {}^{4}B_s \end{bmatrix}.
\end{aligned}
\tag{5.18}
$$

Finally, the remaining unknown coefficients B_1, B_2, B_3, and B_4 need to be solved for by imposing the displacement and traction boundary conditions of the problem at hand, since until this point, the derivations have been generic and independent of the dimensions and boundary conditions of the rectangular domain. The traction increment at an outer surface of the rectangular domain is dictated by the relation $\delta\boldsymbol{t} = \delta\boldsymbol{P}\cdot\boldsymbol{N}$; resulting in

$$
\delta\boldsymbol{t} = -\mu\,k\,\boldsymbol{T}\,{}^{1}_{2}\boldsymbol{W}\,{}^{1}_{2}\boldsymbol{E}(\gamma)\,{}^{1}_{2}\boldsymbol{B} + \mu\,k\,\boldsymbol{T}\,{}^{3}_{4}\boldsymbol{W}\,{}^{3}_{4}\boldsymbol{E}(\gamma)\,{}^{3}_{4}\boldsymbol{B}\,,
\tag{5.19}
$$

where

$$
-\,{}^{1}_{2}\boldsymbol{W} := \begin{bmatrix} -\dfrac{\lambda}{\eta} - D\,\lambda\,\eta & -\sqrt{\rho}\,\dfrac{\theta}{\lambda\eta} - D\,\lambda\,\eta \\ [1 + D\lambda^2] & \sqrt{\rho}\,[1+\omega\,\lambda^2] - 2\,\alpha\,\theta \end{bmatrix},
\tag{5.20}
$$

and

$$ {}^{3}_{4}\boldsymbol{W} := \begin{bmatrix} -\dfrac{\lambda}{\eta} - D\,\lambda\,\eta & -\sqrt{\rho}\,\dfrac{\theta}{\lambda\eta} - D\,\lambda\,\eta \\ -[1 + D\,\lambda^2] & -\sqrt{\rho}\,[1 + \omega\,\lambda^2] + 2\,\alpha\,\theta \end{bmatrix}, \tag{5.21} $$

in which $\omega := D + 2\alpha = 1/J^{\,2} + \alpha + \alpha/J^{\,2}$ and $D := 1/J^{\,2} - \alpha + \alpha/J^{\,2}$. Similarly, the interface boundary conditions, according to the interface model, can be applied using the derived forms of the incremental balance equations (5.7).

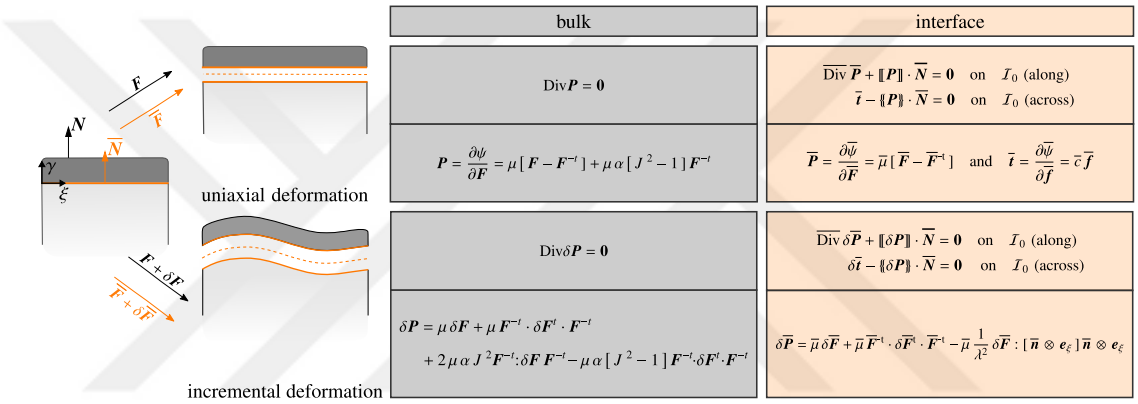


Figure 5.3: Table summarizing the key concepts and relations of the approach developed here.

This concludes the generic part of the incremental instability analysis, and the derived relations for the bulk and interface, together with their incremental counterparts have been summarized in Fig. 5.3. The upcoming sections particularize the generic approach for the case of a coated half-space, coated beam, and finally a bilayer structure with a general interface model, via imposing the appropriate (boundary) conditions. Figure 5.4 briefly outlines and collects together these boundary conditions applied for the domains considered in this contribution, together with the boundary conditions for limit cases that can be found in literature with no interface and at the incompressible limit. This hierarchical structure elucidates the universality of the framework developed here accounting for (i) the compressibility of the domains and (ii) the general interface model.

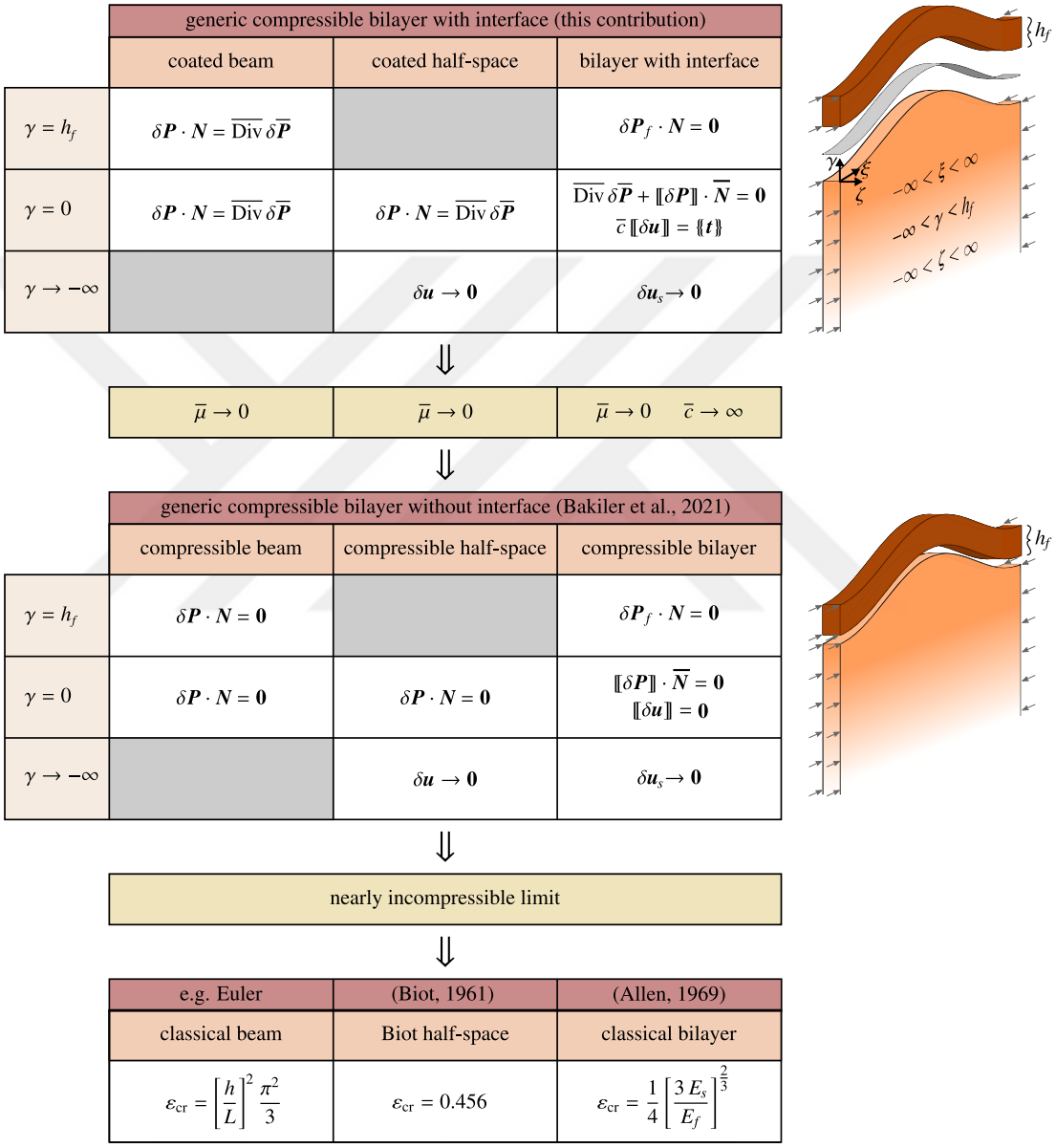


Figure 5.4: Summarizing the boundary conditions applied for the domains considered here, namely for a coated beam, coated half-space, and bilayer with interface, together with the boundary conditions for limit cases of no interfacial effects and at incompressibility. This hierarchical structure elucidates the universality of the framework developed here accounting for (i) the compressibility of the domains and (ii) the general interface model.

5.3 Coated half-space instability

This section particularizes the framework in Section 5.2 to examine the bifurcation behavior of a coated half-space. We start off by imposing that the domain is a half-space, which dictates that the incremental displacements $\delta\boldsymbol{u}$ should decay as the domain depth $\gamma \to -\infty$. Imposing this condition yields the set of constants ${}^{\frac{3}{4}}\boldsymbol{B}$ to be zero, resulting in the incremental displacement profile of

$$\delta\boldsymbol{u} = \boldsymbol{T}^{\frac{1}{2}}\boldsymbol{G}^{\frac{1}{2}}\boldsymbol{E}(\gamma)^{\frac{1}{2}}\boldsymbol{B}\,. \tag{5.22}$$

The boundary on the top surface of the half-space is coated with an elastic interface or rather surface, resulting in

$$\delta\boldsymbol{P}\cdot\overline{\boldsymbol{N}}\Big|_{\gamma=0} = \overline{\mathrm{Div}}\,\delta\overline{\boldsymbol{P}}\,, \tag{5.23}$$

where $\overline{\mathrm{Div}}\,\delta\overline{\boldsymbol{P}}$ for the half-space reads

$$\overline{\mathrm{Div}}\,\delta\overline{\boldsymbol{P}} = k^2\,\overline{\mu}\,\boldsymbol{T}^{\frac{1}{2}}\boldsymbol{M}^{\frac{1}{2}}\boldsymbol{E}(\gamma)^{\frac{1}{2}}\boldsymbol{B}\,, \tag{5.24}$$

rendering the balance equation at $\gamma = 0$ to be

$$-\mu\,k\,\boldsymbol{T}^{\frac{1}{2}}\boldsymbol{W}^{\frac{1}{2}}\boldsymbol{B} = k^2\,\overline{\mu}\,\boldsymbol{T}^{\frac{1}{2}}\boldsymbol{M}^{\frac{1}{2}}\boldsymbol{B}\,. \tag{5.25}$$

Simplifying and rearranging (5.25) yields the final solution

$$\boldsymbol{Q}^{\frac{1}{2}}\boldsymbol{B} = \boldsymbol{0} \quad \text{where} \quad \boldsymbol{Q} := \left[\, f\,{}^{\frac{1}{2}}\boldsymbol{M} + {}^{\frac{1}{2}}\boldsymbol{W} \,\right] \quad \text{with} \quad f := k\,\frac{\overline{\mu}}{\mu}\,, \tag{5.26}$$

in which f has been defined as a dimensionless parameter for the sake of convenience. The system (5.26) can be solved via setting $\mathrm{Det}\,\boldsymbol{Q}\,(\,k\,,\,\lambda) \doteq 0$, and thus solving for the critical stretch λ_{cr}. This system is solved for a range of values of k, and the value of k which renders the highest λ_{cr}, hence the initial instability mode encountered when compressing a domain starting from the reference configuration $\lambda = 1$, and its corresponding wavenumber k_{cr} is sought for. In other words, $\lambda_{\mathrm{cr}} = \max\{\,\lambda\,|\,\mathrm{Det}\,\boldsymbol{Q}\,(\,k\,,\,\lambda) = 0\,,\,\forall\,k \in \mathbb{R}^+\,\}$.

At this point, it proves useful to look at certain limits of the obtained solution. For instance, $\overline{\mu} = 0$ renders the coating-free half-space solution, in other words,

$$\overline{\mu} = 0 \quad \Rightarrow \quad f = 0 \quad \Rightarrow \quad {}^{\frac{1}{2}}\boldsymbol{W}\,{}^{\frac{1}{2}}\boldsymbol{B} = \boldsymbol{0} \qquad \Rightarrow \qquad \mathrm{Det}\,{}^{\frac{1}{2}}\boldsymbol{W} \doteq 0\,, \tag{5.27}$$

which coincides with the findings in [31]. For the case that $\overline{\mu} \neq 0$, so in the presence of coating, there are two limits to be explored, namely (i) $k = 0$ and (ii) $k \to \infty$. It can be seen clearly that at $k = 0$, the defined parameter $f = 0$ once again, and the half-space solution is obtained. For the case of $k \to \infty$, we can see that Eq. (5.25) reduces to

$$k \to \infty \quad \Rightarrow \quad {}^{\frac{1}{2}}\boldsymbol{M}\,{}^{\frac{1}{2}}\boldsymbol{B} = \boldsymbol{0} \qquad \Rightarrow \qquad \mathrm{Det}\,{}^{\frac{1}{2}}\boldsymbol{M} \doteq 0\,, \tag{5.28}$$

which renders the condition

$$-\frac{[\lambda^2+1][\lambda^2-1]}{\lambda^3\,\eta} + \frac{\theta\,[\lambda^2+1][\lambda^2-1]}{\lambda^5\,\eta} \doteq 0\,, \tag{5.29}$$

or alternatively expressed as

$$-[\lambda^2+1][\lambda^2-1][\,\theta - \lambda^2\,] \doteq 0\,, \tag{5.30}$$

which clearly has one trivial root at $\lambda = 1$. To see if the expression (5.30) has another root, we insert the expression for θ and study its consequences. That is

$$\theta - \lambda^2 = \frac{\rho\,[1+\omega\lambda^2]-1}{\omega\sqrt{\rho}} - \lambda^2 = \frac{\eta^2 - \lambda^2\sqrt{\rho}}{\sqrt{\rho}} \quad \Rightarrow \quad \eta^2 - \lambda^2\sqrt{\rho} \doteq 0\,. \tag{5.31}$$

The term $\sqrt{\rho}$ can be simplified to

$$\sqrt{\rho} = \frac{\eta}{\lambda}\sqrt{\frac{\lambda^2+1+\alpha\lambda^2+\alpha}{\eta^2+1+\alpha\eta^2+\alpha}}\,, \tag{5.32}$$

which renders (5.31) to be

$$\eta - \lambda\sqrt{\frac{\lambda^2+1}{\eta^2+1}} \doteq 0 \quad \Rightarrow \quad \eta^2\,[\,\eta^2+1\,] = \lambda^2\,[\,\lambda^2+1\,]\,. \tag{5.33}$$

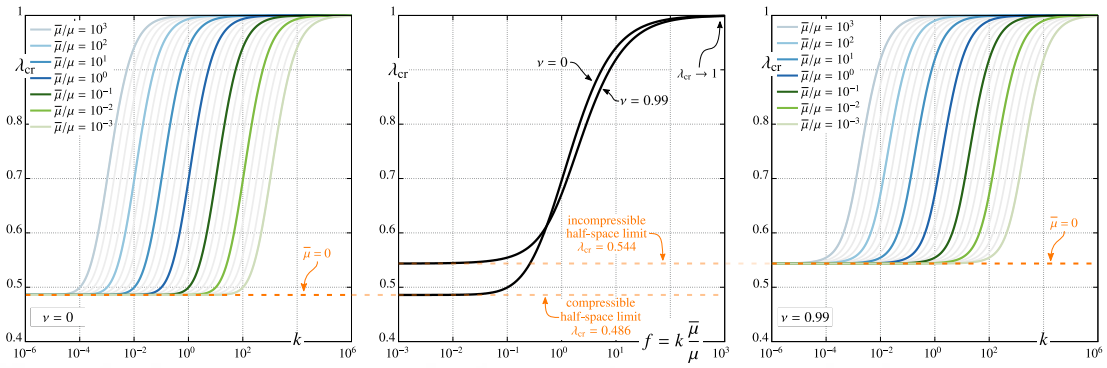


Figure 5.5: Bifurcation curves for a coated half-space, i.e. the solutions for the system $\mathrm{Det}\,\boldsymbol{Q}(k, \lambda) \doteq 0$ for λ_{cr} over changing wavenumber k for fully compressible (left) and nearly incompressible (right) half-space, and plotted against dimensionless parameter $f = k\,\overline{\mu}/\mu$ (center) for both $\nu = 0$ and $\nu = 0.99$. Again, note that the plane-strain definition of Poisson's ratio is employed. That is, excluding the auxetic regime, $0 \leq \nu < 1$, where $\nu = 0$ indicates full compressibility and $\nu \to 1$ indicates incompressibility. This plane-strain definition relates to its 3D counterpart such that $\nu_{\mathrm{3D}} = \nu/(1+\nu)$.

For the problem at hand, (i) $0 < \lambda \leq 1$, since we apply compression, (ii) $0 \leq \alpha < \infty$, for non-auxetic materials, which together, via Eq. (4.4), mean that (iii) $\eta \geq 1$. Given all of these, one can see that the expression (5.33) and more importantly (5.30) is *only* satisfied when $\lambda = \eta = 1$. Hence, we have shown that for any $\overline{\mu} \neq 0$, there exists always, and only, the solution $\lambda_{cr} = 1$ at $k \to \infty$, apart from the trivial solution. This outcome matches the findings of Steigmann and Ogden [97], and in other words means that unless surface elasticity is vanishing, a coated half-space, or rather the interface on top, will buckle with infinite wavenumber right at the start of compression. The limits of $k \to 0$ and $k \to \infty$ can also be seen in Fig. 5.5, where λ_{cr} has been plotted with respect to wavenumber k and the dimensionless parameter f for a fully compressible (left) and nearly-incompressible (right) half-space. When plotted against f, the bifurcation curves for all parameters $\overline{\mu}/\mu$ converge to a single curve. The bifurcation curves shown in Fig. 5.5 portray clearly that unless $\overline{\mu} = 0$, the first bifurcation mode encountered would be at $\lambda_{\mathrm{cr}} = 1$ and $k_{\mathrm{cr}} \to \infty$.

5.4 Coated beam instability

This section particularizes the framework developed in Section 5.2 to investigate the buckling of a coated beam, of length L and thickness h. First off, we need to define some of the interface quantities for the case of a coated beam, such as the incremental deformation gradient along the interface $\delta\overline{\boldsymbol{F}}$, which can be obtained via $\delta\overline{\boldsymbol{F}} = \{\!\!\{\delta\boldsymbol{F}\}\!\!\} \cdot \overline{\boldsymbol{I}}$ which for the case of a coated beam reads simply $\delta\overline{\boldsymbol{F}} = \delta\boldsymbol{F} \cdot \overline{\boldsymbol{I}}$, where

$$\delta\overline{\boldsymbol{F}} = \begin{bmatrix} \delta u_{,\xi} & 0 \\ \delta v_{,\xi} & 0 \end{bmatrix}. \tag{5.34}$$

Using the derived form of the interfacial incremental stress and particularizing it to the case of a coated beam,

$$\overline{\mathrm{Div}}\,\delta\overline{\boldsymbol{P}} = \frac{\overline{\mu}}{\lambda^2} \begin{bmatrix} [\,\lambda^2 + 1\,]\;\delta u_{,\xi,\xi} \\ [\,\lambda^2 - 1\,]\;\delta v_{,\xi,\xi} \end{bmatrix}, \tag{5.35}$$

which can be written as

$$\overline{\mathrm{Div}}\,\delta\overline{\boldsymbol{P}} = k^2\,\overline{\mu}\left[\boldsymbol{T}^{\frac{1}{2}}\boldsymbol{M}^{\frac{1}{2}}\boldsymbol{E}(\gamma)^{\frac{1}{2}}\boldsymbol{B} + \boldsymbol{T}^{\frac{3}{4}}\boldsymbol{M}^{\frac{3}{4}}\boldsymbol{E}(\gamma)^{\frac{3}{4}}\boldsymbol{B}\right]. \tag{5.36}$$

The boundary condition on the upper surface of the beam reads

$$\delta\boldsymbol{P}\cdot\boldsymbol{N}\Big|_{\gamma=h} = \overline{\mathrm{Div}}\,\delta\overline{\boldsymbol{P}}\,, \tag{5.37}$$

where the unit normal to the surface $\boldsymbol{N} = \boldsymbol{e}_\gamma$. Using the expression for incremental Piola stress in (5.37) results in

$$\begin{aligned} -\mu\,k\,\boldsymbol{T}^{\frac{1}{2}}\boldsymbol{W}^{\frac{1}{2}}\boldsymbol{E}(h_f)^{\frac{1}{2}}\boldsymbol{B} + \mu\,k\,\boldsymbol{T}^{\frac{3}{4}}\boldsymbol{W}^{\frac{3}{4}}\boldsymbol{E}(h_f)^{\frac{3}{4}}\boldsymbol{B} \\ = k^2\,\overline{\mu}\,\boldsymbol{T}^{\frac{1}{2}}\boldsymbol{M}^{\frac{1}{2}}\boldsymbol{E}(h_f)^{\frac{1}{2}}\boldsymbol{B} + k^2\,\overline{\mu}\,\boldsymbol{T}^{\frac{3}{4}}\boldsymbol{M}^{\frac{3}{4}}\boldsymbol{E}(h_f)^{\frac{3}{4}}\boldsymbol{B}\,, \end{aligned} \tag{5.38}$$

which when simplified yields

$$-{}^{\frac{1}{2}}\boldsymbol{W}^{\frac{1}{2}}\boldsymbol{E}(h_f)^{\frac{1}{2}}\boldsymbol{B} + {}^{\frac{3}{4}}\boldsymbol{W}^{\frac{3}{4}}\boldsymbol{E}(h_f)^{\frac{3}{4}}\boldsymbol{B} = f^{\frac{1}{2}}\boldsymbol{M}^{\frac{1}{2}}\boldsymbol{E}(h_f)^{\frac{1}{2}}\boldsymbol{B} + f^{\frac{3}{4}}\boldsymbol{M}^{\frac{3}{4}}\boldsymbol{E}(h_f)^{\frac{3}{4}}\boldsymbol{B}\,. \tag{5.39}$$

Moving to the bottom of the beam, the traction boundary condition at $\gamma = 0$ can be written as

$$\delta \boldsymbol{P} \cdot \boldsymbol{N}\Big|_{\gamma=0} = \overline{\mathrm{Div}}\, \delta \overline{\boldsymbol{P}}\,, \tag{5.40}$$

where the unit normal to the surface now reads $\boldsymbol{N} = -\boldsymbol{e}_\gamma$, leading to

$$\mu\, k\, \boldsymbol{T}\, {}^{\frac{1}{2}}\boldsymbol{W}\, {}^{\frac{1}{2}}\boldsymbol{B} - \mu\, k\, \boldsymbol{T}\, {}^{\frac{3}{4}}\boldsymbol{W}\, {}^{\frac{3}{4}}\boldsymbol{B} = k^2\, \overline{\mu}\, \boldsymbol{T}\, {}^{\frac{1}{2}}\boldsymbol{M}\, {}^{\frac{1}{2}}\boldsymbol{B} + k^2\, \overline{\mu}\, \boldsymbol{T}\, {}^{\frac{3}{4}}\boldsymbol{M}\, {}^{\frac{3}{4}}\boldsymbol{B}\,, \tag{5.41}$$

which can be simplified as

$${}^{\frac{1}{2}}\boldsymbol{W}\, {}^{\frac{1}{2}}\boldsymbol{B} - {}^{\frac{3}{4}}\boldsymbol{W}\, {}^{\frac{3}{4}}\boldsymbol{B} = f\, {}^{\frac{1}{2}}\boldsymbol{M}\, {}^{\frac{1}{2}}\boldsymbol{B} + f\, {}^{\frac{3}{4}}\boldsymbol{M}\, {}^{\frac{3}{4}}\boldsymbol{B}\,, \tag{5.42}$$

rendering the relation

$${}^{\frac{3}{4}}\boldsymbol{B} = \boldsymbol{b}\, {}^{\frac{1}{2}}\boldsymbol{B} \quad \text{with} \quad \boldsymbol{b} := \left[{}^{\frac{3}{4}}\boldsymbol{W} + f\, {}^{\frac{3}{4}}\boldsymbol{M} \right]^{-1} \left[{}^{\frac{1}{2}}\boldsymbol{W} - f\, {}^{\frac{1}{2}}\boldsymbol{M} \right]. \tag{5.43}$$

Once again, $f := k\overline{\mu}/\mu$ is defined as previously. Finally using the obtained relation (5.43) in the traction condition (5.39) results in

$$\left[{}^{\frac{1}{2}}\boldsymbol{W}\, {}^{\frac{1}{2}}\boldsymbol{E}(h_f) - {}^{\frac{3}{4}}\boldsymbol{W}\, {}^{\frac{3}{4}}\boldsymbol{E}(h_f)\, \boldsymbol{b} + f \left[{}^{\frac{1}{2}}\boldsymbol{M}\, {}^{\frac{1}{2}}\boldsymbol{E}(h_f) + {}^{\frac{3}{4}}\boldsymbol{M}\, {}^{\frac{3}{4}}\boldsymbol{E}(h_f)\, \boldsymbol{b} \right] \right] {}^{\frac{1}{2}}\boldsymbol{B} = \boldsymbol{0}\,, \tag{5.44}$$

which can be expressed as $\boldsymbol{Q}\, {}^{\frac{1}{2}}\boldsymbol{B}_f = \boldsymbol{0}$, too. The beam considered here is under a clamped-clamped boundary condition. Imposing this final boundary condition on the incremental displacement functions render

$$\begin{cases} \delta u\,|_{\xi=0} = \delta u\,|_{\xi=L} = 0 \quad \Rightarrow \quad \sin(k\,L) = 0 & \Rightarrow\ k = \dfrac{n\,\pi}{L}\,, \\ \delta v\,|_{\xi=0} = \delta v\,|_{\xi=L} \quad \Rightarrow \quad \cos(k\,0) = \cos(k\,L) & \Rightarrow\ k = \dfrac{2\,n\,\pi}{L}\,, \end{cases} \tag{5.45}$$

resulting in the wavenumber $k = 2\,n\,\pi/L$. Solving for the non-trivial solutions of Eq. (5.44) via setting the determinant of the coefficient matrix of ${}^{\frac{1}{2}}\boldsymbol{B}$ to zero, for λ at various values of n, and finding the wavenumber which would render the maximum stretch gives us the critical stretch λ_{cr} and the corresponding critical wavenumber k_{cr} at which bifurcation takes place.

Similar to the approach adopted in Section 5.3, looking at the limits of the developed solution proves useful. If there is no surface elasticity, i.e. if $f = 0$, then the solution converges to the beam solution that has been established previously in [31]. That is

$$\overline{\mu} = 0 \quad \Rightarrow \quad f = 0 \quad \Rightarrow \quad \left[{}^{\frac{1}{2}}\boldsymbol{W}\, {}^{\frac{1}{2}}\boldsymbol{E}(h_f) - {}^{\frac{3}{4}}\boldsymbol{W}\, {}^{\frac{3}{4}}\boldsymbol{E}(h_f)\, \boldsymbol{b} \right] {}^{\frac{1}{2}}\boldsymbol{B} = \boldsymbol{0}\,. \tag{5.46}$$

Since the solution is maximized with respect to wavenumber k, next we look at the behavior of the solution as $k \to \infty$, which renders $f \to \infty$ for all $\overline{\mu}/\mu$, yielding

$$k \to \infty \quad \Rightarrow \quad \frac{1}{f} \to 0 \quad \Rightarrow \quad \left[{}^{\frac{1}{2}}\boldsymbol{M}\, {}^{\frac{1}{2}}\boldsymbol{E}(h_f) + {}^{\frac{3}{4}}\boldsymbol{M}\, {}^{\frac{3}{4}}\boldsymbol{E}(h_f)\, \boldsymbol{b} \right] {}^{\frac{1}{2}}\boldsymbol{B} = \boldsymbol{0}\,. \tag{5.47}$$

It can be shown that the quantity defined as $\boldsymbol{b}$ is finite as $f \to \infty$. Furthermore, given the coefficients of decay in ${}^{\frac{1}{2}}\boldsymbol{E}(h_f)$ and ${}^{\frac{3}{4}}\boldsymbol{E}(h_f)$, positive and negative, respectively, as $f \to \infty$ the former increases without bounds, and the latter approaches $\boldsymbol{0}$. Thus, the expression (5.47) simplifies to

$${}^{\frac{1}{2}}\boldsymbol{M}\, {}^{\frac{1}{2}}\boldsymbol{E}(h_f)\, {}^{\frac{1}{2}}\boldsymbol{B} = \boldsymbol{0}\,, \tag{5.48}$$

the roots of which can clearly be obtained by solving for $\mathrm{Det}\, {}^{\frac{1}{2}}\boldsymbol{M} = 0$, rendering the exact same condition as (5.30). Following through with the same steps in Section 4.3, one can show that if $k \to \infty$, the expression (5.48) has only the root at $\lambda_{\mathrm{cr}} = 1$. Thus, in the presence of only surface elasticity, a coated beam under compression will buckle with infinite wavenumber, right at the start of compression, i.e. at $\lambda_{\mathrm{cr}} = 1$.

5.5 Bilayer with general interface model instability

In this section, the interface between the film and substrate in a bilayer structure corresponds to the general interface model, accounting for both non-zero displacement and traction jumps. Equipped with the generic tools required for the evaluation of the stability behavior of a rectangular, compressible domain, we can now apply the necessary boundary conditions and look at the interface mechanics associated with a bilayer structure. At the interface between two layers, there are two conditions which need to be addressed; namely, that of (i) displacement jump and (ii) traction jump. Using the relations and their interface counterparts given in Section 5.2, we can now apply the boundary conditions for a bilayer structure consisting of a film and a half-space. The top surface of the bilayer structure, at $\gamma = h_f$ where h_f is film thickness, is traction free, rendering

$$\delta \boldsymbol{P}_f \cdot \boldsymbol{N}\Big|_{\gamma=h_f} \doteq \boldsymbol{0}\,, \tag{5.49}$$

in which using the derived expression for traction (5.19) results in

$$-\mu_f\, k_f\, \boldsymbol{T}_f\, {}^{\frac{1}{2}}\boldsymbol{W}_f\, {}^{\frac{1}{2}}\boldsymbol{E}_f(h_f)\, {}^{\frac{1}{2}}\boldsymbol{B}_f + \mu_f\, k_f\, \boldsymbol{T}_f\, {}^{\frac{3}{4}}\boldsymbol{W}_f\, {}^{\frac{3}{4}}\boldsymbol{E}_f(h_f)\, {}^{\frac{3}{4}}\boldsymbol{B}_f = \boldsymbol{0}\,, \tag{5.50}$$

yielding the relation

$${}^{\frac{3}{4}}\boldsymbol{B}_f = \boldsymbol{b}\, {}^{\frac{1}{2}}\boldsymbol{B}_f \quad \text{where} \quad \boldsymbol{b} := [\, {}^{\frac{3}{4}}\boldsymbol{W}_f\, {}^{\frac{3}{4}}\boldsymbol{E}_f(h_f)\,]^{-1}\, {}^{\frac{1}{2}}\boldsymbol{W}_f\, {}^{\frac{1}{2}}\boldsymbol{E}_f(h_f)\,, \tag{5.51}$$

relating the unknown sets of constants ${}^{\frac{1}{2}}\boldsymbol{B}_f$ and ${}^{\frac{3}{4}}\boldsymbol{B}_f$. Furthermore, since the substrate is considered here to be a half-space, the incremental displacements should decay through the substrate depth, in other words,

$$\delta \boldsymbol{u}_s = \boldsymbol{0} \qquad \text{as} \qquad \gamma \to -\infty. \tag{5.52}$$

Imposing this boundary condition results in the constants ${}^{\frac{3}{4}}\boldsymbol{B}_s$ to vanish identically, given the sign of the decay coefficients in their associated decay functions.

Moving onto the interface between the film and substrate, the traction and displacement boundary conditions need to be imposed, using the general interface model. Accordingly, at the interface the traction jump can be written as

$$\begin{aligned}\llbracket \delta \boldsymbol{P} \rrbracket \cdot \overline{\boldsymbol{N}}\Big|_{\gamma=0} &= [\,\delta \boldsymbol{P}_f - \delta \boldsymbol{P}_s\,] \cdot \overline{\boldsymbol{N}}\,, \\ &= \mu_f\, k_f\, \boldsymbol{T}_f \Big[\, -{}^{\frac{1}{2}}\boldsymbol{W}_f + {}^{\frac{3}{4}}\boldsymbol{W}_f\, \boldsymbol{b}\Big]\, {}^{\frac{1}{2}}\boldsymbol{B}_f + \mu_s k_s\, \boldsymbol{T}_s\, {}^{\frac{1}{2}}\boldsymbol{W}_s\, {}^{\frac{1}{2}}\boldsymbol{B}_s\,,\end{aligned} \tag{5.53}$$

where the relation obtained in (5.51) has been used. Following the incremental form of the balance equation along the interface (5.7) and thus using the traction jump at the interface (5.53) and the form for $\overline{\mathrm{Div}}\,\delta\overline{\boldsymbol{P}}$ that has been obtained in (5.14), together with the results of the boundary conditions (5.51) and (5.52), we obtain

$$\begin{aligned}&\frac{\overline{\mu}}{2}\, k_f^2\, \boldsymbol{T}_f \Big[\, {}^{\frac{1}{2}}\boldsymbol{M}_f + {}^{\frac{3}{4}}\boldsymbol{M}_f\, \boldsymbol{b}\Big]\, {}^{\frac{1}{2}}\boldsymbol{B}_f + \frac{\overline{\mu}}{2}\, k_s^2\, \boldsymbol{T}_s\, {}^{\frac{1}{2}}\boldsymbol{M}_s\, {}^{\frac{1}{2}}\boldsymbol{B}_s \\ &+ \mu_f\, k_f\, \boldsymbol{T}_f \Big[\, -{}^{\frac{1}{2}}\boldsymbol{W}_f + {}^{\frac{3}{4}}\boldsymbol{W}_f\, \boldsymbol{b}\Big]\, {}^{\frac{1}{2}}\boldsymbol{B}_f + \mu_s k_s\, \boldsymbol{T}_s\, {}^{\frac{1}{2}}\boldsymbol{W}_s\, {}^{\frac{1}{2}}\boldsymbol{B}_s = \boldsymbol{0}\,,\end{aligned} \tag{5.54}$$

which after some simplification and rearranging yields

$$\begin{aligned}&\frac{k_f}{k_s}\, \boldsymbol{T}_s^{-1} \boldsymbol{T}_f \left[k_f\, \frac{\overline{\mu}}{\mu_s}\, \frac{1}{2} \Big[\, {}^{\frac{1}{2}}\boldsymbol{M}_f + {}^{\frac{3}{4}}\boldsymbol{M}_f\, \boldsymbol{b}\Big] - \frac{\mu_f}{\mu_s} \Big[\, {}^{\frac{1}{2}}\boldsymbol{W}_f - {}^{\frac{3}{4}}\boldsymbol{W}_f\, \boldsymbol{b}\Big] \right] {}^{\frac{1}{2}}\boldsymbol{B}_f \\ &+ \left[{}^{\frac{1}{2}}\boldsymbol{W}_s + k_s\, \frac{\overline{\mu}}{\mu_s} \frac{1}{2}\, {}^{\frac{1}{2}}\boldsymbol{M}_s \right] {}^{\frac{1}{2}}\boldsymbol{B}_s = \boldsymbol{0}\,.\end{aligned} \tag{5.55}$$

For the displacement boundary condition, we need to impose a condition which relates the displacement jump to the traction at the interface, commonly referred to as traction-separation law. That is

$$\overline{c}\, \llbracket \delta \boldsymbol{u} \rrbracket = \{\!\{ \boldsymbol{t} \}\!\}\,, \tag{5.56}$$

which renders

$$\begin{aligned}&\overline{c}\, [\, \boldsymbol{T}_f\, {}^{\frac{1}{2}}\boldsymbol{G}_f\, {}^{\frac{1}{2}}\boldsymbol{B}_f + \boldsymbol{T}_f\, {}^{\frac{3}{4}}\boldsymbol{G}_f\, {}^{\frac{3}{4}}\boldsymbol{B}_f - \boldsymbol{T}_s\, {}^{\frac{1}{2}}\boldsymbol{G}_s\, {}^{\frac{1}{2}}\boldsymbol{B}_s\,] \\ &= \frac{1}{2} \Big[-\, \mu_s\, k_s \boldsymbol{T}_s\, {}^{\frac{1}{2}}\boldsymbol{W}_s\, {}^{\frac{1}{2}}\boldsymbol{B}_s - \mu_f\, k_f \boldsymbol{T}_f\, {}^{\frac{1}{2}}\boldsymbol{W}_f\, {}^{\frac{1}{2}}\boldsymbol{B}_f + \mu_f\, k_f \boldsymbol{T}_f\, {}^{\frac{3}{4}}\boldsymbol{W}_f\, {}^{\frac{3}{4}}\boldsymbol{B}_f \Big]\,,\end{aligned} \tag{5.57}$$

and can be rearranged into

$$
\begin{aligned}
&-\boldsymbol{T}_s \left[{}^{\frac{1}{2}}\boldsymbol{G}_s - \frac{\mu_s}{2\overline{c}}\, k_s\, {}^{\frac{1}{2}}\boldsymbol{W}_s \right] {}^{\frac{1}{2}}\boldsymbol{B}_s \\
&= -\boldsymbol{T}_f \left[\frac{\mu_f}{2\overline{c}}\, k_f \left[{}^{\frac{1}{2}}\boldsymbol{W}_f - {}^{\frac{3}{4}}\boldsymbol{W}_f\, \boldsymbol{b} \right] + {}^{\frac{1}{2}}\boldsymbol{G}_f + {}^{\frac{3}{4}}\boldsymbol{Q}_f\, \boldsymbol{b} \right] {}^{\frac{1}{2}}\boldsymbol{B}_f \,,
\end{aligned}
\tag{5.58}
$$

yielding the relation

$$
{}^{\frac{1}{2}}\boldsymbol{B}_s = \boldsymbol{A}_s{}^{-1}\, \boldsymbol{T}_s{}^{-1}\, \boldsymbol{T}_f\, \boldsymbol{A}_f\, {}^{\frac{1}{2}}\boldsymbol{B}_f \,, \tag{5.59}
$$

where

$$
\begin{aligned}
\boldsymbol{A}_f &:= \left[{}^{\frac{1}{2}}\boldsymbol{G}_s - \frac{\mu_s}{2\overline{c}}\, k_s\, {}^{\frac{1}{2}}\boldsymbol{W}_s \right] \\
\boldsymbol{A}_s &:= \left[\frac{\mu_f}{2\overline{c}}\, k_f \left[{}^{\frac{1}{2}}\boldsymbol{W}_f - {}^{\frac{3}{4}}\boldsymbol{W}_f\, \boldsymbol{b} \right] + {}^{\frac{1}{2}}\boldsymbol{G}_f + {}^{\frac{3}{4}}\boldsymbol{Q}_f\, \boldsymbol{b} \right] .
\end{aligned}
\tag{5.60}
$$

Finally, using the relation (5.59) in the traction condition (5.55), we can obtain

$$
\begin{aligned}
&\frac{k_f}{k_s}\, \boldsymbol{T}_s{}^{-1} \boldsymbol{T}_f \left[k_f\, \frac{\overline{\mu}}{\mu_s}\, \frac{1}{2} \left[{}^{\frac{1}{2}}\boldsymbol{M}_f + {}^{\frac{3}{4}}\boldsymbol{M}_f\, \boldsymbol{b} \right] - \frac{\mu_f}{\mu_s} \left[{}^{\frac{1}{2}}\boldsymbol{W}_f - {}^{\frac{3}{4}}\boldsymbol{W}_f\, \boldsymbol{b} \right] \right] {}^{\frac{1}{2}}\boldsymbol{B}_f \\
&\qquad + \left[{}^{\frac{1}{2}}\boldsymbol{W}_s + k_s\, \frac{\overline{\mu}}{\mu_s} \frac{1}{2}\, {}^{\frac{1}{2}}\boldsymbol{M}_s \right] \boldsymbol{A}_s{}^{-1}\, \boldsymbol{T}_s{}^{-1}\, \boldsymbol{T}_f\, \boldsymbol{A}_f\, {}^{\frac{1}{2}}\boldsymbol{B}_f = \boldsymbol{0} \,.
\end{aligned}
\tag{5.61}
$$

Looking at the obtained form (5.61), we can see that the system remains dependent on the coordinate ξ, and hence virtually unsolvable, since the matrices $\boldsymbol{T}_f$ and $\boldsymbol{T}_s$ still remain in the equation in the form $\boldsymbol{T}_s{}^{-1}\boldsymbol{T}_f$. Thus the relation that $k = k_f = k_s$ is imposed herein, rendering $\boldsymbol{T}_s{}^{-1}\boldsymbol{T}_f = \boldsymbol{I}$, implying that the wavenumber of the two layers are identical. This imposition is later verified via numerical results, as well. Finally, we can obtain the familiar relation

$$
\boldsymbol{Q}\, {}^{\frac{1}{2}}\boldsymbol{B}_f = \boldsymbol{0} \,, \tag{5.62}
$$

where

$$\boldsymbol{Q} := \Bigg[{}^{\frac{1}{2}}\boldsymbol{W}_s \, \boldsymbol{A}_s^{-1} \, \boldsymbol{A}_f - \frac{\mu_f}{\mu_s} {}^{\frac{1}{2}}\boldsymbol{W}_f + \frac{\mu_f}{\mu_s} {}^{\frac{3}{4}}\boldsymbol{W}_f \, \boldsymbol{b} + \frac{\overline{\mu}}{2\,\mu_s} \Big[k_s \, {}^{\frac{1}{2}}\boldsymbol{M}_s \, \boldsymbol{A}_s^{-1} \, \boldsymbol{A}_f + k_f \, {}^{\frac{1}{2}}\boldsymbol{M}_f + k_f \, {}^{\frac{3}{4}}\boldsymbol{M}_f \, \boldsymbol{b} \Big] \Bigg] . \tag{5.63}$$

The system (5.62) can be solved by setting the determinant of $\boldsymbol{Q}$ to zero and solving for the critical stretch λ_{cr} which satisfies this equality. However, the system still remains a function of the wavenumber k, and of the vertical stretches η_f and η_s. Hence, the non-linear Poisson relation (4.3) which relates the vertical stretch η to compressibility parameter α and horizontal stretch λ is used herein to render Eq. (5.62) only a function of λ and k. This system is then solved for a range of values of k, and the value of k which renders the highest λ_{cr}, i.e. the first mode of instability and its corresponding wavenumber k_{cr} that is encountered when compressing a domain from $\lambda = 1$, is sought for, i.e. $\lambda_{\text{cr}} = \max\{\, \lambda \,|\, \text{Det}\, \boldsymbol{Q}\,(\,k\,,\,\lambda) = 0\,,\, \forall\, k \in \mathbb{R}^+ \,\}$.

From previous observations also, we realize that no matter what the cohesive stiffness $\overline{c}$ is, as long as $\overline{\mu} \neq 0$, the structure will buckle immediately at $\lambda_{\text{cr}} = 1$, with infinite wavelength. This follows from the fact that the elastic interface implemented here does not have flexural resistance due to its zero-thickness structure; thus, it fundamentally cannot provide any resistance towards compression and hence buckles immediately. One can introduce a flexural resistance to the interface model following the pioneering contribution of Steigmann and Ogden [102], however, such an extension is out of the scope of the current study. We therefore explore the effect of cohesive stiffness $\overline{c}$ on the bifurcation of a compressible bilayer structure, assuming $\overline{\mu} = 0$ henceforth.

Figure 5.6 displays the widely studied critical stretch λ_{cr} plotted against a broad range of film-to-substrate stiffness ratio of the bilayer structure, covering also the range for relatively more compliant films on substrates, for a fully compressible bilayer with $\nu_f = \nu_s = 0$ and a nearly incompressible bilayer with $\nu_f = \nu_s = 0.99$, with film thickness $h_f = 1$. Remember that the parameter $\overline{c}$ is

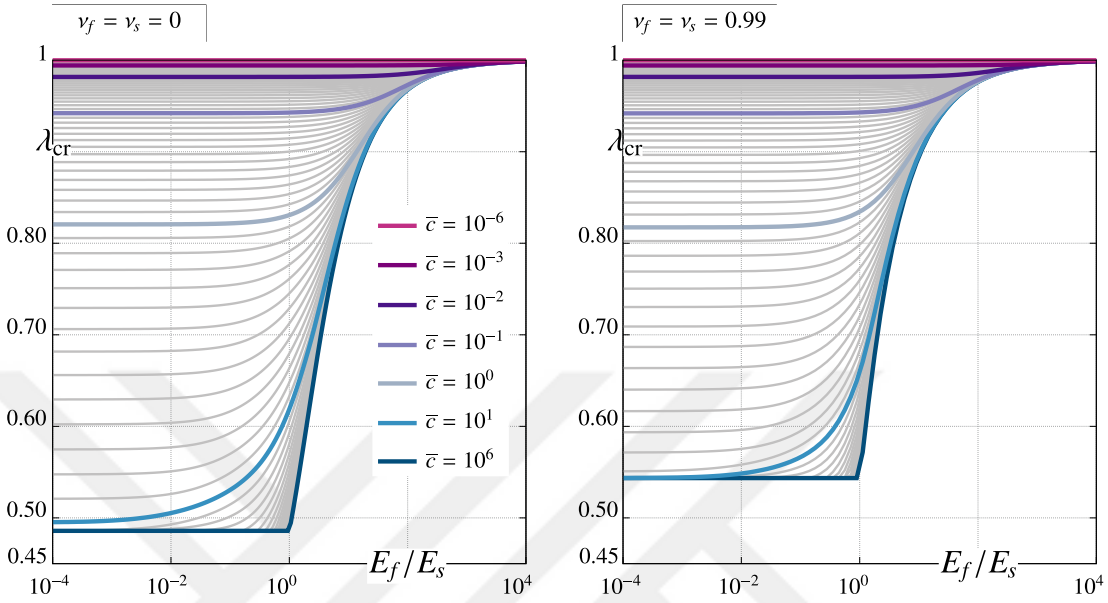


Figure 5.6: Critical stretch λ_{cr} versus film-to-substrate stiffness ratio E_f/E_s, plotted over a range of cohesive stiffness $\overline{c}$, for a fully compressible bilayer structure with $h_f = 1$ and $\nu_f = \nu_s = 0$ (left), and an incompressible one with $\nu_f = \nu_s = 0.99$ (right). As $\overline{c} \to \infty$, the classical bilayer case is recovered.

the cohesive resistance against the separation of film and substrate. Hence, as $\overline{c} \to \infty$, our solutions here converge to the classical (perfectly bonded) bilayer case, as shown in Fig. 5.6, where the curve for $\overline{c} = 10^6$ recovers the results presented in [31], with a clear flattening of the bifurcation curve at $E_f/E_s = 1$. The case of a classical bilayer structure therefore is essentially the lower-most curve on the graphs. As the cohesive stiffness $\overline{c}$ decreases and approaches zero, we observe two behaviors. Firstly, the flattening out of the bifurcation curve at and beyond $E_f/E_s = 1$ is still present, yet a transition region begins to form in between, which can be clearly seen. Secondly, the structure starts to buckle at increasing λ_{cr}, as we see the lines approaching a constant of $\lambda_{\text{cr}} = 1$. This happens because as $\overline{c} \to 0$, what we expect to see is complete delamination of the film from the substrate, and hence for the film to behave as a beam. This can be explained better using the next illustration.

Figure 5.7 illustrates clearly the buckling behavior of the bilayer structure for several values of $\overline{c}$, via numerical results obtained from FEM enhanced with eigenvalue analysis. The deformation profiles given in Fig. 5.7 are essentially the

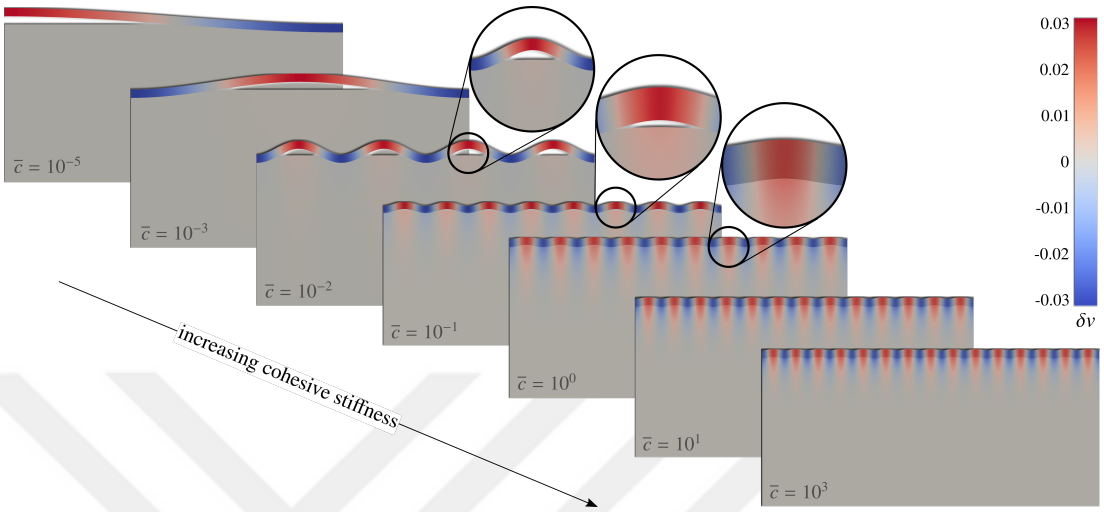


Figure 5.7: Deformation profiles for a bilayer structure with different cohesive stiffnesses, $h_f = 1$ and $\nu_f = \nu_s = 0$, obtained from FEM enhanced with eigenvalue analysis. Deformation profiles are portrayed by looking at the eigenvector corresponding to the first negative eigenvalue. Color scale maps incremental displacement in the γ direction.

eigenvectors corresponding to the first negative eigenvalues of the system. Since an infinite half-space is impossible to realize, the substrate has been truncated at a suitable depth and horizontal roller supports have been placed at the bottom. The right and left sides are on vertical roller supports. Clearly, as $\bar{c} \to 0$, for instance at $\bar{c} = 10^{-5}$, the film is almost completely delaminated from the substrate, and itself behaves as a beam. The half-wave mode observed in the beam here is due to the roller boundary conditions on the vertical axis. As the cohesive stiffness $\bar{c}$ increases, film delamination is still observed, however, to a lesser degree, accompanied by increasing wavenumbers. The coloring maps the incremental vertical displacements, and it can be seen that as cohesive stiffness increases and the film is bound more strongly to the substrate, the wrinkling of the film moves "further down" the substrate before it fully decays, as expected.

After observing the general trend of how critical stretch changes over a wide range of stiffness ratios in Fig. 5.6 and with respect to changing cohesive stiffness, the surface graphs in Fig. 5.8 illustrate this behavior for a continuous range of cohesive stiffnesses and for $E_f/E_s \geq 1$. One key aspect of this work is that the compressibility of the domains are kept as material parameters throughout.

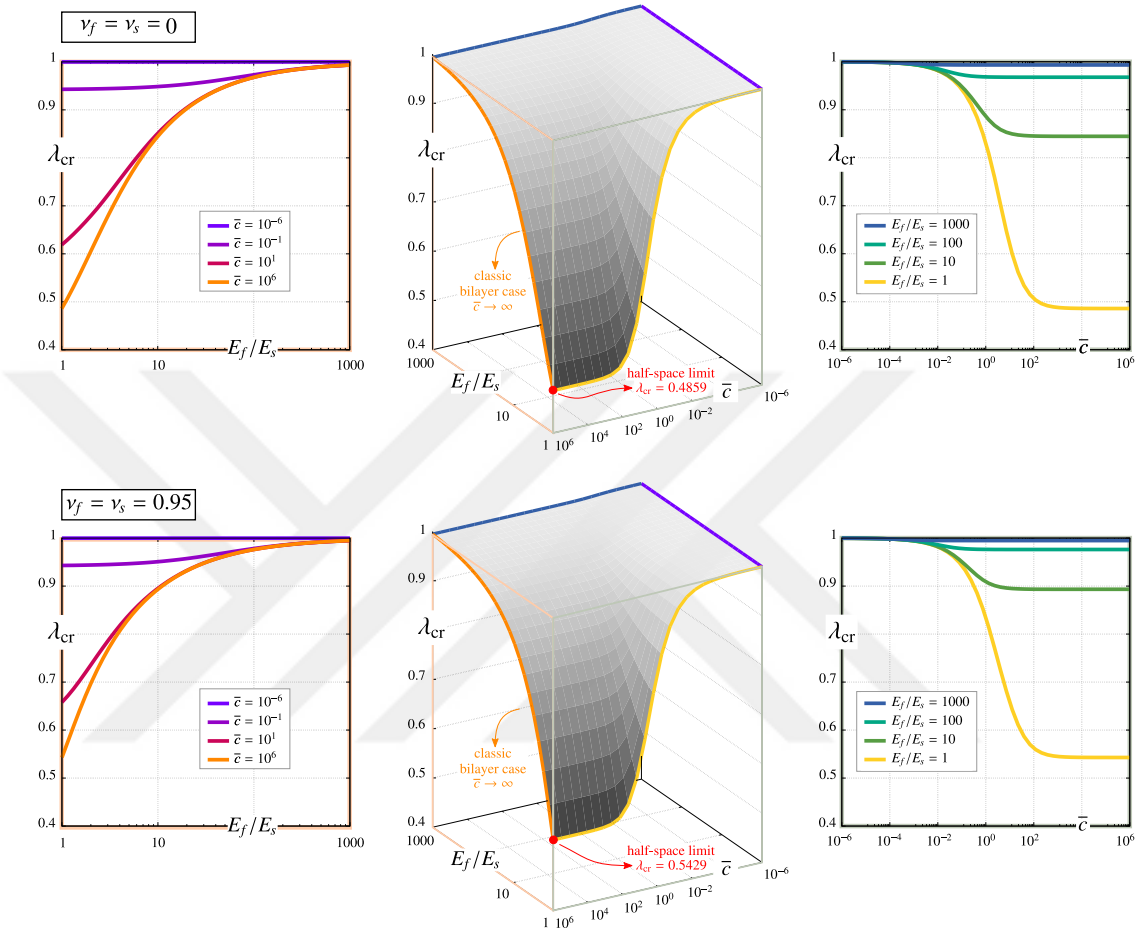


Figure 5.8: Surface graphs (center) of critical stretch λ_{cr} versus E_f/E_s and $\bar{c}$, for two different compressibilities, $\nu_f = \nu_s = 0$ and $\nu_f = \nu_s = 0.95$. 2D insets show projections of λ_{cr} versus E_f/E_s for several values of $\bar{c}$ (left), and λ_{cr} versus $\bar{c}$ for several values of E_f/E_s (right), for $h_f = 1$.

Hence, Fig. 5.8 also illustrates the results for two different Poisson's ratios in each row, assuming film and substrate have the same Poisson's ratio, although the formulation allows for different Poisson's ratios also. Once again, the classical bilayer limit which is recovered with increasing $\bar{c}$ has been marked, and the point on this line where $E_f/E_s = 1$ indicates the well-known half-space limit, which renders $\lambda_{\text{cr}} = 0.486$ for a fully compressible half-space [30, 95] and $\lambda_{\text{cr}} = 0.543$ for an almost incompressible half-space, recovering the findings of Biot [89]. The framework for a bilayer system with a general interface formulated here is hence shown to recover both the classical bilayer limit and the half-space solutions.

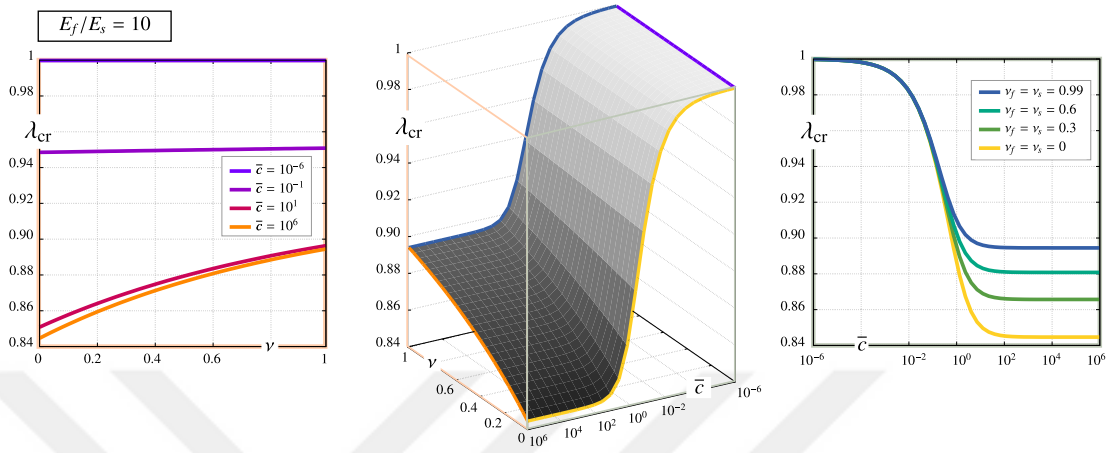


Figure 5.9: Surface graphs (center) of critical stretch λ_{cr} versus $\nu = \nu_f = \nu_s$ and $\bar{c}$, for stiffness ratio $E_f/E_s = 10$. 2D insets show projections of λ_{cr} versus ν for several values of $\bar{c}$ (left), and λ_{cr} versus $\bar{c}$ for several values of ν (right), for $h_f = 1$.

Cohesive stiffness has a clear effect on critical stretch, more significant with decreasing stiffness ratio, and we see that the commonly accepted classical bilayer constitutes only a limit of the solution. Looking at the effect of compressibility, we see that a change in compressibility most influences the result for more stiff cohesive interfaces, which is also illustrated clearly in Fig. 5.9.

Figure 5.9 plots the critical stretch λ_{cr} with respect to changing cohesive stiffness $\bar{c}$ and Poisson's ratio $\nu = \nu_f = \nu_s$. Clearly, the effect of changing cohesive stiffness increases significantly as we move from incompressibility at $\nu = 1$ towards a fully compressible system with $\nu = 0$. Once again, from the 2D insets on the left, we see that as cohesive stiffness decreases, the system becomes increasingly less dependent on changing Poisson's ratio, and the greatest effect of changing Poisson's ratio is observed in a system with $\bar{c} = 10^6$.

Figure 5.10 investigates further the effect of Poisson's ratio on the bifurcation behavior of a bilayer system, along changing the cohesive stiffness $\bar{c}$, where the film and substrate are no longer assumed to have the same Poisson's ratio. An interesting observation here is that changing film compressibility, i.e. moving from column to column, has little effect on bifurcation point, whereas changing substrate compressibility, i.e. looking among the three different colors of lines, has a significant effect on critical stretch. For stiffness ratio $E_f/E_s = 2$, shown

in the top row, moving from a fully compressible substrate to an incompressible one influences an almost 17% change in critical stretch λ_{cr} for the higher cohesive stiffness regime. This trend is also observed for other stiffness ratios and for all film Poisson's ratios.

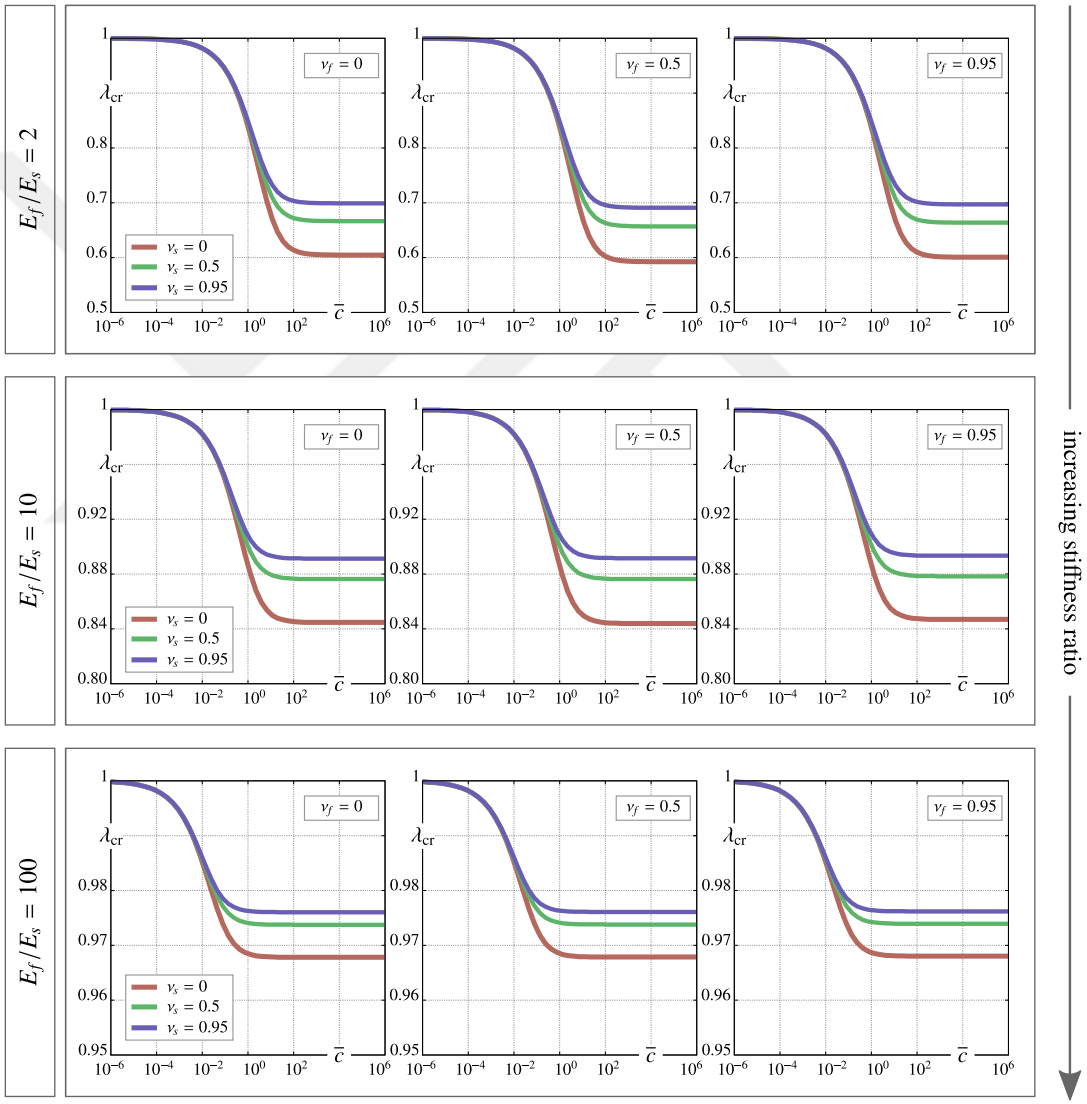


Figure 5.10: Critical stretch λ_{cr} versus cohesive stiffness $\overline{c}$, for different Poisson's ratio combinations for film and substrate, each row depicting a different stiffness ratio E_f/E_s, for $h_f = 1$.

Next, we compare the numerical results obtained via FEM with their theoretical counterparts that have been presented thus far. Figures 5.11 and 5.12 display results for critical stretch λ_{cr} and critical wavenumber k_{cr}, respectively,

with changing cohesive stiffness $\overline{c}$, for three different stiffness ratios in each inset, and each inset for a different combination of film and substrate Poisson's ratio.

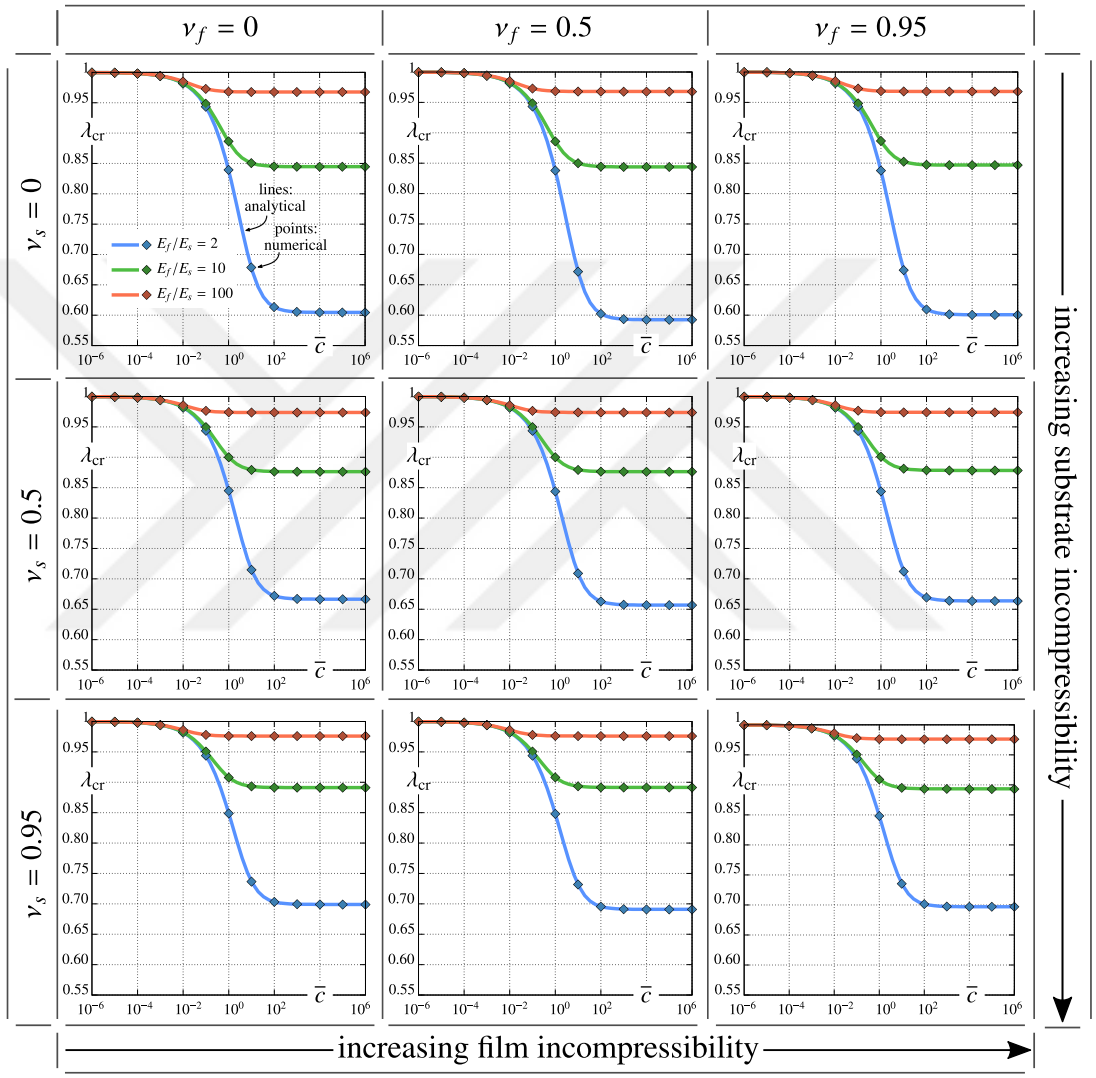


Figure 5.11: Critical stretch λ_{cr} versus $\overline{c}$, displayed together with numerical findings, shown as points, over a range of stiffness ratio and combinations of film and substrate Poisson's ratio, for $h_f = 1$.

Once again, the influence of substrate and film compressibility on critical stretch and wavenumber can be seen here. For both critical stretch and critical wavenumber, an excellent agreement between the theoretical results and numerical findings is observed. An interesting observation stemming from Fig. 5.12 is that the critical wavenumber converges to a different value for each stiffness ratio as $\overline{c}$ is increased, seen by the flattening and separation of the curves. On

the other end of the cohesive stiffness spectrum, where the cohesive stiffness approaches zero, however, we see that stiffness ratio ceases to have any influence on critical wavenumber. This happens because with relatively low cohesive stiffness, the film is weakly bonded to the substrate; hence we mostly observe "beam buckling" of the film, similar to delamination, and hence the stiffness of the film or the substrate no longer affects the bifurcation pattern.

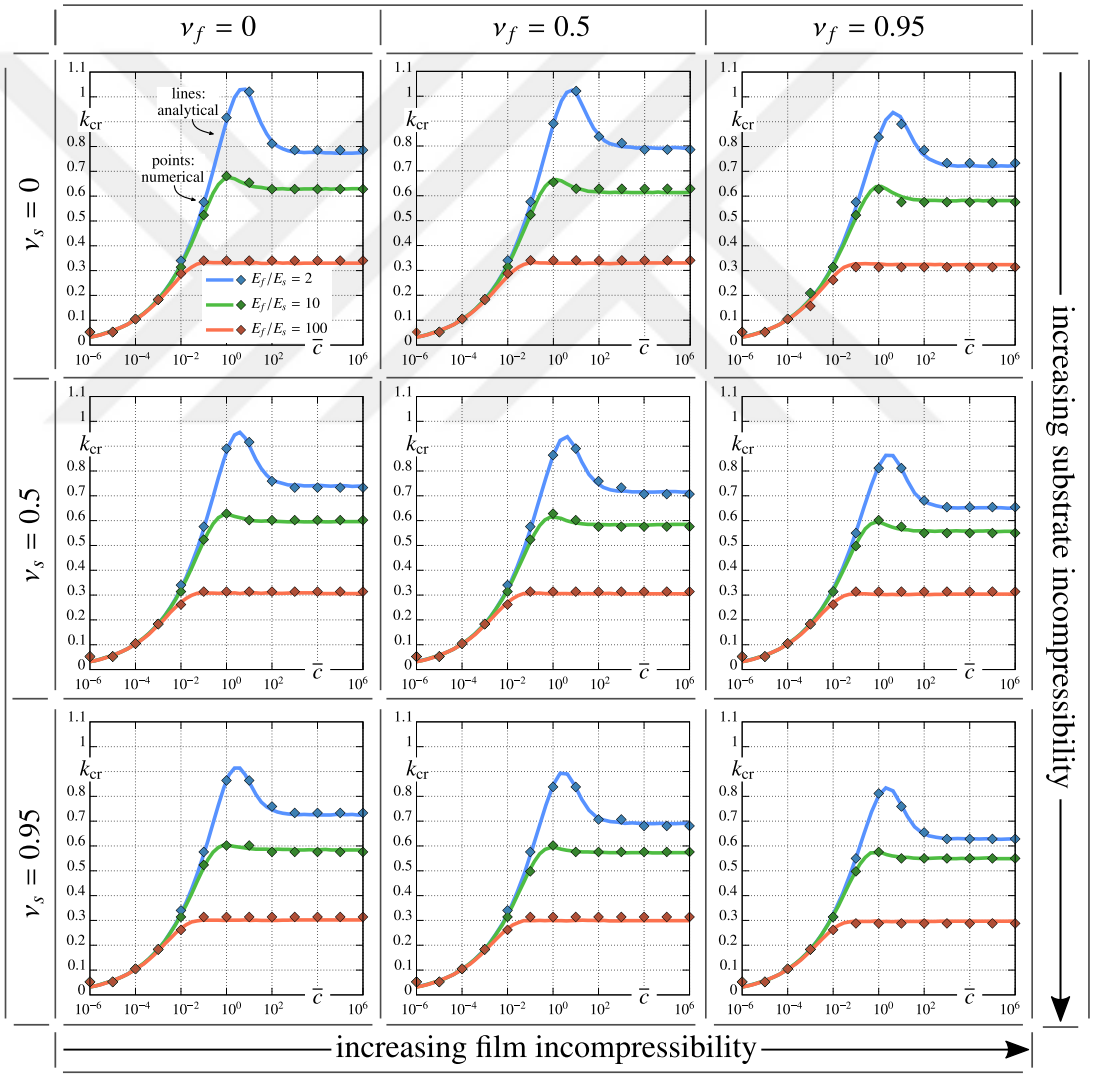


Figure 5.12: Critical wavelength k_{cr} versus $\bar{c}$, displayed together with numerical findings, shown as points, over a range of stiffness ratio and combinations of film and substrate Poisson's ratio, for $h_f = 1$.

Finally, we investigate the influence of film thickness on bifurcation behavior, in Fig. 5.13. The critical stretch of a classical bilayer system is expected to be

independent of film thickness, see e.g. [29] among others. Here, we observe that the critical stretch becomes less dependent on film thickness *for increasing* $\overline{c}$, however if the cohesive stiffness is not extremely high, we actually *see a significant dependence of the critical stretch* λ_{cr} *on the film thickness*. This behavior originates from the fact that in classical bilayers there exists only one length scale, namely the film thickness h and thus, the wavelength becomes proportional to the film thickness such that the wavenumber k multiplied by the film thickness kh becomes a dimensionless parameter characterizing the system. However, by incorporating an interface into the bilayer model and hence introducing cohesive stiffness to the system, another length scale $\mu/\overline{c}$ is introduced that influences the bifurcation behavior. More precisely, the wavenumber appears also in the dimensionless parameter $\mu k/\overline{c}$, see for instance in Eq. (5.60). A continuous surface highlighting the change of bifurcation point with changing film thickness over a range of cohesive stiffness values is illustrated in Fig. 5.13 (left).

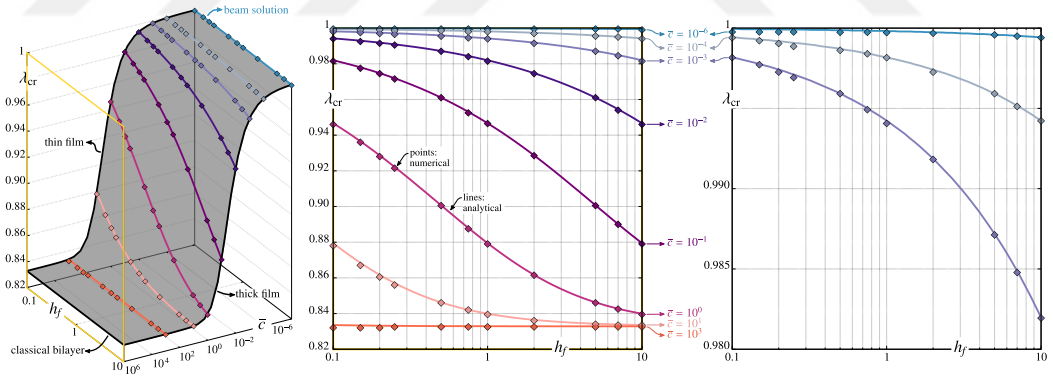


Figure 5.13: Critical stretch λ_{cr} versus film thickness h_f, displayed together with numerical findings, shown as points, over a range of cohesive stiffness $\overline{c}$, for $E_f/E_s = 5$ and $\nu_f = \nu_s = 0.95$, as a continuous surface (left) and a 2D projection (center). The right inset displays an enlarged version of the upper range of the center inset.

Chapter 6

Finite strain instabilities due to growth and compression

The derivations herein follow mainly the same route as the foundations presented in Chapter 2 and framework presented in Section 4.1, with the main difference that the initial configuration is no longer stress free. The source of this pre-stress can be a variety of factors, including thermal expansion, biological growth or swelling. To account for this pre-stress, we employ the commonly accepted concept of the multiplicative decomposition of the deformation gradient into its elastic and "pre"part as $\boldsymbol{F} = \boldsymbol{F}_e \cdot \boldsymbol{F}_{\text{PRE}}$, see [142, 151, 176, 214] among others. Clearly, the grown (intermediate) state $\mathcal{B}_g$ need not be necessarily compatible. Here, we look at the case where the source for the pre-stress in the configuration is biological (morphological) growth, such that the decomposed deformation gradient reads $\boldsymbol{F} = \boldsymbol{F}_e \cdot \boldsymbol{F}_g$.

6.1 Theoretical framework

Figure 6.1 illustrates the kinematics of growth and the associated instabilities within the framework of nonlinear continuum mechanics. In this case, the decomposed deformation gradient reads

$$\boldsymbol{F} = \boldsymbol{F}_e \cdot \boldsymbol{F}_g \,, \tag{6.1}$$

where $\boldsymbol{F}_e$ is the elastic component of the deformation and $\boldsymbol{F}_g$ corresponds to the growth component.

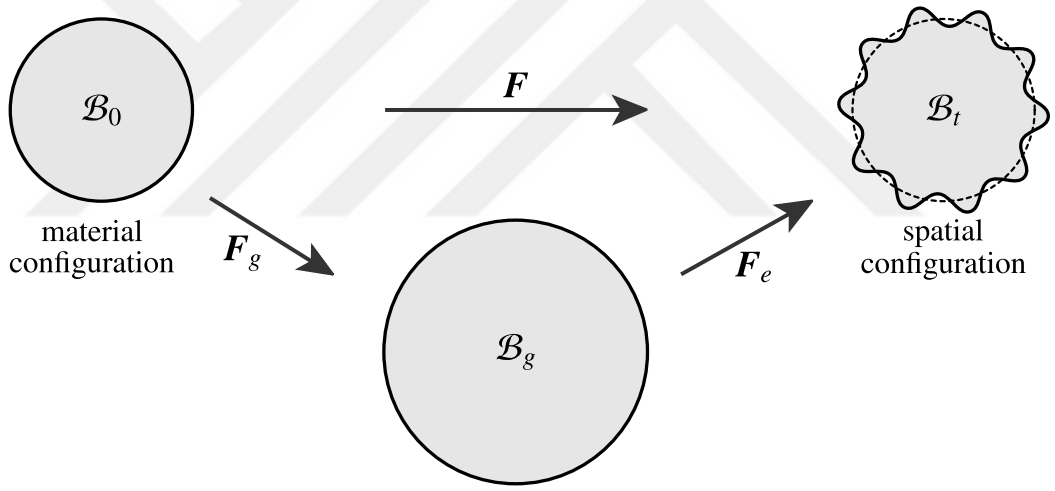


Figure 6.1: Kinematics of growth with multiplicative decomposition of the deformation gradient $\boldsymbol{F}$ into it elastic part $\boldsymbol{F}_e$ and growth part $\boldsymbol{F}_g$. The material configuration $\mathcal{B}_0$ is mapped to the spatial configuration $\mathcal{B}_t$. The deformation gradient $\boldsymbol{F}$ maps the line elements $\mathrm{d}\boldsymbol{X}$ from $\mathcal{B}_0$ to $\mathrm{d}\boldsymbol{x}$ in $\mathcal{B}_t$ according to $\mathrm{d}\boldsymbol{x} = \boldsymbol{F}\cdot\mathrm{d}\boldsymbol{X}$. The intermediate state $\mathcal{B}_g$ is, in general, incompatible, and thus is not a "configuration".

The stored energy in the material does not alter due to morphogenetic nature of the growth and thus, the free energy of a growing continuum would only be a function of the elastic part of the deformation as

$$\psi(\boldsymbol{F}) = \psi_e(\boldsymbol{F}_e) = \frac{1}{2}\,\mu\,\left[\boldsymbol{F}_e : \boldsymbol{F}_e - 3 - 2\ln J_e\right] + 2\mu\,\alpha\left[\,\tfrac{1}{4}\left[J_e^2 - 1\right] - \tfrac{1}{2}\,\ln J_e\,\right], \tag{6.2}$$

where ψ and ψ_e denote the total free energy density and the elastic free energy

density, respectively, and $J_e = \mathrm{Det}\boldsymbol{F}_e$ corresponding to the Jacobian of the elastic part of the deformation. Thus, the total Piola stress $\boldsymbol{P} = \mathrm{d}\psi/\mathrm{d}\boldsymbol{F}$ can be calculated from the elastic Piola stress $\boldsymbol{P}_e = \partial\psi_e/\partial\boldsymbol{F}_e$ via the relation $\boldsymbol{P} = \boldsymbol{P}_e \cdot \boldsymbol{F}_g{}^{-\mathrm{t}}$. In other words,

$$\boldsymbol{P} = \frac{\mathrm{d}\psi}{\mathrm{d}\boldsymbol{F}} = \frac{\partial\psi_e}{\partial\boldsymbol{F}_e} : \frac{\partial\boldsymbol{F}_e}{\partial\boldsymbol{F}} = \frac{\partial\psi_e}{\partial\boldsymbol{F}_e} : [\boldsymbol{I} \overline{\otimes} \boldsymbol{F}_g{}^{-\mathrm{t}}] = \boldsymbol{P}_e : [\boldsymbol{I} \overline{\otimes} \boldsymbol{F}_g{}^{-\mathrm{t}}]\,, \tag{6.3}$$

where

$$\boldsymbol{P}_e = \frac{\partial\psi_e}{\partial\boldsymbol{F}_e} = \mu\,[\,\boldsymbol{F}_e - \boldsymbol{F}_e^{-t}\,] + \mu\,\alpha\,[\,J_e^2 - 1\,]\,\boldsymbol{F}_e^{-t}\,. \tag{6.4}$$

Note that because the growth here is morphological and hence is independent of deformation, $\partial\psi/\partial\boldsymbol{F}_g$. The derivative of the elastic Piola stress (6.4) renders the fourth order tensor $\mathbb{A}_e$, which reads

$$\mathbb{A}_e = \frac{\partial\boldsymbol{P}_e}{\partial\boldsymbol{F}_e} = \mu\,[\,\mathbb{I} - \mathbb{D}_e\,] + \mu\,\alpha\,[\,J_e^2 - 1\,]\,\mathbb{D}_e + 2\,\mu\,\alpha\,J_e^2\,\boldsymbol{F}_e{}^{-\mathrm{t}} \otimes \boldsymbol{F}_e{}^{-\mathrm{t}}\,, \tag{6.5}$$

where

$$\mathbb{I} := \frac{\partial\boldsymbol{F}_e}{\partial\boldsymbol{F}_e} = \boldsymbol{i} \overline{\otimes} \boldsymbol{I} \qquad \text{and} \qquad \mathbb{D}_e := \frac{\partial\boldsymbol{F}_e{}^{-\mathrm{t}}}{\partial\boldsymbol{F}_e} = -\boldsymbol{F}_e{}^{-\mathrm{t}} \underline{\otimes} \boldsymbol{F}_e{}^{-1}\,. \tag{6.6}$$

For the incremental Piola stress $\delta\boldsymbol{P}$, we have the relation

$$\delta\boldsymbol{P} = \frac{\mathrm{d}\boldsymbol{P}}{\mathrm{d}\boldsymbol{F}} : \delta\boldsymbol{F} = \left[\frac{\partial\boldsymbol{P}}{\partial\boldsymbol{F}_e} : \frac{\partial\boldsymbol{F}_e}{\partial\boldsymbol{F}}\right] : \delta\boldsymbol{F} = \left[\frac{\partial\boldsymbol{P}}{\partial\boldsymbol{P}_e} : \frac{\partial\boldsymbol{P}_e}{\partial\boldsymbol{F}_e} : \frac{\partial\boldsymbol{F}_e}{\partial\boldsymbol{F}}\right] : \delta\boldsymbol{F}\,, \tag{6.7}$$

which simplifies to

$$\delta\boldsymbol{P} = \left[\,[\,\boldsymbol{I} \overline{\otimes} \boldsymbol{F}_g{}^{-1}\,] : \mathbb{A}_e : [\,\boldsymbol{I} \overline{\otimes} \boldsymbol{F}_g{}^{-\mathrm{t}}\,]\,\right] : \delta\boldsymbol{F}\,, \tag{6.8}$$

where

$$\frac{\partial\boldsymbol{P}}{\partial\boldsymbol{P}_e} = \boldsymbol{I} \overline{\otimes} \boldsymbol{F}_g{}^{-1} \qquad \text{and} \qquad \frac{\partial\boldsymbol{F}_e}{\partial\boldsymbol{F}} = \boldsymbol{I} \overline{\otimes} \boldsymbol{F}_g{}^{-\mathrm{t}}\,. \tag{6.9}$$

The expression for incremental Piola stress $\delta \boldsymbol{P}$ can be written out as

$$\begin{aligned}\frac{\delta \boldsymbol{P}}{\mu} = \delta \boldsymbol{F} \cdot \boldsymbol{F}_g^{-1} \cdot \boldsymbol{F}_g^{-\mathrm{t}} + \Big[1 - \alpha \left[J_e^2 - 1\right]\Big] \boldsymbol{F}_e^{-\mathrm{t}} \cdot \boldsymbol{F}_g^{-\mathrm{t}} \cdot \delta \boldsymbol{F}^{\mathrm{t}} \cdot \boldsymbol{F}_e^{-\mathrm{t}} \cdot \boldsymbol{F}_g^{-\mathrm{t}} \\ + 2\,\alpha\, J_e^2 \left[\boldsymbol{F}_e^{-\mathrm{t}} \cdot \boldsymbol{F}_g^{-\mathrm{t}}\right] : \delta \boldsymbol{F}\, \boldsymbol{F}_e^{-\mathrm{t}} \cdot \boldsymbol{F}_g^{-\mathrm{t}} .\end{aligned} \tag{6.10}$$

Note that when there is no growth, i.e. when $\boldsymbol{F}_g = \boldsymbol{I}$ and hence $\boldsymbol{F}_e = \boldsymbol{F}$, Eq. (6.10) becomes identical to Eq. (2.17) as expected.

Similar to the steps taken in previous chapters, upon prescribing an elastic free energy density ψ_e and obtaning the corresponding expressions for Piola stress and incremental Piola stress, next, the incremental momentum balance $\mathrm{Div}\delta \boldsymbol{P} = \boldsymbol{0}$ is satisfied and the boundary conditions of the problem at hand are applied.

6.2 Uniaxial compression and growth in rectangular domains

Having defined the governing equations and kinematics of the problem, we now look at the case of a uniaxial compression or tension together with growth. The first step is to satisfy the incremental linear momentum balance $\mathrm{Div}\delta \boldsymbol{P} = \boldsymbol{0}$ using the incremental Piola stress established in (6.7). The deformation gradient $\boldsymbol{F}$ is essentially the homogenous deformation we apply in uniaxial tension, hence reads

$$\boldsymbol{F} = \lambda\, \boldsymbol{e}_\xi \otimes \boldsymbol{e}_\xi + \eta\, \boldsymbol{e}_\gamma \otimes \boldsymbol{e}_\gamma + 1\, \boldsymbol{e}_\zeta \otimes \boldsymbol{e}_\zeta . \tag{6.11}$$

The growth tensor can be constructed such that $\boldsymbol{F}_g = \boldsymbol{I} + g\, \overline{\boldsymbol{I}}$ where g is the anisotropic growth coefficient along the surface, and $\overline{\boldsymbol{I}} = \boldsymbol{I} - \boldsymbol{N} \otimes \boldsymbol{N}$ is the identity tensor along the surface with $\boldsymbol{N}$ being the unit tangent to the surface. In other words,

$$\boldsymbol{F}_g = [1 + g]\, \boldsymbol{e}_\xi \otimes \boldsymbol{e}_\xi + 1\, \boldsymbol{e}_\gamma \otimes \boldsymbol{e}_\gamma + 1\, \boldsymbol{e}_\zeta \otimes \boldsymbol{e}_\zeta . \tag{6.12}$$

Hence, one can also write $\boldsymbol{F}_e$ as

$$\boldsymbol{F}_e = \boldsymbol{F} \cdot \boldsymbol{F}_g^{-\mathrm{t}} = \frac{\lambda}{1+g}\, \boldsymbol{e}_\xi \otimes \boldsymbol{e}_\xi + \eta\, \boldsymbol{e}_\gamma \otimes \boldsymbol{e}_\gamma + 1\, \boldsymbol{e}_\zeta \otimes \boldsymbol{e}_\zeta\,. \tag{6.13}$$

On the other hand, the incremental deformation gradient $\delta\boldsymbol{F}$ remains identical to its previous definition

$$\delta\boldsymbol{u} = \begin{bmatrix} \delta u \\ \delta v \end{bmatrix} \quad , \quad \delta\boldsymbol{F} := \mathrm{Grad}\, \delta\boldsymbol{u} = \begin{bmatrix} \delta u_{,\xi} & \delta u_{,\gamma} \\ \delta v_{,\xi} & \delta v_{,\gamma} \end{bmatrix}. \tag{6.14}$$

Having defined the related deformation gradients, we are ready to evaluate $\delta\boldsymbol{P}$ (6.10) in terms of the incremental displacement functions (6.14), such that

$$\frac{\delta\boldsymbol{P}}{\mu} = \frac{1}{G^2}\begin{bmatrix} \delta u_{,\xi} & G^2\delta u_{,\gamma} \\ \delta v_{,\xi} & G^2\delta v_{,\gamma} \end{bmatrix} + \frac{D}{G^2}\begin{bmatrix} \eta^2\, \delta u_{,\xi} & \lambda\eta\, \delta v_{,\xi} \\ \lambda\eta\, \delta u_{,\gamma} & \lambda^2\, \delta v_{,\gamma} \end{bmatrix} + \frac{2\,\alpha}{G^2}\big[\eta\delta u_{,\xi} + \lambda\delta v_{,\gamma}\big]\begin{bmatrix} \eta & 0 \\ 0 & \lambda \end{bmatrix}, \tag{6.15}$$

where the parameters G and D has been defined for the sake of brevity as

$$G := 1 + g \qquad \text{and} \qquad D := \frac{1 - \alpha\,[\,J_e^2 - 1\,]}{J_e^2}\,, \tag{6.16}$$

and $J_e = \lambda\eta/G$. Now turning to the incremental linear momentum balance for the given incremental Piola stress (6.15),

$$\mathrm{Div}\delta\boldsymbol{P} = \boldsymbol{0} \Rightarrow \begin{cases} \big[\delta u_{,\xi,\xi} + G^2\, \delta u_{,\gamma,\gamma}\big] + \omega\, \big[\eta^{\,2}\, \delta u_{,\xi,\xi} + \lambda\eta\, \delta v_{,\xi,\gamma}\big] & = 0\,, \\ \big[\delta v_{,\xi,\xi} + G^2\, \delta v_{,\gamma,\gamma}\big] + \omega\, \big[\lambda\eta\, \delta u_{,\gamma,\xi} + \lambda^2\, \delta v_{,\gamma,\gamma}\big] & = 0\,, \end{cases} \tag{6.17}$$

with $\omega := D + 2\alpha = 1/J_e^{\,2} + \alpha + \alpha/J_e^{\,2}$, yielding a differential equation in terms of the incremental displacement functions. The incremental displacements which constitute a general solution to the differential equation (6.17) read

$$\begin{cases} \delta u = A\, \exp(r\,\gamma)\, \sin(k\,\xi)\,, \\ \delta v = B\, \exp(r\,\gamma)\, \cos(k\,\xi)\,, \end{cases} \qquad \Rightarrow \qquad \delta\boldsymbol{u} = \boldsymbol{T}\, \boldsymbol{E}(\gamma)\, \boldsymbol{\Xi}\,, \tag{6.18}$$

with

$$\boldsymbol{T} := \begin{bmatrix} \sin(k\xi) & 0 \\ 0 & \cos(k\xi) \end{bmatrix} \;,\; \boldsymbol{E}(\gamma) := \begin{bmatrix} \exp(r\gamma) & 0 \\ 0 & \exp(r\gamma) \end{bmatrix} \;,\; \boldsymbol{\Xi} := \begin{bmatrix} A \\ B \end{bmatrix} . \tag{6.19}$$

Using the proposed incremental displacements (6.18) in the differential equation (6.17) renders

$$\begin{cases} \Big[\left[G^2 r^2 - k^2 \right] - \omega \eta^2 k^2 \Big] A - \omega \lambda \eta k r B = 0 \,, \\ \Big[\left[G^2 r^2 - k^2 \right] + \omega \lambda^2 r^2 \Big] B + \omega \lambda \eta k r A = 0 \,, \end{cases} \tag{6.20}$$

with its matrix representation

$$\boldsymbol{Z}(r) \cdot \boldsymbol{\Xi} = \boldsymbol{0} \;\text{ with }\; \boldsymbol{Z}(r) := \begin{bmatrix} \big[G^2 r^2 - k^2 \big] - \omega \eta^2 k^2 & -\omega \lambda \eta k r \\ \omega \lambda \eta k r & \big[G^2 r^2 - k^2 \big] + \omega \lambda^2 r^2 \end{bmatrix} . \tag{6.21}$$

Setting the determinant of the coefficient matrix in the homogeneous system (4.13) to zero yields the characteristic equation

$$\text{Det}\, \boldsymbol{Z}(r) = 0 \quad \Rightarrow \quad \big[G^2 r^2 - k^2 \big] \, \big[\left[G^2 r^2 - k^2 \right] + \omega \left[\lambda^2 r^2 - \eta^2 k^2 \right] \big] = 0 \,, \tag{6.22}$$

that has the following four solutions

$$r_1 = k/G \quad , \quad r_2 = k\sqrt{\rho} \quad , \quad r_3 = -k/G \quad , \quad r_4 = -k\sqrt{\rho} \,. \tag{6.23}$$

where

$$\rho := \frac{1 + \omega \eta^2}{G^2 + \omega \lambda^2} \,. \tag{6.24}$$

The proposed, generic form of the incremental displacement functions (6.18) are updated in order to accommodate for the four possible values of r. The set of vectors $\boldsymbol{\Xi}$ corresponding to the solutions (6.23) then allows for us to obtain expressions relating the constants A_i of the horizontal incremental displacement

δu, to B_i of the vertical incremental displacement δv such that

$$\begin{aligned} \boldsymbol{Z}(r_1)\cdot\boldsymbol{\Xi}_1=\boldsymbol{0} \;\Rightarrow\; A_1=-\,B_1\,\frac{\lambda}{G\eta} \quad , \quad \boldsymbol{Z}(r_3)\cdot\boldsymbol{\Xi}_3=\boldsymbol{0} \;\Rightarrow\; A_3=\;B_3\,\frac{\lambda}{G\eta}\,, \\ \boldsymbol{Z}(r_2)\cdot\boldsymbol{\Xi}_2=\boldsymbol{0} \;\Rightarrow\; A_2=-\,B_2\,\frac{\theta}{\lambda\eta} \quad , \quad \boldsymbol{Z}(r_4)\cdot\boldsymbol{\Xi}_4=\boldsymbol{0} \;\Rightarrow\; A_4=\;B_4\,\frac{\theta}{\lambda\eta}\,, \end{aligned} \tag{6.25}$$

with $\theta := [\,G^2\rho\,[\,1+\omega\,\lambda^2\,]-1]/[\omega\sqrt{\rho}]$. Writing the displacement functions in matrix form results in

$$\delta\boldsymbol{u}=\;\boldsymbol{T}\,{}^{1}_{2}\boldsymbol{G}\,{}^{1}_{2}\boldsymbol{E}(\gamma)\,{}^{1}_{2}\boldsymbol{B}\;+\boldsymbol{T}\,{}^{3}_{4}\boldsymbol{G}\,{}^{3}_{4}\boldsymbol{E}(\gamma)\,{}^{3}_{4}\boldsymbol{B}\;\text{ with }\;\boldsymbol{T}:=\begin{bmatrix}\sin(k\xi) & 0\\ 0 & \cos(k\xi)\end{bmatrix}, \tag{6.26}$$

and in which

$$\begin{aligned} {}^{1}_{2}\boldsymbol{G}&:=\begin{bmatrix}-\dfrac{\lambda}{G\eta} & -\dfrac{\theta}{\lambda\eta}\\ 1 & 1\end{bmatrix}\;,\;{}^{1}_{2}\boldsymbol{E}(\gamma):=\begin{bmatrix}\exp(r_1\gamma) & 0\\ 0 & \exp(r_2\gamma)\end{bmatrix}\;,\;{}^{1}_{2}\boldsymbol{B}:=\begin{bmatrix}B_1\\ B_2\end{bmatrix}\;,\\ {}^{3}_{4}\boldsymbol{G}&:=\begin{bmatrix}\dfrac{\lambda}{G\eta} & \dfrac{\theta}{\lambda\eta}\\ 1 & 1\end{bmatrix}\;,\;{}^{3}_{4}\boldsymbol{E}(\gamma):=\begin{bmatrix}\exp(r_3\gamma) & 0\\ 0 & \exp(r_4\gamma)\end{bmatrix}\;,\;{}^{3}_{4}\boldsymbol{B}:=\begin{bmatrix}B_3\\ B_4\end{bmatrix}\;. \end{aligned} \tag{6.27}$$

Note that the steps until now have been for a generic domain under plane compression and experiencing anisotropic growth. In order to apply traction boundary conditions specific to the geometries at hand, a relation for the traction at a surface of the domain is needed, dictated by $\delta\boldsymbol{t}=\delta\boldsymbol{P}\cdot\boldsymbol{N}$, which can be written as

$$\delta\boldsymbol{t}=-\frac{\mu\,k}{G^2}\,\boldsymbol{T}\,{}^{1}_{2}\boldsymbol{W}\,{}^{1}_{2}\boldsymbol{E}(\gamma)\,{}^{1}_{2}\boldsymbol{B}+\frac{\mu\,k}{G^2}\,\boldsymbol{T}\,{}^{3}_{4}\boldsymbol{W}\,{}^{3}_{4}\boldsymbol{E}(\gamma)\,{}^{3}_{4}\boldsymbol{B}\;, \tag{6.28}$$

in which

$$\begin{aligned} -{}^{1}_{2}\boldsymbol{W}&:=\begin{bmatrix}-\dfrac{\lambda}{\eta}-D\,\lambda\,\eta & -G^2\dfrac{\theta\sqrt{\rho}}{\lambda\eta}-D\,\lambda\,\eta\\ \dfrac{1}{G}[G^2+D\lambda^2] & \sqrt{\rho}\,[G^2+\omega\,\lambda^2]-2\,\alpha\,\theta\end{bmatrix}\;,\\ {}^{3}_{4}\boldsymbol{W}&:=\begin{bmatrix}-\dfrac{\lambda}{\eta}-D\,\lambda\,\eta & -G^2\dfrac{\theta\sqrt{\rho}}{\lambda\eta}-D\,\lambda\,\eta\\ -\dfrac{1}{G}[G^2+D\lambda^2] & -\sqrt{\rho}\,[G^2+\omega\,\lambda^2]+2\,\alpha\,\theta\end{bmatrix}\;. \end{aligned} \tag{6.29}$$

Next, we look at the case of a growing film layer placed on an infinite half-space, by applying the non-linear, large deformation framework developed here to the said geometry and comparing the results of the non-linear formulation with the linear formulation presented in Chapter 3.

6.3 Bilayer with growing film

Herein we look at the bifurcation behavior of a bilayer with growing layers and going under applied deformation using the framework developed in Section 6.2. Note that the strategy followed here essentially follows the approach in Section 4.4, with the only difference being that now we use the quantites defined in Section 6.2.

First off, imposing the traction-free boundary condition at $\gamma = h$ yields the relation

$$ {}^{\frac{3}{4}}\boldsymbol{B}_f = \boldsymbol{b}\, {}^{\frac{1}{2}}\boldsymbol{B}_f \,, \tag{6.30} $$

with

$$ \boldsymbol{b} := \left[{}^{\frac{3}{4}}\boldsymbol{W}_f \, {}^{\frac{3}{4}}\boldsymbol{E}_f(h) \right]^{-1} {}^{\frac{1}{2}}\boldsymbol{W}_f \, {}^{\frac{1}{2}}\boldsymbol{E}_f(h) \,. \tag{6.31} $$

Secondly, we impose traction continuity at the interface between the film and substrate, such that $\delta \boldsymbol{t}_f \,|_{\gamma=0} + \delta \boldsymbol{t}_s \,|_{\gamma=0} \doteq \boldsymbol{0}$, which renders

$$ \frac{\mu_f \, k}{G_f^2} \boldsymbol{T} \, {}^{\frac{1}{2}}\boldsymbol{W}_f \, {}^{\frac{1}{2}}\boldsymbol{B}_f - \frac{\mu_f \, k}{G_f^2} \boldsymbol{T} \, {}^{\frac{3}{4}}\boldsymbol{W}_f \, {}^{\frac{3}{4}}\boldsymbol{B}_f - \frac{\mu_s \, k}{G_s^2} \boldsymbol{T} \, {}^{\frac{1}{2}}\boldsymbol{W}_s \, {}^{\frac{1}{2}}\boldsymbol{B}_s \doteq \boldsymbol{0} \,. \tag{6.32} $$

It should be noted that here, based on our previous observations, we directly start off with the assumption that $k = k_f = k_s$ and hence $\boldsymbol{T} = \boldsymbol{T}_s = \boldsymbol{T}_f$. Subsequently, inserting the relation (6.30) into Eq. (6.32) furnishes

$$ \frac{\mu_f}{G_f^2} \boldsymbol{Q}_f \, {}^{\frac{1}{2}}\boldsymbol{B}_f + \frac{\mu_s}{G_s^2} \boldsymbol{Q}_s \, {}^{\frac{1}{2}}\boldsymbol{B}_s = \boldsymbol{0} \,, \tag{6.33} $$

with

$$ \boldsymbol{Q}_f := {}^{\frac{1}{2}}\boldsymbol{W}_f - {}^{\frac{3}{4}}\boldsymbol{W}_f \, \boldsymbol{b} \quad \text{and} \quad \boldsymbol{Q}_s := -{}^{\frac{1}{2}}\boldsymbol{W}_s \,. \tag{6.34} $$

Now turning to the displacement-continuity condition, we can evaluate the incremental displacement functions of the film and the substrate at $\gamma = 0$ and set them equal to each other, resulting in

$$\delta \boldsymbol{u}_f \,|_{\gamma=0} = \delta \boldsymbol{u}_s \,|_{\gamma=0} \qquad \Rightarrow \qquad \boldsymbol{T}\ {}^{\frac{1}{2}}\boldsymbol{G}_f\ {}^{\frac{1}{2}}\boldsymbol{B}_f + \boldsymbol{T}\ {}^{\frac{3}{4}}\boldsymbol{G}_f\ {}^{\frac{3}{4}}\boldsymbol{B}_f = \boldsymbol{T}\ {}^{\frac{1}{2}}\boldsymbol{G}_s\ {}^{\frac{1}{2}}\boldsymbol{B}_s \,. \tag{6.35}$$

Again, using the relation (4.38), and rearranging, yields

$${}^{\frac{1}{2}}\boldsymbol{B}_s = \boldsymbol{A}\ {}^{\frac{1}{2}}\boldsymbol{B}_f \,, \tag{6.36}$$

with

$$\boldsymbol{A} := {}^{\frac{1}{2}}\boldsymbol{G}_s^{-1}\ \left[{}^{\frac{1}{2}}\boldsymbol{G}_f + {}^{\frac{3}{4}}\boldsymbol{G}_f\ \boldsymbol{b} \right] . \tag{6.37}$$

Finally, we evaluate the traction continuity condition at the interface (6.33) by plugging in the relation we obtained from the displacement-continuity condition (6.36). This results in

$$\left[\frac{\mu_f}{G_f^2}\, \boldsymbol{Q}_f + \frac{\mu_s}{G_s^2}\, \boldsymbol{Q}_s\ \boldsymbol{A} \right] {}^{\frac{1}{2}}\boldsymbol{B}_f = \boldsymbol{0} \,, \tag{6.38}$$

that can be alternatively expressed in the canonical form

$$\boldsymbol{Q}\ {}^{\frac{1}{2}}\boldsymbol{B}_f = \boldsymbol{0} \qquad \text{with} \qquad \boldsymbol{Q} := \frac{\mu_f}{\mu_s}\, \frac{G_s^2}{G_f^2}\, \boldsymbol{Q}_f + \boldsymbol{Q}_s\, \boldsymbol{A} \,. \tag{6.39}$$

Furthermore, employing Young's modulus E to account for the stiffness of the structure instead of the shear modulus results in

$$\boldsymbol{Q}\ {}^{\frac{1}{2}}\boldsymbol{B}_f = \boldsymbol{0} \qquad \text{with} \qquad \boldsymbol{Q} := \left[\frac{G_s}{G_f} \right]^2 \frac{E_f}{E_s}\, \frac{[1+\nu_s]}{[1+\nu_f]}\, \boldsymbol{Q}_f + \boldsymbol{Q}_s\, \boldsymbol{A} \,, \tag{6.40}$$

and the parameter E_f/E_s is denoted as the stiffness ratio of the structure, and the parameter G_s/G_f is the growth ratio of substrate to film. It is important to note that the ratio of the growths are the defining parameter here, meaning differential growth governs the behavior of the system. Remember that the parameter defined as G relates to growth g such that $G = 1 + g$.

Solving for the non-trivial solutions of the system (6.40) by setting $\mathrm{Det}\boldsymbol{Q} \doteq 0$

gives us the bifurcation point of the system. Again, we employ the non-linear Poisson relation, setting once again the variation of (6.2) to zero, which renders a relation identical to that found in Chapter 4, i.e. Eq. (4.4). A crucial point here is to note that now, in its most general form (6.40) our system is a function of both applied stretch λ, and the growth coefficients of the film and substrate, g_s and g_f. Thus, depending on our system and what we want to solve for, we need to minimze and search for the solutions accordingly. In order to simplify the derivations and compare our results to the ones obtained in Chapter 3, we will first look at the bilayer system with (i) an applied stretch of $\lambda = 1$, meaning there is no external displacement applied and (ii) $g_s = 0$ which translates to $G_s = 1$, meaning that there is no growth in the substrate. Hence, the only unknown in our system becomes the growth of the film g_f and wavenumber k, which we will minimize our system over. In other words, we look for the solution

$$g_{\text{cr}} = \min\{\, g_f \,|\, \text{Det}\, \boldsymbol{Q}\,(\,k\,,\,g_f\,) = 0\,,\, \forall\, k \in \mathbb{R}^+ \,\}\,, \tag{6.41}$$

where the critical growth value g_{cr} is actually critical growth for the *film*, but for the sake of convenience is written without the subscript. Figure 6.2 further elaborates on this minimization scheme and illustrates the bifurcation curves for stiffness ratios $E_f/E_s = 2$, 10, and 100, for a range of combinations of compressibilities. Figure 6.2 is meant to be compared with its counterpart Fig. 4.10 in Chapter 4, where we were calculating critical stretch λ_{cr}.

Following the minimization scheme outlined in Fig. 6.2, we can now look at critical growth g_{cr} values over a range of stiffness ratios E_f/E_s, with the results illustrated in Fig. 6.3. Herein we look at a bilayer structure with film thickness $h = 1$ and film Poisson's ratio $\nu_f = 0.99$. The goal here is to compare the results of the large deformation framework developed here with that of the linear framework established in Chapter 3. More specifically, we compare the solutions of the system (6.40) with Eq. $(3.41)_2$. Clearly, the solution presented here is far more generic than the one developed in Chapter 3 and which is frequently, almost exclusively, used in literature. This is because the solution here allows for (i) large deformations including both growth and applied compression, (ii) thick film layers, (iii) a compressible film layer. Hence to be able to conduct an accurate

comparison among the two sets of results, the system in (6.40) has been solved for $\nu_f = 0.99$, since in Fig. 4.9 and the following discussion we had established that the Euler beam solution, used to model the beam in (3.41), is recovered at the incompressible limit of the non-linear beam solution here. Furthermore, applied stretch $\lambda = 1$, so that there is no external compression or tension applied to the system, and there is only growth in the film.

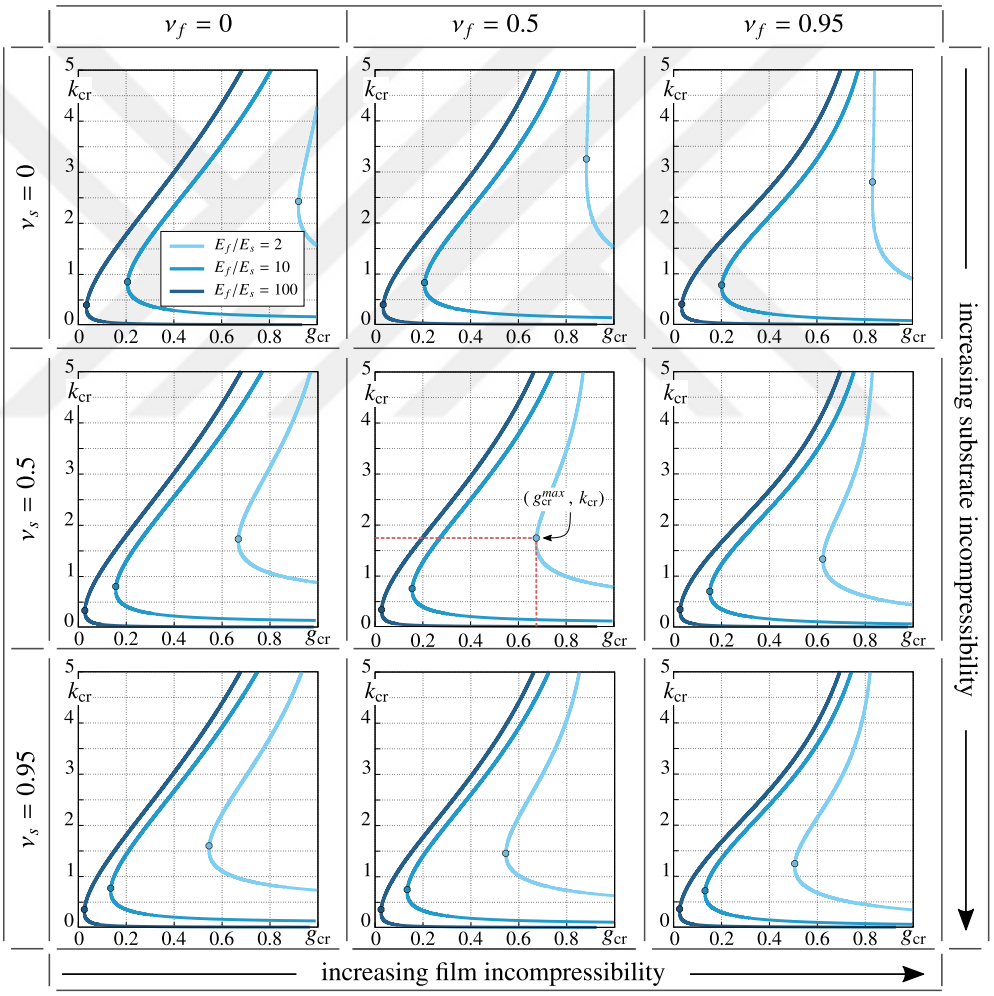


Figure 6.2: The variation of g_{cr} for values of k, for a range of stiffness ratio (E_f/E_s) and film and substrate compressibilities.

The results in Fig 6.3 clearly illustrate the shortcomings of the previous solution, especially in the lower stiffness ratio regime where critical growth increases and the deformations can no longer be regarded as small. In this range, the percentage difference between the two results is as much as 40%. Given the

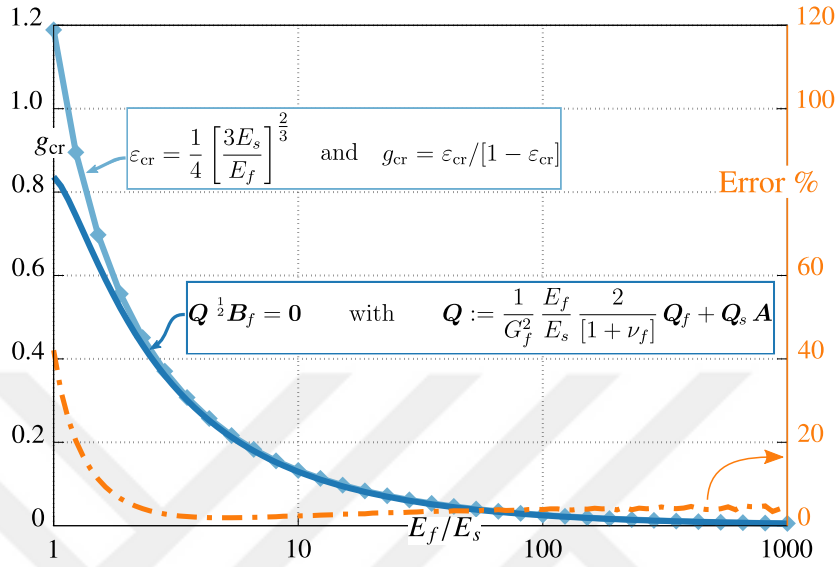


Figure 6.3: The variation of $g_{\rm cr}$ over a range of stiffness ratio (E_f/E_s) and substrate compressibilities. To recover the Euler beam assumption, $\nu_f = \nu_s \to 0.99$. Light blue line denotes the small strain linear elastic approach in Chapter 3. Dark blue line is the solution found in Eq. 6.40. The percentage error between the two sets of results has been given on the y_2 axis.

genericness of the framework developed here, it is also possible to explore the effect of compressibility on growth-induced instabilities. From preliminary investigations, it is seen that when the substrate in the system in Fig. 6.3 is made increasingly more compressible, a flattening out behavior is observed at lower stiffness ratios, similar to that observed in Fig. 4.11, but this time at values larger than $E_f/E_s = 1$. This behavior warrants more in-depth investigation and shall be pursued in upcoming works.

Since the formulation here allows for both growth and prescribed deformation, next we look at the combination of both applied compression and a growing film. Clearly, when there is no external compression applied, i.e. when $\lambda = 1$, the solution recovers the pure growth case studied extensively in the literature, and also formulated in Chapter 6, in a linear framework. Similarly, when there is no growth and only external compression is applied, the results recover those formulated in Chapter 4. These results are elaborated on further in Fig. 6.4, where the bifurcation behavior of a system which undergoes growth and compression at the same time has been plotted. The two limit cases of critical growth $g_{\rm cr}$ plotted

against stiffness ratio for zero compression is shown on the left, and critical stretch λ_{cr} against stiffness ratio for zero growth is shown on the right. There clearly is a linear relationship between the critical growth g_{cr} and critical stretch λ_{cr}, for all stiffness ratios, which can be seen from the sample contours shown in blue of the g_{cr} vs. λ_{cr} relationship at sample stiffness ratios. This means that for a structure of a specific stiffness ratio, the system will bifurcate at (g_{cr}, λ_{cr}). Clearly, which deformation will trigger the bifurcation depends on how the loading or growth is applied and the order.

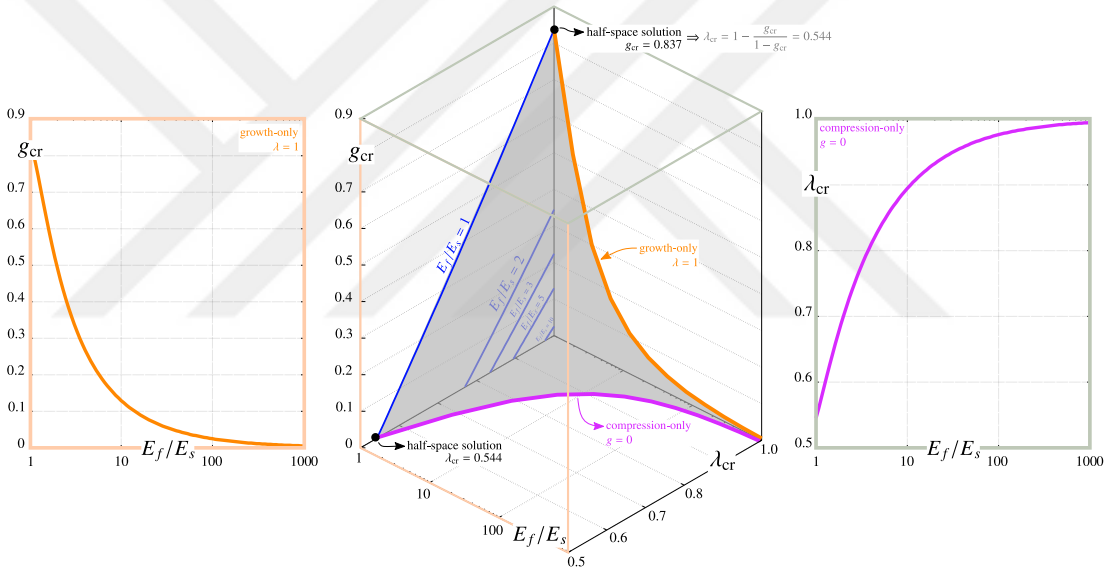


Figure 6.4: The variation of g_{cr} and λ_{cr} over a range of stiffness ratio (E_f/E_s), for $\nu_s = \nu_f = 0.99$ (center). Critical growth g_{cr} plotted against stiffness ratio for zero compression (left), and critical stretch λ_{cr} against stiffness ratio for zero growth (right).

This concludes this chapter on formulation of a theoretical framework which can capture both the growth-induced and deformation-induced instabilities of compressible domains. Even though the examples of the framework illustrated here are for an incompressible bilayer structure, for the sake of comparison with previous findings, it should be noted that the framework is generic and can be used to solve for compressible systems, as well as other geometries. The influence of compressibility, non-linearity, and low stiffness ratios on growth-induced instabilities, both growth alone and combined with prescribed deformation, remain open questions which will be investigated in future works.

Chapter 7

Summary and outlook

A generic, theoretical framework has been developed and presented herein to capture the wrinkling instabilities of rectangular, multilayer domains; with/without interfaces and including growth effects. The results of the theoretical framework have been evaluated at certain limits which have been established previously in the literature, such as the incompressible limit or the pure-growth and pure-compression cases. Apart from the limit cases, wide ranges of sizes and material/interfacial parameters have been examined. Furthermore, the analytical results for all these parameters and regimes have been compared exhaustively with results from numerical analyses obtained via the finite element method (FEM) using eigenvalue analysis, presenting an excellent agreements.

Firstly, in Chapter 3, a small-deformations, displacement-based approach to analyze geometric instabilities in linear elastic bilayer structures has been presented. In particular, introducing the notion of effective stiffness here provided a great insight into instabilities of bilayer systems and equipped us with a powerful methodology to deal with more complicated cases beyond the classical bilayer structures. Seeing that the deformations that bilayer structures go under cannot be sufficiently captured all throughout the material parameter range by a small-deformations approach, next, a large-deformation approach was developed, accounting for the non-linearities in material behavior.

Hence, a generic theoretical framework has been outlined next in Chapter 4 wherein Poisson's ratio has come into light since incompressibility is not assumed from the onset. More importantly, we have established that (i) a non-linear description of Poisson's ratio is required for this problem and (ii) the commonly accepted definitions for non-linear Poisson's ratio are not suitable for the problem at hand. Thus, we have introduced a novel non-linear Poisson's ratio definition that sufficiently fulfills the traction-free boundary condition. Throughout the derivations and the subsequent applications for the geometries of half-space, beam, bilayer and trilayer, it has been demonstrated that the compressible model, at the incompressibility limit, recovers its incompressible counterparts. *Implicit* analytical solutions for the critical stretch of a compressible elastic half-space, beam, bilayer, and trilayer structure have been derived.

Half-space results have been shown to recover the well established limits in the literature and match numerical results perfectly, underpinning the utility of the unified framework proposed here, also demonstrating the large influence of compressibility on critical stretch. An *explicit* estimate in the form of a quadratic polynomial that conforms to the analytical solution for the critical stretch of a half-space has been provided. Beam bifurcation has been studied in depth, looking at the effect of compressibility and beam slenderness on bifurcation behavior, and the results have been shown to recover the Euler beam theory at the incompressible and slender limit, while also being in excellent agreement with numerical results independent of the slenderness, hence useful for thick beams. An important conclusion to be drawn here is that the compressibility not only affects the critical compression, but also the resulting deformation profiles. Bilayer results for critical compression and critical wavelength were shown to match the numerical findings obtained through computational simulations, and displayed subtle dependencies on the compressibility of the film and substrate, and various combinations of the two. The effect of compressibility on the bifurcation behavior of a trilayer structure with various stiffness ratios and dimensions was investigated next. Changing compressibility was found to have a profound effect on both critical stretch and critical wavelength especially in cases where the interphase layer is more compliant than the substrate. Furthermore, the analytical solution, for

critical wavelength, yielded a single, broader solution which allows for the capturing of the different wrinkling modes. In particular, the two-mode bifurcation associated with trilayers was shown to actually be a part of a continuous trend as interphase thickness is increased, as opposed to what has been regarded as a two-part problem in the literature. All analytical solutions have been compared with numerical simulations using the finite element method, and an excellent agreement among the two sets of results have been observed, even close to the incompressibility limit.

The framework has then been extended to include the general interface model, and corresponding geometries have been analyzed. Substrate compressibility together with cohesive stiffness was seen to have a significant effect on the overall bifurcation behavior of a bilayer system. Although the bifurcation onset of classical bilayers is commonly accepted to be independent of film thickness, it is seen that this notion is merely one limit of a much broader spectrum when interface is accounted for. That is, the onset of bifurcation depends substantially on film thickness in the presence of a cohesive interface between the film and substrate, due to the additional length scale introduced to the system, which is entirely absent in classical bilayers. This extension provides grounds for further studies on how an interphase layer can be approximated via an interface model.

Finally, in order to compare the results of a non-linear, large deformations framework to those of a linear elastic framework, the theoretical framework has been extended to include growth, and the results have been analyzed for a bilayer structure. The results of the non-linear framework captured the well-established linear-elastic solution perfectly at large stiffness ratios, while actually presenting more accurate results for smaller stiffness ratios where deformations get larger. Furthermore, the interplay between growth and applied compression was analyzed and it was seen that for each set of material parameters there exists a combination of critical growth and critical stretch values.

Overall, with the implementations of the frameworks developed here, it is possible to explore the wrinkling instability of a wide range of domains, without conforming to unrealistic limits such as incompressibility or linear elasticity. This

allows for a more accurate prediction of the structures' behavior, since the crucial contributions the compressibility of the materials make to the bifurcation behavior of the structures they form was clearly demonstrated in all sections. Having established this framework, we can readily explore many other problems, such as double or three-layer beams, which are frequently used in buckling applications, and other multilayer domains, by also accounting for interface or growth effects.

All the analysis here is limited to the onset of bifurcation; exploring the post-bifurcation regime and the effect of compressibility or nature of loading on the post-bifurcation behavior of multilayer domains also constitutes a future path of study. One other possible extension of this work is to enhance the general interface model to take into account the flexural resistance [102] in addition to elasticity along the interface and cohesive resistance across the interface. Finally, the work done here can be further extended to other geometries such as axisymmetric problems, and include surface tension following roughly the steps taken in incorporating the general interface model. This would allow for the analysis of the buckling of structures such as nano-beams [215], or for capturing phenomena such as the Plateau-Rayleigh instability of soft solids [216].

Appendix A

Further information on FEM using eigenvalue analysis

In this section, we provide further details about the computational analysis. In particular, we elaborate on our calculations of critical stretches associated with Biot instability using the finite element method. The underlying feature of our computational study is that (i) the perturbations are suppressed and (ii) the finite element method is enhanced with eigenvalue analysis. More precisely, we carry out our calculations within the eigenspace of the system tangent

$$\boldsymbol{K} = \sum_{i=1}^{n} K_i \, \boldsymbol{\lambda}_i \otimes \boldsymbol{\lambda}_i \, ,$$

where K_i and $\boldsymbol{\lambda}_i$, denote eigenvalues and their associated *unit* eigenvectors, respectively, for a system with n degrees of freedom. *Biot instabilities occur when the smallest eigenvalue of the stiffness matrix approaches zero and thus the system loses its positive definiteness.*

Starting from the reference configuration corresponding to $\lambda = 1$, we *incrementally* prescribe compression in the horizontal direction. After prescribing displacements of each increment, we let the domain relax via iterations of a Newton–Raphson scheme. The equilibrium state is reached when the L_2-norm of

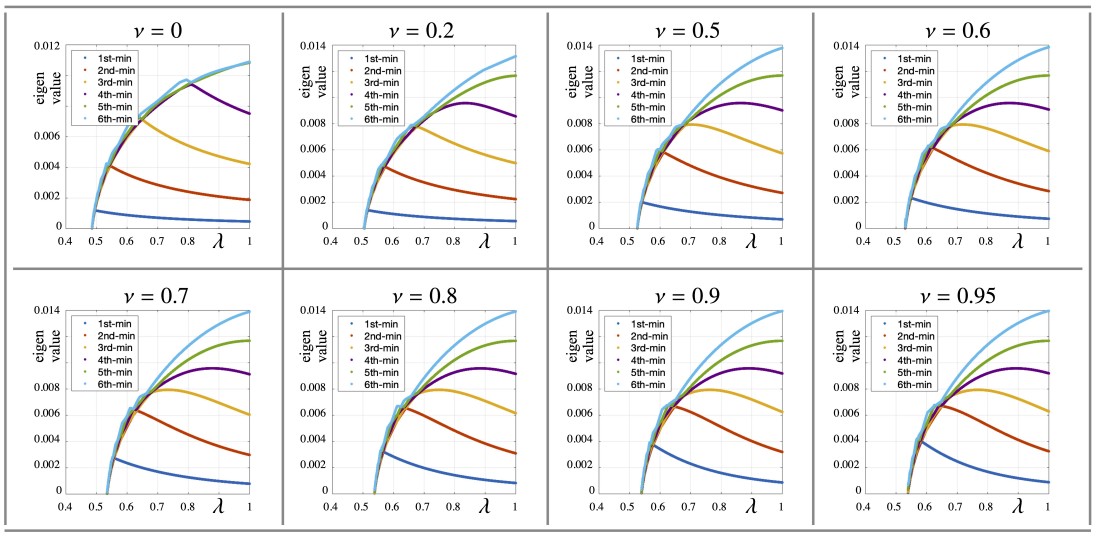


Figure A.1: The six smallest eigenvalues of the tangent stiffness versus the stretch λ for various Poisson's ratios. The reference configuration corresponds to $\lambda = 1$ and compression is prescribed incrementally until λ_{cr} is reached.

the residual reaches zero. Throughout the iterations, the quadratic rate of convergence associated with the Newton–Raphson scheme is consistently obtained. At each increment, we carry out an eigenvalue analysis at the equilibrium configuration. If all the eigenvalues are positive, we proceed with the next increment. If any of the eigenvalues is sufficiently close to zero, then (i) we record the prescribed stretch as the critical stretch λ_{cr}, (ii) we compute the eigenvector of the smallest eigenvalue and impose it as a deformation and (iii) we terminate the computations. We repeat this procedure for all Poisson's ratios. Further details of the methodology are given in Fig. A.1 for a select set of Poisson's ratio.

Figure A.1 gathers the plots of the six smallest eigenvalues of the tangent stiffness versus the stretch λ. A key characteristic of the Biot instability is that all eigenvalues of the system collapse to zero as it can be seen in Fig. A.1. Each curve consists of individual points corresponding to increments. Equipped with the critical stretch, we calculate the eigenvector associated with the smallest eigenvalue and impose it as deformation on the domain. Figure A.2 gathers the smallest eigenvalues of the stiffness matrix for different Poisson's ratio. In addition, the eigenvector associated with the smallest eigenvalue for each case is illustrated. The color pattern on the domain corresponds to the normalized

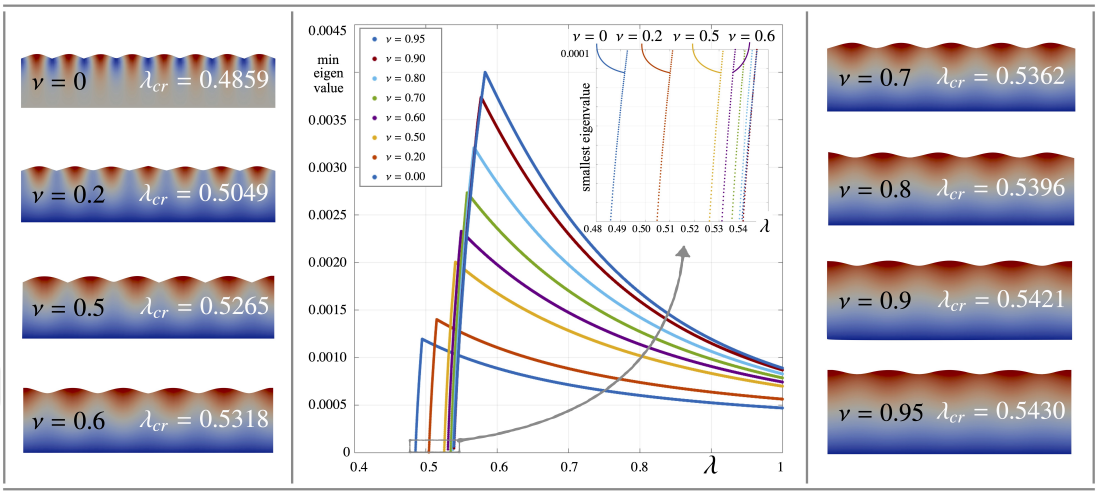


Figure A.2: Illustration of the smallest eigenvalues of the tangent stiffness of the domain for various Poisson's ratio together with their associated eigenvectors. The color pattern on the domain corresponds to the normalized displacement in the vertical direction.

displacement in the vertical direction.

The computational simulations demonstrated in Fig. A.1 and Fig. A.2 correspond to a domain with a width-to-height aspect ratio of 10. Figure A.3 shows the domain and its discretization to 1000 bi-quadratic elements. The compression is applied via prescribed displacements on the left and right edges. The domain at the bottom is on roller supports that prevent displacement in the vertical direction but do not pose any restriction on displacement in the horizontal direction. The upper surface fulfills the traction-free boundary condition and is thus free of essential boundary conditions. The color bars show the normalized vertical displacement in each case where the deformation is again the eigenvector of the smallest eigenvalue imposed on the domain. It can be seen that the height of the fully compressible domain on the left remains constant in contrast to the nearly incompressible domain on the right whose height almost doubles. This observation is in agreement with our expectation that a fully compressible material does not retain its volume in contrast to an incompressible material whose volume remains constant throughout deformations.

We shall emphasize that this particular geometry and discretization is used

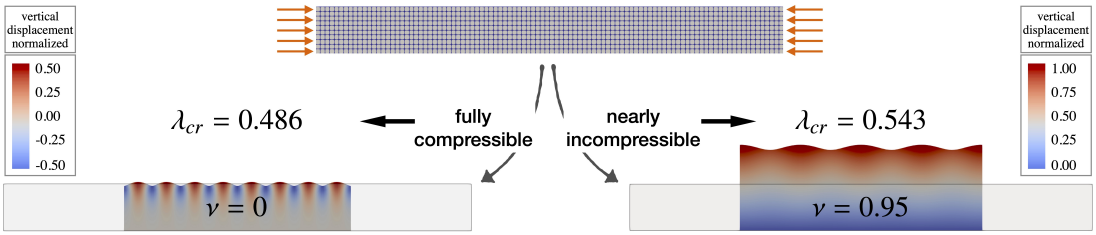


Figure A.3: Illustration of the domain, the finite element discretization and the deformation. The color bars show the normalized vertical displacement which is the eigenvector of the smallest eigenvalue imposed on the domain. The height of the fully compressible domain (left) remains constant in contrast to the nearly incompressible domain (right) whose height nearly doubles.

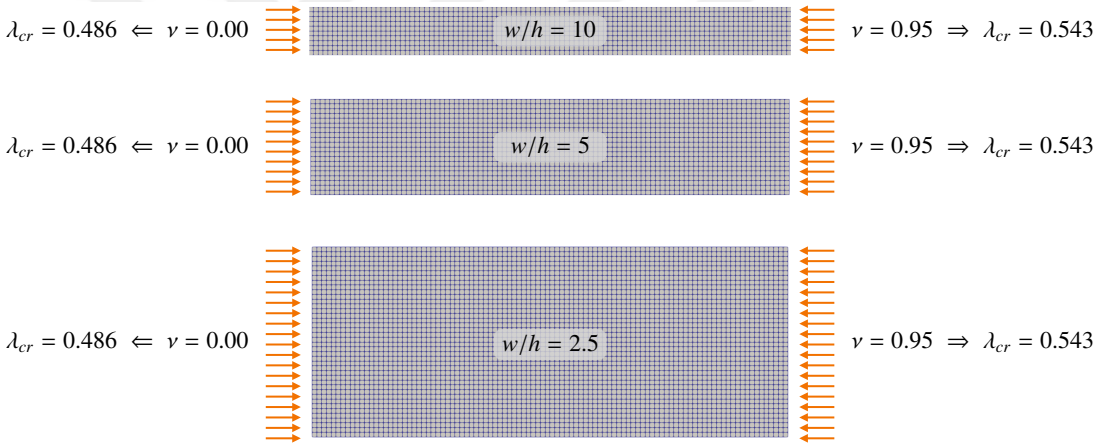


Figure A.4: Illustration of the domain and the finite element discretization for various aspect ratios.

only for the sake of illustrations in this section. To ensure the accuracy of our approach and to learn about its sensitivity to various numerical factors, we carry out a convergence study as well. That is, we repeat the process for various aspect ratios as well as finer and coarser finite element discretizations and compare the results. Subsequently, we repeat this process again with finer increments to achieve a higher precision in calculation of the critical stretch. For instance, Fig. A.4 illustrates our spatial discretization for three different aspect ratios. For all three examples, we obtain the same critical stretch up to the third decimal digit, which demonstrates the robustness and reliability of our approach. We omit further details of the convergence study for the sake of brevity.

Appendix B

Incompressible half-space

Here we formulate the well-established problem of surface instabilities of an *incompressible elastic half-space*, see [89, 93] among others, starting from the constitutive behavior established in 2.4.2. Let u and v denote the displacements in ξ and γ directions, respectively, thereby no stretch occurs in the thickness direction ζ. The incompressibility of the material is imposed through the condition $J = 1$. Denoting λ as the stretch in ξ direction, the deformation gradient reads $\boldsymbol{F} = \lambda\, \boldsymbol{e}_\xi \otimes \boldsymbol{e}_\xi + 1/\lambda\, \boldsymbol{e}_\gamma \otimes \boldsymbol{e}_\gamma + 1\, \boldsymbol{e}_\zeta \otimes \boldsymbol{e}_\zeta$ with $1/\lambda$ being the stretch in γ direction such that $J = 1$ is a priori satisfied. The constitutive behavior of an incompressible elastic material is dictated by Eq. (2.20). The traction-free boundary condition, namely $\boldsymbol{P} \cdot \boldsymbol{N} = \boldsymbol{0}$, shall be applied with $\boldsymbol{N}$ being the outward unit normal in the material configuration and in γ direction. That is

$$\boldsymbol{P} \cdot \boldsymbol{N} = \boldsymbol{0} \qquad \Rightarrow \qquad \mu\, \boldsymbol{F} \cdot \boldsymbol{N} - p\, \boldsymbol{F}^{-\mathrm{t}} \cdot \boldsymbol{N} = \boldsymbol{0} \qquad \Rightarrow \qquad p = \frac{\mu}{\lambda^2}\,. \tag{B.1}$$

Thus, the traction-free boundary condition furnishes a relation for the Lagrange multiplier p in terms of the stretch λ and shear modulus μ. The incremental deformation gradient $\delta\boldsymbol{F}$ then results in the incremental Piola stress

$$\delta\boldsymbol{P} = \mu \begin{bmatrix} \delta u_{,\xi} & \delta u_{,\gamma} \\ \delta v_{,\xi} & \delta v_{,\gamma} \end{bmatrix} - \delta p \begin{bmatrix} \frac{1}{\lambda} & 0 \\ 0 & \lambda \end{bmatrix} + p \begin{bmatrix} \frac{\delta u_{,\xi}}{\lambda^2} & \delta v_{,\xi} \\ \delta u_{,\gamma} & \lambda^2 \delta v_{,\gamma} \end{bmatrix}, \tag{B.2}$$

with δp being the incremental Lagrange multiplier, and δu and δv denoting incremental displacements. For the given problem, we assume a general form of the solution for the incremental problem. The incremental functions for δu, δv and δp are constituted of (i) a decay term, $\exp(r\,\gamma)$, to account for the decay of the surface instability through the depth of the substrate and (ii) a waviness term, $\sin(k\,\xi)$ or $\cos(k\,\xi)$, along the ξ direction. That is

$$\delta u = A\,\exp(r\,\gamma)\,\sin(k\,\xi) \quad , \quad \delta v \;\; = B\,\exp(r\,\gamma)\,\cos(k\,\xi) \quad , \tag{B.3}$$

and

$$\delta p = C\,\exp(r\,\gamma)\,\cos(k\,\xi)\,. \tag{B.4}$$

The coefficient r is referred to as the decay coefficient while k is the wavenumber. Furthermore, the incompressibility condition must also be satisfied for the incremental analysis. More precisely, we impose the condition $\delta J = 0$ with $J = 1$ in which we plug in the corresponding directional derivatives associated with the ansatz (B.3). After some mathematical manipulations, a relation between the constants A and B is obtained as

$$A = -\frac{B\,\lambda^2\,r}{k}\,. \tag{B.5}$$

Inserting $\delta\boldsymbol{P}$ from Eq. (B.2) into the incremental linear momentum balance, after some mathematical steps, yields

$$\mathrm{Div}\delta\boldsymbol{P} = \boldsymbol{0} \qquad \Rightarrow \qquad \begin{cases} A\,\left[k^2\,\left[\lambda^4+1\right] - \,r^2\,\lambda^4\right] + B\,kr\lambda^2 - \,\dfrac{C}{\mu}\,\lambda^3\,k = 0\,, \\ A\,k\,r - B\,\lambda^2\,\left[\,k^2 - 2r^2\right] - \,\dfrac{C}{\mu}\,\lambda^3\,r = 0\,. \end{cases} \tag{B.6}$$

Replacing the relation (B.5) between A and B in Eq. (B.6) renders

$$\begin{cases} \left[k^2 - r^2\right]\,B + \dfrac{k^2}{\lambda^3\,r}\,\dfrac{C}{\mu} = 0\,, \\ \left[k^2 - r^2\right]\,B + \lambda\,r\,\dfrac{C}{\mu} = 0\,, \end{cases} \qquad \Rightarrow \qquad \begin{bmatrix} [k^2-r^2] & \dfrac{k^2}{\lambda^3\,r\,\mu} \\ [k^2-r^2] & \dfrac{\lambda r}{\mu} \end{bmatrix} \begin{bmatrix} B \\ C \end{bmatrix} = \begin{bmatrix} 0 \\ 0 \end{bmatrix}. \tag{B.7}$$

The non-trivial solutions for B and C are obtained by setting the determinant of the coefficient matrix to zero. That is

$$\Big[\, k^2 - r^2 \,\Big]\Big[\, \lambda r - \frac{k^2}{\lambda^3 r} \,\Big] = 0 \qquad \Rightarrow \qquad r_{1,3} = \pm k \qquad \text{and} \qquad r_{2,4} = \pm \frac{k}{\lambda^2}\,, \tag{B.8}$$

indicating that the system has four roots. Owing to the initial definition, $\gamma < 0$ in the decay direction. That is, among the roots of Eq. (B.8) only the positive values for r are admissible. By plugging in the admissible solutions for r into Eq. (B.7), we find out the relations between the coefficients B and C. Furthermore, from Eq. (B.5), the corresponding relations between the coefficients A and B can be obtained. That is

$$\begin{cases} r_1 = k & \Rightarrow \quad C_1 = 0 & \text{and} \quad A_1 = -B_1\,\lambda^2\,, \\ r_2 = \dfrac{k}{\lambda^2} & \Rightarrow \quad C_2 = B_2\,\mu\,k\,\left[\dfrac{1}{\lambda^3} - \lambda\right] & \text{and} \quad A_2 = -B_2\,. \end{cases} \tag{B.9}$$

The proposed incremental relations (B.3) are then expanded according to the two solutions in Eq. (B.9) as

$$\begin{aligned} \delta u &= [A_1\, \exp(r_1\,\gamma) + A_2\, \exp(r_2\,\gamma)]\, \sin(k\,\xi)\,, \\ \delta v &= [B_1\, \exp(r_1\,\gamma) + B_2\, \exp(r_2\,\gamma)]\, \cos(k\,\xi)\,, \\ \delta p &= [C_1\, \exp(r_1\,\gamma) + C_2\, \exp(r_2\,\gamma)]\, \cos(k\,\xi)\,. \end{aligned} \tag{B.10}$$

Next, we enforce the incremental traction-free boundary condition $\delta \boldsymbol{P} \cdot \boldsymbol{N} = \boldsymbol{0}$ at $\gamma = 0$. That is

$$\begin{cases} \delta P_{12} = 0 & \Rightarrow \quad \mu\,[r_1 A_1 + r_2 A_2] - \dfrac{\mu}{\lambda^2}\,k\,[B_1 + B_2] = 0\,, \\ \delta P_{22} = 0 & \Rightarrow \quad 2\mu\,[r_1 B_1 + r_2 B_2] - \lambda\,[C_1 + C_2] = 0\,. \end{cases} \tag{B.11}$$

Using the relations (B.9) for the coefficients, the two equations (B.11) can be alternatively expressed as

$$\underbrace{\begin{bmatrix} \left[\,\lambda^2 + \dfrac{1}{\lambda^2}\,\right] & \dfrac{2}{\lambda^2} \\ 2 & \left[\,\lambda^2 + \dfrac{1}{\lambda^2}\,\right] \end{bmatrix}}_{\boldsymbol{M}} \begin{bmatrix} B_1 \\ B_2 \end{bmatrix} = \begin{bmatrix} 0 \\ 0 \end{bmatrix} . \tag{B.12}$$

Finally, the determinant of $\boldsymbol{M}$ is set to zero to find the non-trivial solutions of the system (B.12). That is

$$\text{Det}\,\boldsymbol{M} = 0 \quad \Rightarrow \quad \left[\lambda^2 + \frac{1}{\lambda^2}\right]^2 - \frac{4}{\lambda^2} = 0 \quad \Rightarrow \quad \lambda_{cr} = 1.0 \quad \text{and} \quad \lambda_{cr} = 0.5437\,. \tag{B.13}$$

The solutions of the equation $\text{Det}\boldsymbol{M} = 0$ are precisely the critical stretches recovering the classical results that have been reported by Biot [89] and Nowinski [90], among others, and also the incompressible limit of the results of Chapter 4 as presented in Eq. (4.29). Figure B.1 illustrates the behavior of $\text{Det}\,\boldsymbol{M}$ and its roots.

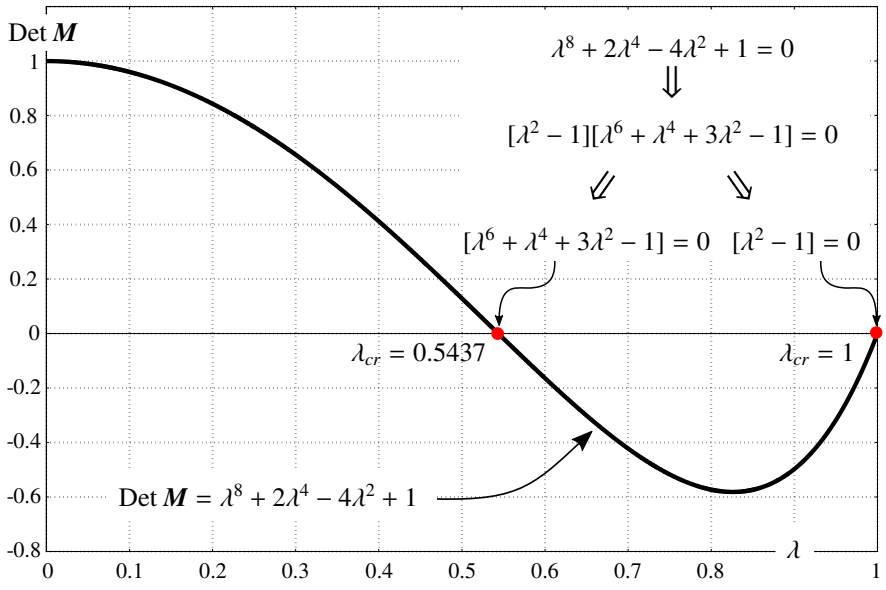


Figure B.1: Illustration of $\text{Det}\,\boldsymbol{M}$ and its roots associated with Eq. (B.13).

Appendix C

Non-linear Poisson's ratio

In its classical definition, that being a kinematic definition in a small deformations context, Poisson's ratio is a constant obtained from the deformation of a domain under uni-axial tension or compression in the axial and lateral directions, illustrated in Fig. C.1. More precisely, it relates to the case where an isotropic domain is subject to an axial strain ε_{ext} in a uni-axial tension test, resulting in the lateral strain ε_{lat}. For the small-strain case the Poisson's ratio definition reads

$$\nu = -\frac{\varepsilon_{\text{lat}}}{\varepsilon_{\text{ext}}}\,, \tag{C.1}$$

which is obviously a *purely geometrical description* in that only geometrical, and not material parameters, are present. The definition of the Poisson ratio (C.1) is the most elementary one. It stems from a purely kinematic stand point, relating the two different resultant strain values of a body, rendering a constant that essentially describes the compressibility of the material.

Note that, on the one hand, Poisson's ratio definition is geometrical in nature and is constant for a material at small strains. On the other hand, from the linear elasticity analysis of isotropic Neo-Hookean materials, one can immediately establish a one-to-one relationship between the geometrical description of Poisson's

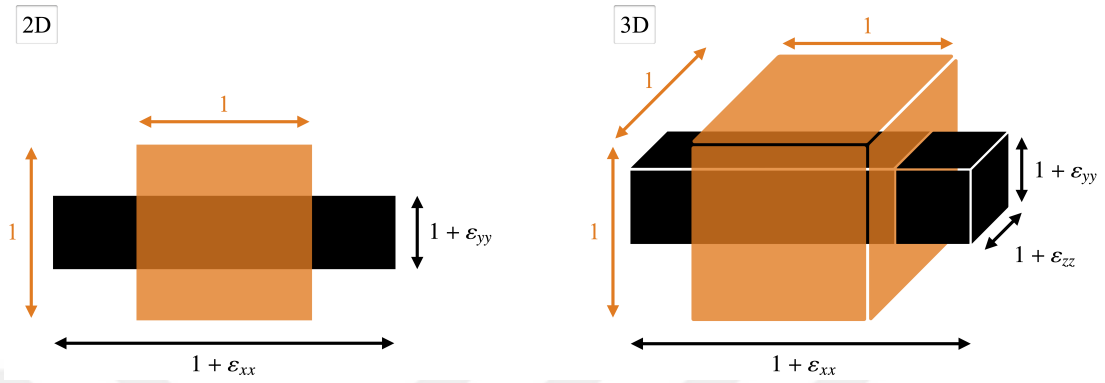


Figure C.1: Affine deformation of a unit domain under uni-axial tension test. Lateral deformations occur naturally to minimize the energy, while extension ε_{xx} is a prescribed value.

ratio (C.1) and Lamé parameters as

$$\text{2D} \quad : \quad \nu = \frac{\Lambda}{\Lambda + 2\mu} \quad , \qquad \text{3D} \quad : \quad \nu = \frac{\Lambda}{2\left[\Lambda + \mu\right]} \, , \tag{C.2}$$

where Λ and μ are the first and second Lamé parameters, respectively. Table C.1 elucidates the dual nature of Poisson's ratio associated with small-strain linear elasticity. For common (non-auxetic) materials, the Poisson ratio ranges from zero associated with a *fully compressible* material, to $\nu = 0.5$ corresponding to *incompressibility limit* in three-dimensional elasticity. The incompressibility limit for two-dimensional or plane-strain elasticity corresponds to $\nu = 1$, as it can be immediately realized from the geometrical constraints that correspond to a constant area of the domain. Henceforth, for the sake of brevity, we use the term "2D" to represent plane-strain conditions or purely two-dimensional elasticity similar to the interface elasticity theory, see [217]. Poisson's ratio can also take values less than zero, attributed to auxetic materials.

In this section, we elaborate on the variational approach used to capture Poisson's ratio in classical continuum mechanics (CCM). The variational approach at small-strain linear elasticity does not result in new findings. At large deformations, however, it leads to an alternative description of the Poisson ratio, different from those that stem from the commonly accepted approach by [185]. To set the stage and convey the idea, we begin with the case of small-strain linear elasticity.

Table C.1: Poisson's ratio in small-strain linear elasticity and its dual nature as a material parameter (left) or a geometrical definition (right).

	material description	geometrical description
2D	$\dfrac{\Lambda}{\Lambda + 2\mu} = \nu = -\dfrac{\varepsilon_{yy}}{\varepsilon_{xx}}$	
3D	$\dfrac{\Lambda}{2\,[\Lambda + \mu]} = \nu = -\dfrac{\varepsilon_{yy}}{\varepsilon_{xx}} = -\dfrac{\varepsilon_{zz}}{\varepsilon_{xx}}$	

We then employ the same variational approach at large deformations nonlinear elasticity. For both discussions on small strains as well as finite deformations, the underlying equation is the equilibrium of a domain under uni-axial tension. Hence, next we formulate equilibrium for the problem at hand.

Under prescribed boundary conditions, equilibrium corresponds to a relaxed state where the deformation field results in the minimum total energy functional. The total energy functional Ψ_{tot} consists of the internal and external contributions denoted Ψ_{int} and Ψ_{ext}, respectively. To minimize Ψ_{tot}, its first variation with respect to deformation, or rather motion, is set to zero as

$$\Psi_{\text{tot}} = \Psi_{\text{int}} + \Psi_{\text{ext}} \quad , \quad \delta\Psi_{\text{tot}} \doteq 0 \quad \Rightarrow \quad \delta\Psi_{\text{tot}} = \delta\Psi_{\text{int}} + \delta\Psi_{\text{ext}} \doteq 0\,. \tag{C.3}$$

The external energy Ψ_{ext}, in first-order classical continuum mechanics, is essentially minus work as

$$\delta\Psi_{\text{ext}} = -\delta\mathcal{W} \qquad \text{with} \qquad \delta\mathcal{W} = \int_{\mathcal{B}_0} \boldsymbol{b}_0 \cdot \delta\boldsymbol{\varphi}\,\mathrm{d}V + \int_{\partial\mathcal{B}_0} \boldsymbol{t}_0 \cdot \delta\boldsymbol{\varphi}\,\mathrm{d}A\,, \tag{C.4}$$

in which $\mathcal{W}$ denotes the "working", and $\boldsymbol{b}_0$ and $\boldsymbol{t}_0$ are the external body force density and surface force density in the material configuration, respectively. For further details and generalized boundary conditions, see [218–221]. The arbitrary variation of motion, denoted as $\delta\boldsymbol{\varphi}$, is a vector-valued test function that is vanishing where Dirichlet-type boundary conditions are imposed. For a uni-axial

Table C.2: Poisson's ratio at large deformations nonlinear elasticity. The geometrical description of Poisson's ratio has been extended to large deformations (top). We propose an extension of the material description of Poisson's ratio (bottom), via a variational approach. At the reference configuration, both nonlinear variants coincide with their linear counterparts in Table C.1.

	Beatty & Stalnaker (extension of geometrical description)	
2D	$\nu = -\dfrac{E_{yy}}{E_{xx}}$	$\begin{cases} \boldsymbol{E} = \ln \boldsymbol{U} & m = 0 \\ \boldsymbol{E} = \dfrac{1}{m}[\,\boldsymbol{U}^m - \boldsymbol{I}\,] & m \neq 0 \end{cases}$
3D	$\nu = -\dfrac{E_{yy}}{E_{xx}} = -\dfrac{E_{zz}}{E_{xx}}$	

	current approach (extension of material description)
2D	$\boldsymbol{F} = \mathrm{Diag}(\lambda, \eta) \quad \& \quad \delta\psi = 0 \quad \Rightarrow \quad \nu = \nu(\lambda, \eta)$
3D	$\boldsymbol{F} = \mathrm{Diag}(\lambda, \eta, \eta) \quad \& \quad \delta\psi = 0 \quad \Rightarrow \quad \nu = \nu(\lambda, \eta)$

tension test which is of interest here, the external body forces are zero and therefore the first integral in Eq. (C.4) vanishes identically. The second integral in Eq. (C.4) vanishes too, since (i) $\delta\boldsymbol{\varphi}$ is zero where displacements are prescribed on the two ends of the domain and (ii) $\boldsymbol{t}_0$ is zero everywhere that a homogeneous Neumann-type boundary condition is imposed. That is, *for the particular problem of a uni-axial tension test*, we seek for the solutions of $\delta\Psi_{\text{int}} = 0$. The internal energy Ψ_{int} reads

$$\Psi_{\text{int}} = \int_{\mathcal{B}_0} \psi \, \mathrm{d}V \,, \tag{C.5}$$

and therefore equilibrium for the current problem reduces to

$$\delta\Psi_{\text{int}} = \int_{\mathcal{B}_0} \delta\psi \, \mathrm{d}V \doteq 0 \,. \tag{C.6}$$

For a uniform deformation in the domain, which holds for a uni-axial tension test,

the equilibrium (C.6) then corresponds to

$$\delta\psi \doteq 0\,. \tag{C.7}$$

The variational constraint (C.7) is an underlying relationship that holds throughout this discussion, and also holds for finite deformations as well as small strains.

Let $\boldsymbol{\varepsilon}$ be the strain tensor associated with small-strain linear elasticity. In order to establish a variational approach, one needs to begin from the scalar free energy density ψ corresponding to small-strain linear elasticity

$$\psi = \frac{1}{2}\boldsymbol{\varepsilon} : \mathbb{C} : \boldsymbol{\varepsilon}\,, \tag{C.8}$$

with $\mathbb{C}$ being the fourth-order constitutive tensor. The fourth-order constitutive tensor in terms of the first and second Lamé parameters Λ and μ, respectively, reads

$$\mathbb{C} = \mu\,[\boldsymbol{I}\overline{\otimes}\boldsymbol{I} + \boldsymbol{I}\underline{\otimes}\boldsymbol{I}] + \Lambda\,\boldsymbol{I}\otimes\boldsymbol{I}\,, \tag{C.9}$$

and therefore

$$\psi = \psi(\boldsymbol{\varepsilon}) = \mu\,\boldsymbol{\varepsilon} : \boldsymbol{\varepsilon} + \frac{1}{2}\Lambda\,\mathrm{Tr}^2\boldsymbol{\varepsilon}\,. \tag{C.10}$$

Using the relationship (C.2), the free energy density (C.10) in terms of μ and Poisson's ratio ν reads

$$\begin{cases} \text{2D} \quad : \quad \psi = \mu\,\boldsymbol{\varepsilon} : \boldsymbol{\varepsilon} + \dfrac{\mu\nu}{1-\nu}\mathrm{Tr}^2\boldsymbol{\varepsilon}\,, \\ \text{3D} \quad : \quad \psi = \mu\,\boldsymbol{\varepsilon} : \boldsymbol{\varepsilon} + \dfrac{\mu\nu}{1-2\nu}\mathrm{Tr}^2\boldsymbol{\varepsilon}\,. \end{cases} \tag{C.11}$$

For a uni-axial tension test in Fig. C.1, the strain tensor simplifies to a diagonal tensor

$$\text{2D} \;:\; \boldsymbol{\varepsilon} = \mathrm{Diag}(\varepsilon_{xx}, \varepsilon_{yy}) \qquad , \qquad \text{3D} \;:\; \boldsymbol{\varepsilon} = \mathrm{Diag}(\varepsilon_{xx}, \varepsilon_{yy}, \varepsilon_{zz})\,, \tag{C.12}$$

wherein $\varepsilon_{yy} = \varepsilon_{zz}$ is the lateral strain in 3D. Inserting strains (C.12) into the

internal energy density (C.11) furnishes

$$\begin{cases} \text{2D} \quad : \quad \psi = \mu\,[\varepsilon_{xx}^2 + \varepsilon_{yy}^2] + \dfrac{\mu\nu}{1-\nu}\,[\varepsilon_{xx} + \varepsilon_{yy}]^2\,, \\ \text{3D} \quad : \quad \psi = \mu\,[\varepsilon_{xx}^2 + 2\,\varepsilon_{yy}^2] + \dfrac{\mu\nu}{1-2\nu}\,[\varepsilon_{xx} + 2\,\varepsilon_{yy}]^2\,. \end{cases} \tag{C.13}$$

Next, we set $\delta\psi \doteq 0$ in order to impose equilibrium (C.7). In doing so, note that $\psi = \psi(\varepsilon_{xx}, \varepsilon_{yy})$ and therefore

$$\delta\psi = \frac{\partial\psi}{\partial\varepsilon_{xx}}\,\delta\varepsilon_{xx} + \frac{\partial\psi}{\partial\varepsilon_{yy}}\,\delta\varepsilon_{yy} \doteq 0\,. \tag{C.14}$$

However, for the problem at hand, the extension ε_{xx} is a prescribed quantity and therefore ε_{yy} is the only remaining variable. This immediately results in

$$\delta\psi \doteq 0 \qquad \Rightarrow \qquad \frac{\partial\psi}{\partial\varepsilon_{yy}} \doteq 0\,. \tag{C.15}$$

Finally, we insert the energy densities (C.13) into the *reduced equilibrium equation* (C.15). That is

$$\frac{\partial\psi}{\partial\varepsilon_{yy}} \doteq 0 \quad \Rightarrow \quad \begin{cases} \text{2D} \quad : \quad 2\mu\,\varepsilon_{yy} + \dfrac{2\mu\nu}{1-\nu}\,[\varepsilon_{xx} + \varepsilon_{yy}] \doteq 0\,, \\ \text{3D} \quad : \quad 2\mu\,\varepsilon_{yy} + \dfrac{2\mu\nu}{1-2\nu}\,[\varepsilon_{xx} + 2\,\varepsilon_{yy}] \doteq 0\,. \end{cases} \tag{C.16}$$

Solving each relation in Eq. (C.16), results in

$$\text{2D} \quad : \quad \nu = -\frac{\varepsilon_{yy}}{\varepsilon_{xx}} \qquad , \qquad \text{3D} \quad : \quad \nu = -\frac{\varepsilon_{yy}}{\varepsilon_{xx}}\,, \tag{C.17}$$

which shall be compared with Eq. (C.2). That is, *starting from energy, via a variational procedure for a uni-axial tension test, one can show that the material description of Poisson's ratio indeed coincides with its geometrical definition.* This finding per se is not surprising. Nonetheless, as we will see shortly, the same procedure at finite deformations results in relationships for Poisson's ratio that are different from those previously reported in literature.

Consider the deformation of a continuum body, as illustrated in Fig 2.1. For

large deformations, and from a geometrical perspective, the Poisson ratio can still be expressed as minus the ratio of lateral strain to extensional strain, similar to small-strain linear elasticity, if the strain measures themselves correspond to large deformations. That is

$$\nu = -\frac{\text{lateral strain}}{\text{extensional strain}} \qquad \text{with} \qquad \text{strain} \equiv \text{any finite strain measure}\,, \tag{C.18}$$

holds intuitively as an extension of the geometrical description of Poisson's ratio to finite strains. This case has been first explored by [185], who essentially constructed the general definition for nonlinear Poisson's ratio (C.18). In its original definition, extensional and lateral strains were the (Biot) strain measures $E_{xx} = \lambda - 1$ and $E_{yy} = \eta - 1$, respectively, with λ and η being the extensional and lateral stretches, respectively, associated with a uni-axial tension test. Nonetheless, the term "strain" can be extended to a larger Seth-Hill family of strain functions, collectively expressed as

$$\boldsymbol{E}(\boldsymbol{U}) = \begin{cases} \ln \boldsymbol{U} & \text{if} \quad m = 0\,, \\ \dfrac{1}{m}\left[\,\boldsymbol{U}^m - \boldsymbol{I}\,\right] & \text{if} \quad m \neq 0\,, \end{cases} \tag{C.19}$$

with $\boldsymbol{U}$ being the (right) stretch tensor. In particular, the most commonly used strain measures are

$$\begin{aligned} m = 1 \quad &\Rightarrow \quad \text{Biot} \quad : \quad \boldsymbol{E}_B = \boldsymbol{U} - \boldsymbol{I}\,, \\ m = 0 \quad &\Rightarrow \quad \text{Hencky} \quad : \quad \boldsymbol{E}_H = \ln \boldsymbol{U}\,, \\ m = 2 \quad &\Rightarrow \quad \text{Green} \quad : \quad \boldsymbol{E}_G = \tfrac{1}{2}\left[\boldsymbol{U}^2 - \boldsymbol{I}\right], \\ m = -2 \quad &\Rightarrow \quad \text{Almansi} \quad : \quad \boldsymbol{E}_A = -\tfrac{1}{2}\left[\boldsymbol{U}^{-2} - \boldsymbol{I}\right]. \end{aligned} \tag{C.20}$$

Obviously, the definition (C.18) is in essence the same as the previously mentioned Poisson ratio measure for linear, small deformations. What makes this case different is that for finite deformations, there is not a single measure for strain. Hence every strain measure renders a different definition of nonlinear Poisson ratio. This prohibits us from directly equating the two kinematic measures of Poisson's ratio associated with Eq. (C.1) and Eq. (C.18). For instance,

for the most commonly used strain measures, the nonlinear Poisson ratio reads

$$\begin{aligned} &\text{Biot} \quad : \quad \nu = \frac{1-\eta}{\lambda-1} \quad , \quad \text{Hencky} \quad : \quad \nu = -\frac{\ln \eta}{\ln \lambda}\,, \\ &\text{Green} \quad : \quad \nu = \frac{1-\eta^2}{\lambda^2-1} \quad , \quad \text{Almansi} \quad : \quad \nu = \frac{1-\eta^{-2}}{\lambda^{-2}-1}\,. \end{aligned} \tag{C.21}$$

Note that in all the definitions (C.21), but also throughout this contribution, λ and η denote the extensional and lateral stretches, respectively, associated with the deformation gradient

$$\text{2D} \ : \ \boldsymbol{F} = \text{Diag}(\lambda, \eta) \qquad , \qquad \text{3D} \ : \ \boldsymbol{F} = \text{Diag}(\lambda, \eta, \zeta)\,, \tag{C.22}$$

wherein $\zeta = \eta$ is the lateral stretch in 3D. Notice that we now have a definition for a nonlinear Poisson's ratio where the Poisson's ratio is not simply a constant for a given material, but changes according to the stretch applied to the material.

Now moving onto the material description in a nonlinear setting, we employ the variational approach established previously. To do so, we begin from a (polyconvex) hyperelastic free energy density $\psi = \psi(\boldsymbol{F})$. For instance, for a compressible Neo-Hookean model ψ reads

$$\psi = \psi(\boldsymbol{F}) = \frac{1}{2}\,\mu\,[\boldsymbol{F} : \boldsymbol{F} - 3 - 2\ln J] + \Lambda\,[\,\frac{1}{4}\,[J^2-1] - \frac{1}{2}\,\ln J\,]\,, \tag{C.23}$$

where $\boldsymbol{F}$ is the deformation gradient defined previously, and $J := \text{Det}\boldsymbol{F}$. The free energy density (C.23) shall be compared with its counterpart (C.10) for small-strain linear elasticity. Analogous to what was established previously, using the relationship (C.2), the free energy density in terms of μ and Poisson's ratio ν reads

$$\begin{cases} \text{2D} \ : \ \psi = \dfrac{1}{2}\,\mu\,[\boldsymbol{F} : \boldsymbol{F} - 2 - 2\ln J] + \dfrac{2\mu\nu}{1-\nu}\,[\,\dfrac{1}{4}\,[J^2-1] - \dfrac{1}{2}\,\ln J\,]\,, \\ \text{3D} \ : \ \psi = \dfrac{1}{2}\,\mu\,[\boldsymbol{F} : \boldsymbol{F} - 3 - 2\ln J] + \dfrac{2\mu\nu}{1-2\nu}\,[\,\dfrac{1}{4}\,[J^2-1] - \dfrac{1}{2}\,\ln J\,]\,. \end{cases} \tag{C.24}$$

For a uni-axial tension test, the deformation gradient $\boldsymbol{F}$ simplifies to a diagonal

tensor expressed in Eq. (C.22). Inserting the corresponding deformation gradient (C.22) into the internal energy density (C.24) furnishes

$$\begin{cases} \text{2D} \;:\quad \psi = \dfrac{1}{2}\,\mu\,\left[\lambda^2+\eta^2-2-2\ln(\lambda\eta)\right] \\ \qquad\qquad\quad + \dfrac{2\mu\nu}{1-\nu}\,[\,\dfrac{1}{4}\,[(\lambda\eta)^2-1]-\dfrac{1}{2}\,\ln(\lambda\eta)\,]\,, \\ \text{3D} \;:\quad \psi = \dfrac{1}{2}\,\mu\,\left[\lambda^2+2\eta^2-3-2\ln(\lambda\eta^2)\right] \\ \qquad\qquad\quad + \dfrac{2\mu\nu}{1-2\nu}\,[\,\dfrac{1}{4}\,[(\lambda\eta^2)^2-1]-\dfrac{1}{2}\,\ln(\lambda\eta^2)\,]\,. \end{cases} \tag{C.25}$$

Next, we set $\delta\psi \doteq 0$ in order to impose equilibrium (C.7). In doing so, note that $\psi = \psi(\lambda,\eta)$ and therefore

$$\delta\psi = \frac{\partial\psi}{\partial\lambda}\,\delta\lambda + \frac{\partial\psi}{\partial\eta}\,\delta\eta \doteq 0\,. \tag{C.26}$$

However, for the problem at hand, the extension λ is a prescribed quantity and therefore η is the only remaining variable. This immediately results in

$$\delta\psi \doteq 0 \qquad \Rightarrow \qquad \frac{\partial\psi}{\partial\eta} \doteq 0\,. \tag{C.27}$$

Finally, we use the energy densities (C.25) in the *reduced equilibrium equation* (C.27). That is

$$\frac{\partial\psi}{\partial\eta} \doteq 0 \quad \Rightarrow \quad \begin{cases} \text{2D} \;:\; \dfrac{1}{2}\,\mu\,\left[2\eta-\dfrac{2}{\eta}\right] + \dfrac{2\mu\nu}{1-\nu}\,\left[\dfrac{1}{2}\lambda^2\eta-\dfrac{1}{2\eta}\right] \doteq 0\,, \\ \text{3D} \;:\; \dfrac{1}{2}\,\mu\,\left[4\eta-\dfrac{4}{\eta}\right] + \dfrac{2\mu\nu}{1-2\nu}\,\left[\lambda^2\eta^3-\dfrac{1}{\eta}\right] \doteq 0\,. \end{cases} \tag{C.28}$$

Solving each relation in Eq. (C.28), results in

$$\text{2D} \quad : \quad \nu = \frac{1-\eta^{-2}}{1-\lambda^2} \qquad , \qquad \text{3D} \quad : \quad \nu = \frac{1-\eta^{-2}}{2-\eta^{-2}-\lambda^2\eta^2}\,, \tag{C.29}$$

which shall be compared with Eq. (C.21). That is, *for large deformations too, starting from energy, via a variational procedure for a uni-axial tension test, one can establish a material description of Poisson's ratio that no longer coincides*

Table C.3: Poisson's ratio at large deformations nonlinear elasticity. The geometrical description of Poisson's ratio has been extended to large deformations (top). Via a variational approach, we propose an extension of the material description of Poisson's ratio (bottom).

	Beatty & Stalnaker	
2D	$\nu = -\dfrac{E_{yy}}{E_{xx}}$	$\begin{cases} \boldsymbol{E} = \ln \boldsymbol{U} & m = 0 \\ \boldsymbol{E} = \dfrac{1}{m}[\,\boldsymbol{U}^m - \boldsymbol{I}\,] & m \neq 0 \end{cases}$
3D	$\nu = -\dfrac{E_{yy}}{E_{xx}} = -\dfrac{E_{zz}}{E_{xx}}$	

2D	Biot : $\nu_B = \dfrac{1-\eta}{\lambda - 1}$	Hencky : $\nu_H = -\dfrac{\ln \eta}{\ln \lambda}$
3D	Green : $\nu_G = \dfrac{1-\eta^2}{\lambda^2 - 1}$	Almansi : $\nu_A = \dfrac{1-\eta^{-2}}{\lambda^{-2} - 1}$

	current approach
2D	$\boldsymbol{F} = \text{Diag}(\lambda, \eta) \quad \& \quad \delta\psi = 0 \quad \Rightarrow \quad \nu = \nu(\lambda, \eta)$
3D	$\boldsymbol{F} = \text{Diag}(\lambda, \eta, \eta) \quad \& \quad \delta\psi = 0 \quad \Rightarrow \quad \nu = \nu(\lambda, \eta)$

2D	$\nu = \dfrac{1-\eta^{-2}}{1-\lambda^2}$
3D	$\nu = \dfrac{1-\eta^{-2}}{2-\eta^{-2}-\lambda^2\eta^2}$

with its commonly accepted geometrical definitions. Table C extends Table C.2 and summarizes the aspects of Poisson's ratio at large deformations.

Fig. C.2 illustrates the different kinematic measures of Poisson's ratio, namely that of Biot, Hencky, Green and Almansi, as gathered in Eq. (C.21), at the incompressibility limit, against the current kinetic definition (C.29). The nonlinear Poisson ratio ν, obtained for the various definitions, is plotted versus the axial stretch λ, which ranges from 0.5 to 1.5, thus covering both contraction and extension. Clearly, all of the definitions coincide at $\lambda = 1$, to the expected, incompressible value of $\nu = 1$ for 2D and $\nu = \frac{1}{2}$ for 3D. The significance of this

point lies in the fact that deformations close to $\lambda = 1$ correspond to small stains. Hence as we move away from this small-strain limit, the geometrical and material descriptions of Poisson's ratio move away from each other, since the nonlinearity of the Poisson ratio becomes more pronounced and consequently, the different functions begin to portray different behaviors. Only the current definition and the Hencky definition at the incompressibility limit remain constant regardless of the stretch λ.

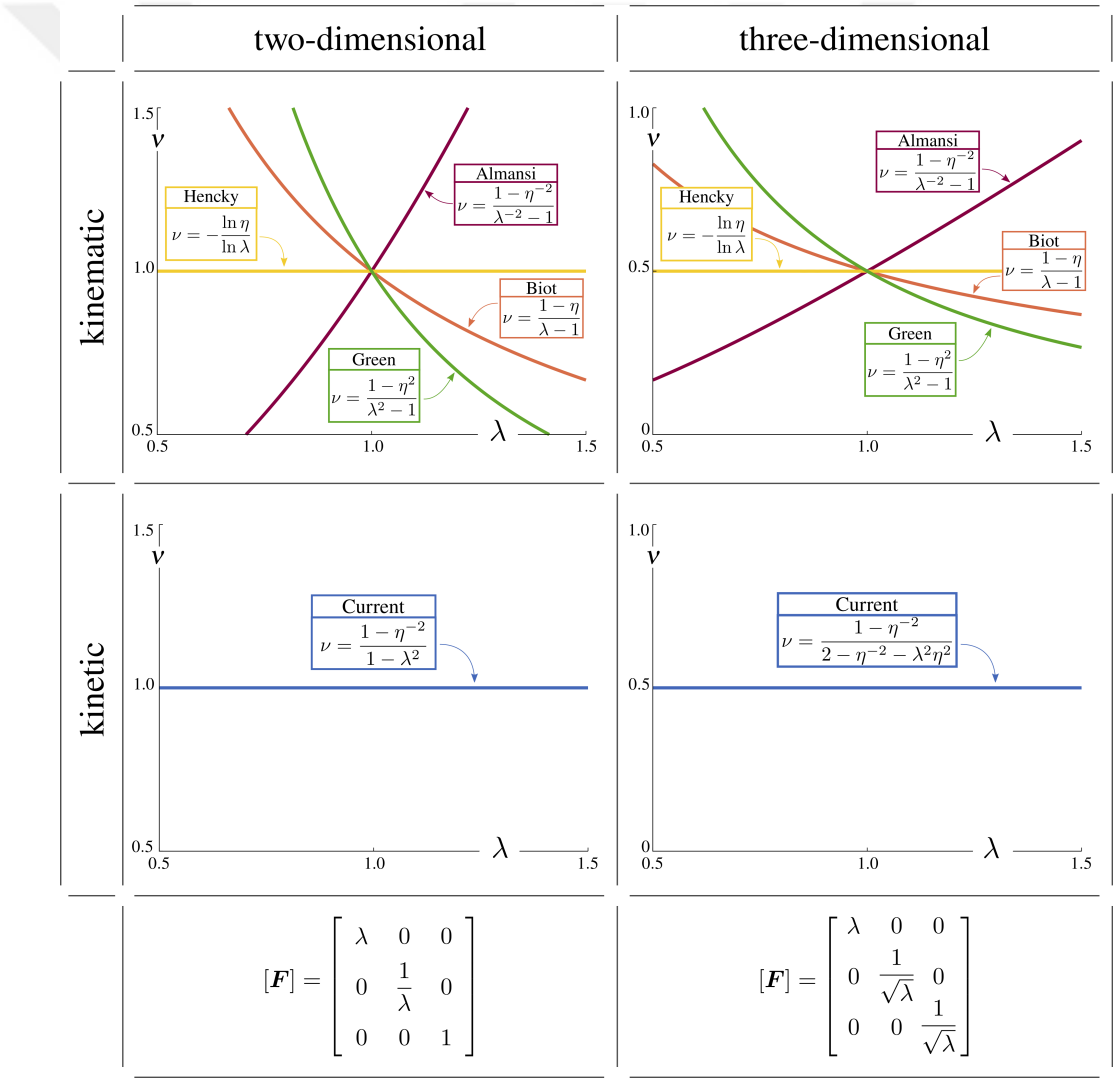


Figure C.2: Comparison of the current kinetic nonlinear Poisson's ratio definition with previously established, kinematic definitions.

Equipped with the nonlinear Poisson's ratio (C.29), another interesting aspect

to investigate is the relationship between the lateral stretch η and the Jacobian J. This combination is particularly intriguing since $J = \mathrm{Det}\boldsymbol{F}$ is the ratio of the current over reference volume of the domain for 3D and the ratio of the current over reference area of the domain for 2D. Therefore J serves as an indication of compressibility of a material too. That is, for nearly incompressible materials we expect $J \to 1$. In doing so, it proves helpful to define a dimensionless "compressibility parameter" $\alpha = \Lambda/2\mu$, with α ranging from 0 at full compressibility, to $\alpha \to \infty$ at the incompressibility limit. Using the relationships established for the nonlinear Poisson ratio (C.29), we can immediately see that α boils down to the same function in terms of η and J, for both 2D and 3D. That is

$$\alpha = \frac{\Lambda}{2\,\mu} \quad \Rightarrow \quad \left\{ \begin{array}{l} \text{2D} \;:\; \alpha = \dfrac{\nu}{1-\nu} \\ \\ \text{3D} \;:\; \alpha = \dfrac{\nu}{1-2\nu} \end{array} \right\} \quad \Rightarrow \quad \alpha = \frac{1-\eta^2}{J^2-1}\,. \tag{C.30}$$

Therefore, it is possible to express the lateral stretch η as a function of the compressibility parameter α and the Jacobian J, where for a uni-axial tension test, $J = \lambda\eta$ in 2D and $J = \lambda\eta^2$ in 3D. That is

$$\eta = \sqrt{1 - \alpha\,[J^2 - 1]}\,. \tag{C.31}$$

Even though the definition (C.31) is obtained through a variational approach associated with the material description of the Poisson ratio, the geometrical interpretation of it is still visible. As the domain becomes increasingly compressible, this suggests geometrically that no matter what the axial stretch, λ is, there would be close to no contraction in the lateral direction, corresponding to $\eta \to 1$. This is clearly seen in Fig. C.3, for both 2D (left) and 3D (right), with the curve flattening and converging to a single value of $\eta = 1$, regardless of J hence of λ, as $\alpha \to 0$. On the other hand, as the material gets more and more incompressible with increasing α, the range of admissible values for η increases. Additionally, as we move towards full incompressibility, since at full incompressibility the volume is preserved, J converges to 1. We also see that the whole range of η becomes

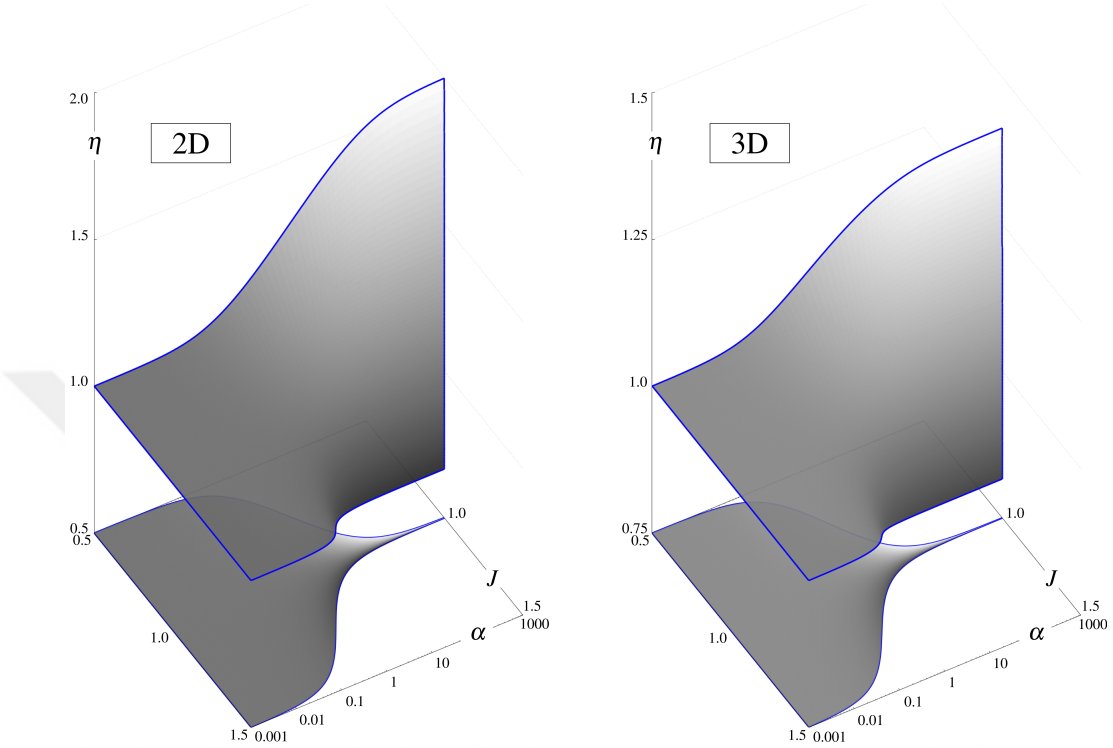


Figure C.3: Illustration of the lateral stretch η versus Jacobian J and compressibility parameter α for 2D (left) and 3D (right). As we move towards full incompressibility, J converges to 1, as expected.

viable at the incompressible limit. This stems from the fact that incompressibility dictates that $J = 1$ and therefore $\eta = 1/\lambda$ in 2D, or $\eta = 1/\sqrt{\lambda}$ in 3D, which shows that for any value of axial stretch λ there exists a solution for the lateral stretch η to ensure incompressibility.

Remark on generalizing the methodology. *The variational framework here to extend the material description of Poisson's ratio to large deformations was carried out so far for the hyperelastic free energy density (C.23). This particular choice of (Ogden) free energy density was only made to simplify the derivations and highlights the key features of the procedure while avoiding technical complexities. Nonetheless, the developed framework itself is generic and can be applied to any other free energy density of an elastic material. That is, while the nonlinear Poisson ratio (C.29) is exclusively derived for the free energy density (C.23), it*

can be shown that any $\psi = \psi(\boldsymbol{F} : \boldsymbol{F}, J)$ *furnishes a relationship between* λ, η *and* ν *akin to the nonlinear Poisson ratio (C.29). Generalizing even further, the framework can also be applied to any isotropic free energy density* $\psi = \psi(I_1, I_2, I_3)$ *with* $I_1 := Tr\boldsymbol{C}$, $I_2 := Tr\, Cof\boldsymbol{C}$ *and* $I_3 := Det\boldsymbol{C}$ *being the three principal invariants of the right Cauchy–Green tensor* $\boldsymbol{C}$.

Bibliography

[1] M. Biot, "Bending of an infinite beam on an elastic foundation," *J. Appl. Math. Mech.*, vol. 203, pp. A–1–A–7, 1937.

[2] H. G. Allen, *Analysis and design of structural sandwich panels*. Pergamon Press, 1969.

[3] J. Genzer and J. Groenewold, "Soft matter with hard skin: From skin wrinkles to templating and material characterization," *Soft Matter*, vol. 2, pp. 310–323, 2006.

[4] M. Destrade, R. W. Ogden, I. Sgura, and L. Vergori, "Straightening wrinkles," *J. Mech. Phys. Solids*, vol. 65, pp. 1–11, 2014.

[5] G. Limbert and E. Kuhl, "On skin microrelief and the emergence of expression micro-wrinkles," *Soft Matter*, vol. 14, pp. 1292–1300, 2018.

[6] C. P. Brangwynne, F. C. MacKintosh, S. Kumar, N. A. Geisse, J. Talbot, L. Mahadevan, K. K. Parker, D. E. Ingber, and D. A. Weitz, "Microtubules can bear enhanced compressive loads in living cells because of lateral reinforcement," *J. Cell Biol.*, vol. 173, pp. 733–741, 2006.

[7] E. Hohlfeld and L. Mahadevan, "Unfolding the sulcus," *Phys. Rev. Lett.*, vol. 106, p. 105702, 2011.

[8] S. Budday, P. Steinmann, and E. Kuhl, "The role of mechanics during brain development," *J. Mech. Phys. Solids*, vol. 72, pp. 75–92, 2014.

[9] S. N. Verner and K. Garikipati, "A computational study of the mechanisms of growth-driven folding patterns on shells, with application to the developing brain," *Extreme Mech. Lett.*, vol. 18, pp. 58–69, 2018.

[10] E. Lejeune, B. Dortdivanlioglu, E. Kuhl, and C. Linder, "Understanding the mechanical link between oriented cell division and cerebellar morphogenesis," *Soft Matter*, vol. 15, pp. 2204–2215, 2019.

[11] P. Ciarletta, V. Balbi, and E. Kuhl, "Pattern selection in growing tubular tissues," *Phys. Rev. Lett.*, vol. 113, p. 248101, 2014.

[12] M. Eskandari, A. Javili, and E. Kuhl, "Elastosis during airway wall remodeling explains multiple co-existing instability patterns," *J. Theor. Biol.*, vol. 403, pp. 209–218, 2016.

[13] C. Chen, C. A. Airoldi, C. A. Lugo, R. K. Bay, B. J. Glover, and A. J. Crosby, "Flower Inspiration: Broad-Angle Structural Color through Tunable Hierarchical Wrinkles in Thin Film Multilayers," *Adv. Funct. Mater.*, vol. 31, p. 2006256, 2021.

[14] N. Bowden, S. Brittain, A. G. Evans, J. W. Hutchinson, and G. M. Whitesides, "Spontaneous formation of ordered structures in thin films of metals supported on an elastomeric polymer," *Nature*, vol. 393, pp. 146–149, 1998.

[15] W. T. S. Huck, N. Bowden, P. Onck, T. Pardoen, J. W. Hutchinson, and G. M. Whitesides, "Ordering of spontaneously formed buckles on planar surfaces," *Langmuir*, vol. 16, pp. 3497–3501, 2000.

[16] P. M. Asdaque, S. Banerjee, and S. Roy, "An electromechanically coupled intrinsic, mixed variational formulation for geometrically nonlinear smart composite beam," *Appl. Math. Model*, vol. 65, pp. 549–565, 2019.

[17] Y. Zheng, G. Y. Li, Y. Cao, and X. Q. Feng, "Wrinkling of a stiff film resting on a fiber-filled soft substrate and its potential application as tunable metamaterials," *Extreme Mech. Lett.*, pp. 121–127, 2017.

[18] A. J. Nolte, R. E. Cohen, and M. F. Rubner, "A two-plate buckling technique for thin film modulus measurements: Applications to poly electrolyte multilayers," *Macromolecules*, vol. 39, pp. 4841–4847, 2006.

[19] Y. Su, H. Conroy Broderick, W. Chen, and M. Destrade, "Wrinkles in soft dielectric plates," *J. Mech. Phys. Solids*, vol. 119, pp. 298–318, 2018.

[20] S. Seifi and H. S. Park, "Electro-elastocapillary rayleigh–plateau instability in dielectric elastomer films," *Soft Matter*, vol. 13, pp. 4305–4310, 2017.

[21] M. T. Lam, S. Sim, X. Zhu, and S. Takayama, "The effect of continuous wavy micropatterns on silicone substrates on the alignment of skeletal muscle myoblasts and myotubes," *Biomaterials*, vol. 27, pp. 4340–4347, 2006.

[22] C. M. Stafford, B. D. Vogt, C. Harrison, D. Julthongpiput, and R. Huang, "Elastic moduli of ultrathin amorphous polymer films," *Macromolecules*, vol. 39, pp. 5095–5099, 2006.

[23] J. Y. Chung, A. J. Nolte, and C. M. Stafford, "Surface wrinkling: a versatile platform for measuring thin-film properties," *Adv. Mater.*, vol. 23, pp. 349–368, 2011.

[24] J. W. Hutchinson, "The role of nonlinear substrate elasticity in the wrinkling of thin films," *Phil. Trans. R. Soc. A*, vol. 371, p. 20120422, 2013.

[25] M. Watanabe, H. Shirai, and T. Hirai, "Wrinkled polypyrrole electrode for electroactive polymer actuators," *J. Appl. Phys.*, vol. 92, p. 4631, 2002.

[26] S. P. Lacour, S. Wagner, Z. Huang, and Z. Suo, "Stretchable gold conductors on elastomeric substrates," *Appl. Phys. Lett.*, vol. 82, pp. 2404–2406, 2003.

[27] S. P. Lacour, J. Jones, Z. Suo, and S. Wagner, "Design and performance of thin metal film interconnects for skin-like electronic circuits," *IEEE Electron Device Lett.*, vol. 25, pp. 179–181, 2004.

[28] D. H. Kim, Y. S. Kim, J. Wu, Z. Liu, J. Song, H. S. Kim, Y. Y. Huang, K. C. Hwang, and J. A. Rogers, "Ultrathin silicon circuits with strain-isolation

layers and mesh layouts for high-performance electronics on fabric, vinyl, leather, and paper," *Adv. Mater.*, vol. 21, pp. 3703–3707, 2009.

[29] A. Javili and A. D. Bakiler, "A displacement-based approach to geometric instabilities of a film on a substrate," *Math. Mech. Solids*, vol. 24, pp. 2999–3023, 2019.

[30] A. D. Bakiler and A. Javili, "Bifurcation behavior of compressible elastic half-space under plane deformations," *Int. J. Nonlin. Mech.*, vol. 126, p. 103553, 2020.

[31] A. D. Bakiler, B. Dortdivanlioglu, and A. Javili, "From beams to bilayers: A unifying approach towards instabilities of compressible domains under plane deformations," *International Journal of Non-Linear Mechanics*, vol. 135, p. 103752, 2021.

[32] A. D. Bakiler and A. Javili, "Wrinkling of a compressible trilayer domain under large plane deformations," *International Journal of Solids and Structures*, vol. 241, p. 111465, 2022.

[33] A. D. Bakiler and A. Javili, *"A Different Catch for Poisson"*, pp. 3–23. Cham: Springer International Publishing, 2022.

[34] A. D. Bakiler and A. Javili, "Understanding the role of interfacial mechanics on the wrinkling behavior of compressible bilayer structures under large plane deformations," *Mathematics and Mechanics of Solids*, p. 10812865221094833, 2022.

[35] E. Cerda and L. Mahadevan, "Geometry and Physics of Wrinkling," *Physical Review Letters*, vol. 90, p. 074302, 2003.

[36] R. Huang, C. M. Stafford, and B. D. Vogt, "Effect of surface properties on wrinkling of ultrathin films," *J. Aerospace Eng.*, vol. 20, pp. 38–44, 2007.

[37] M. Taffetani, X. Jiang, D. P. Holmes, and D. Vella, "Static bistability of spherical caps," *Proc. R. Soc. A*, vol. 474, p. 20170910, 2018.

[38] C. Fu, T. Wang, F. Xu, Y. Huo, and M. Potier-Ferry, "A modeling and resolution framework for wrinkling in hyperelastic sheets at finite membrane strain," *J. Mech. Phys. Solids*, vol. 124, pp. 446–470, 2019.

[39] B. Li, F. Jia, Y. P. Cao, X.-Q. Feng, and H. Gao, "Surface wrinkling patterns on a core-shell soft sphere," *Phys. Rev. Lett.*, vol. 106, p. 234301, 2011.

[40] D. E. Moulton and A. Goriely, "Circumferential buckling instability of a growing cylindrical tube," *J. Mech. Phys. Solids*, vol. 59, pp. 525–537, 2011.

[41] F. Sozio and A. Yavari, "Nonlinear mechanics of surface growth for cylindrical and spherical elastic bodies," *J. Mech. Phys. Solids*, vol. 98, pp. 12–48, 2017.

[42] C. Zhang, Y.-K. Hao, B. Li, X.-Q. Feng, and H. Gao, "Wrinkling patterns in soft shells," *Soft Matter*, vol. 14, pp. 1681–1688, 2018.

[43] B. Li, Y.-P. Cao, X.-Q. Feng, and H. Gao, "Mechanics of morphological instabilities and surface wrinkling in soft materials: a review," *Soft Matter*, vol. 8, pp. 5728–5745, 2012.

[44] F. Iacopi, S. H. Brongersma, and K. Maex, "Compressive stress relaxation through buckling of a low-k polymer-thin cap layer system," *Appl. Phys. Lett.*, vol. 82, pp. 1380–1382, 2003.

[45] P. J. Yoo, K. Y. Suh, Y. Park, and H. H. Lee, "Physical self-assembly of microstructures by anisotropic buckling," *Adv. Mater.*, vol. 14, pp. 1383–1387, 2002.

[46] T. Ohzono and M. Shimomura, "Ordering of microwrinkle patterns by compressive strain," *Phys. Rev. B*, vol. 69, p. 132202, 2004.

[47] A. L. Volynskii, S. Bazhenov, O. V. Lebedeva, and N. F. Bakeev, "Mechanical buckling instability of thin coatings deposited on soft polymer substrates," *J. Mater. Sci.*, vol. 35, pp. 547–554, 2000.

[48] R. Huang and Z. Suo, "Instability of a compressed elastic film on a viscous layer," *Int. J. Solids Struct.*, vol. 39, pp. 1791–1802, 2002.

[49] Z. Cai and Y. Fu, "Exact and asymptotic stability analyses of a coated elastic half-space," *Int. J. Solids Struct.*, vol. 37, pp. 3101–3119, 2000.

[50] J. Groenewold, "Wrinkling of plates coupled with soft elastic media," *Phys. A*, vol. 298, pp. 32–45, 2001.

[51] J. Song, H. Jiang, Z. J. Liu, D. Y. Khang, Y. Huang, J. A. Rogers, C. Lu, and C. G. Koh, "Buckling of a stiff thin film on a compliant substrate in large deformation," *Int. J. Solids Struct.*, vol. 45, pp. 3107–3121, may 2008.

[52] Y. Cao and J. W. Hutchinson, "Wrinkling phenomena in neo-hookean film/substrate bilayers," *ASME J. Appl. Mech.*, vol. 79, p. 031019, 2012.

[53] X. Chen and J. W. Hutchinson, "Herringbone buckling patterns of compressed thin films on compliant substrates," *ASME J. Appl. Mech.*, vol. 71, pp. 597–603, 2004.

[54] Z. Y. Huang, W. Hong, and Z. Suo, "Nonlinear analyses of wrinkles in a film bonded to a compliant substrate," *J. Mech. Phys. Solids*, vol. 53, pp. 2101–2118, 2005.

[55] B. Audoly and A. Boudaoud, "Buckling of a stiff film bound to a compliant substrate-Part I: Formulation, linear stability of cylindrical patterns, secondary bifurcations," *J. Mech. Phys. Solids*, vol. 56, pp. 2401–2421, 2008.

[56] F. Xu and M. Potier-Ferry, "A multi-scale modeling framework for instabilities of film/substrate systems," *J. Mech. Phys. Solids*, vol. 86, pp. 150–172, 2016.

[57] W. Hong, X. Zhao, and Z. Suo, "Formation of creases on the surfaces of elastomers and gels," *Appl. Phys. Lett.*, vol. 95, p. 111901, 2009.

[58] L. Jin, S. Cai, and Z. Suo, "Creases in soft tissues generated by growth," *EPL*, vol. 95, p. 64002, 2011.

[59] Y. Cao and J. W. Hutchinson, "From wrinkles to creases in elastomers: the instability and imperfection-sensitivity of wrinkling," *Proc. R. Soc. A*, vol. 468, pp. 94–115, 2012.

[60] P. Ciarletta, "Matched asymptotic solution for crease nucleation in soft solids," *Nat. Commun.*, vol. 9, p. 496, 2018.

[61] H. Mei, C. M. Landis, and R. Huang, "Concomitant wrinkling and buckle-delamination of elastic thin films on compliant substrates," *Mech. Mater.*, vol. 43, pp. 627–642, 2011.

[62] Y. Yang, K. Y. Lee, and X. F. Li, "Surface effects on delamination of a thin film bonded to an elastic substrate," *Int. J. Fract.*, vol. 210, pp. 81–94, 2018.

[63] L. Zhuo and Y. Zhang, "From period-doubling to folding in stiff film/soft substrate system: The role of substrate nonlinearity," *Int. J. Nonlin. Mech.*, vol. 76, pp. 1–7, 2015.

[64] Z. X. Cai and Y. B. Fu, "Effects of pre-stretch, compressibility and material constitution on the period-doubling secondary bifurcation of a film/substrate bilayer," *Int. J. Nonlin. Mech.*, vol. 115, pp. 11–19, 2019.

[65] J.-Y. Sun, S. Xia, M.-W. Moon, K. H. Oh, and K.-S. Kim, "Folding wrinkles of a thin stiff layer on a soft substrate," *Proc. R. Soc. A*, vol. 468, pp. 932–953, 2012.

[66] F. Brau, P. Damman, H. Diamant, and T. A. Witten, "Wrinkle to fold transition: influence of the substrate response," *Soft Matter*, vol. 9, p. 8177, 2013.

[67] J. Zang, X. Zhao, Y. Cao, and J. W. Hutchinson, "Localized ridge wrinkling of stiff films on compliant substrates," *J. Mech. Phys. Solids*, vol. 60, pp. 1265–1279, 2012.

[68] S. Budday, E. Kuhl, and J. W. Hutchinson, "Period-doubling and period-tripling in growing bilayered systems," *Philos. Mag.*, vol. 95, pp. 3208–3224, 2015.

[69] F. Xu, M. Potier-Ferry, S. Belouettar, and Y. Cong, "3D finite element modeling for instabilities in thin films on soft substrates," *Int. J. Solids Struct.*, vol. 51, pp. 3619–3632, 2014.

[70] F. Xu, M. Potier-Ferry, S. Belouettar, and H. Hu, "Multiple bifurcations in wrinkling analysis of thin films on compliant substrates," *Int. J. Non-Linear Mech.*, vol. 76, pp. 203–222, 2015.

[71] R. Zhao, T. Zhang, M. Diab, H. Gao, and K. S. Kim, "The primary bilayer ruga-phase diagram I: Localizations in ruga evolution," *Extrem. Mech. Lett.*, vol. 4, pp. 76–82, 2015.

[72] Z. Li, R. J. Young, D. G. Papageorgiou, I. A. Kinloch, X. Zhao, C. Yang, and S. Hao, "Interfacial stress transfer in strain engineered wrinkled and folded graphene," *2D Materials*, vol. 6, no. 4, 2019.

[73] N. Stoop, R. Lagrange, D. Terwagne, P. M. Reis, and J. Dunkel, "Curvature-induced symmetry breaking determines elastic surface patterns," *Nat. Mater.*, vol. 14, pp. 337–342, 2015.

[74] R. Zhao and X. Zhao, "Multimodal surface instabilities in curved film-substrate structures," *ASME J. Appl. Mech.*, vol. 84, p. 081001, 2017.

[75] J. Wu and X. Chen, "Buckling patterns of conical thin film/substrate systems," *J. Phys. D*, vol. 46, p. 155306, 2013.

[76] M. A. Holland, B. Li, X.-Q. Feng, and E. Kuhl, "Instabilities of soft films on compliant substrates," *J. Mech. Phys. Solids*, vol. 98, pp. 350–365, 2017.

[77] Y.-P. Cao, F. Jia, Y. Zhao, X.-Q. Feng, and S.-W. Yu, "Buckling and post-buckling of a stiff film resting on an elastic graded substrate," *Int. J. Solids Struct.*, vol. 49, pp. 1656–1664, 2012.

[78] D. Lee, N. Triantafyllidis, J. R. Barber, and M. D. Thouless, "Surface instability of an elastic half space with material properties varying with depth," *J. Mech. Phys. Solids*, vol. 56, pp. 858–868, 2008.

[79] Y. Liu, Z. Zhang, G. Devillanova, and Z. Cai, "Surface instabilities in graded tubular tissues induced by volumetric growth," *Int. J. Nonlin. Mech.*, vol. 127, p. 103612, 2020.

[80] Z. Huang, W. Hong, and Z. Suo, "Evolution of wrinkles in hard films on soft substrates," *Phys. Rev. E*, vol. 70, p. 030601, 2004.

[81] J. Dervaux, P. Ciarletta, and M. Ben Amar, "Morphogenesis of thin hyperelastic plates: A constitutive theory of biological growth in the föppl–von kármán limit," *J. Mech. Phys. Solids*, vol. 57, pp. 458 – 471, 2009.

[82] M. Vangbo, "An analytical analysis of a compressed bistable buckled beam," *Sens. Actuator A Phys.*, vol. 69, pp. 212–216, 1998.

[83] B. Camescasse, A. Fernandes, and J. Pouget, "Bistable buckled beam: Elastica modeling and analysis of static actuation," *Int. J. Solids Struct.*, vol. 50, pp. 2881–2893, 2013.

[84] M. Gomez, D. E. Moulton, and D. Vella, "Dynamics of viscoelastic snap-through," *J. Mech. Phys. Solids*, vol. 124, pp. 781–813, 2019.

[85] A. A. Almet, H. M. Byrne, P. K. Maini, and D. E. Moulton, "Post-buckling behaviour of a growing elastic rod," *J. Math. Biol.*, vol. 78, pp. 777–814, 2019.

[86] R. De Pascalis, M. Destrade, and A. Goriely, "Nonlinear correction to the Euler buckling formula for compressed cylinders with guided-guided end conditions," *J. Elast.*, vol. 102, pp. 191–200, 2011.

[87] B. Dortdivanlioglu, A. Javili, and C. Linder, "Computational aspects of morphological instabilities using isogeometric analysis," *Comput. Methods Appl. Mech. Eng*, vol. 316, pp. 261–279, 2017.

[88] J. N. Reddy, "Nonlocal theories for bending, buckling and vibration of beams," *Int. J. Eng. Sci.*, vol. 45, pp. 288–307, 2007.

[89] M. A. Biot, "Surface Instability of Rubber in Compression," vol. 12, pp. 168–182, 1961.

[90] J. L. Nowinski, "Surface instability of a half-space under high two-dimensional compression," *J. Franklin Inst.*, vol. 288, pp. 367–376, 1969.

[91] B. D. Reddy, "Surface instabilities on an equibiaxially stretched elastic half-space," *Math. Proc. Cambridge Philos. Soc.*, vol. 91, pp. 491–501, 1982.

[92] B. D. Reddy, "The occurrence of surface instabilities and shear bands in plane-strain deformation of an elastic half-space," *Q. J. Mech. Appl. Math.*, vol. 36, pp. 337–350, 1983.

[93] R. W. Ogden, "Nonlinear elasticity: Incremental equations and bifurcation phenomena," in *Math. Sci. Eng.*, vol. 185, pp. 437–468, 1992.

[94] A. Goriely, M. Destrade, and M. Ben Amar, "Instabilities in elastomers and in soft tissues," *Q. J. Mech. Appl. Math.*, vol. 59, pp. 615–630, 2006.

[95] J. Murphy and M. Destrade, "Surface waves and surface stability for a pre-stretched, unconstrained, non-linearly elastic half-space," *Int. J. Nonlin. Mech.*, vol. 44, pp. 545–551, 2009.

[96] T. Sigaeva, R. Mangan, L. Vergori, M. Destrade, and L. Sudak, "Wrinkles and creases in the bending, unbending and eversion of soft sectors," *Proc. R. Soc. A*, vol. 474, p. 20170827, 2018.

[97] D. J. Steigmann and R. W. Ogden, "Plane deformations of elastic solids with intrinsic boundary elasticity," *Proc. R. Soc. A*, vol. 453, pp. 853–877, 1997.

[98] S. A. Usmani and M. F. Beatty, "On the surface instability of a highly elastic half-space," *J. Elast.*, vol. 4, pp. 249–263, 1974.

[99] M. F. Beatty and S. A. Usmani, "On the indentation of a highly elastic half-space," *The Quarterly Journal of Mechanics and Applied Mathematics*, vol. 28, pp. 47–62, 1975.

[100] P. Chadwick and D. A. Jarvis, "Surface Waves in a Pre-Stressed Elastic Body.," *Proc. R. Soc. A*, vol. 366, pp. 517–536, 1979.

[101] M. E. Gurtin and A. Ian Murdoch, "A continuum theory of elastic material surfaces," *Archive for Rational Mechanics and Analysis*, vol. 57, no. 4, pp. 291–323, 1975.

[102] D. J. Steigmann and R. W. Ogden, "Elastic surface–substrate interactions," *Proc. R. Soc. A*, vol. 455, pp. 437–474, 1999.

[103] A. Javili, A. Mcbride, and P. Steinmann, "Thermomechanics of solids with lower-dimensional energetics: On the importance of surface, interface, and curve structures at the nanoscale. A unifying review," *Appl. Mech. Rev.*, vol. 65, p. 010802, 2013.

[104] T. Zhang, "Symplectic analysis for wrinkles: a case study of layered neo-hookean structures," *ASME J. Appl. Mech.*, vol. 84, p. 071002, 2017.

[105] R. Kessentini, O. Klinkova, I. Tawfiq, and M. Haddar, "Transient hygro-thermo-mechanical stresses analysis in multi-layers bonded structure with coupled bidirectional model," *Int. J. Mech. Sci.*, vol. 150, pp. 188–201, 2019.

[106] Y. Sun, W. M. Choi, H. Jiang, Y. Y. Huang, and J. A. Rogers, "Controlled buckling of semiconductor nanoribbons for stretchable electronics," *Nat. Nanotechnol.*, vol. 1, pp. 201–207, 2006.

[107] F. Jia, Y.-P. Cao, T.-S. Liu, Y. Jiang, X.-Q. Feng, and S.-W. Yu, "Wrinkling of a bilayer resting on a soft substrate under in-plane compression," *Phil. Mag.*, vol. 92, pp. 1554–1568, 2012.

[108] H. Cheng, Y. Zhang, K. C. Hwang, J. A. Rogers, and Y. Huang, "Buckling of a stiff thin film on a pre-strained bi-layer substrate," *Int. J. Solids Struct.*, vol. 51, pp. 3113–3118, 2014.

[109] E. Lejeune, A. Javili, and C. Linder, "Understanding geometric instabilities in thin films via a multi-layer model," *Soft Matter*, vol. 12, pp. 806–816, 2016.

[110] E. Lejeune, A. Javili, and C. Linder, "An algorithmic approach to multi-layer wrinkling," *Extreme Mech. Lett.*, vol. 7, pp. 10–17, 2016.

[111] W. Xia and S. Keten, "Interfacial stiffening of polymer thin films under nanoconfinement," *Extreme Mech. Lett.*, vol. 4, pp. 89–95, 2015.

[112] C. Wang, S. Zhang, S. Nie, Y. Su, W. Chen, and J. Song, "Buckling of a stiff thin film on a bi-layer compliant substrate of finite thickness," *Int. J. Solids Struct.*, vol. 188-189, pp. 133–140, 2020.

[113] M. Zhou, Z. Cai, and Y. Fu, "Post-buckling of an elastic half-space coated by double layers," *Math. Mech. Solids*, p. 108128652110108, 2021.

[114] Y. Chen, X. Liao, W. Zhao, P. Yang, H. Xiao, Y. Liu, and X. Chen, "Post-wrinkling behaviors of a bilayer on a soft substrate," *Int. J. Solids Struct.*, vol. 214-215, pp. 74–79, 2021.

[115] B. Wang, H. Bi, H. Ouyang, Y. Wang, Y. Shi, and Z. Deng, "Nonlinear dynamic analysis for a corrugated thin film on a pre-strained finite-thickness bi-layer substrate," *Appl. Math. Model.*, vol. 98, pp. 652–664, 2021.

[116] H. Bi, B. Wang, C. Su, B. Zhang, H. Ouyang, Y. Huang, and Z. Deng, "Buckling behaviour of a stiff thin film on a finite-thickness bi-layer substrate," *Int. J. Solids Struct.*, vol. 219-220, pp. 177–187, 2021.

[117] G. Lin, W. Sun, and P. Chen, "Topography-driven delamination of thin patch adhered to wrinkling surface," *Int. J. Mech. Sci.*, vol. 178, p. 105622, 2020.

[118] Y. Cao, Y. Jiang, B. Li, and X. Feng, "Biomechanical modeling of surface wrinkling of soft tissues with growth-dependent mechanical properties," *Acta Mech. Solida Sin.*, vol. 25, pp. 483–492, 2012.

[119] M. Kim, S. Kim, and S. Im, "Wrinkling behavior of bilayer graphene sheets bonded to an elastic foundation," *Int. J. Solids Struct.*, vol. 178-179, pp. 36–47, 2019.

[120] S. S. Yoo, G. H. Choi, W. Lee, J. Park, G. R. Yi, D. Y. Ryu, and P. J. Yoo, "Cumulative energy analysis of thermally-induced surface wrinkling of heterogeneously multilayered thin films," *Soft Matter*, vol. 14, pp. 704–710, 2018.

[121] C. Zong, U. Azhar, C. Zhou, J. Wang, L. Zhang, Y. Cao, S. Zhang, S. Jiang, and C. Lu, "Photocontrollable Wrinkle Morphology Evolution on Azo-Based Multilayers for Hierarchical Surface Micropatterns Fabrication," *Langmuir*, vol. 35, pp. 2601–2609, 2019.

[122] Y. Li, N. Kaynia, S. Rudykh, and M. C. Boyce, "Wrinkling of interfacial layers in stratified composites," *Adv. Eng. Mater.*, vol. 15, pp. 921–926, 2013.

[123] K. Bertoldi and O. Lopez-Pamies, "Some remarks on the effect of interphases on the mechanical response and stability of fiber-reinforced elastomers," *ASME J. Appl. Mech.*, vol. 79, p. 031023, 2012.

[124] C. Gao and Y. Li, "Tuning the wrinkling patterns of an interfacial/coating layer via a regulation interphase," *Int. J. Solids Struct.*, vol. 104-105, pp. 92–102, 2017.

[125] J. M. Colin, M. Darayi, and M. A. Holland, "Stiffness Contrast and Separation Influence Wrinkling of Adjacent Layers in a Homogeneous Matrix," *ASME J. Appl. Mech.*, vol. 86, pp. 1–7, 2019.

[126] S. Firooz, P. Steinmann, and A. Javili, "Homogenization of Composites With Extended General Interfaces: Comprehensive Review and Unified Modeling," *Applied Mechanics Reviews*, vol. 73, no. 4, 2021.

[127] Z. Jia and T. Li, "Effect of interfacial stiffness on the stretchability of metal/elastomer bilayers under in-plane biaxial tension," *Theoretical and Applied Mechanics Letters*, vol. 11, no. 3, p. 100247, 2021.

[128] A. Javili, "Variational formulation of generalized interfaces for finite deformation elasticity," *Math. Mech. Solids*, vol. 23, pp. 1303–1322, 2018.

[129] E. Lejeune, A. Javili, J. Weickenmeier, E. Kuhl, and C. Linder, "Tri-layer wrinkling as a mechanism for anchoring center initiation in the developing cerebellum," *Soft Matter*, vol. 12, pp. 5613–5620, 2016.

[130] H. P. Huy and E. Sanchez-Palencia, "Phénomènes de transmission à travers des couches minces de conductivité élevée," *Journal of Mathematical Analysis and Applications*, vol. 47, no. 2, pp. 284–309, 1974.

[131] E. Sanchez-Palencia, "Comportements local et macroscopique d'un type de milieux physiques heterogenes," *International Journal of Engineering Science*, vol. 12, no. 4, pp. 331–351, 1974.

[132] Z. Hashin, "Thermoelastic properties of particulate composites with imperfect interface," *Journal of the Mechanics and Physics of Solids*, vol. 39, no. 6, pp. 745–762, 1991.

[133] Y. Benveniste and T. Miloh, "Imperfect soft and stiff interfaces in two-dimensional elasticity," *Mechanics of Materials*, vol. 33, no. 6, pp. 309–323, 2001.

[134] E. Fried, "Correspondence between a phase-field theory and a sharp-interface theory for crystal growth," *Continuum Mechanics and Thermodynamics*, vol. 9, pp. 33–60, 1997.

[135] K. M. Hu, Y. Q. Liu, L. W. Zhou, Z. Y. Xue, B. Peng, H. Yan, Z. F. Di, X. S. Jiang, G. Meng, and W. M. Zhang, "Delamination-Free Functional Graphene Surface by Multiscale, Conformal Wrinkling," *Advanced Functional Materials*, vol. 30, no. 34, pp. 1–11, 2020.

[136] Y. Xuan, X. Guo, Y. Cui, C. Yuan, H. Ge, B. Cui, and Y. Chen, "Crack-free controlled wrinkling of a bilayer film with a gradient interface," *Soft Matter*, vol. 8, no. 37, pp. 9603–9609, 2012.

[137] D. Vella, J. Bico, A. Boudaoud, B. Roman, and P. M. Reis, "The macroscopic delamination of thin films from elastic substrates," *Proceedings of the National Academy of Sciences of the United States of America*, vol. 106, no. 27, pp. 10901–10906, 2009.

[138] L. Pocivavsek, J. Pugar, R. O'Dea, S. H. Ye, W. Wagner, E. Tzeng, S. Velankar, and E. Cerda, "Topography-driven surface renewal," *Nature Physics*, vol. 14, no. 9, pp. 948–953, 2018.

[139] S. Andres, P. Steinmann, and S. Budday, "The origin of compression influences geometric instabilities in bilayers," *Proc. R. Soc. A*, vol. 474, p. 20180267, 2018.

[140] N. Emuna and D. Durban, "On rate boundary conditions for soft tissue bifurcation analysis," *J. Biomech. Eng.*, vol. 140, pp. 1–10, 2018.

[141] M. A. Dowaikh and R. W. Ogden, "On surface waves and deformations in a pre-stressed incompressible elastic solid," *IMA J. Appl. Math.*, vol. 44, pp. 261–284, 1990.

[142] A. Goriely and M. Ben Amar, "Differential growth and instability in elastic shells," *Phys. Rev. Lett.*, vol. 94, p. 198103, 2005.

[143] M. R. Nelson, D. Howard, O. E. Jensen, J. R. King, F. R. Rose, and S. L. Waters, "Growth-induced buckling of an epithelial layer," *Biomech. Model. Mechanobiol.*, vol. 10, pp. 883–900, 2011.

[144] S. G. O'Keeffe, D. E. Moulton, S. L. Waters, and A. Goriely, "Growth-induced axial buckling of a slender elastic filament embedded in an isotropic elastic matrix," *Int. J. Non-Linear Mech.*, vol. 56, pp. 94–104, 2013.

[145] A. Javili, P. Steinmann, and E. Kuhl, "A novel strategy to identify the critical conditions for growth-induced instabilities," *J. Mech. Behav. Biomed. Mater.*, vol. 29, pp. 20–32, 2014.

[146] Q. Wang and X. Zhao, "A three-dimensional phase diagram of growth-induced surface instabilities.," *Sci. Rep.*, vol. 5, p. 8887, 2015.

[147] B. R. Wiggs, C. A. Hrousis, J. M. Drazen, and R. D. Kamm, "On the mechanism of mucosal folding in normal and asthmatic airways," *J. Appl. Physiol.*, vol. 83, pp. 1814–1821, 1997.

[148] E. Kuhl, "Biophysics: Unfolding the brain," *Nat. Phys.*, vol. 12, pp. 1–2, 2016.

[149] S. Budday and P. Steinmann, "On the influence of inhomogeneous stiffness and growth on mechanical instabilities in the developing brain," *Int. J. Solids Struct.*, vol. 132-133, pp. 31–41, 2018.

[150] E. Kuhl, "Growing matter: A review of growth in living systems," *J. Mech. Behav. Biomed. Mater.*, vol. 29, pp. 529–543, 2014.

[151] E. K. Rodriguez, A. Hoger, and A. D. McCulloch, "Stress-dependent finite-growth in soft elastic tissues," *J. Biomech.*, vol. 27, pp. 455–467, 1994.

[152] K. Garikipati, E. M. Arruda, K. Grosh, H. Narayanan, and S. Calve, "A continuum treatment of growth in biological tissue: The coupling of mass transport and mechanics," *J. Mech. Phys. Solids*, vol. 52, pp. 1595–1625, 2004.

[153] V. A. Lubarda and A. Hoger, "On the mechanics of solids with a growing mass," *Int. J. Solids Struct.*, vol. 39, pp. 4627–4664, 2002.

[154] R. Skalak, S. Zargaryan, R. K. Jain, P. A. Netti, and A. Hoger, "Compatibility and the genesis of residual stress by volumetric growth," *J. Math. Biol.*, vol. 34, pp. 889–914, 1996.

[155] A. Yavari, "A geometric theory of growth mechanics," *J. Nonlinear Sci.*, vol. 20, pp. 781–830, 2010.

[156] J. D. Humphrey, "Continuum biomechanics of soft biological tissues," *Proc. R. Soc. A*, vol. 459, pp. 3–46, 2003.

[157] A. Menzel and E. Kuhl, "Frontiers in growth and remodeling," *Mech. Res. Commun.*, vol. 42, pp. 1–14, 2012.

[158] M. Epstein and G. A. Maugin, "Thermomechanics of volumetric growth in uniform bodies," *Int. J. Plast.*, vol. 16, pp. 951–978, 2000.

[159] G. A. Ateshian, "On the theory of reactive mixtures for modeling biological growth," *Biomech. Model. Mechanobiol.*, vol. 6, pp. 423–445, 2007.

[160] A. Grillo, G. Wittum, G. Giaquinta, and M. V. Mićunović, "A multiscale analysis of growth and diffusion dynamics in biological materials," *Int. J. Eng. Sci.*, vol. 47, pp. 261–283, 2009.

[161] J. D. Humphrey and K. R. Rajagopal, "A constrained mixture model for growth and remodeling of soft tissues," *Math. Models Methods App. Sci.*, vol. 12, pp. 407–430, 2002.

[162] K. Garikipati, "The kinematics of biological growth," *Appl. Mech. Rev.*, vol. 62, p. 030801, 2009.

[163] P. Ciarletta, L. Preziosi, and G. A. Maugin, "Mechanobiology of interfacial growth," *J. Mech. Phys. Solids*, vol. 61, pp. 852–872, 2013.

[164] D. E. Moulton, T. Lessinnes, and a. Goriely, "Morphoelastic rods. Part I: A single growing elastic rod," *J. Mech. Phys. Solids*, vol. 61, pp. 398–427, 2013.

[165] D. Ambrosi, G. A. Ateshian, E. M. Arruda, S. C. Cowin, J. Dumais, A. Goriely, G. A. Holzapfel, J. D. Humphrey, R. Kemkemer, E. Kuhl, J. E. Olberding, L. A. Taber, and K. Garikipati, "Perspectives on biological growth and remodeling," *J. Mech. Phys. Solids*, vol. 59, pp. 863–883, 2011.

[166] H. S. Hosseini and L. A. Taber, "How mechanical forces shape the developing eye," *Prog. Biophys. Mol. Biol.*, vol. 137, pp. 25–36, 2018.

[167] H. S. Hosseini, D. C. Beebe, and L. A. Taber, "Mechanical effects of the surface ectoderm on optic vesicle morphogenesis in the chick embryo," *J. Biomech.*, vol. 47, pp. 3837–3846, 2014.

[168] R. P. Araujo and D. L. S. McElwain, "A history of the study of solid tumour growth: The contribution of mathematical modelling," *Bull. Math. Biol.*, vol. 66, pp. 1039–1091, 2004.

[169] H. S. Hosseini, K. E. Garcia, and L. A. Taber, "A new hypothesis for foregut and heart tube formation based on differential growth and actomyosin contraction," *Development*, vol. 144, pp. 2381–2391, 2017.

[170] K. Efimenko, M. Rackaitis, E. Manias, A. Vaziri, L. Mahadevan, and J. Genzer, "Nested self-similar wrinkling patterns in skins," *Nat. Mater.*, vol. 4, pp. 293–297, 2005.

[171] B. Li, Y.-P. Cao, X.-Q. Feng, and H. Gao, "Surface wrinkling of mucosa induced by volumetric growth: Theory, simulation and experiment," *J. Mech. Phys. Solids*, vol. 59, pp. 758–774, 2011.

[172] P. Ciarletta, M. Destrade, A. L. Gower, and M. Taffetani, "Morphology of residually stressed tubular tissues: Beyond the elastic multiplicative decomposition," *J. Mech. Phys. Solids*, vol. 90, pp. 242–253, 2016.

[173] A. Buganza Tepole, C. Joseph Ploch, J. Wong, A. K. Gosain, and E. Kuhl, "Growing skin: A computational model for skin expansion in reconstructive surgery," *J. Mech. Phys. Solids*, vol. 59, pp. 2177–2190, 2011.

[174] A. DiCarlo and S. Quiligotti, "Growth and balance," *Mech. Res. Commun.*, vol. 29, pp. 449–456, 2002.

[175] Y. Du, C. Lü, W. Chen, and M. Destrade, "Modified multiplicative decomposition model for tissue growth: Beyond the initial stress-free state," *J. Mech. Phys. Solids*, vol. 118, pp. 133–151, 2018.

[176] L. A. Taber, "Biomechanics of growth, remodeling, and morphogenesis," *Appl. Mech. Rev.*, vol. 48, p. 487, 1995.

[177] J. E. Marsden and T. J. R. Hughes, *Mathematical Foundations of Elasticity*. Dover, 1994.

[178] G. A. Holzapfel, *Nonlinear Solid Mechanics: A Continuum Approach for Engineering*. John Wiley & Sons, 2000.

[179] P. Steinmann, *Geometrical Foundations of Continuum Mechanics: An Application to First- and Second-Order Elasticity and Elasto-Plasticity*. Springer, 2015.

[180] R. W. Ogden, "Large deformation isotropic elasticity - on the correlation of theory and experiment for incompressible rubberlike solids," *Proc. R. Soc. Lond. A*, vol. 328, pp. 567–583, 1972.

[181] A. Javili, B. Dortdivanlioglu, E. Kuhl, and C. Linder, "Computational aspects of growth-induced instabilities through eigenvalue analysis," *Comput. Mech.*, vol. 56, pp. 405–420, 2015.

[182] E. Kuhl, A. Menzel, and P. Steinmann, "Computational modeling of growth," *Comput. Mech.*, vol. 32, pp. 71–88, 2003.

[183] R. Moran, J. H. Smith, and J. J. García, "Fitted hyperelastic parameters for human brain tissue from reported tension, compression, and shear tests," *J. Biomech.*, vol. 47, pp. 3762–3766, 2014.

[184] J. Cappello, V. d'Herbemont, A. Lindner, and O. du Roure, "Microfluidic in-situ measurement of poisson's ratio of hydrogels," *Micromachines*, vol. 11, no. 3, 2020.

[185] M. Beatty and D. Stalnaker, "The poisson function of finite elasticity," *Journal of Applied Mechanics, Transactions ASME*, vol. 53, no. 4, pp. 807–813, 1986.

[186] L. A. Mihai and A. Goriely, "How to characterize a nonlinear elastic material? A review on nonlinear constitutive parameters in isotropic finite elasticity," *Proc. R. Soc. A*, vol. 473, p. 20170607, 2017.

[187] S. P. Timoshenko and J. M. Gere, *Theory of Elastic Stability*. McGraw-Hill, 1961.

[188] A. Javili, "A note on traction continuity across an interface in a geometrically non-linear framework," *Mathematics and Mechanics of Solids*, vol. 24, no. 8, pp. 2478–2496, 2019.

[189] N. Daher and G. A. Maugin, "The method of virtual power in continuum mechanics application to media presenting singular surfaces and interfaces," *Acta Mechanica*, vol. 60, no. 3-4, pp. 217–240, 1986.

[190] G. I. Barenblatt, "The formation of equilibrium cracks during brittle fracture. General ideas and hypotheses. Axially-symmetric cracks," *Journal of Applied Mathematics and Mechanics*, vol. 23, no. 3, pp. 622–636, 1959.

[191] G. I. Barenblatt, "The Mathematical Thsory of Equilibrium Cracks in Brittle Fracture (Initial Experiment for Hydogel as a Medium for...)," *Advances in Applied Mechanics*, vol. 7, pp. 55–129, 1962.

[192] D. Dugdale, "Yielding of steel sheets containing slits," *Journal of the Mechanics and Physics of Solids*, vol. 8, no. 2, pp. 100–104, 1960.

[193] Y. Wei and J. W. Hutchinson, *Interface strength, work of adhesion and plasticity in the peel test*, pp. 315–333. Dordrecht: Springer Netherlands, 1998.

[194] G. Alfano and M. A. Crisfield, "Finite element interface models for the delamination analysis of laminated composites: Mechanical and computational issues," *International Journal for Numerical Methods in Engineering*, vol. 50, no. 7, pp. 1701–1736, 2001.

[195] M. J. Van Den Bosch, P. J. Schreurs, and M. G. Geers, "On the development of a 3D cohesive zone element in the presence of large deformations," *Computational Mechanics*, vol. 42, no. 2, pp. 171–180, 2008.

[196] J. Reinoso, M. Paggi, and A. Blázquez, "A nonlinear finite thickness cohesive interface element for modeling delamination in fibre-reinforced composite laminates," *Composites Part B: Engineering*, vol. 109, pp. 116–128, 2017.

[197] L. Brassart, H. M. Inglis, L. Delannay, I. Doghri, and P. H. Geubelle, "An extended Mori-Tanaka homogenization scheme for finite strain modeling of debonding in particle-reinforced elastomers," *Computational Materials Science*, vol. 45, no. 3, pp. 611–616, 2009.

[198] M. Fagerström and R. Larsson, "Theory and numerics for finite deformation fracture modelling using strong discontinuities," *International Journal for Numerical Methods in Engineering*, vol. 66, no. 6, pp. 911–948, 2006.

[199] K. Park, G. H. Paulino, and J. R. Roesler, "A unified potential-based cohesive model of mixed-mode fracture," *Journal of the Mechanics and Physics of Solids*, vol. 57, no. 6, pp. 891–908, 2009.

[200] X. P. Xu and A. Needleman, "Numerical simulations of fast crack growth in brittle solids," *Journal of the Mechanics and Physics of Solids*, vol. 42, no. 9, pp. 1397–1434, 1994.

[201] M. Ortiz and A. Pandolfi, "Finite-deformation irreversible cohesive elements for three-dimensional crack-propagation analysis," *International Journal for Numerical Methods in Engineering*, vol. 44, no. 9, pp. 1267–1282, 1999.

[202] M. Charlotte, J. Laverne, and J. J. Marigo, "Initiation of cracks with cohesive force models: a variational approach," *European Journal of Mechanics, A/Solids*, vol. 25, no. 4, pp. 649–669, 2006.

[203] L. F. Kawashita and S. R. Hallett, "A crack tip tracking algorithm for cohesive interface element analysis of fatigue delamination propagation in composite materials," *International Journal of Solids and Structures*, vol. 49, no. 21, pp. 2898–2913, 2012.

[204] T. C. Gasser and G. A. Holzapfel, "Geometrically non-linear and consistently linearized embedded strong discontinuity models for 3D problems with an application to the dissection analysis of soft biological tissues," *Computer Methods in Applied Mechanics and Engineering*, vol. 192, no. 47-48, pp. 5059–5098, 2003.

[205] J. Mergheim and P. Steinmann, "A geometrically nonlinear FE approach for the simulation of strong and weak discontinuities," *Computer Methods in Applied Mechanics and Engineering*, vol. 195, no. 37-40, pp. 5037–5052, 2006.

[206] T. Chen, M. S. Chiu, and C. N. Weng, "Derivation of the generalized Young-Laplace equation of curved interfaces in nanoscaled solids," *Journal of Applied Physics*, vol. 100, no. 7, 2006.

[207] G. P. Moeckel, "Thermodynamics of an interface," *Archive for Rational Mechanics and Analysis*, vol. 57, no. 3, pp. 255–280, 1975.

[208] E. Fried and M. E. Gurtin, "Thermomechanics of the interface between a body and its environment," *Continuum Mechanics and Thermodynamics*, vol. 19, no. 5, pp. 253–271, 2007.

[209] E. Fried and R. E. Todres, "Mind the gap: The shape of the free surface of a rubber-like material in proximity to a rigid contactor," *Journal of Elasticity*, vol. 80, no. 1-3, pp. 97–151, 2005.

[210] Z. Hashin, "Thin interphase/imperfect interface in elasticity with application to coated fiber composites," *Journal of the Mechanics and Physics of Solids*, vol. 50, no. 12, pp. 2509–2537, 2002.

[211] V. Monchiet and G. Bonnet, "Interfacial models in viscoplastic composites materials," *International Journal of Engineering Science*, vol. 48, no. 12, pp. 1762–1768, 2010.

[212] Y. Benveniste, "Models of thin interphases with variable moduli in plane-strain elasticity," *Mathematics and Mechanics of Solids*, vol. 18, no. 2, pp. 119–134, 2013.

[213] A. Javili, P. Steinmann, and J. Mosler, "Micro-to-macro transition accounting for general imperfect interfaces," *Computer Methods in Applied Mechanics and Engineering*, vol. 317, pp. 274–317, 2017.

[214] M. Ben Amar and A. Goriely, "Growth and instability in elastic tissues," *J. Mech. Phys. Solids*, vol. 53, pp. 2284–2319, 2005.

[215] R. Ansari, V. Mohammadi, M. Faghih Shojaei, R. Gholami, and S. Sahmani, "Postbuckling characteristics of nanobeams based on the surface elasticity theory," *Compos. B Eng.*, vol. 55, pp. 240–246, dec 2013.

[216] S. Mora, T. Phou, J.-M. Fromental, L. M. Pismen, and Y. Pomeau, "Capillarity driven instability of a soft solid," *Phys. Rev. Lett.*, vol. 105, p. 214301, Nov 2010.

[217] F. dell'Isola and A. Romano, "On the derivation of thermomechanical balance equations for continuous systems with a nonmaterial interface," *International Journal of Engineering Science*, vol. 25, no. 11-12, pp. 1459–1468, 1987.

[218] F. dell'Isola, A. Madeo, and L. Placidi, "Linear plane wave propagation and normal transmission and reflection at discontinuity surfaces in second gradient 3D continua," *ZAMM Zeitschrift fur Angewandte Mathematik und Mechanik*, vol. 92, no. 1, pp. 52–71, 2012.

[219] F. dell'Isola, P. Seppecher, and A. Madeo, "How contact interactions may depend on the shape of Cauchy cuts in Nth gradient continua: Approach "à la D'Alembert"," *Zeitschrift fur Angewandte Mathematik und Physik*, vol. 63, no. 6, pp. 1119–1141, 2012.

[220] A. Javili, F. dell'Isola, and P. Steinmann, "Geometrically nonlinear higher-gradient elasticity with energetic boundaries," *Journal of the Mechanics and Physics of Solids*, vol. 61, no. 12, pp. 2381–2401, 2013.

[221] N. Auffray, F. dell'Isola, V. Eremeyev, A. Madeo, and G. Rosi, "Analytical continuum mechanics à la Hamilton-Piola least action principle for second gradient continua and capillary fluids," *Mathematics and Mechanics of Solids*, vol. 20, no. 4, pp. 375–417, 2015.